Computer modelling and experimental characterisation of amorphous semiconductor thin films and devices

A thesis pesented by
Wei Gao
to the University of Abertay, Dundee
(Collaborating establishment: the Department of APEME,
The University of Dundee)
in partial fulfilment of the requirements
for the degree of Doctor of Philosophy
September 1995

I certify that this thesis is the true and accurate version of the thesis approved by the examiners.

Signed [redacted] Date 15.12.95.
(Director of Studies)

To my wife Lucy

Acknowledgements

I would like to thank wholeheartedly my supervisors Dr. Charlie Main and Dr. Steve Reynolds for their constant support, advice, generosity with their time, enthusiasm and repeated explanations of amorphous semiconductor theory. I would also like to thank my external supervisor Dr. R.A.G. Gibson for his kind help in supplying the experimental samples and measurement facilities in the University of Dundee.

Thanks are also due to the following:
The School of Engineering, University of Abertay, Dundee.
The technical staff of the School of Engineering of the University of Abertay, Dundee
Dr. Rudi Brüggemann for his consistent help throughout the course of this study.
The University of Abertay for supplying the studentship.

Finally special thanks go to Patrick Webb for his consistent help on every aspect of this three year research project.

ABSTRACT

Computer modelling and experimental characterisation of amorphous semiconductor thin films and devices

Computer source codes for modelling amorphous semiconductors have been developed during the course of the study. The major program *SPIN.F* deals with steady state electronic processes for amorphous semiconductor materials and devices under different optical excitation and applied voltage conditions. It uses both standard one-electron state statistics and statistics developed for divalent states to deal with trapping and recombination processes via band tails and defect states. The latest defect pool model has been included into the model as well as other standard defect models.

Chapter 2 describes the mathematical basis of the *SPIN.F* modelling algorithms. A Gummel approach is used to solve Poisson's equation and the carrier continuity equations, modified to deal with special conditions in disordered materials, such as trapped space charge. Evaluation of the *SPIN.F* program accuracy and speed of computation for *p-i-n* diode structures is described in chapter 3. This testing gives an overview of the capability of the computer program and will be helpful for further applications on amorphous semiconductors.

A detailed description of the defect pool model and its incorporation into the numerical model is given in chapter 4. The original model formulation and parameters have been proved unsuitable when applied to model *p-i-n* diode performance. The reason for this is that the sensitivity of the dangling bond density on the Fermi-level position is overestimated giving an excessively high defect density near the doped layers, with the result that the modelled performance of the *p-i-n* diode is much poorer than for actual devices. A modification to the defect pool expression, changing the effective number of hydrogen atoms involved in defect formation kinetics is shown to give a substantial improvement. When comparing various defect models' fit to *p-i-n* diode *I-V* characteristics the best fit is now found for the modified defect pool model.

Computer simulation and error testing of the Dynamic Inner Collection Efficiency (*DICE*) method and the associated *SVD* solution algorithm for probing internal processes in solar cells is described in chapter 5. The *DICE* method is proved still to be a useful approach to investigate the inner characteristics or processes in semiconductor devices if some data processing treatments can reduce effects of measurement error. Otherwise it is shown that the random error introduced from spectral response measurement seriously affects the resolution of the final results. By minimising the error from the measurement, the accuracy of the final *DICE* profile may be kept within several percent. However, the work shows that only broad low resolution features may be revealed in practice by the *DICE* method.

A detailed study of a "photogating" effect has been carried out and described in chapter 6. A quantum efficiency (*QE*) much larger than unity has been found both theoretically and experimentally, under reverse bias voltage conditions for the first time. Experimental results show the *QE* increasing with reverse bias voltage, achieving values over 100 at high reverse bias voltage. From computer simulations, the underlying reason for the photogating effect has been clearly demonstrated, and a good fit has been achieved with experiment. The combination of strongly absorbed blue bias light from the *p*-side and green probe light from the *n*-side under high reverse bias gives optimum *QE* gain, and raises the possibility of an optically controlled amplifier which may be useful in photodetection. It is also shown by modelling that the *QE* is a sharply peaked function of defect density.

By using numerical modelling, a recently debated question regarding the carrier type controlling collection in a solar cell has been solved. During charge collection measurement, under reverse bias voltage, or short circuit condition, it is the carrier which has the shorter drift length which controls the behaviour of the device. A detailed analysis on this issue is described in chapter 6, showing a clear picture of the transport processes occurring during the measurement.

It is demonstrated in chapter 6 that the one dimensional computer model developed in this work can be applied to two or three dimensional situations under certain symmetry conditions. The method is applied to investigate the effects of surface states in coplanar photoconductivity in *n*-type *a-Si:H*. Although the model does not fully explain the experimental results, it demonstrates the consistency of this model with similar models proposed by other authors, and proves the validity of the approach.

Table of contents

Symbols and abbreviations list

c	capture coefficient or capture rate constant (cm^3s^{-1})
c_n, c_p	electron and hole capture coefficients by a defect state
c_{na}, c_{nd}	electron capture coefficients by conduction and valence band tail states
c_n^+, c_n^o, c_p^o, c_p^-	electron and hole capture coefficients by D^+, D^o, D^- respectively. The subscripts n and p are for carrier type, and superscripts are the charge states of the dangling bond state
$D(E)$	defect distribution in defect pool model ($cm^{-3}eV^{-1}$)
D_p, D_n	hole and electron diffusion constants (cm^2s^{-1})
D^+, D^o, D^-	density of three charged dangling bond states (cm^{-3})
$D^{+/o}$, $D^{o/-}$	D^+ to D^o transition and D^o to D^- transition
$Dope$	ionized dopant charge density (cm^{-3})
$E(x)$	electric field intensity(Vcm^{-1})
E_a, E_d E_{co}, E_{vo}	bandtail slopes for conduction and valence bandtails (eV).
E_c, E_v	conduction and valence bandedge energies,
e_n, e_p	electron and hole emission probabilities from a defect state (s^{-1})
E_F	Fermi energy at thermal equilibrium state (eV)
E_{Fp}, E_{Fn}	Fermi energy at doped p- and n-layers
E_g	bandgap (eV)
E_p	the most probable energy in the distribution of available sites for defect formation in defect pool model (eV)
$E^{+/o}$	energy for $D^{+/o}$ transition (eV)
F_o	photon flux ($cm^{-2}s^{-1}$)
F^+, F^o, F^-	occupation function of D^+, D^o, D^- states at steady states
$f(E)$	Shockley-Read-Hall steady state occupation function
$f_o(E)$	Fermi-Dirac thermal equilibrium occupancy
$f_a(E)$, $f_d(E)$	Shockley-Read-Hall steady state occupation function for conduction and valence bandtails
$f^+(E), f^o(E), f^-(E)$	occupation function of D^+, D^o, D^- states at thermal equilibrium states
$G(x)$	total generation rate in continuity equation ($cm^{-3}s^{-1}$)
G_c, G_v	density of states at conduction and valence band edges ($cm^{-3}eV^{-1}$)
$g(E)$	the distribution function of density of bandtail states ($cm^{-3}eV^{-1}$)
$g_a(E)$, $g_d(E)$	the distribution functions of density of states for conduction and valence bandtails ($cm^{-3}eV^{-1}$)
H	hydrogen density in *a-Si:H* material (cm^{-3})

In	number of points in an I-V curve
inl	number of energy divisions
jnl	number of spatial divisions
$J_p(x)$, $J_n(x)$	hole and electron current densities (Acm^{-2})
L	the thickness of the device (cm)
l_p, l_n	drift lengths for hole and electron (cm)
$N(E)$	bandtail density of energy states (cm^{-3})
N_c,N_v	effective density of states in conduction and valence band (cm^{-3})
N_{db}	density of dangling bond states (cm^{-3})
N_D, N_A	positive and negative dandling bond state densities (cm^{-3})
N_n	a defect density (cm^{-3})
N_{vo}	density of states at valence bandedge used in defect pool model ($cm^{-3}eV^{-1}$)
N^+, N^o, N^-, P^+, P^o, P^-	abbreviated terms used in occupancy expressions ($cm^{-3}eV^{-1}$)
$n(x)$, $p(x)$	free electron and hole densities at steady states (cm^{-3})
n_o, p_o	free electron and hole densities at thermal equilibrium (cm^{-3})
n_q	quality factor
n_t, p_t	densities of negative and positive bandtail states ($cm^{-3}eV^{-1}$)
$n_1(E)$, $p_1(E)$	effective electron and hole emission densities (cm^{-3})
n_1^+,p_1^+,n_1^o,p_1^o,n_1^-,p_1^-	effective electron and hole emission densities by D^+, D^o, D^- states
Q_{int}	interface charge density (Ccm^{-2})
q	the elementary electron charge(C)
R	total recombination rate in continuity equations ($cm^{-3}s^{-1}$)
R_a, R_d	capture coefficient ratio for conduction and valence bandtail states
R_b, R_m	best ranks for bifacial and monofacial method
R_D	ratio of capture coefficient between neutral and charged dangling bond states
R_{db}	recombination rate through dangling bond states ($cm^{-3}s^{-1}$)
R_t	ratio of capture coefficient between neutral and charged bandtail states
rf	reflection coefficient at the back electrode
rr, R_r	recombination rate ($cm^{-3}s^{-1}$)
T^*	frozen-in temperature ($°K$)
T_c	equivilent bandtail slope temperature [from $E_{co}=kT_c$] ($°K$)
t_n, t_p	thickness of n-type and p-type doped layers (cm)
U	correlation energy between D^o and D^- states (eV)
v	thermal velocity of the carriers ($cm\ s^{-1}$)
V_b	bias voltage (V)
V_T	thermal voltage ($=kT/q$) (V)
$\alpha(\lambda)$	absorption coefficient (cm^{-1})

γ	the power index in $\sigma_p \sim G^{\gamma}$ plot
δ	capture cross section (cm^2)
$\varepsilon, \varepsilon_o$	permittivities of silicon and vacuum (Fcm^{-1})
$\eta_q(x)$	internal collection efficiency
$\eta_{coll}(\lambda)$	external collection efficiency
$\eta_n(\lambda)$	normalized external collection efficiency
λ	wavelength of the light (cm)
μ_p, μ_n	hole and electron extended-state mobilities $(cm^2v^{-1}s^{-1})$
σ	pool width in defect pool and Gaussian distribution of defect states (eV)
σ_p	photoconductivity $(\Omega^{-1}cm^{-1})$
τ, τ_p, τ_n	life time of the carrier, hole and electron life times (s)
ψ	the potential in Poisson equation (V)
Δ	energy separation between negatively charged defects in *n*-type *a-Si:H* and positively charged defects in *p*-type *a-Si:H* (eV)
Φ_{jk}	normalized photon flux (k_{th} wavelength) absorbed in slice j
$\Psi(\lambda,x)$	absorbed number of photons in unit of thickness $(cm^{-3}s^{-1})$

Chapter one

GENERAL INTRODUCTION

1.1 History

Compared with other amorphous semiconductors, hydrogenated amorphous silicon (*a-Si:H*) was a late arrival, becoming a focus of interest in the 1970s. The first *a-Si:H* was made in the late 1960s, before which research was only on amorphous silicon without hydrogen, prepared by sputtering or by thermal evaporation. The unhydrogenated material has a very high defect density of energy states (*DOS*) so that it is impossible to dope, and exhibits no photoconductivity and the other desirable characteristics of a useful semiconductor. Electronic measurements were mostly limited to the investigation of conduction through the defect states (see Street 1991b).

Chittick and co-workers were the first to make hydrogenated amorphous silicon using glow discharge as the deposition technique (Chittick et al. 1969). The technique was basically the same as that used more recently, although the equipment was more primitive. These early experiments demonstrated the deposition processes of silicon films, the lack of conduction in defect states (implying a low defect density) and increased conduction due to impurities. The infra-red (*IR*) vibrations of silicon-hydrogen bonds were also observed although they were not recognized as such. The significance of the results was not recognised fully and the study was terminated.

In the following years, Spear and LeComber showed that the material had good electrical transport properties with a fairly high carrier mobility and also strong photoconductivity resulting from a very low defect density (LeComber and Spear 1970). A major turning point in the development of *a-Si:H* was the report in 1975 of detailed work on substitutional *n*-type or *p*-type doping by the addition of phosphine or diborane to the deposition gas (Spear and LeComber 1975). The significance of all these observations was widely acknowledged and the subsequent years saw a period of rapidly increasing interest in this form of amorphous silicon.

That *a-Si:H* could be successfully doped was surprising at the time. No doped amorphous semiconductors had been known prior to 1975. The explanation is that the positions of atoms in a glass or amorphous material will normally be such that all available electrons are taken up in bonds (for example Mott 1967). It appeared that the successful doping of amorphous silicon was due to the incorporation of hydrogen. The density of hydrogen in *a-Si:H* can be as high as 10%, which saturates the dangling bonds in the material and lowers the density of energy states in the bandgap so that a small fraction of the dopant atoms which are not incorporated according to their valency can shift the Fermi level significantly in the direction of the conduction or valence band. In the following years it became clear that the dopant atoms create also extra energy states

in the bandgap. Several authors (see for example Stutzmann et al 1987) proposed that these energy states are an essential feature of the doping mechanism and that the structure is not free from lattice constraints.

Due to this discovery, this semiconductor has been of interest not only to researchers but also to industry for many years. One of the reasons is that *a-Si:H* opened up interesting possibilities for the fabrication of cheap, thin-film electronic devices on large substrates, such as solar cells and driving circuitry for liquid crystal displays. A second reason is due to its scientific attractions, such as a continuously adjustable bandgap through alloying the material with nitrogen, carbon and germanium, efficient optical transitions, a usable carrier-diffusion length, and the capability of employing *n*- and *p*-type dopants.

Over the last 20 years, substantial progress has been made in understanding the properties of amorphous silicon, although many questions remain to be answered. Some of the important results which have led to the present level of understanding and application are discussed in the following section.

The development of electronic devices such as solar cells and thin-film transistors led to the fabrication of structures with layers as thin as a few nanometers. Progress in the understanding of the devices has been hindered because detailed structural information is lacking, interfaces between the different layers of the structures are sensitive to the execution of fabrication steps, and the equations which govern the electrical characteristics of the devices are difficult to solve. Generally, the equations can only be solved numerically with computer programs which have only recently become available.

Despite these problems, the technology base for amorphous silicon grew successfully during the 1980s. Due to great industrial interest, electronic devices such as solar cells and thin-film transistors have become fashionable. Since Carlson and Wronski in 1976 reported the first amorphous-silicon solar cell, this device has had much development over an extensive period of time. In the following 15 years, many companies in the United States, Japan and Europe established either amorphous-silicon solar-cell pilot production or full-scale manufacturing plants. (Wallace et al 1987), Several companies established a roll-on roll-off process, (Ovshinsky and Yang 1987 and Jacobsen et al 1987) and nearly 40% of the solar cell market was based on amorphous-silicon devices, overtaking other opponents and becoming dominant in the semiconductor product market share (see for example Carlson 1989). The *a-Si:H* solar cell has been used in consumer products such as calculators, watches, walklights, and battery chargers since its commercial introduction by Sanyo in 1980. However, since the price of large solar cell panels is still relatively high, the application in power generation markets was not practicable at that time.

In order to reduce the price, larger computer-integrated manufacturing (*CIM*) plant is one approach. There were various plants with a capacity of $10 MW_p/year$ existing

in many countries in the late 1980s, and a plant with a capacity of $>60MW_p/year$ was in planning (Carlson 1989).

Increasing the conversion efficiency is another approach to reducing the price of the solar cell panel. The reported conversion efficiency in the 1980's had reached 13% for triple-junction stacked solar cells in the laboratory (Ovshinsky 1985) and nearly 12% for a single-juction solar cell (Nakano et al 1987). It is unfortunate that continued development of amorphous silicon solar cells has been hindered by the so called Staebler-Wronski effect (Staebler and Wronski 1977) since the late 1970s. In the following years, even though the conversion efficiency of the solar cell in laboratories is still increasing slowly (a conversion efficiency of more than 13% has been reported on a small area ($1cm^2$) single *p-i-n* type *a-Si:H* solar cell, see for example Miyachi et al 1992), there have been little optimistic developments either in the fabrication technologies to stop the Staebler-Wronski effect or in the industrial applications. The stabilized conversion efficiency after one year outdoor operation has only stayed at 5% or so, and many production plants have closed. However, applications of amorphous silicon in consumer products such as calculators and watches and applications in thin film transistors for matrix addressing of liquid-crystal displays have been developing smoothly to such a level in the 1990s that scaled industrial production of these kinds of products has been achieved. An 8 inch flat-screen color *TV* has been seen in the market, and the lap-top computer using an amorphous silicon addressed flat screen has achieved a speed and quality comparable to that of the normal personal *PC*.

Besides the applications mentioned above, *a-Si:H* appears also to be suitable for use in other devices, such as image sensors, photodetectors and mass storage systems.

1.2 Properties of amorphous silicon

1.2.1 Structure

The disorder of the atomic structure is the main feature which distinguishes amorphous from crystalline materials. It is of particular significance in semiconductors, because the periodicity of the atomic structure is central to the theory of crystalline semiconductors. Bloch's theorem is a direct consequence of the periodicity and describes the electrons and holes by wavefuctions which are extended in space with quantum states defined by the momentum. The theory of lattice vibrations has a similar basis in the lattice symmetry. The absence of an ordered atomic structure in amorphous semiconductors necessitates a different theoretical approach. The description of these materials is developed instead from the chemical bonding between the atoms, with emphasis on the short range bonding interactions rather than the long range order.

Fig1.1 shows the structural difference between crystalline silicon and hydrogenated amorphous silicon material. It is a simplified two dimension structure. The

crystalline silicon structure shows a regular tetrahedral lattice structure with exactly the same bond angle and bond length for every *Si* atom. In the *a-Si:H* structure, the tetrahedral lattice structure is basically satisfied locally around each *Si* atom even though the bond angle and length are distorted to some extent, but due to the randomly located *Si* atoms, there are some broken bonds dangling in the structure which cause a high spin density observed in Electron Spin Resonance (*ESR*) measurements. These dangling bonds are the major source of the deep defect states.

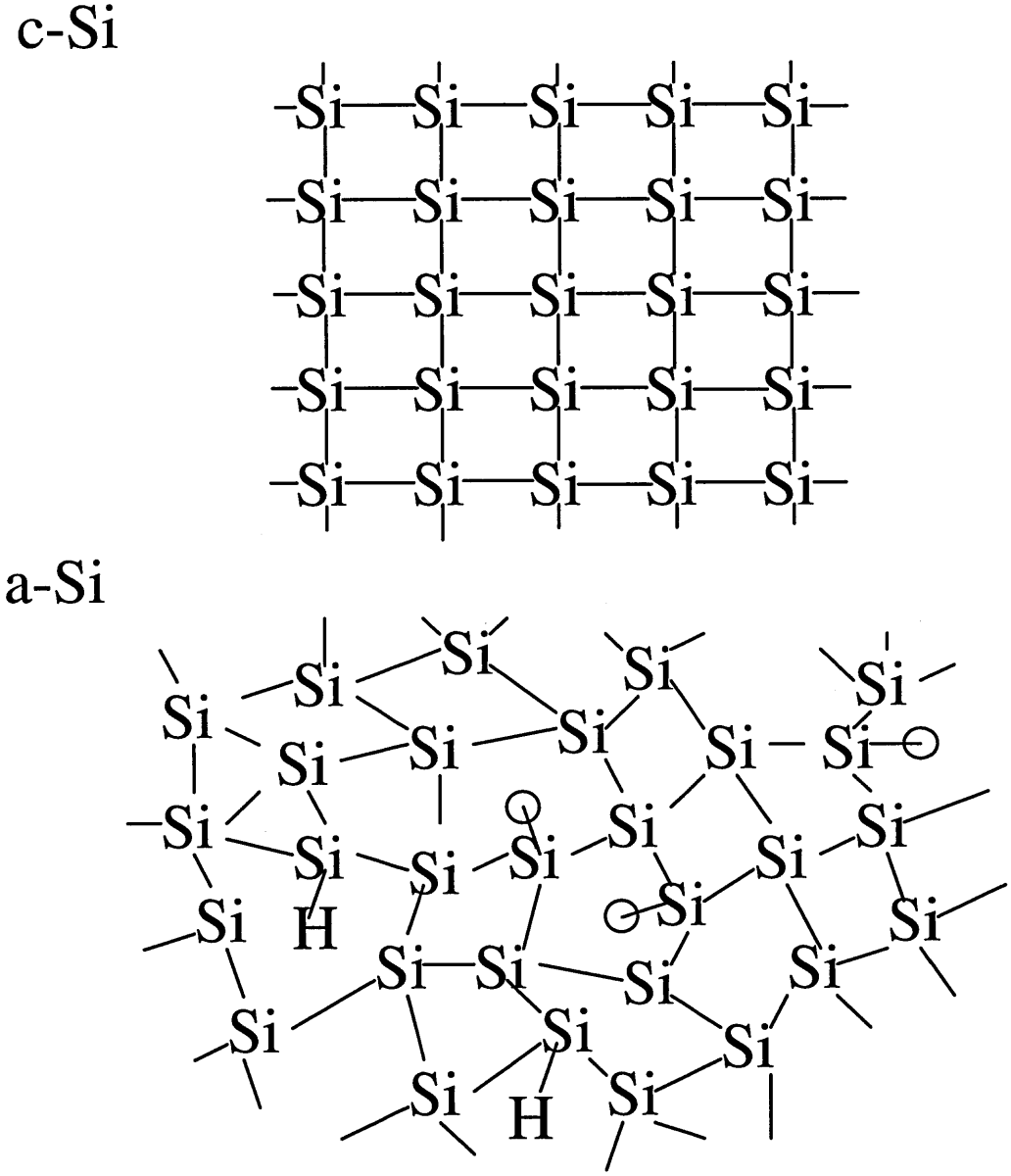

Fig 1.1 A schematic illustration of the atomic structural difference between crystalline silicon and hydrogenated amorphous silicon. In the *c-Si* case, all the silicon atoms are in a regular lattice, while in the *a-Si:H* case, the silicon atoms are not in regular lattice positions. The "H" in the figure are hydrogen atoms that saturate dangling bonds, while there are still some dangling bonds that are not saturated (circles in the figure). This is the source of the deep defect density.

When a hydrogen atom is involved, some of the dangling bonds are saturated, satisfying the 8-*N* rule, reducing the bulk spin density significantly, so that now addition of a dopant can shift the Fermi-level towards the conduction or valence band.

1.2.2. Density of energy states

The electrical and optical properties of an amorphous semiconductor are predominantly determined by energy states in the bandgap, since these states act as traps and recombination centres for excess carriers. The density of energy states, that is the number of energy states per unit volume per unit energy $N(E)$, is therefore an important parameter.

The first picture we have of the density of energy states is from Spear and LeComber's (1972) field-effect experiment. The experiment demonstrated that the Fermi level in *a-Si:H* could be moved by applying an electric field. Since the field-effect experiment probes energy states in the first hundred nanometers from the interface with the insulator and, therefore, also energy states related to the interface, this experiment gives only an upper limit for the bulk density of these energy states.

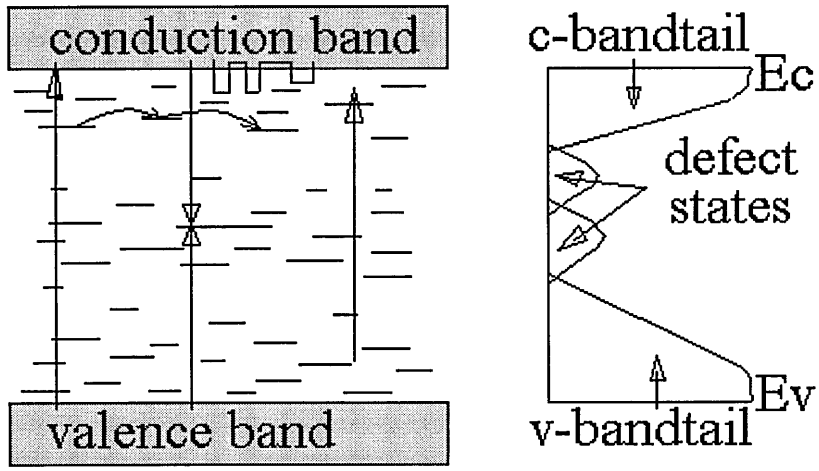

Fig 1.2 An illustration of the energy states distribution of amorphous semiconductors. Compared with their crystalline partner, there are bandtail states and defect states in the gap which change the electronic properties significantly. The mobility edges are not clearly defined and many transitions can happen between conduction and valence bands, bandtail states and dangling bond states.

A sketch of the density of energy states is shown in figure 1.2. On the left hand side of the figure, a few electronic processes are briefly illustrated between conduction band and valence band, eg. hopping transport via band tail states, recombination through dangling bond states and bandtail to bandtail transition etc. On the right hand side, is shown the bandtail state distribution (exponential bandtail with a linear part near the band edge) and defect states within the forbiden gap. Compared with their crystalline

counterparts, this extra density of states introduces much more complicated electronic processes besides the basic ones similar to crystalline materials. The energy levels E_c and E_v in the figure are the mobility edges of the conduction band and the valence band, and define the mobility gap. The mobility-edge concept originates from Mott (1967) who first pointed out its existence in weakly and moderately disordered systems. The mobility edge separates the localized energy states in the bandgap from the extended energy states outside the bandgap where the carrier transport is assumed to take place. The position of the mobility edges with respect to the optical band edges is not very well known since there is little experimental information on the density of energy states at the mobility edge. There are no well-defined band edges, but the density of energy states decreases smoothly but rapidly to low values in the band tails. The band tails are due to disorder in bond angles and bond lengths in the amorphous structure.

The valence-and conduction-band densities of energy states have been measured with the use of *x*-ray photoemission spectroscopy and inverse photoemission spectroscopy, respectively, (Jackson et al 1985). From inverse photoemission spectroscopy, the density of states at the conduction band mobility edge was found to be $4\text{-}8\times10^{21}\ cm^{-3}eV^{-1}$. Other estimations of the density of energy states at the mobility edge vary between 5×10^{20} and $5\times10^{21} cm^{-3}eV^{-1}$ (see for example Marshall et al. 1987a). The density of energy states at the valence-band mobility edge is believed to be in the same range. Because of these uncertainties, the mobility gap is not precisely known. If the mobility gap is taken as twice the conductivity activation energy at which the thermoelectric power changes sign, the mobility gap of undoped amorphous silicon is about $1.7eV$ (Stuke 1987). The measurements carried out by Wronski et al (1989) give a mobility gap of $1.9eV$

Within the tails, away from the mobility edges, the density of energy states decreases strongly in some tenths of electron volts. The valence band-tail state distribution is usually described by

$$N(E)=N(E_v)exp[-(E-E_v)/E_{vo}]$$

where $N(E_v)$ is the density of energy states at the valence-band edge energy $E_v(eV)$ and $E_{vo}(eV)$ the characteristic decay energy of the band tail. For the conduction band tail, a similar expression with a characteristic decay energy E_{co} is often be used. E_{vo} is about 0.045 eV and E_{co} is about 0.025 eV (Vanacek et al 1991).

The valence-band tail is somewhat broader than the conduction band tail due to the fact that the bonding energy states are more sensitive to bond angle variations in the structure than the anti-bonding energy states. From optical absorption spectra of high-quality amorphous silicon with various hydrogen concentrations of 9-14%, (Cody 1984), and from theoretical calculations, (Allan and Joannapoulos 1984), it can be concluded that hydrogen removes energy states from the top of the valence band tail.

The exponential form for the density of energy states in the band tails is not only used for amorphous silicon but also for various other amorphous semiconductors, since it facilitates the modelling of the carrier transport in these materials significantly. However, recent time-of flight experiments on hole and electron transport which provide information about the tail-state distributions suggest rather different tail state distributions for amorphous silicon.

Around midgap, there is a significant density of defect-related energy states which depends on the conditions under which the material was fabricated. Extensive work on defects in amorphous silicon led to the conclusion that the paramagnetic center which can be observed by electron-spin resonance measurements, and which is usually identified as the dangling bond, is the predominant defect center. There is no experimental evidence for a significant density of other energy states around midgap which are spinless. Therefore, dangling bonds are assumed to be the predominant defect in the present work.

The dangling bond is a defect which can be positive (D^+), neutral (D°) or negative (D^-). Important parameters are the energy distribution of the D° energy states and the correlation energy which is the energy difference between the two-electron D^- energy state and the one-electron energy D° state. In view of the general importance of the dangling bond, it is surprising that there has been so much controversy over the values of these parameters. Based on different measurements in different kinds of samples, LeComber and Spear(1986) compiled the published values for the energy of the D° state. They found the energy position for D° can vary from $0.9eV$ to $1.3eV$ below the conduction band mobility edge E_c. The correlation energy U is also not known accurately. Early measurements (see for example Stutzmann and Jackson 1987) relied on the assumption that the energy dependence of the density of states does not change with doping, which is not correct according to the more recent defect pool model. Recent measurements (Lee and Schiff 1992) give U values between 0.2 and $0.3eV$ with a relatively low accuracy. The inconsistency of these measurements has resulted in another hypothesis that the location of the dangling bond energy states may not be fixed, which was the starting point of the defect pool model (Smith and Wagner 1989) and the defect relaxation model (Cohen et al 1992, Farmer and Su 1993 and Cohen and Leen 1994) which are popular at the time of writing.

1.3. Computer modelling of an amorphous silicon solar cell.

The interest in the numerical simulation of semiconductor devices began nearly 30 years ago, when it became clear that this approach could be successfully used to explain the operation of many solid-state devices. Since that time, this field of research has continued to grow and has become firmly established as a major area of interest in

semiconductor device technology, receiving considerable publicity with entire conferences dedicated to the subject.

Prior to the widespread availaiblity of powerful modern digital computers, semiconductor problems were solved using analytical techniques with closed-form solutions. This technique, which was pioneered by workers such as Shockley (1952), approached the problem by dividing the device into areas over which linear approximations applied ('segmentation'), joined by appropriate boundary conditions. This method of device analysis has been extended to include carrier velocity saturation and two-dimensional effects in silicon and gallium arsenide devices. However, although this approach allows a rapid analysis and provides a basic insight into device behaviour, it cannot produce the generalised and accurate solutions required for device design and optimisation. These types of application demand the type of rigorous solutions obtained only from numerical simulations.

Early numerical device simulations were centred around one-dimensional models. A steady-state (short for non-equilibrium steady state) transistor simulation was described by Gummel as early as 1964. Limitations in computing power meant that numerical device simulations at the time were limited to one-dimensional models based on a set of 'phenomenological equations'. With the quickly developing computer technology, two and three dimension models have been applied to different semiconductor devices which provide many powerful approaches for researchers all over the world (see Snowden 1985 for details).

Computer modelling of amorphous silicon solar cells began to develop over ten years ago due to the special demand for explaining the electronic processes of *a-Si:H* material and devices. Computer modelling for *a-Si:H* takes many advantages from its precursor crystalline silicon and other semiconductors. Although the defect states in the amorphous silicon case introduce much more complicated electronic processes, the special device geometry possessed by *a-Si:H* solar cells and *p-i-n* devices studied in this work allows the problem to be solved by only one dimension modelling.

The definition of true computer modelling requires an approach where Poisson's equation and the two continuity equations are all solved using numerical techniques. Under this definition, the first comprehensive computer simulation of an amorphous silicon *p-i-n* solar cell was carried out by Swartz (1982) of *RCA* laboratories. In that work the Scharfetter-Gummel (1969) function was used and Poisson's equation and the two continuity equations were solved numerically. Swartz assumed, however, a single Shockley-Read-Hall (Shockley and Read 1952, Hall 1952) recombination level and ignored trapped charge in the *i*-layer in this computer model. The former assumption is incorrect because *a-Si:H* has a complicated *DOS* with a number of levels participating in recombination. The latter assumption has important consequences for the performance of *a-Si:H* based devices since trapped charge dominates the space charge in amorphous semiconductor materials. In addition Swartz's model treated the carrier transport in the

doped contact layers by assuming boundary conditions at the *p/i* and *n/i* interfaces; the model did not address transport nor electrostatics in the doped layers.

In the same year Chen and Lee (1982) reported a computer model for analyzing *a-Si:H p-i-n* and Schottky diodes that used a numerical solution scheme based on integral techniques to solve Poisson's equation and the continuity equation. Like Swartz's approach, this model used a single-level Shockley-Read-Hall formalism to compute recombination, hence it did not fully account for situations where recombination is occurring in a variety of states across the gap. Their work did, however, for the first time allow for the possibility of band tail states. These band tails could only trap in their computer model and did not participate in recombination. In their model - and in a succession of subsequent computer models -the band tail states were represented by an exponential tail of acceptor like states (neutral when empty; negatively charged when occupied by an electron) coming out the conduction band and an exponential tail of donorlike states (neutral when occupied by an electron, positively charged when empty) coming out from the valence band. For the boundary conditions needed in this solution scheme, they fixed the front and back surface values of the potential and they fixed the electron and hole concentrations at the front and back contacts at their thermodynamic equilibrium values. This last statement means that they assumed ideal ohmic contacts. However, they did not clearly specify whether these "boundaries" are the boundaries of the *i*-layer or of the external contacts to the doped layers.

Ikegaki et al (1985) also developed a similar computer model and used it to model *a-Si:H p-i-n* solar cells. It also only allowed for a single recombination level. However, rather than forcing the carrier populations to their thermodynamic equilibrium values at the device boundaries, they used recombination velocities at the *p/i* and *n/i* interfaces as boundary conditions. Hence, they too do not consider the transport kinetics in the p^+- and n^+-layers. However, their model did represent an evolutionary step toward a more correct and complete computer model.

In 1985 Hack and Shur published the first computer modelling work for solar cells that tried to account for the fact that a variety of gap states can support recombination and charge storage and tried to allow for a more complete *DOS*. They solved the three governing equations (Poisson's equation and the two free carrier continuity equations) by using a more general *DOS* profile than used by earlier workers and, as noted, accounted for both trapping and recombination in these states. Their gap state model used an exponential conduction band tail of acceptorlike states and a valence band tail of donorlike states. This DOS picture used by Hack and Shur marks the first published use of a computer model that allowed both *DOS* variation across the gap as well as trapping and recombination in all those states. The model incorporated band tails, found in all semiconductors to various degrees (even crystalline semiconductors but there they are very sharp) and a mid-gap *DOS* which in any semiconductor can come from defects and which in *a-Si:H* comes from dangling bonds. In Hack and Shur's model only

the Simmons-Taylor (1971) approximation was used to compute the occupancy of this *DOS*. In addition the Hack and Shur model did consider the transport kinetics in the doped layers, but assumed ideal ohmic contacts.

At nearly the same time, Schwartz et al (1984) published a computer model that allowed an even more general *DOS* to be used than that of Hack and Shur. In its more developed forms this model included amphoteric dangling bond states in the gap where occupancy was determined by the statistics developed by Sah (1967). This model initially only assumed ideal ohmic contacts but this restriction was removed with subsequent work.

Pawlikiewicz and Guha (1988) used a computer model with an approach similar to that of Hack and Shur, for a more general *DOS* distribution. They simulated *a-Si:H p-i-n* devices using a two donor - two acceptor set of exponentials to describe both the tail states and the deep states of *a-Si:H* and had the computer determine their occupancy with the approximation of Taylor-Simmons (one-electron state) statistics. The evolutionary step in their model was that it allowed for band-related properties that can vary with position, however, the boundary condition used in their model assumed ideal ohmic contacts.

Tasaki et al (1988) also reported a computer model that has been developed to address the physical problems present in *a-Si:H*-based *p-i-n* heterojunction solar cells. Hence this model includes a *DOS* picture for the whole gap, of several materials and accounts for recombination and trapping in these states. The model use exponential and discrete levels for mid-gap states. The model allows for discontinuities in semiconductor properties at the heterojunction and can even simulate graded materials. They used the Taylor-Simmons statistics in the solution scheme. The latter is used to compute trapped charge and recombination through localized states.

Another model developed by Misiakos and Lindholm (1988) solves Poisson's equation and the continuity equations using an exponential distribution for acceptor- and donor-like states in the bandgap. Recombination and trapped charge were computed assuming a $T=0°K$ occupation function for the localized states. The boundary conditions for the minority carriers were surface recombination speeds that characterize minority current flow across the contacts. This model also assumed that majority carrier concentrations are not altered from their equilibrium values at the front and back contacts under different bias and illumination conditions.

Also in 1988, McElheny et al published their computer model called *AMPS*. Based on previous work, this model allows a complete arbitrary distribution of gap states which can vary with energy and with position. Two exponential expressions represent two sets of bandtail states. The model allows extensive flexibility on input parameters. The capture cross sections, the carrier mobilities and electron and hole affinities or even the mobility gap can all vary with energy and position. The model includes surface recombination speed in the boundary conditions and also takes the electron and hole

affinities into account on the boundaries. It is said to be the most general transport-simulation computer program that has been developed for analyzing semiconductor device hehaviour under illumination in one dimension. However, it only uses Shockley-Read-Hall statistics to deal with trapping and recombination processes through the localised states and does not take the amphoteric dangling bond characteristics into account.

The one dimension computer models for amorphous silicon *p-i-n* devices have been developed successfully as outlined above. They have been used to solve many different problems occurring during research on these materials and devices. However, there are still quite a few technological problems in modelling itself which can not be successfully tackled. For example, the boundary conditions have always been a difficult problem for computer models. Also, with the development of theories of defect formation, the algorithm to deal with the midgap density of states has become more and more complicated, and this is not to mention the time dependency of Staebler-Wronski degradation through illumination. As computer models advance, becoming more complete, the assumptions on transport and recombination mechanisms may be reduced, but it appears that the physical model development may result in a growing list of parameters which may be less accurately known.

1.5. The scope of this thesis

This thesis is dedicated to the following topics

(1). Source code. Since there is no similar computer program commerically available dealing with various aspects of electronic transport for amorphous semiconductors in the way we wish to pursue, the first target of this thesis is to describe the setting up of the *SPIN.F* Fortran program. This program deals with the steady state photoconductivity of amorphous semiconductor devices. To deal with the trapping and recombination processes due to the midgap density, Shockley-Read-Hall statistics are used to calculate the trapping and recombination processes via two exponential bandtail states, and in addition the modified statistic developed e.g. by Main et al (1990) is used to deal with the trapping and recombination processes via dangling bond states. The model allows three dangling bond distributions in the midgap, also three dangling bond distributions with position. The most updated defect formation mechanism - the defect pool model is also included in the program.

(2). Test of the model. The source code needs to be tested under different circumstances before it can be treated as a useful tool for analysing electronic processes occurring in amorphous semiconductor material and devices.

(3). Application of the model. The program has been used on several practical problems encountered in the research project. Computer modelling is demonstrated to be of great

use in finding explanations for these problems. The applications covered in this thesis include

(i). Quantum efficiency much greater than unity

(ii). The controlling carrier type in charge collection;

(iii). The *DICE* method and

(vi). the application to two dimensional situations such as the *TFT* .

(4). A special chapter has been dedicated to the defect pool model. The full details of the installation procedures for this defect generation mechanism are described. The basic testing of the model's characteristics is carried out. Based on the knowledge gained from the modelling, an application of the defect pool model is demonstrated which shows a good fit of this particular model to experimental measurements.

Chapter two

COMPUTER MODEL

2.1 Introduction

In the past decade, computer modelling has become an increasingly popular tool for analyzing the behaviour and performance of amorphous silicon solar cells, and for optimizing the design of amorphous semiconductor devices structure (see Rubinelli et al 1992 for an overview).

Comprehensive modelling of semiconductor devices requires simultaneous solution of three coupled differential equations, Poisson's equation for electric potential, and the two continuity equations for electron and hole currents. As a result of the above coupling, electron and hole densities are nonlinear functions of the electric potential which leads to the nonlinear Poisson equation.

One conventional approach to the numerical solution of the nonlinear Poisson equation is based on the application of Newton's method to simultaneous discretized equations. This approach encounters the following well-known difficulties. First, Newton's method has local convergence. This means that the method converges only if the initial guess is close enough to the actual solution. Secondly, numerical implementation of Newton's method requires the solution of simultaneous linear algebraic equations to update each previous iteration. This leads to high storage demands, especially for fine meshes. This partially explains why supercomputers are more often being used for the numerical modelling of semiconductor devices.

Gummel's method is an alternative method based on a highly effective decoupling algorithm that is heavily used in crystalline semiconductor device simulation (Gummel 1964). Using a nonlinear modification of Poisson's equation by taking into account the exponential dependence of electron and hole density on electrostatic potential, Gummel proposed an iterative scheme that was recently proven rigorously to be convergent for realistic device geometries in one, two, and three dimensions. In hydrogenated amorphous silicon based devices however, there is the additional problem that the dynamics of trapped electrons and holes are coupled to the dynamics of conduction electrons and holes and one must adapt the classical Gummel method to account for this fact.

Using the classic Gummel algorithm to simulate transport processes in amorphous silicon solar cells has been thought an economical way to improve the performance of the devices. Several programs have been produced in the last few years which have been used intensively on amorphous silicon solar cells and other devices (for example Hack and Shur 1983, or Gray 1989, also see chapter 1 of this thesis). Recently, the computer models have been aiming to be the most inclusive of detail and closest to

realistic device structure and physical characteristics (for example McElheny et al 1988). This means, in the special case of *a-Si:H* devices, the best choice of boundary conditions and the most reliable results from defect formation mechanism research are applied. The program used in this thesis is called *SPIN.F* which stands for Steady state simulation for *PIN* solar cells. In this program, the most recently developed defect formation mechanism model - the defect pool model is included as well as the traditional 'standard' models.

2.2 Amorphous semiconductor theory

The most significant differences between amorphous semiconductors and their crystalline counterparts are the bandtail states due to the distorted bond length and angle and the midgap defect states due to dangling bonds ie. unsaturated broken bonds. Even if we ignore the difficulties in defining the mobility edges (ie to decide the band gap), the electronic transport has already become much more complicated due to the inclusion of trapping and recombination processes via distributions of bandtail states and dangling bond states. In addition, the Poisson equation now includes the trapped space charge density in both bandtail states and dangling bond states. During the processes of solving the transport equations, the change of trapped space charge density arising from the change of free electron and hole densities has to be taken into account in every iteration.

2.2.1 Charge density in the bandtail states

We adopt the simplified single exponential bandtail model, in which the conduction and valence bandtail density of states can be expressed as

$$g_a(E)=G_c exp(-(E_c-E)/E_a) \tag{2.1}$$

$$g_d(E)=G_v exp(-(E-E_v)/E_d) \tag{2.2}$$

where G_c and G_v is the band edge density of states which we assume to be equal at both band edges. E_c and E_v are conduction and valence band edge energies; E_a and E_d are the bandtail slopes. Due to the characteristics of the amorphous silicon structure, the valence bandtail slope will be larger than conduction bandtail slope.

In thermal equilibrium, the charge distribution function is simply the Fermi-Dirac distribution since in this situation no nett electron and hole transitions occur between conduction and valence band and defect states in the gap. We then have

$$f_o(E)=\frac{1}{1+\exp\left(\frac{E-E_F}{kT}\right)} \tag{2.3}$$

where E_F is the Fermi-energy in thermal equilibrium.

In the non-equilibrium steady state, the Fermi-Dirac distribution is no longer valid, and special treatment must be invoked to derive the occupancy expression which is the so called Shockley-Read-Hall statistic (see Simmons and Taylor 1971 for details):

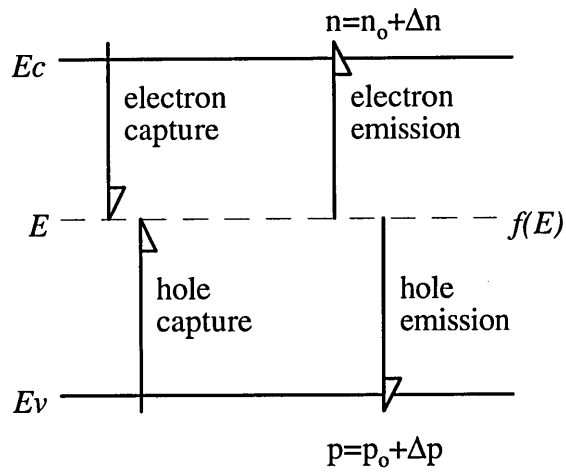

Fig 2.1 schematic of the electron and hole transitions in the non-equilibrium steady state.

Fig 2.1 shows the four transitions considered, which determine the steady state occupancy function $f(E)$. The band-band transition is not included here. The occupancy statistic can be written down simply, using transition probablilities for each mechanism ie,

$$f(E) = \frac{prob.\ of\ state\ gaining\ electron/\ s}{prob.\ of\ all\ possible\ transitions/\ s}$$

$$so\ we\ have\ f(E) = \frac{c_n\, n + e_p}{e_n + c_n\, n + e_p + c_p\, p}$$

where n and p are free electron and hole densities, c_n and c_p are electron and hole capture coefficients by that state, e_n and e_p are electron and hole emission probabilities from that state. Parameters c_n and e_n are not independent of each other, as in thermal equilibrium where capture and release rates balance in detail we have:

$$c_n n_o[1-f_o(E)] = e_n f_o(E)$$

where n_o is free electron density in the thermal equilibrium state

so giving $\quad e_n = c_n n_o \dfrac{1-f_o(E)}{f_o(E)}.$

Using the standard expression for $n_o = N_c \exp\left(-\dfrac{E_c - E_F}{kT}\right)$ and the expression for $f_o(E)$

we have $\quad e_n = c_n N_c \exp\left(-\dfrac{E_c - E}{kT}\right).$

Defining $$n_1(E) = N_c \exp\left(-\frac{E_c - E}{kT}\right)$$

which is an effective 'electron emission density' for the state, equal to the conduction band electron density if E_F were at the trap level E, we have $e_n = c_n\, n_1$ and with a similar derivation we have $e_p=c_p p_1$ where p_1 is the effective hole emission density for the state. With this notation we have the steady state occupancy at any energy level E as

$$f(E) = \frac{c_n\, n + c_p\, p_1}{c_n\, n_1 + c_n\, n + c_p\, p_1 + c_p\, p} \tag{2.4}$$

It should be noticed that both capture coefficients may be energy dependent, but in order not to introduce too much complexity, a further simplification is convenient. For the conduction bandtail, we assign ratio $R_a=c_n/c_p$. At these accepter like states, c_n represents electron capture into a neutral state and c_p represents hole capture into a negative state. Similarly for the donor like valence bandtail states, we assign $R_d=c_n/c_p$. Thus it is likely that $R_a<<1$ and $R_d>>1$ but not necessarily true.

2.2.2 Recombination through bandtail states

In the non-equilibrium steady state, the recombination rate at any state with energy E is equal to the difference between the total electron trapping rate and the total electron emission rate back the conduction band. i.e., any electron which is not released must have recombined. For any given level, the recombination rate can be written as

$$rr = [c_n n(1-f(E)) - c_n n_1 f(E)]g(E)$$

substituting the expression for $f(E)$ and simplifying we have

$$rr = c_n\, g(E)\left[\frac{np - n_o\, p_o}{R(n + n_1) + p + p_1}\right].$$

This is also a general expression for any state in the gap on the condition that the ratio of electron and hole capture coefficients R is energy independent. For the total recombination rate via bandtail states, the following integral is the solution

$$R_r = \int_{E_v}^{E_c} (np - n_o\, p_o)\left\{\left[\frac{c_{na}\, g_a(E)}{R_a(n + n_1(E)) + p + p_1}\right] + \left[\frac{c_{nd}\, g_d(E)}{R_d(n + n_1(E)) + p + p_1}\right]\right\} dE \tag{2.5}$$

When the steady state is changed to the thermal equilibrium state, $np=n_o p_o$, the net recombination rate reduces to zero automatically.

2.2.3 Occupation function for dangling bond states

The difference between bandtail states and dangling bond states is that the dangling bond states have three different charge states, ie +1, 0 and -1 electronic charges corresponding to a dangling bond being occupied by 0, 1 and 2 electrons. Due to this amphoteric characteristic of dangling bond states, the Fermi-Dirac distribution function cannot be used, and instead, a special treatment is needed.

At thermal equilibrium, for dangling bond states with two transition energy levels E and $E+U$ for transitions $D^{+/o}$ and $D^{o/-}$, respectively, a similar derivation to that in eq. 2.4 can be done to give the occupation function for each charge state as

$$f^{+}(E)=\frac{1}{1+2\exp\left[(E_F-E)/kT\right]+\exp\left[(2E_F-2E-U)/kT\right]} \tag{2.6}$$

$$f^{0}(E)=\frac{2\exp\left[(E_F-E)/kT\right]}{1+2\exp\left[(E_F-E)/kT\right]+\exp\left[(2E_F-2E-U)/kT\right]} \tag{2.7}$$

$$f^{-}(E)=\frac{\exp\left[(2E_F-2E-U)/kT\right]}{1+2\exp\left[(E_F-E)/kT\right]+\exp\left[(2E_F-2E-U)/kT\right]} \tag{2.8}$$

These distribution functions apply to discrete dangling bond states or continuously distributed states. In these expressions, it is worth pointing out that the correlation energy U is not yet known accurately.

In the non-equilibrium steady state, the derivation becomes more complicated. Generally, the occupation function for dangling bond states can be expressed as following (see Okamoto et al, 1984, Main 1985 for details):

$$F^{+}=\frac{P^{0}P^{-}}{N^{+}P^{-}+P^{0}P^{-}+N^{0}N^{+}} \tag{2.9}$$

$$F^{-}=\frac{N^{0}N^{+}}{N^{+}P^{-}+P^{0}P^{-}+N^{0}N^{+}} \tag{2.10}$$

$$F^{0}=\frac{N^{+}P^{-}}{N^{+}P^{-}+P^{0}P^{-}+N^{0}N^{+}} \tag{2.11}$$

where

$$P^{o}=n_1{}^{+}c_n{}^{+}+p\,c_p{}^{o}$$
$$P^{-}=n_1{}^{o}c_n{}^{o}+p\,c_p{}^{-}$$
$$N^{o}=n\,c_n{}^{o}+p_1{}^{-}c_p{}^{-}$$
$$N^{+}=n\,c_n{}^{+}+p_1{}^{o}c_p{}^{o}$$

In these expressions, $c_n^+, c_n^o, c_p^o, c_p^-$ are electron and hole capture coefficients by D^+, D^o, D^- respectively. Superscripts stand for the charge states of the defect state, subscripts stand for the carrier type being captured. The group of notations with subscript 1 have similar meanings to their counterparts in the bandtail case, and are given below.

$$n_1^{\,0}(E) = 2N_C \exp\left(-\frac{E_C - E - U}{kT}\right) \qquad n_1^{\,+}(E) = 0.5N_C \exp\left(-\frac{E_C - E}{kT}\right)$$

$$p_1^{\,0}(E) = 2N_V \exp\left(-\frac{E - E_V}{kT}\right) \qquad p_1^{\,-}(E) = 0.5N_V \exp\left(-\frac{E + U - E_V}{kT}\right)$$

It can be seen for example that a dangling bond has *two* electron emission terms, $n_1^{\,+}$ and $n_1^{\,0}$ in contrast to the single term for a bandtail state. These terms denote the emission of an electron to the conduction band from a singly occupied D^o defect and a doubly occupied D^- defect respectively, and include the effects of state degeneracy in the numerical prefactor.

2.2.4 Recombination through the dangling bond states

Also, in a similar way to the bandtail situation, the recombination via dangling bond states can still be expressed as the difference between the electron capture to and emission from the dangling bond states, only now we are dealing with two sets of transitions for each state, i.e. $D^{+/o}$ and $D^{o/-}$ transitions at different energy levels, E and $E+U$, giving:

$$R_{db} = nc_n^+ N_{db} F^+ + nc_n^0 N_{db} F^0 - n_1^+ c_n^+ N_{db} F^0 - n_1^0 c_n^0 N_{db} F^- \tag{2.12}$$

where N_{db} is the total dangling bond density in that defect state.

If all the expressions in this equation were simply expanded using eqs. 2.9 - 2.11 the result becomes very cumbersome. Main et al (1990) obtained a simpler exact result in this case, giving an explicit expression as follows:

$$R_{db} = (np - n_o\, p_o) N_{db}\, F^o \left[\left(\frac{n}{c_p^o} + \frac{p_1^o}{c_n^+} \right)^{-1} + \left(\frac{n_1^o}{c_p^-} + \frac{p}{c_n^o} \right)^{-1} \right] \tag{2.13}$$

the first term in the square bracket corresponds to the recombination via electron capture by a D^+ state and then hole capture by the resulting D^o state, while the second one

corresponds to the recombination via electron capture by a D^0 state and then hole capture by the resulting D^- state.

2.3 Implementation of numerical model

In this section, the semiconductor equations governing amorphous silicon devices are introduced, and the solution algorithm is described.

2.3.1 The semiconductor equations

The semiconductor device operation is governed by the Poisson equation and by the continuity and current-density equations. For the amorphous silicon solar cell, it is quite accurate to treat it as a one-dimensional device. In the steady state, no time factor is involved, and the equations can be simplified to the following form:

$$\frac{d^2\psi}{dx^2} = -\frac{e}{\varepsilon\varepsilon_0}(p - n + p_t - n_t + N_D - N_A - Dope) \tag{2.14}$$

$$\frac{dJ_p}{dx} = q(G - R) \tag{2.15}$$

$$\frac{dJ_n}{dx} = -q(G - R) \tag{2.16}$$

$$J_p = -q\mu_p\, p\frac{d\psi}{dx} - qD_p\frac{dp}{dx} \tag{2.17}$$

$$J_n = -q\mu_n\, n\frac{d\psi}{dx} + qD_n\frac{dn}{dx} \tag{2.18}$$

where x is the space coordinate (cm)

ψ is the potential (V)

R is the recombination rate of electrons and holes ($cm^{-3}s^{-1}$)

G is the generation rate of electrons and holes ($cm^{-3}s^{-1}$)

J_p and J_n are the hole and electron current densities (Acm^{-2})

p and n are free hole and electron densities

p_t and n_t are the bandtail charge state densities

N_D and N_A are dangling bond charge densities (+ and - respectively)

$Dope$ is ionized dopant charge density

q is the elementary charge(C)

ε and ε_o are the permittivities of the semiconductor and the vacuum (Fcm^{-1})

μ_p and μ_n are the hole and electron extended-state mobilities ($cm^2v^{-1}s^{-1}$)

D_p and D_n are the hole and electron diffusion constants (cm^2s^{-1})

Variables ψ, R, G, n, p, J_p, J_n, p_t, n_t, N_D, N_A and *Dope* are the functions of the space coordinates x, and the three basic variables $n(x)$, $p(x)$, $\psi(x)$ are coupled.

2.3.2 Numerical model overview

It is not possible to solve the semiconductor equations analytically. A numerical method to deal with the equations for crystalline semiconductors was set up by Gummel (1964). Fig 2.2 is the flow chart of the present program developed specifically for amorphous semiconductors to illustrate the algorithm which has been used in this project to solve the equations.

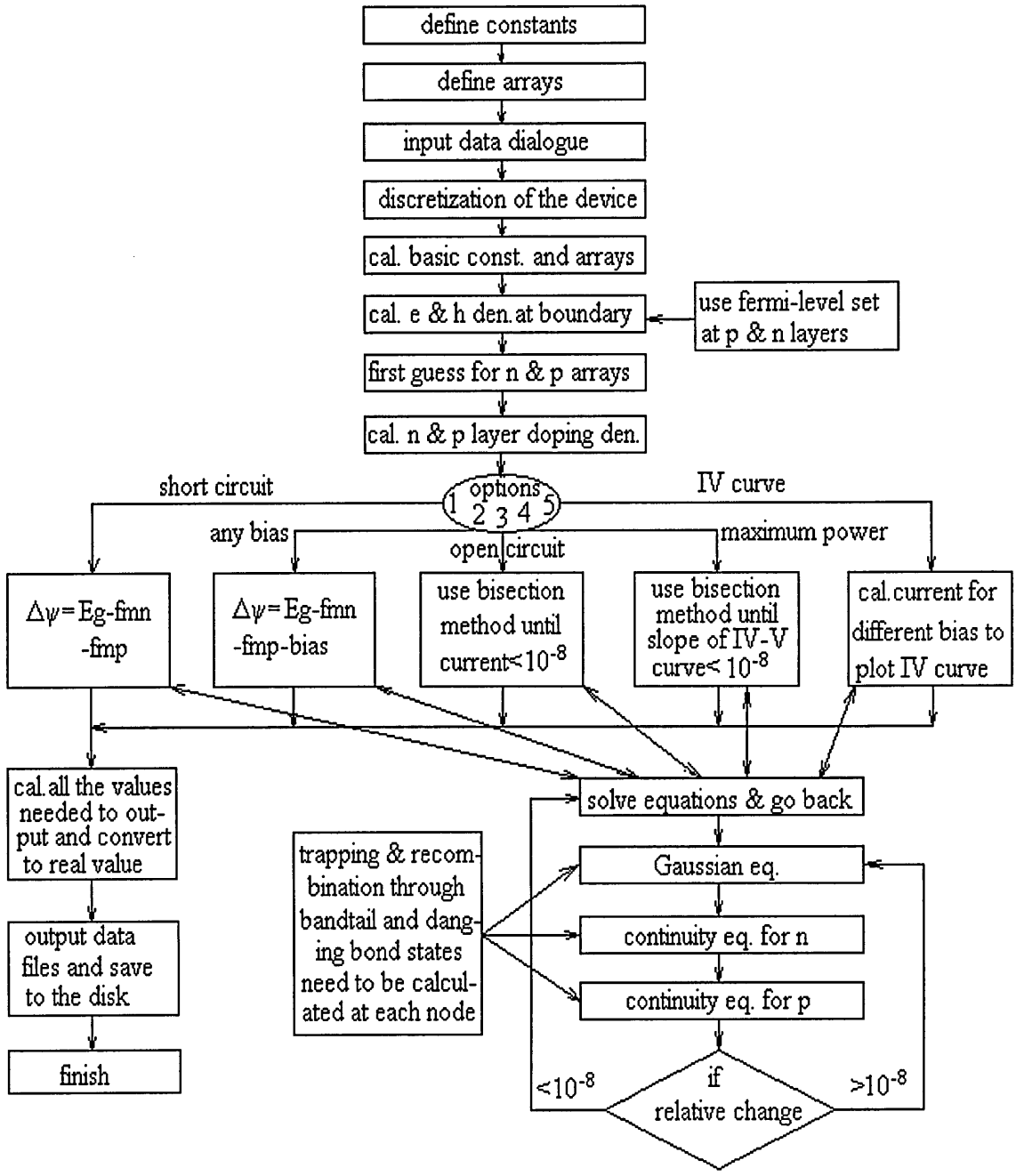

Fig 2.2 Brief flow chart of the *SPIN.F* program used to solve transport equations governing the transport processes in amorphous semiconductors.

2.3.3 Discretization of the device

In order to solve the equations numerically, it is essential to 'discretize' the device so as to convert the equations 2.14 to 2.18 into finite difference equations. This is a one dimensional device, with device thickness L, and number of slices denoted in the program by *jnl*. The device can be discretized into a nonuniform slice distribution as well as a uniform distribution to facilitate different usages. Basically the purpose of a non-uniform grid is to show more detail in some rapidly changing or more interesting regions such as the *p-i* or *i-n* interface etc, and the uniform grid will give details evenly throughout the device. There are many ways to divide up the device, and the following method allows at least 7 or 8 nodes in both p and n layers so that rapid changes of the field or the electron and hole densities can be monitored. The nonuniform slice width distribution can be generated in the program as follows:

The step increment $incr=dx(i+1)/dx(i)$

$cc=1/log(incr)$

$dx(i)=exp(-abs(jnl/2-i)/cc)$

nomalizing, we update the slice width

$$dx(i) = dx(i)\, L \Big/ \sum_{i=1}^{jnl} dx(i) \tag{2.19}$$

In this case, the slice width dx increases from one slice to the next by the same ratio from the edge towards the centre of the device which allows more slices inside the relatively thin p and n layers. After the total number of slices is defined, the parameter *incr* can be adjusted to change the slice width distribution.

For a thicker device, the p and n layers are relatively even thinner, or they may have different thicknesses, so to deal with this situation, we have for example used

$$dx(i) = \exp\left[-\left| \frac{jnl}{6}\left(3 + \frac{t_n - t_p}{t_n + t_p} \right) - i \right| \Big/ const \right]. \tag{2.20}$$

where

$$const = 50 \Big/ \left(\frac{L}{t_p + t_n} \right)^{0.35},$$

and where t_n and t_p are the thicknesses of the n and p layers. The value of *const* is adjustable to allow changing the distribution, so this formula will allow at least 6 slices inside the p and n layers for a thick device up to 40μm thick. This is purely an empirical formula used by the present author, and is not guaranteed to be applicable in any other cases encountered.

In the more general case, a subroutine has been introduced to iterate the step increment *incr* to make sure there will be a certain number of slices in the p and n layer independent of the device thickness.

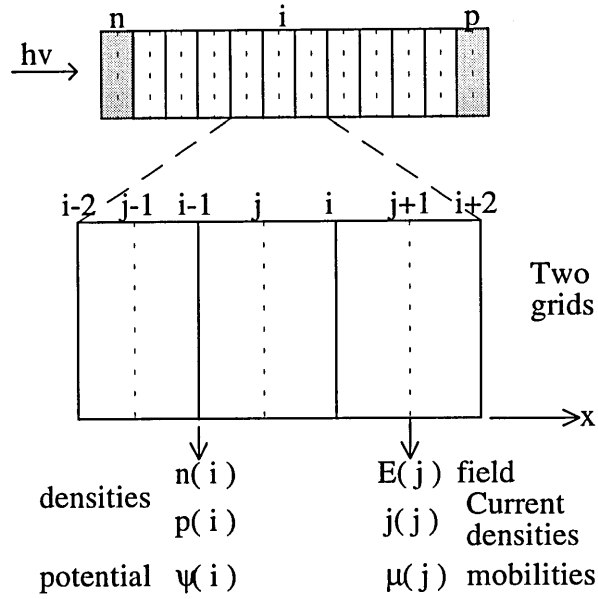

Fig 2.3 the discretization of the device and the location of the variables during the computer modelling.

Fig 2.3 shows the discretization of the device and the location of the variables during the calculation. There are *jnl*+1 nodes *x*(0)...*x*(*jnl*) out of *jnl* slices where the thickness of i_{th} slice is *dx*(*i*)=*x*(*i*)-*x*(*i*-1). The main computed quantities *n*, *p*, ψ(*i* series) are located *on* the main nodes, and the derived quantities (*j* series) are located at the *middle* of each slice.

The number of slices is normally taken from 100 to 500 or even 1000 depending on the operating conditions and the thickness of the device. For some difficult conditions, for example, thick sample and forward bias, a large number of slices is needed in order to improve the solution convergence behaviour, otherwise, the convergence may be very poor or even may not occur. However, simply increasing the number of slices may not solve this problem since the computing time will increase accordingly and convergence may not occur anyway because of other factors.

2.3.4 Boundary Conditions

It is always important to set up proper boundary conditions before the calculation is carried out (for an overview see Rubinelli et al 1992), and it is believed that as far as boundary conditions are concerned, it is always difficult to make an appropriate approximation to the real situation in semiconductor devices. In the present study, thermal equilibrium conditions were applied at the two boundaries. The thermal equilibrium condition implies infinite recombination velocity at the boundaries or in other words, ohmic contacts at the electrode semiconductor interfaces. Compared with the limited surface recombination speed boundary condition, the thermal equilibrium condition may in fact not be the best assumption if the boundaries are close to the *n-i* and

p-i junctions, because the depletion region can extend to the boundary and the presence of a Schottky barrier will change the condition for the calculation. However, the thermal equilibrium condition makes the calculation simpler and quicker. We will also show in this work that the influence of the thermal equilibrium boundary conditions appears to be limited to within a narrow region near the boundaries, so that the influence of the exact choice of boundary condition may not be important. Fig 2.4 shows the band edge and Fermi-level distribution across the device in the steady light illuminated condition. It can be seen that within 2 or 3 slices the quasi-Fermi level is shifted to its normal position, so the influence of the boundary may be considered to be small.

Based on the charge neutrality condition on the two boundaries, (ie. $np=n_o p_o$), the relations between electron and hole densities and Fermi-level can be established. By using the program *ssb8.for* (a program developed from an earlier code by Main) the electron and hole densities can be calculated according to the doping densities, so that we get *n(0), p(0), n(jnl), p(jnl)* and the Fermi-levels at two boundaries. The other way of setting boundary conditions is just to set Fermi levels at the two boundaries first, and then by using a charge neutrality subroutine, the electron and hole densities can be calculated, and the doping densities can also be calculated in due course. The latter approach is more convenient in this research to allow changing the operating condition of the device, and it is also easier and shorter for source code writing.

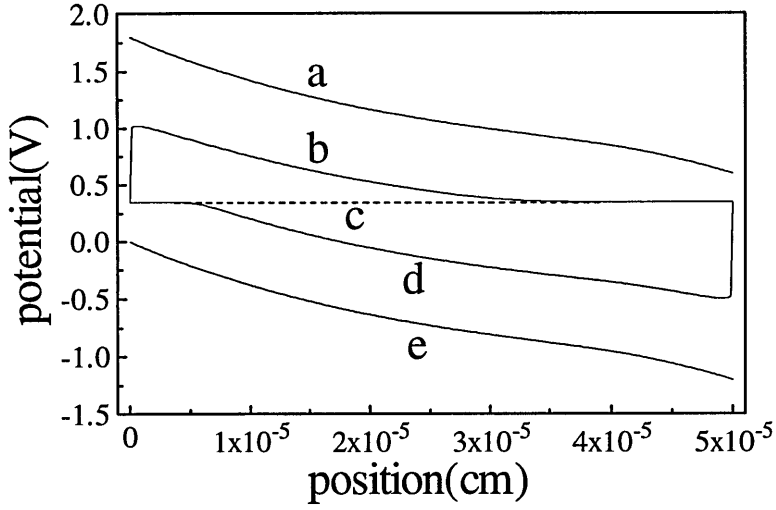

Fig 2.4 Variation of the band edge and Fermi-level in a 0.5μ*m* pin diode. (a) conduction band edge, (b) electron quasi-Fermi-level, (c) Fermi-energy position in dark, (d) hole quasi-Fermi-level and (e) valence band edge. Please note the change at the boundary where the quasi-Fermi-levels change quickly. The width of one slice in this uniform slice width case is 16.7*Å*

No matter which approach is used, the boundary electron and hole densities will be obtained from the boundary conditions. Based on this, the 'first guess' needed to solve the transport equations can be made.

According to the required operating condition (open circuit, short circuit, maximum power etc) we can define $\psi(0) = 0$, and then $\psi(jnl)$ will be equal to the built-in potential plus the applied bias voltage. If the boundary condition includes a Schottky barrier, the work function difference will be included as well. Thus $p(i)$, $n(i)$ and $\psi(i)$ are the three basic variable arrays to be computed. The first guess is made as follows

$$n(i) = n(0)\left[\frac{n(jnl)}{n(0)}\right]^{\frac{i-1}{jnl-1}} \qquad i = 1, jnl \tag{2.21}$$

$$p(i) = p(0)\left[\frac{p(jnl)}{p(0)}\right]^{\frac{i-1}{jnl-1}} \qquad i = 1, jnl \tag{2.22}$$

$$\psi(i) = \psi(0) + \frac{\psi(jnl) - \psi(0)}{jnl - 1}(i-1) \qquad i = 1, jnl \tag{2.23}$$

For the first guess, potential array ψ is a straight line between the two boundaries, while for the electron and hole density distributions, a power law relation is applied as a more reasonable interpolation rather than a linear interpolation. This is a universal first guess, and applies to all the situations computed. This procedure has not given many problems so far, implying robustness of this part of the solution.

2.3.5 Poisson Equation

After assignment of the first guess to n, p & ψ arrays, the Poisson equation is solved by assuming n and p are fixed.

Assume at the k+1 iteration

$$\psi^{k+1} = \psi^k + \delta\psi^k \tag{2.24}$$

where $\delta\psi$ is a correction term, substituting (2.24) into (2.14), and using *Taylor's* expansion gives

$$\frac{d^2\psi^k}{dx^2} + \frac{d^2\delta\psi^k}{dx^2} = -\frac{e}{\varepsilon\varepsilon_0}\left[(p - n + p_t - n_t + N_D - N_A - Dope) + \frac{\partial}{\partial\psi}(p - n + p_t - n_t + N_D - N_A - Dope)\delta\psi^k\right] \tag{2.25}$$

The derivative in the second term on the *RHS* of (2.25) can be written as

$$\frac{\partial p \partial p}{\partial p \partial \psi}+\frac{\partial p \partial n}{\partial n \partial \psi}-\frac{\partial n \partial p}{\partial p \partial \psi}-\frac{\partial n \partial n}{\partial n \partial \psi}+\frac{\partial p_t \partial p}{\partial p \partial \psi}+\frac{\partial p_t \partial n}{\partial n \partial \psi}-\frac{\partial n_t \partial p}{\partial p \partial \psi}-\frac{\partial n_t \partial n}{\partial n \partial \psi}$$

$$+\frac{\partial N_D \partial p}{\partial p \partial \psi}+\frac{\partial N_D \partial n}{\partial n \partial \psi}-\frac{\partial N_A \partial p}{\partial p \partial \psi}-\frac{\partial N_A \partial n}{\partial n \partial \psi}-\frac{\partial Dope \partial p}{\partial p \partial \psi}-\frac{\partial Dope \partial n}{\partial n \partial \psi}$$

$$\because \frac{\partial p}{\partial p}=\frac{\partial n}{\partial n}=1, \qquad \frac{\partial p}{\partial n}=\frac{\partial n}{\partial p}=\frac{\partial Dope}{\partial p}=\frac{\partial Dope}{\partial n}=0$$

$$\therefore RHS=\frac{\partial p}{\partial \psi}\left(1+\frac{\partial p_t}{\partial p}-\frac{\partial n_t}{\partial p}+\frac{\partial N_D}{\partial p}-\frac{\partial N_A}{\partial p}\right)$$

$$-\frac{\partial n}{\partial \psi}\left(1-\frac{\partial p_t}{\partial n}+\frac{\partial n_t}{\partial n}-\frac{\partial N_D}{\partial n}+\frac{\partial N_A}{\partial n}\right) \tag{2.26}$$

so equation (2.25) can be written as

$$\frac{d^2\delta\psi^k}{dx^2}+\frac{e}{\varepsilon\varepsilon_0}\left[\frac{\partial p}{\partial\psi}(1+\cdots)-\frac{\partial p}{\partial\psi}(1-\cdots)\right]\delta\psi^k=-\frac{d^2\psi^k}{dx^2}-\frac{e}{\varepsilon\varepsilon_0}(p-n+\cdots-Dope) \tag{2.27}$$

Converting partial differential equation 2.27 into finite difference form as follows, i.e. obtain

$$\frac{\dfrac{\delta\psi_{i+1}^k-\delta\psi_i^k}{dx_{i+1}}-\dfrac{\delta\psi_i^k-\delta\psi_{i-1}^k}{dx_i}}{\dfrac{dx_{i+1}+dx_i}{2}}+\frac{e}{\varepsilon\varepsilon_0}\left[\frac{\partial p}{\partial\psi}(1+\cdots)-\frac{\partial n}{\partial\psi}(1+\cdots)\right]\delta\psi_i^k$$

$$=-\frac{\dfrac{\psi_{i+1}^k-\psi_i^k}{dx_{i+1}}-\dfrac{\psi_i^k-\psi_{i-1}^k}{dx_i}}{\dfrac{dx_{i+1}+dx_i}{2}}-\frac{e}{\varepsilon\varepsilon_0}(p-n+\cdots-Dope) \tag{2.27a}$$

the superscript k is for k_{th} iteration, the subscripts i-1, i and i+1 are the position of the node on the spatial array. In this finite difference form of the equation, the equation changes to a linear equation with $\delta\psi^{k-1}$, $\delta\psi^k$ and $\delta\psi^{k+1}$ as unknowns. At each node, we have equation (2.27a), so for *jnl*-1 nodes (the two boundaries are not included), we have a (*jnl-1*)×(*jnl-1*) matrix equation.

$$[A][\delta\psi]=[B]$$

[*A*] is a tridiagonal matrix and we define *sub*(*i*), *diag*(*i*) and *sup*(*i*) the three one dimension arrays as the three sets of the elements in the matrix [*A*], their expression are as following:

$$sub(i) = A_{i,i-1} = 2/[dx_i\,(dx_{i+1} + dx_i)] \tag{2.28}$$

$$diag(i) = A_{i,i} = 2/(dx_i dx_{i+1}) + \frac{e}{\varepsilon\varepsilon_0}\left[\frac{\partial p}{\partial \psi}(1+\cdots) - \frac{\partial n}{\partial \psi}(1-\cdots)\right] \tag{2.29}$$

$$sup(i) = A_{i,i+1} = 2/[dx_{i+1}\,(dx_{i+1} + dx_i)] \tag{2.30}$$

$$B(i) = -2\frac{\dfrac{\psi_{i+1}-\psi_i}{dx_{i+1}} - \dfrac{\psi_i - \psi_{i-1}}{dx_i}}{dx_i + dx_{i+1}} - \frac{e}{\varepsilon\varepsilon_0}(p - n + p_t - n_t + N_D - N_A - Dope) \tag{2.31}$$

$$i=1,jnl-1$$

by inputting three arrays $p(i)$, $n(i)$ and $\psi(i)$, the correction $\delta\psi(i)$ for $\psi(i)$ can be calculated. One iteration finishs with $\psi(i)^{k+1} = \psi(i)^k + \delta\psi(i)^k$, $i = 1, jnl\text{-}1$. A tridiagonal solver routine was used (*tridag.for*, from *Numerical Recipes in FORTRAN*, 1992). During the calculation for Poisson's equation, the arrays $p(i)$, $n(i)$ are both fixed.

2.3.6 Continuity Equations

It has been pointed out (for example Kurata 1982) that the straightforward replacement of the hole and electron continuity equations by finite difference equations leads to numerical instability when the potential between two mesh points is larger than the thermal voltage V_T (V_T=kT/q), This problem can be solved by Scharfetter and Gummel's (1969) method. The algorithm is briefly described as follows:

Assume that electric field E, mobility μ, hole and electron currents J_p, J_n are constant between mid node points $x(j)$ and $x(j+1)$. From equations (2.17) and (2.18), we have the differential equations for electrons and holes.

$$J_{pj} = q\mu_p pE_j - kT\mu_p \frac{\partial p}{\partial x} \tag{2.32}$$

$$J_{nj} = q\mu_n nE_j + kT\mu_n \frac{\partial n}{\partial x} \tag{2.33}$$

Solving *analytically* for n and p (integrate from node i to $i+1$), using

$$\Delta\psi_{i+1} = \psi_{i+1} - \psi_i = E_j dx_{i+1}$$

and V_T=kT/q

we obtain

$$\frac{p_{i+1}-\dfrac{J_{pj}}{q\mu_p E_j}}{p_i-\dfrac{J_{pj}}{q\mu_p E_j}}=\exp\left(-\frac{\Delta\psi_{i+1}}{V_T}\right) \tag{2.34}$$

$$\frac{n_{i+1}-\dfrac{J_{nj}}{q\mu_n E_j}}{n_i-\dfrac{J_{nj}}{q\mu_n E_j}}=\exp\left(\frac{\Delta\psi_{i+1}}{V_T}\right) \tag{2.35}$$

from these two expressions, we can get

$$J_{pj}=q\mu_p E_j\frac{P_i\exp\left(-\dfrac{\Delta\psi_{i+1}}{V_T}\right)-p_{i+1}}{\exp\left(-\dfrac{\Delta\psi_{i+1}}{V_T}\right)-1}$$

$$=-q\mu_p\frac{\Delta\psi_{i+1}}{\Delta x_{i+1}}\left[\frac{p_i}{1-\exp(+\Delta\psi_{i+1}/V_T)}+\frac{p_{i+1}}{1-\exp(-\Delta\psi_{i+1}/V_T)}\right] \tag{2.36}$$

$$J_{nj}=-q\mu_n\frac{\Delta\psi_{i+1}}{\Delta x_{i+1}}\left[\frac{n_i}{1-\exp(-\Delta\psi_{i+1}/V_T)}+\frac{n_{i+1}}{1-\exp(+\Delta\psi_{i+1}/V_T)}\right] \tag{2.37}$$

Substituting (2.36), (2.37) into (2.15), (2.16) (discretized), we get(for k_{th} iteration for p)

$$a^k_{i,i-1}p^{k+1}_{i-1}+a^k_{i,i}p^{k+1}_i+a^k_{i,+1}p^{k+1}_{i+1}=B \tag{2.38}$$

where tridiagonal matrix elements are

$$a^k_{i,i-1}=sub=\frac{\mu_p\Delta\psi_i}{\Delta x_j\Delta x_i(1-\exp(\Delta\psi_i/V_T))}$$

$$a^k_{i,i}=diag=\frac{-\mu_p}{\Delta x_j}\left[\frac{\Delta\psi_{i+1}}{\Delta x_{i+1}(1-\exp(\Delta\psi_{i+1}/V_T))}-\frac{\Delta\psi_i}{\Delta x_i(1-\exp(-\Delta\psi_i/V_T))}\right]+\frac{\partial R_i}{\partial p}+\frac{\partial R_i}{\partial n}\frac{n_i}{p_i}$$

$$a^k_{i,i+1}=sup=-\frac{\mu_p\Delta\psi_{i+1}}{\Delta x_j\Delta x_{i+1}(1-\exp(-\Delta\psi_{i+1}/V_T))}$$

and $B=G_i-R^k_i+\dfrac{\partial R^k_i}{\partial p}p^k_i+\dfrac{\partial R^k_i}{\partial n}n^k_i$

For n, similarly we have

$$a^k_{i,i-1} n^{k+1}_{i-1} + a^k_{i,i} n^{k+1}_i + a^k_{i,+1} n^{k+1}_{i+1} = B$$

where

$$a^k_{i,i-1} = sub = -\frac{\mu_n \Delta\psi_i}{\Delta x_j \Delta x_i (1 - \exp(-\Delta\psi_i / V_T))}$$

$$a^k_{i,i} = diag = \frac{\mu_n}{\Delta x_j}\left[\frac{\Delta\psi_{i+1}}{\Delta x_{i+1}(1-\exp(-\Delta\psi_{i+1}/V_T))} - \frac{\Delta\psi_i}{\Delta x_i(1-\exp(\Delta\psi_i/V_T))}\right] + \frac{\partial R_i}{\partial n} + \frac{\partial R_i}{\partial p}\frac{p_i}{n_i}$$

$$a^k_{i,i+1} = \sup = \frac{\mu_n \Delta\psi_{i+1}}{\Delta x_j \Delta x_{i+1}(1-\exp(\Delta\psi_{i+1}/V_T))}$$

$$B = G_i - R^k_i + \frac{\partial R^k_i}{\partial p} p^k_i + \frac{\partial R^k_i}{\partial n} n^k_i$$

For all the nodes, $\psi(i)$ and $n(i)$ arrays are fixed when we solve the tridiagonal matrix equation for $p(i)$, $\psi(i)$ and $p(i)$ arrays are fixed when we solve the equation for $n(i)$. Unlike the step where we solve the Poisson equation, here the electron or hole density array is updated directly on every iteration. Any error introduced by the Scharfetter-Gummel approximation in (2.32) and (2.33) is normally found to be unimportant when the thickness of the slices is small, which is quite easily achieved (for example *jnl*=500 for 0.5μm thick sample)

2.3.7 Trapping and recombination

In this subsection the formulae related to the trapping and recombination through band tail states and dangling bond defect states will be developed specifically with computation in mind. The basic rate equations describing capture and emission of the carriers in an arbitrary distribution of tail-states, are as originally developed by Shockley and Read (1952) , and generalised by Simmons and Taylor (1971). These states may be treated as 'one-electron' states, with only two occupancy conditions. Conduction band tail states are assumed to be acceptor-like and valence band tail states donor-like in terms of their charge-occupancy characteristics. Similarly, rate equations can be written for dangling bond states, taking into account their divalent nature, and three possible occupancy conditions - empty (D^+), singly occupied (D^o), and doubly occupied (D^-)

(Main et al 1990). Figure 2.5 shows schematically the states and transitions we would wish to include in the description.

For each bandtail state, there are four transitions which can proceed: the trapping and re-emission of electron and hole from and to the conduction and valence band respectively. When these processes happen, there is also a chance that an electron and hole can recombine in the defect state. For dangling bond states, there are two transition paths available; one is the $D^{+/o}$ transition which is located in the lower part of the gap (closer to the valence band edge), the other is the $D^{o/-}$ transition which located in the upper part of the gap. The difference between these two transitions is accounted for by the correlation energy U (assuming positive here). The correlation energy can be positive or negative in different circumstances. The transitions included in dangling bond states are electron and hole trapping and reemission to and from D^+ and D^o and D^- states according to the charge status of the state.

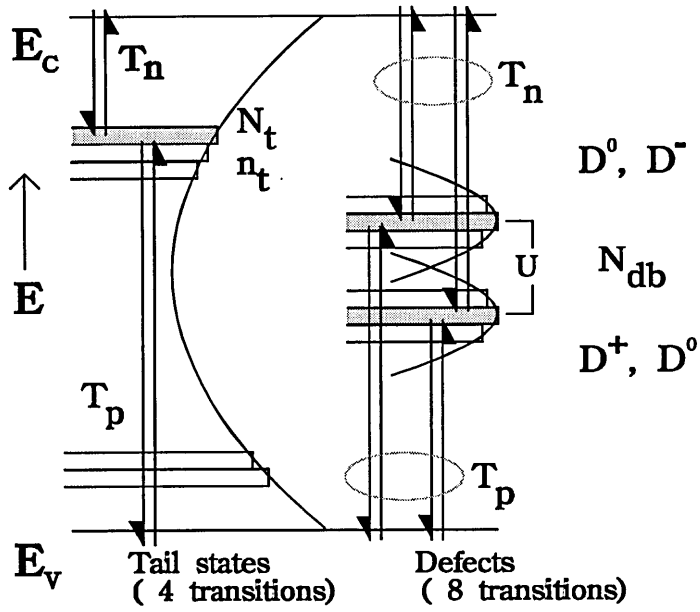

Fig 2.5 Schematic diagram of density-of-states model and transitions used in the simulation.

(1) Bandtail states

There have been many detailed measurements and methods to deal with the *DOS* distribution (e.g. Marshall et al 1987b) It is often accepted that the band tail states consist of a linearly decreasing part followed by exponential distributions into the midgap. In this simulation only the exponential part of the band tail was taken into account. The derivation of occupation function for bandtail states according to the Shockley-Read-Hall statistics has been done analytically in section **2.2.1**, while in this subsection, we give the rest of the derivation in the *discrete* form which is used in the source code.

By multiplying the band tail states expression by the occupation function (eq 2.1, 2.2 and 2.4), the charge density in bandtail states can be expressed as

$$p_t = \sum_{j=1}^{inl} g_d(j) f_d(j) \tag{2.39}$$

$$n_t = \sum_{j=1}^{inl} g_a(j) f_a(j) \tag{2.40}$$

This is the total charge density in the band tail states and it is in discrete equation form. The following partial derivative of the charge densities will be used in the algorithm for solving Poisson and continuity equations.

$$\frac{\partial p_t}{\partial n} = \sum_{j=1}^{inl} g_d(j) \frac{\partial f_d(j)}{\partial n} \qquad \frac{\partial f_d(j)}{\partial n} = -\frac{R_d\,(R_d\,n_1(j)+p)}{\left[R_d\,n_1(j)+p+R_d\,n+p_1(j)\right]^2}$$

$$\frac{\partial p_t}{\partial p} = \sum_{j=1}^{inl} g_d(j) \frac{\partial f_d(j)}{\partial p} \qquad \frac{\partial f_d(j)}{\partial p} = -\frac{R_d\,n+p_1(j)}{\left[R_d\,n_1(j)+p+R_d\,n+p_1(j)\right]^2}$$

$$\frac{\partial n_t}{\partial n} = \sum_{j=1}^{inl} g_a(j) \frac{\partial f_a(j)}{\partial n} \qquad \frac{\partial f_a(j)}{\partial n} = -\frac{R_a\,(R_a\,n_1(j)+p)}{\left[R_a\,n_1(j)+p+R_a\,n+p_1(j)\right]^2}$$

$$\frac{\partial n_t}{\partial p} = \sum_{j=1}^{inl} g_a(j) \frac{\partial f_a(j)}{\partial p} \qquad \frac{\partial f_a(j)}{\partial p} = -\frac{R_a\,n+p_1(j)}{\left[R_a\,n_1(j)+p+R_a\,n+p_1(j)\right]^2}$$

The analytical form of the expressions of recombination rate via bandtail states are in section **2.2.2.** The partial derivatives of the recombination rates for n and p are needed when solving Poisson and Continuity equations. From equation 2.5, we have

$$\frac{\partial R_{bt}}{\partial n} = \sum_{j=1}^{inl} \left[C_{na}\, g_a(j) \frac{(R_a\,n_1(j)+p)(p+p_1(j))}{\left(R_a\,(n+n_1(j))+p+p_1(j)\right)^2} + C_{nd}\, g_d(j) \frac{(R_d\,n_1(j)+p)(p+p_1(j))}{\left(R_d\,(n+n_1(j))+p+p_1(j)\right)^2} \right]$$

$$\frac{\partial R_{bt}}{\partial p} = \sum_{j=1}^{inl} \left[C_{na}\, g_a(j) \frac{(R_a\,n+p_1(j))(n+n_1(j))}{\left(R_a\,(n+n_1(j))+p+p_1(j)\right)^2} + C_{nd}\, g_d(j) \frac{(R_d\,n+p_1(j))(n+n_1(j))}{\left(R_d\,(n+n_1(j))+p+p_1(j)\right)^2} \right]$$

(2) Dangling Bonds

The dangling bond is the most significant characteristic of amorphous semiconductors compared with its crystalline partners. Research on this topic has been active for more than 20 years, and still has not reached a definitive conclusion. In computer modelling, the simplest approach is to fix the dangling bonds at two discretized energy levels E_0 and E_0+U to deal with trapping and recombination via these amphoteric defect states. A little advance on this model is to extend the single energy δ function defect density distribution into a Gaussian distribution to approach the actual situation with the peak positions of the $D^{+/o}$ and $D^{o/-}$ still at E_0 and U. A recently popular model is the so called defect pool model, which starts from the point that the weak bonds can be broken into dangling bonds, and with the involvement of hydrogen diffusion, the broken dangling bonds can be saturated and separated spatially so as to reduce the free energy of the system to a minimum. From this model, the dangling bond density and its distribution can be self-consistently calculated. The present work has included all of the models mentioned, from the simplest single energy dangling bond model to the latest defect pool model. Also the spatial distribution of the total dangling bond density across the device can be changed arbitrarily in different ways in case the comparisons between different distributions is necessary.

(i). Discrete.

$$N_D = N_{db} F^+ \qquad \frac{\partial N_D}{\partial p} = N_{db} \frac{\partial F^+}{\partial p} \qquad \frac{\partial N_D}{\partial n} = N_{db} \frac{\partial F^+}{\partial n}$$

$$N_A = N_{db} F^- \qquad \frac{\partial N_A}{\partial p} = N_{db} \frac{\partial F^-}{\partial p} \qquad \frac{\partial N_A}{\partial n} = N_{db} \frac{\partial F^-}{\partial n}$$

where F^+ and F^- are fractional occupation functions in the non-equilibrium steady state for D^+ and D^- states; detailed derivation can be found in section **2.2.3** (equations 2.9 to 2.11). The partial derivatives of these occupation functions to free electron and hole densities are needed when the finite difference transport equation is solved. From equation 2.9-11 the partial derivatives are:

$$\frac{\partial F^+}{\partial p} = \frac{N^+\left[c_p^0 P^-\left(P^- + N^0\right) + c_p^- P^0 N^0\right]}{\left[N^+P^- + P^0P^- + N^0N^+\right]^2} \qquad \frac{\partial F^+}{\partial n} = -\frac{P^0P^-\left[c_n^+\left(P^- + N^0\right) + c_n^0 N^+\right]}{\left[N^+P^- + P^0P^- + N^0N^+\right]^2}$$

$$\frac{\partial F^-}{\partial p} = -\frac{N^0N^+\left[c_p^-\left(P^0 + N^+\right) + c_p^0 P^-\right]}{\left[N^+P^- + P^0P^- + N^0N^+\right]^2} \qquad \frac{\partial F^-}{\partial n} = \frac{P^-\left[c_n^0 N^+\left(N^+ + P^0\right) + c_n^+ P^0 N^0\right]}{\left[N^+P^- + P^0P^- + N^0N^+\right]^2}$$

$$\frac{\partial F^0}{\partial p} = \frac{N^+\left[c_p^- N^0 N^+ - c_p^0 P^{-2}\right]}{\left[N^+P^- + P^0P^- + N^0N^+\right]^2} \qquad \frac{\partial F^0}{\partial n} = \frac{P^-\left[c_n^+ P^0 P^- - c_n^0 N^{+2}\right]}{\left[N^+P^- + P^0P^- + N^0N^+\right]^2}$$

To obtain the above derivatives, the following relations have been used

$$\frac{\partial P^0}{\partial n} = \frac{\partial P^-}{\partial n} = \frac{\partial N^+}{\partial p} = \frac{\partial N^0}{\partial p} = 0$$

$$\frac{\partial P^0}{\partial p} = c_p^0 \qquad \frac{\partial P^-}{\partial p} = c_p^- \qquad \frac{\partial N^+}{\partial n} = c_n^+ \qquad \frac{\partial N^0}{\partial n} = c_n^0$$

Recombination through dangling bonds is actually the difference between the total capture rate and the total re-emission rate of the electrons (or holes) via different paths. In the source code, the general form has been taken, from eq 2.12, giving:

$$\frac{\partial R_{db}}{\partial p} = N_{db}\left[nc_n^+ \frac{\partial F^+}{\partial p} + (nc_n^0 - n_1^+ c_n^+)\frac{\partial F^0}{\partial p} - n_1^0 c_n^0 \frac{\partial F^-}{\partial p}\right]$$

$$\frac{\partial R_{db}}{\partial n} = N_{db}\left[c_n^+ F^+ + c_n^0 F^0 + nc_n^+ \frac{\partial F^+}{\partial n} + (nc_n^0 - n_1^+ c_n^+)\frac{\partial F^0}{\partial n} - n_1^0 c_n^0 \frac{\partial F^-}{\partial n}\right]$$

The total recombination rate can be reduced to following form. This is the form used in computer source code which uses many values used in the occupation function expressions for the sake of simplicity.

$$R_{db} = R_{D^+} + R_{D^o}$$

$$= nc_n^+ N_{db} F^+ - n_1^+ c_n^+ N_{db} F^0 + nc_n^0 N_{db} F^0 - n_1^0 c_n^0 N_{db} F^-$$

$$= \frac{N_{db}\left(np - n_o\, p_o\right)P^- c_n^+ c_p^-}{N^+P^- + P^oP^- + N^+N^o} + \frac{N_{db}\left(np - n_o\, p_o\right)N^+ c_n^o c_p^-}{N^+P^- + P^oP^- + N^+N^o}$$

$$= \frac{N_{db}\left(np - n_o p_o\right)\left(P^- c_n^+ c_p^- + N^+ c_n^o c_p^-\right)}{N^+P^- + P^oP^- + N^+N^o} \qquad (2.41)$$

In computer modelling, attention is needed to reduce the error introduced from the recombination term, especially at low excitation rates, or in the dark with bias voltage, where the very small currents from thermal emission under reverse bias sometimes causes instability of the system solution. In thermal equilibrium conditions, the

recombination term has usually to be explicitly set as zero, otherwise the numerical error caused by the recombination term will also jeopardize the convergence of the iteration.

(ii) Gaussian distribution of dangling bonds

The calculation for a Gaussian defect distribution is similar to the single energy case, but now many discrete $D^{+/o}$ levels are defined at different energy positions, plus the same number of $D^{o/-}$ levels according to the number of energy divisions used for dangling band defect states. The occupation function and recombination rate derived for these states takes the same form as for the single energy model. For the Gaussian distribution, the total charge density and recombination rate needs to be calculated by integral - or in this case, by summation. Due to the energy shift by the correlation energy U for each level, great care is needed in installing this option into source code.

(iii) Defect pool

The defect pool model was first introduced by Winer (1989) and modified by others including Deane and Powell (1993). This self-consistent model results in the following expression for total defect density - using Deane and Powell's notation (for the details of the defect pool, see chapter 4):

$$D(E) = \gamma \left[\frac{2}{f^{\,0}(E)} \right]^{\rho kT / E_{v0}} P\left[E + \frac{\rho \sigma^{\,2}}{E_{v0}} \right] \tag{2.42}$$

where

$$\gamma = \left[\frac{2 N_{v0} E_{v0}^{\,2}}{2E_{v0} - kT} \right]^{\rho} \left[\frac{i}{2H} \right]^{\rho - 1} \exp\left[-\frac{\rho}{E_{v0}} \left(E_p - E_v - \frac{\rho \sigma^{\,2}}{2E_{v0}} \right) \right]$$

$$P(E) = \left(2\sigma^2 \pi\right)^{-1/2} \exp\left[-\frac{\left(E - E_p\right)^2}{2\sigma^2} \right]$$

$$\rho = \frac{2E_{v0}}{2E_{v0} + ikT}$$

In thermal equilibrium state at the 'freeze-in' temperature (thermal quench temperature, typically 500°K), the occupation functions of the dangling bonds take the simple form of equation 2.6-8. the components for different charge state dangling bonds

can be calculated by multiplying the defect density distribution with the occupation functions

$$D^+(E) = D(E)f^+(E)$$
$$D^0(E) = D(E)f^0(E)$$
$$D^-(E) = D(E)f^-(E)$$

These are approximately three Gaussian distributions, which when plotted together result in the total defect pool distribution. Since defect distributions and occupation functions are both energy dependent, the partial derivatives of the charged defect densities now take a slightly different form as follows:

$$\frac{\partial D^+(E)}{\partial p} = \frac{\partial D(E)}{\partial p} f^+(E) + D(E)\frac{\partial f^+(E)}{\partial p}$$

$$\frac{\partial D^-(E)}{\partial p} = \frac{\partial D(E)}{\partial p} f^-(E) + D(E)\frac{\partial f^-(E)}{\partial p}$$

$$\frac{\partial D^+(E)}{\partial n} = \frac{\partial D(E)}{\partial n} f^+(E) + D(E)\frac{\partial f^+(E)}{\partial n}$$

$$\frac{\partial D^-(E)}{\partial n} = \frac{\partial D(E)}{\partial n} f^-(E) + D(E)\frac{\partial f^-(E)}{\partial n}$$

where

$$\frac{\partial f^+(E)}{\partial p} = \frac{\partial f^+(E)}{\partial E_F}\frac{\partial E_F}{\partial p} = f^+(E)\left[f^0(E) + 2f^-(E)\right]/p$$

$$\frac{\partial f^+(E)}{\partial n} = \frac{\partial f^+(E)}{\partial E_F}\frac{\partial E_F}{\partial n} = -f^+(E)\left[f^0(E) + 2f^-(E)\right]/n$$

$$\frac{\partial f^-(E)}{\partial p} = \frac{\partial f^-(E)}{\partial E_F}\frac{\partial E_F}{\partial p} = -f^-(E)\left[f^0(E) + 2f^+(E)\right]/p$$

$$\frac{\partial f^-(E)}{\partial n} = \frac{\partial f^-(E)}{\partial E_F}\frac{\partial E_F}{\partial n} = f^-(E)\left[f^0(E) + 2f^+(E)\right]/n$$

$$\frac{\partial f^0(E)}{\partial p} = \frac{\partial f^0(E)}{\partial E_F}\frac{\partial E_F}{\partial p} = f^0(E)\left[f^-(E) - f^+(E)\right]/p$$

$$\frac{\partial f^0(E)}{\partial n} = \frac{\partial f^0(E)}{\partial E_F}\frac{\partial E_F}{\partial n} = -f^0(E)\left[f^-(E) - f^+(E)\right]/n$$

and

$$\frac{\partial D(E)}{\partial p} = \frac{\partial D(E)}{\partial E_F}\frac{\partial E_F}{\partial p}$$

$$\frac{\partial D(E)}{\partial n} = \frac{\partial D(E)}{\partial E_F}\frac{\partial E_F}{\partial n}$$

where

$$\frac{\partial D(E)}{\partial E_F} = D(E)\frac{\rho}{E_{v0}}\left[f^-(E) - f^+(E)\right].$$

At this point, the parameters needed for the equations can be calculated

$$\frac{\partial D^+(E)}{\partial p} = D(E)\frac{f^+(E)}{p}\left\{\frac{\rho kT}{E_{v0}}\left[f^+(E) - f^-(E)\right] + \left[f^0(E) + 2f^-(E)\right]\right\}$$

$$\frac{\partial D^+(E)}{\partial n} = D(E)\frac{f^+(E)}{n}\left\{\frac{\rho kT}{E_{v0}}\left[f^-(E) - f^+(E)\right] - \left[f^0(E) + 2f^-(E)\right]\right\}$$

$$\frac{\partial D^-(E)}{\partial p} = D(E)\frac{f^-(E)}{p}\left\{\frac{\rho kT}{E_{v0}}\left[f^+(E) - f^-(E)\right] - \left[f^0(E) + 2f^+(E)\right]\right\}$$

$$\frac{\partial D^-(E)}{\partial n} = D(E)\frac{f^-(E)}{n}\left\{\frac{\rho kT}{E_{v0}}\left[f^-(E) - f^+(E)\right] + \left[f^0(E) + 2f^+(E)\right]\right\}$$

When all these derivatives are calculated, the processes for solving the transport equations can be carried out. This procedure is described below.

(a). At the freeze-in temperature (say, 500°*K*) calculate the boundary conditions (define Fermi-levels in *p*-layer and *n*-layer), output the electron and hole densities and the dangling bond density according to the defect pool model. At the same time, the appropriate doping densities at the boundaries are calculated, and will be used as the doping density for whole doped *p*- and *n*-layers.

(b). Again at the freeze-in temperature and in thermal equilibrium, make the first guess for the electron and hole density distribution and potential profile, solve the transport equations including the calculation of the spatial defect pool distribution (which depends on the local position of the Fermi level) across the device. This is the crucial part of the calculation, since not only do *n*, *p* and ψ need to be updated at each iteration, but also the spatial defect distribution needs to be updated. The convergence rate is slower at this stage and the source code must be precise.

(c). Once the spatial variation of the defect density and the energy distribution of the defect pool have been computed, they will be frozen-in and no longer change during the later calculations. At the operational temperature (eg. 300°*K*) and conditions (eg. light, high bias voltage etc), everything except the defect density and distribution will be calculated again while holding this fixed defect distribution.

2.3.8 Generation rate profile

When the transport equations are converted into finite difference equations, numerical error inevitably will be introduced. By increasing the number of slices, the error in this respect should be reduced, but on the other hand, the rounding error due to the larger number of elements will be increased. So there is a problem of compromise. The error introduced from the generation rate is one example.

The generation rate profile is used in the continuity equation. In a very simple case, for example, with weakly absorbed red light and a thick sample, a single exponential decay is good enough.

$$G(x) = F_o \alpha \exp(-\alpha\, x) \tag{2.43}$$

where F_o is the photon flux, α is the absorption coefficent for a wavelength. If the reflection is going to be taken into account, then

$$G(x) = F_o \alpha\left[\exp(-\alpha x) + rf \exp\left(-\alpha(x-2L)\right)\right] \tag{2.44}$$

where rf is the reflection coefficient and L is the thickness of the device.

In the case of equations 2.43 and 2.44, when converted into finite difference equations, the number of photons absorbed in each slice is the value calculated from the product *G(x)dx*. When high accuracy in calculation is needed, considering the thickness of each slice, the *integration* of *G(x)* in that slice should be used for the total loss of the photons in that slice, ie. the photons absorbed in the slice are given by the photon flux difference between two edges of the slice. The mean generation rate value used in the continuity equation should thus be equal to the total photon flux loss in the slice divided by the thickness of the slice. This effect becomes more important when blue light is used and the thickness of each slice is not very thin compared to the absorption depth. In this case we must use (in discrete form):

$$G(i) = \frac{2F_o \exp(-\alpha x(i))}{dx(i)+dx(i+1)}\left[\exp\left(\frac{\alpha dx(i)}{2}\right) - \exp\left(-\frac{\alpha dx(i+1)}{2}\right)\right] +$$

$$+ \frac{2F_o\, rf \exp(\alpha x(i))\exp(-\alpha 2L)}{dx(i)+dx(i+1)}\left[\exp\left(\frac{\alpha dx(i+1)}{2}\right) - \exp\left(-\frac{\alpha dx(i)}{2}\right)\right] \tag{2.45}$$

where we use a discrete expression for the generation profile in the computer modelling. $dx(i)$ and $dx(i+1)$ are the thicknesses of the adjacent slices around the node $x(i)$.

The relation between the absorption coefficient and the wavelength is strongly dependent on the fabrication of the material. For amorphous silicon, detailed measurements have been conducted and published by Dawson.et al (1992) and these are tabulated in the Appendix. Warning is given that these data are not a unique representation of the various *a-Si:H* based materials that can be produced under different conditions. Caution should be taken in using these data in the subgap region ($E<1.3eV$) where the absorption coefficient is most sensitive to deposition conditions and sample history. It is also to be mentioned that the above data are particularly useful in the energy region $3.54eV(350nm)$ to $1.55eV(800nm)$ where *a-Si:H* based solar cells have a measurable quantum efficiency which can be used to model solar cell operation. We do realize that difficulties may arise in applying these data arbitrarily to particular samples.

2.3.9 Special algorithms for different applications.

Solving the transport equations is a basic element for the computer modelling. However, for particular conditions, special additional routines are still needed.

(i) Short circuit condition

For short circuit conditions, the Fermi-level on the two boundaries should at the same energy level, eg. the potential

$\psi(jnl)-\psi(0) = E_g-E_{fp}-E_{fn}$.

this is a case which usually converges easily.

(ii) Arbitrary bias condition

When a bias voltage V_b is applied, the potential at the right hand (n) side will be changed to $\psi(jnl)-V_b$ (set $\psi(0)=0$). where $\psi(jnl)$ is the built-in potential calculated in the thermal equilibrium condition. This is a useful option, and nearly all the important applications include this 'any bias' algorithm.

(iii) Open circuit condition

The criterion to judge the open circuit condition is the zero current condition. In order to fulfill this, two first guesses have to be made. eg. $\psi(jnl)=0$ and $\psi(jnl)=E_g$, These will give one positive and one negative current. The iteration has to be carried out by using a bisection method until the total current density becomes smaller than a pre-set value say, $10^{-10}\ A/cm^2$.

(iv) Maximum power point

In the maximum power option, the criterion is to judge whether the maximum power has been reached. To realize this, the following algorithm has been used.

On an (*IV*) vs *V* curve, there must be a peak representing the maximum power point, so a first pair of bias voltage guesses is made to make sure the maximum power point falls between them. Aware of the difficulty in applying the bisection method here, a different approach is used. For the k_{th} iteration, the slope of the *IV* vs *V* curve or the *IV* value relative to the previous *IV* value is calculated. If *d(IV)/dV* is positive, it means the *IV* value is still increasing, so that the next step will still be to higher *V*. However, it does not matter if *dIV/dV* is negative - this means the maximum power point has been passed, and the next step will be backward. At the same time, the step width will be halved in order to reach convergence. This kind of zigzag iteration is continued until the slope *dIV/dV* is smaller than a specified value (for example$10^{-9}A$).

(v) *I-V* curve

To best plot the *I-V* curve, a set of non-uniformly spaced bias voltage values should be set. To do this, the slope of the *I-V* curve has to be taken into account in order to distribute the data points reasonably uniformly. The relation being used now is as follows

$$V(i) = V_1 + (V_2 - V_1)\left\{1.0975 - 0.545\exp\left[0.7 - \frac{2.45(i-1)}{In-1}\right]\right\} \tag{2.46}$$

where V_1 and V_2 are the starting and finishing points of the *I-V* curve, and *In* is the number of data points on the *I-V* curve. This expression allows the data points to have a reasonable distribution. The other approach is to use a routine to calculate each voltage step by a certain rule to make sure the best *I-V* curve can be ploted.

2.4 Data output description

The computation starts by solving the Poisson equation, assuming the $n(i)$ and $p(i)$ arrays are fixed, and then solves the continuity equation for $n(i)$ by assuming the $\psi(i)$ and $p(i)$ arrays are fixed, and similarly for the solution of the continuity equation for $p(i)$. The convergence is assumed to be satisfied when the relative improvement in all iteration variables becomes smaller than a prefixed value. For example

$$MAX\left(\frac{p_i^{k+1} - p_i^k}{p_i^k}\right) \le 10^{-8}$$

when this condition is satisfied, the calculation is stopped and the final results $p(i)$, $n(i)$ and $\psi(i)$ are used to calculate other useful physical characteristics, listed below.

(i). Electric field

E_j=-$\Delta\psi_j/\Delta x_j$

The j series values are located in the middle of the i series nodes. The electric field intensity at each node is calculated, and the spatial variation of the field intensity is saved in a data file. This is a very useful data file, giving valuable insight for solving different problems.

(ii). Currents

Since equations (2.36) and (2.37) derived using the Scharfetter-Gummel formalism have been used to solve the continuity equations, the calculation of the current densities will not give accurate results if the more straightforward original finite difference versions of equations (2.17) and (2.18) are used. However, the problem in using eqs (2.36) and (2.37) is that there are no explicit expressions for drift current and diffusion current. A further derivation, carried out in this work, is needed in order to separate these two.

From eq (2.36), if we assume p has a linear relation with x between node i and node $i+1$, we have the following expression

$$p(x) = \exp\left(-\frac{\psi(x)-\psi_{i-1}}{V_T}\right)p_{i-1} + \left[1-\exp\left(-\frac{\psi(x)-\psi_{i-1}}{V_T}\right)\right]\frac{J_{pj}}{q\mu_p E_j}$$

so that

$$J_{p_j drift} = q\mu_p p(x_j) E_j$$

$$= q\mu_p E_j \left\{ p_{i-1}\exp\left(\frac{\Delta\psi_i}{V_T\Delta x_i}\frac{dx_i}{2}\right) + \frac{J_{pj}}{q\mu_p E_j}\left[1-\exp\left(\frac{\Delta\psi_i}{V_T\Delta x_i}\frac{dx_i}{2}\right)\right]\right\}$$

$$= q\mu_p E_j p_{i-1}\exp\left(-\frac{\Delta\psi_i}{2V_T}\right) + J_{pj}\left[1-\exp\left(-\frac{\Delta\psi_i}{2V_T}\right)\right]$$

subsitituting equation 2.36 and setting $\gamma_i=\Delta\psi_i/2V_T$ we can get

$$J_{p_j drift} = q\mu_p E_j\left[\frac{1-\exp(\gamma_i)}{1-\exp(2\gamma_i)}p_{i-1} + \frac{1-\exp(-\gamma_i)}{1-\exp(-2\gamma_i)}p_i\right]$$

similarly we have

$$J_{n_j drift} = q\mu_n E_j\left[\frac{1-\exp(-\gamma_i)}{1-\exp(-2\gamma_i)}n_{i-1} + \frac{1-\exp(\gamma_i)}{1-\exp(2\gamma_i)}n_i\right],$$

and for diffusion currents,

$$J_{p_j diff} = q\mu_p E_j \left[\frac{\exp(\gamma_i)}{1-\exp(2\gamma_i)} p_{i-1} + \frac{\exp(-\gamma_i)}{1-\exp(-2\gamma_i)} p_i \right]$$

$$J_{n_j diff} = q\mu_n E_j \left[\frac{\exp(-\gamma_i)}{1-\exp(-2\gamma_i)} n_{i-1} + \frac{\exp(\gamma_i)}{1-\exp(2\gamma_i)} n_i \right]$$

From these nicely symmetrical expressions, the highest accuracy can be obtained.

In the output current data file, detailed spatial current distributions are plotted, these are - total current, electron and hole total currents, electron and hole partial drift and diffusion currents etc. It becomes very clear in this plot which carrier in which part of the device contributes most to the total current.

(iii) Other results

The other results like the spatial variation of the recombination rate through bandtail states and dangling bonds, the charge density distribution in the bandtail and dangling bond states (energy dimension), the spatial variation of the band edges and Fermi (or quasi-Fermi) levels etc. are easily calculated during the iterations. The data output also includes electron and hole life times, electron and hole drift and diffusion lengths, energy distribution of bandtail and dangling bond states, spatial variation of the space charge density distribution of bandtail and dangling bond states and total dangling bond density distribution (eg. in the defect pool case). These output data have proved to be useful in investigating special problems in amorphous semiconductor material and devices. Many data files are produced so a great deal of disk storage space is needed to do any serious number of simulations!

2.5 Summary

In this chapter, the fundamental theory of amorphous silicon material and the simple derivation of the algorithm to solve the transport equation are briefly described. At the same time, the construction of the *SPIN.F* computer program is demonstrated in flow chart and also in text. Incorporation of the defect pool into the computer model is described. Special attention is paid to the accuracy of calculation. More accurate forms for drift and diffusion current have are presented and different forms of generation rate expressions are used for appropriate accuracy in different situations.

Chapter three

EVALUATION OF THE PROGRAM

3.1 Introduction

With the development of amorphous silicon theory and the use of high speed computers, numerical modelling has become a viable approach to investigate the behaviour of *a-Si:H* material and devices. In principle, numerical modelling can make a minimum of assumptions and approximations, taking as many influences as necessary into account. The input parameters are normally the most reliable values obtained through measurements. There have been several computer models on this subject developed over the last several years (see chapter 1 and Rubinelli et al 1992 for an overview), and the programs are gradually becoming more and more complete so that most influences can be taken into account, for example boundary conditions, trapping and recombination through defect states etc. However, with the continued improvement of our understanding of *a-Si:H* material and devices, computer modelling must continually improve in order to keep up. New models to explain the behaviour of the defect states provide a good example. During recent years, several new models concerning defect behaviour like the defect pool and the defect relaxation model have been introduced (see for example Cohen et al 1992 and Farmer and Su 1993), so it becomes necessary to incorporate these new ideas into numerical models to test their validity and then to apply them to solve real problems.

In this chapter the modelling program described in chapter 2 will be evaluated for speed, accuracy and robustness - i.e. ability to converge under a range of conditions. The topics described in the following are covered to demonstrate the program. Firstly the convergence rate and evolution of the solution during iteration are described. This will give a brief idea of the convergence process. After this, various tests on *p-i-n* devices are reported, including calculations of the influence of the capture coefficient on several internal and external characteristics of the device, such as the carrier life time, internal field, recombination rate and *I-V* characteristics. This part will demonstrate the use of the program in displaying and interpreting the basic operating properties of a thin *p-i-n* device. In the last part, we test the programs ability to simulate much thicker devices, showing some special phenomena existing in thick devices situation under illumination and in the dark, under reverse bias, forward bias and zero bias voltage conditions. We illustrate band bending, effects of changing conditions on internal field, on spatial variation of space charge density, recombination rate and other internal characteristics. It will be seen that the situation in thick device is significantly different from that in a thin device.

3.2 Testing the modelling program

In order to probe the limits of the program developed in this project, i.e. its robustness and flexibility, it is worthwhile and necessary to test the program over a range of conditions. The purpose of this section is to describe the testing processes and give the basic results. In order to make all the tests comparable, some basic running conditions have been fixed and are listed below.

The Fermi-levels at the p and n boundaries are set to $0.55eV$ above the valence band and $0.35eV$ below the conduction band, respectively, (equivalent to $1\times10^{16}cm^{-3}$ doping for p- and n-layers for the single energy dangling bond model) which gives a built-in potential of 0.9 volts. The thickness of both doped n- and p-layers is 100 $\AA$. Illumination is from the p-side, the photon flux is typically about $1\times10^{16}cm^{-2}s^{-1}$ and wavelength $\lambda=679\mu m$ (equivalent to photon energy $E_{photon}=1.83eV$, or absorption coefficient $\alpha=5\times10^{3}$). The mobility gap is set at $1.8eV$ and band edge density is 2×10^{21} $cm^{-3}eV^{-1}$. The band tail slopes for conduction and valence bandtails are $0.025eV$ and $0.045eV$, respectively. The dangling bond density is set to $1.0\times10^{16}cm^{-3}$ and two fixed transition energies are set at $E^{+/o}=0.8eV$ and correlation energy $U=0.35eV$. The drift mobilities for free electrons and holes in amorphous silicon are set to 10 and $1cm^2V^{-1}s^{-1}$, respectively. The test is run at room temperature ($300°K$) with -1 volt reverse bias voltage. The capture coefficient for electrons by conduction band tail states is $10^{-8}cm^3/s$ and also for holes by valence bandtail states. The capture coefficient of electrons by valence bandtail states or holes by conduction band tail states when these bandtail states are charged is 100 times higher than for neutral case, ie. $c_{nd}=10^{-6}cm^3/s$. The capture coefficients of electrons and holes by neutral dangling bond states are also set to $10^{-8}cm^3/s$ and by charged dangling bond states $10^{-6}cm^3/s$. Reflection from the back electrode is temporarily neglected. The number of spatial slices used in the program is 300 with a nonuniform slice width distribution which keep 7 slices within the doped p^+ and n^+ layers.

3.2.1 Convergence rate

The convergence rate is an important factor in judging a program. When the program is written, several detailed strategies have to be decided, for example, the sequence in which to solve the Poisson equation and continuity equations, whether to solve them with updates to variables only after each cycle of three solutions or to compute one equation to some certain accuracy and then another. Another example concerns the initial guess for n, p and ψ. After much trial and error, the best way was found to solve the equations for the above conditions, although this may by no means be universally optimum. According to the properties of the three basic variables, it was appropriate to use power law interpolation between boundaries to assign the first guesses

for free electron and hole density distributions, and to use a linear interpolation to assign the first guess for potential ψ. Starting with the Poisson equation, the three equations are updated only once each cycle of three so that the solution can converge simultaneously. When the iteration is carried out, it is possible to monitor the converging processes of all three equations. The relative change for all of three variables with respect to the value in the previous iteration is used to evaluate the convergence processes, the maximum relative change among all the nodes being selected as the maximum relative change for a given variable array in a given iteration and the largest relative change value among three variables will be output as the relative change for the iteration cycle (*Bmax*). Fig 3.1 shows the convergence processes for different device thicknesses (in the dark) to demonstrate the convergence process. The number of energy divisions (*inl*) and spatial divisions (*jnl*) are kept constant, while the thicknesses of the doped layers are not changed with the total thickness.

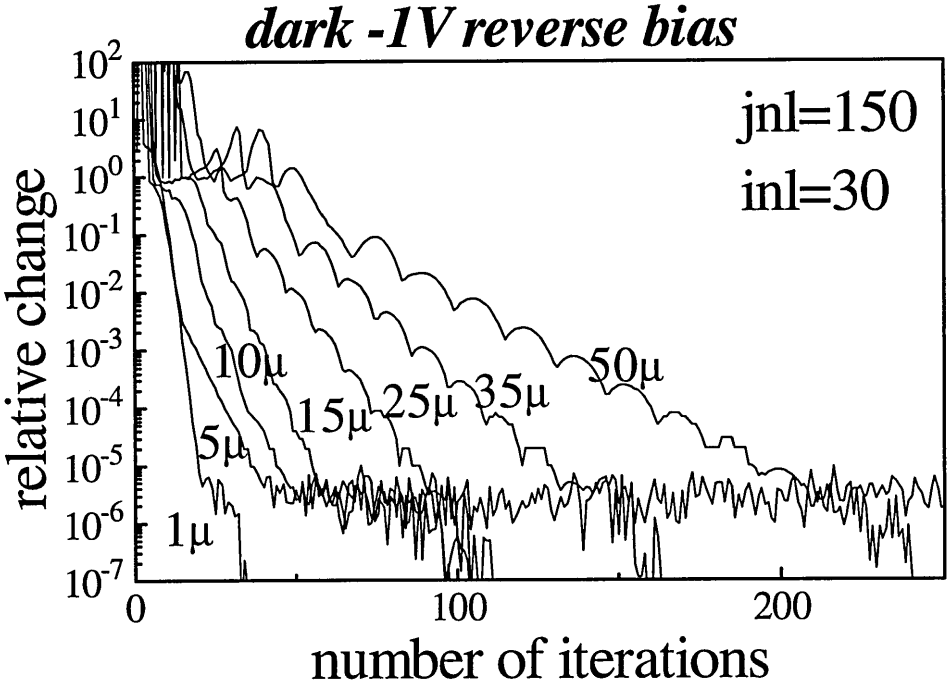

Fig 3.1 The convergence of the program for different thicknesses of an *a-Si:H p-i-n* diode. The graph shows that the slopes of the curves are roughly inversely proportional to the thickness of the device.

It is reasonable to imagine that that the convergence rate will slow down when the thickness of the sample is increased. This is mainly because when the thickness of the device is larger, the amount of charge within one single slice also increases, especially in the case of nonuniform slice width distributions, where the slice width in the middle of the sample will be much larger than the slice width near the edge (ratio $>10^3$). From Fig 3.1 we can see that in the beginning of the iteration, there is always a small number of loops which appear unstable, ie not entering the eventual convergence process yet, but after this instability, the convergence proceeds steadily with small oscillations. When the

accuracy approaches 1×10^{-6}, there seems to be another barrier (for the test conditions at least) which slows down further relative improvement. After overcoming this barrier, the convergence resumes and approaches final numerical limits. When the convergences for n, p and ψ are all separately monitored, they were found to be quite different for the three variable arrays. The three arrays converge at different rates - for example when the relative change for the p array is only 1×10^{-6}, the relative change for the n array may already have approached 1×10^{-11}, five orders lower. The explanation for this phenomenon is not clear. It was not attempted in the project to improve the convergence speed by adjusting this unbalanced converging process, and all the programs simply use the largest relative change as the judge for the convergence of the calculation.

3.2.2 Evolution of the convergence process

"Snap shots" of the improving solutions at selected numbers of iterations give a clear picture of the convergence process. Considering the large change in the beginning of the iteration, the snap shot is taken starting from the relative change of 10^2. and then one snap shot every decade lower. The number of iterations between each snap shot is varied. In the first part of the iteration, accuracy changes quickly, so the snap shot may be taken every iteration since the relative change drops more than a decade. After entering the eventual convergence process, the number of iterations for every decade of relative change is very much determined by all the conditions applied and the parameters input for the device itself. It needs to be mentioned here that even though a snap shot is a simple way to look at the convergence process, the actual convergence has very complicated properties. Some dramatic change might happen beyond the limit that the naked eye can discern. For example, quantum efficiencies greater than unity are a typical example of this (see chapter 6).

Fig 3.2 is a snapshot graph of the hole density distribution during the convergence process for dark conditions. It can be seen that it does not take long to reach a precision where improvement is indistinguishable on the plot. Not much change occurs after snapshot number 3 (less than 10 iterations) which is taken when error $Bmax$=0.488 which is very large. The reason for this lies in the way *Bmax* is calculated. The *Bmax* error for each equation is the largest one within any array and the *Bmax* used to judge the convergence of the program is the largest *Bmax* among three equations. It is quite common that when one of the equations has approached very high precision, say, $Bmax=10^{-8}$, the other is still wandering around 10^{-3}. So from this point of view, the preset accuracy for the iteration does not have to be very small, but better to be small for safety. The value used in this program is between 10^{-6} to 10^{-8}.

Fig 3.3 shows the same snapshot under illumination. Note the change of scale. It was found that the convergence process under light conditions is much more steady than in the dark, possibly because under illumination, the free carrier density is much higher

than at thermal equilibrium, so that small numerical disturbances in n and p become relatively less effective under light conditions compared with the dark.

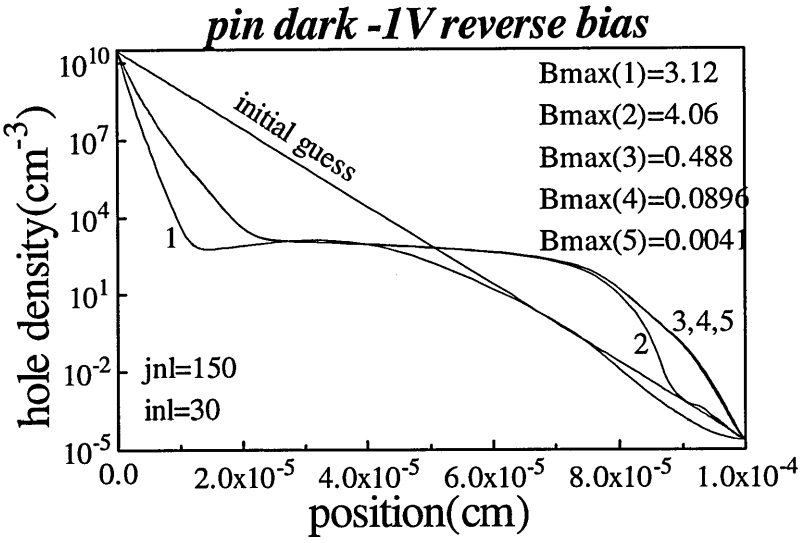

Fig 3.2 Snap shot of the hole density distribution in *p-i-n* solar cell under reverse bias dark conditions. It can be seen that when the relative change is smaller than 1×10^{-1} the solution looks no different to the final result.

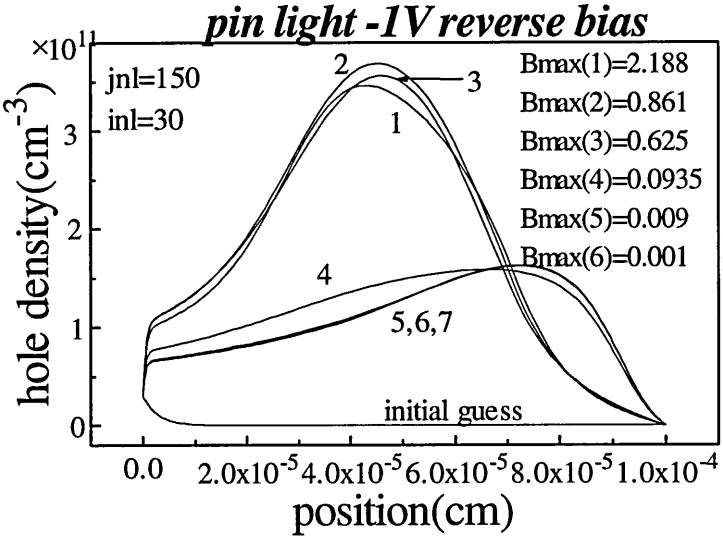

Fig 3.3 The snapshots for hole density distribution for a *p-i-n* solar cell under reverse bias and light conditions. During the iteration it is seen that an accuracy of 10^{-3} appears to be close enough to the final result.

3.2.3 Limitations of the program

The program converges under most normal operation conditions. However, it does fail to converge for some extreme situations. For example, when the thickness of the device is increased, the number of slices has to increase accordingly, otherwise, it may fail to converge. When the bias voltage is small in dark conditions, convergence becomes more difficult since small disturbances may become significant.

3.3 Testing *p-i-n* devices

The name of the program *SPIN.F* stands for steady state simulation for *p-i-n* devices. The tests of the program on a *p-i-n* diode either in light or in dark conditions is an important practice for any further applications. We emphasise here that the tests described in this chapter are basically trying to test the robustness of the program and demonstrate its capabilities rather than trying to solve specific practical problems.

3.3.1 Thin devices and capture cross sections

Thin samples (normally thickness<1μm) represent the thickness of most photovoltaic devices, and the results obtained from thin *p-i-n* devices will represent the most important characteristics of amorphous silicon in practice. It is of extreme importance to understand the behaviour of the basic *a-Si:H p-i-n* structure. With the help of experimental measurement and computer modelling, the understanding of this material is much better than the understanding of 20 years ago, however there are still many problems unsolved and parameters ill defined. In this section, one example is investigated as a demonstration- the capture coefficient.

At temperatures above 100°*K*, the defect recombination mechanism changes gradually from tunneling to direct capture of mobile electrons or holes by defects (Street 1991b). Recombination through either dangling bonds or band tail states becomes important in determining the transport properties of amorphous silicon *p-i-n* devices. These recombination processes mentioned are mostly governed by the capture and release processes of carriers into or out of deep states. The simplest model to describe this processes is the ballistic model. From this model, the relation between capture cross-section and carrier life time is as follows:

$$1/\tau=\delta v N_n \tag{3.1}$$

where v is the velocity of the carriers, N_n is the defect density. τ is carrier life time and δ is the capture cross section. This model is only valid when the capture length is smaller than the scattering mean free path of the carriers. If not, the capture becomes diffusive, and the diffusion length will decide the carrier life time. Although the capture cross-section defined above is a simple concept, measurements have turned out to be quite variable, and Table 3.1 summarizes the capture cross-section δ or capture coefficient c used or obtained by different authors.

From Table 3.1, it can be seen that either δ or c varies by many orders of magnitude as reported by different authors. The ratio between the values for neutral and charged states is to some extent more consistent. It has also been reported that δ values

are almost independent of temperature (Street 1991b), but still may have some relation to the energy state of the defect. It is of great importance to investigate the influence of δ or c in order to use an appropriate value in modelling.

Table 3.1 Capture cross-section or capture coefficient used in different simulations

Author		*BT*(0)	*BT*(+-)	*DB*(0)	*DB*(+-)	Ratio
Street (1984)	hole $\delta(cm^2)$			8×10^{-15}	2×10^{-14}	~2.5
	electron $\delta(cm^2)$			2.7×10^{-15}	1.3×10^{-14}	~5
Kemp et al (1989)	$\delta(cm^2)$	10^{-19}	10^{-16}	10^{-18}	10^{-16}	10^3,10^2
Mittiga et al(1989)	$\delta(cm^2)$	10^{-16}	10^{-14}	10^{-16}	10^{-14}	10^2
Misiakos and Lindholm(1988)	$c(cm^3/s)$	10^{-11}	10^{-9}	10^{-11}	10^{-9}	10^2
F.Shapiro et al (1989)	$c(cm^3/s)$	5×10^{-11}	5×10^{-9}	5×10^{-11}	5×10^{-9}	10^2
Zeman et al(1994)	$c(cm^3/s)$	1.2×10^{-10}	1.2×10^{-8}	1.2×10^{-9}	1.2×10^{-7}	10^2
Zeman et al(1995)	$c(cm^3/s)$	7×10^{-10}	7×10^{-10}	3×10^{-9}	3×10^{-8}	1, 10

BT(0) stands for the capture of electron or hole by neutral bandtail states,
BT(+-) stands for the capture of electron or hole by charged bandtail states,
DB(0) stands for the capture of electron or hole by neutral dangling bond states,
DB(+-) stands for the capture of electron or hole by charged dangling bond states,

In our model, the electron capture coefficient by conduction bandtail states c_{na} is used as an input parameter. By assuming ballistic capture, with carrier velocity is about 10^7cm/s at room temperature, the capture coefficient is converted to capture cross-section as follows:

$$\delta = c/v$$

The following investigation is carried out in the illuminated condition which was mentioned in the early part of this chapter. The electron capture coefficient by neutral conduction bandtail states c_{na} is varied from 10^{-9} to 10^{-7}, while the hole capture coefficient by neutral valence bandtail states and the carrier capture coefficient by neutral dangling bond states are kept the same as c_{na}. The ratio of capture coefficients between neutral and charged states R is changed from 1 to 0.01 (R_t for tail states and R_D for dangling bond states)

Fig 3.4 plots the spatial variation of the carrier lifetime in a device as described above with various values of capture coefficient parameter. It shows a good linear relation between c_{na} and inverse carrier lifetime as in the basic equation 3.1. We believe that the ballistic model (eq. 3.1) is a good approximation to the capture processes in this case though the diffusive model might also apply (Street 1991b). Figure 3.4 also shows the carrier lifetimes are depressed to a lower value as expected when the capture coefficients of carriers by charged states are increased in case (b). This change mainly happens in the front part of the device which is subjected to a series of changes due to the change of c_{na} and the ratio R. The reason for this will be clearer when the following two figures are analysed.

Fig 3.5 shows the spatial variation of electric field under similar changes in c_{na}. Due to the larger values of R_t and R_D in case (a), the recombination due to the higher capture coefficient value for the charged states is not as high as in case (b). In this case more space charge will accumulate inside the device, so as to screen out the field more, so causing a low field region near the rear side of the device.

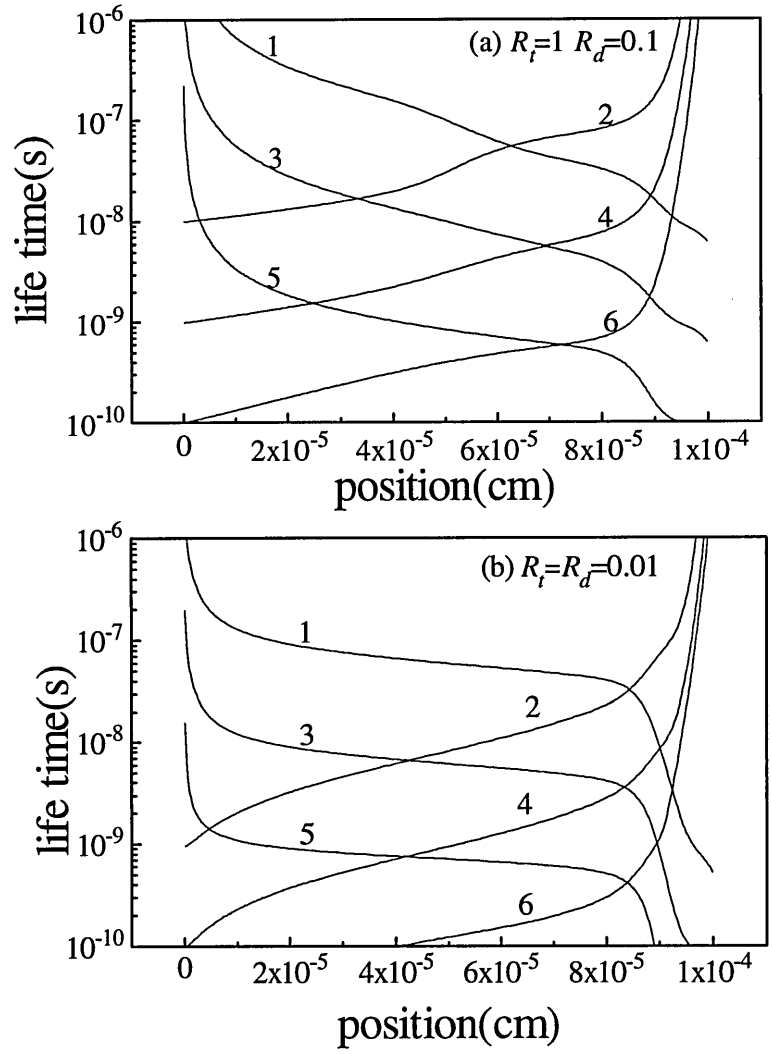

Fig 3.4 The electron and hole lifetime spatial distributions with capture coefficient as a parameter. Curves 1,3,5 are the hole life time for capture coefficients of 10^{-7}, 10^{-8}, 10^{-9} cm^3s^{-1}. Curves 2, 4, 6 are for electrons. The graph shows a linear relation between life time and capture coefficient. Graph (a) for the case when R_t=1 and R_D=0.1, graph (b) for R_t=R_D=0.01

This effect is enhanced with the reduction of the c_{na} value. When R_t and R_D value are smaller, as in the (b) case, the recombination rate will increase accordingly, so as to reduce the space charge density, leaving a relatively uniform internal field. Please notice the difference in field scales.

This effect is further supported by Fig 3.6 which shows the recombination via dangling bond states (recombination via bandtail states is relatively small). It can be seen

that the recombination rate profile possesses the same trend in relation to the c_{na} value though not as good a linear relation as in fig 3.4. It can also be seen that when R_t and R_D are small as in the (b) case, the recombination rate near the front of the device is significantly enhanced both via D^+ and D^o states and accordingly decreased near the rear of the device though not much change can be identified near the rear surface of the heavily doped n-layer. It is seen that the recombination rate in case (b) is comparatively uniformly distributed in the central part of the device. This is mainly due to the more uniformly distributed electric field in case (b) when the capture coefficient by charged states is increased by changing the value R.

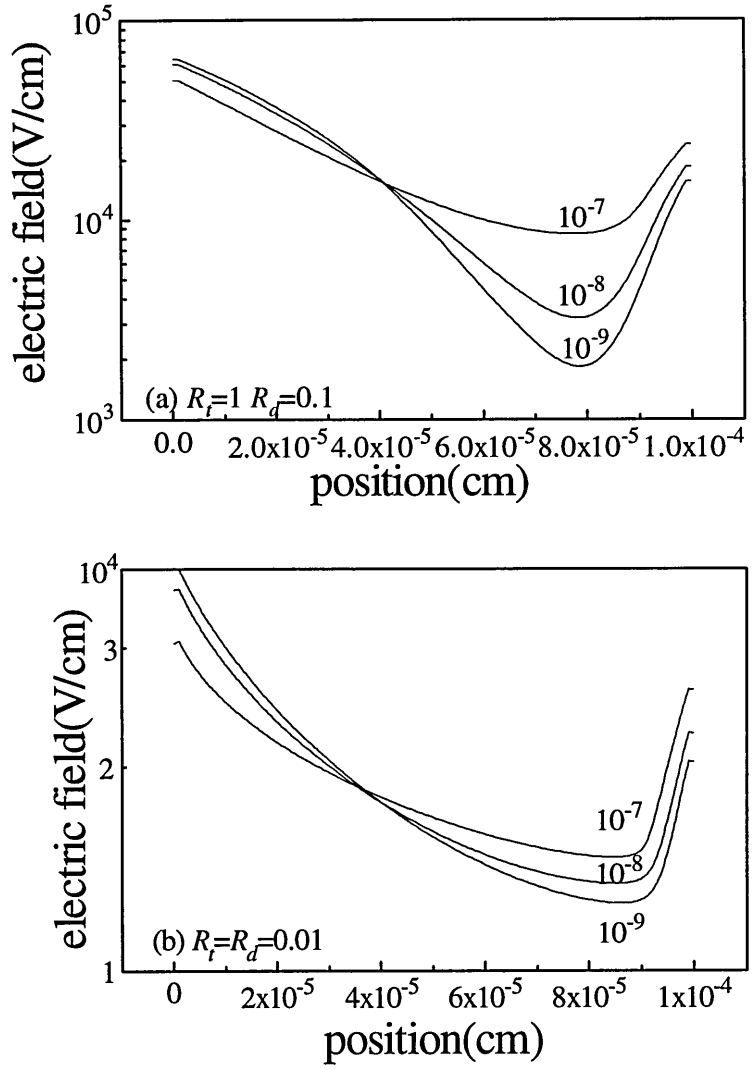

Fig.3.5 The field distribution varying with capture coefficients. With capture coefficient varying from 10^{-7}, 10^{-8} to $10^{-9} cm^3/s$, the field at the rear side of the device drops showing a low field region and the front part of the device shows an increase in field. Graph (a) for the case when R_t=1 and R_D=0.1, graph (b) for R_t=R_D=0.01.

It is clear from the above that that low field regions correspond to regions of low space charge which in this context means that the fraction of neutral D^o states

predominates. This situation naturally leads to a higher recombination rate in low field regions, while a situation with uniform field will make the recombination rate relatively uniformly distributed across the device.

We have shown that the effect of capture coefficient on internal characteristics is significant. Also we will show the effect of capture coefficient c_{na} on the external characteristics, as an example, *I-V* characteristics. The effect of the capture coefficient change on *I-V* characteristics is shown in Fig 3.7, for a similar variation to that mentioned above except that the thickness of the device is reduced to 0.5μm in order to simulate a similar operation situation to that of a solar cell. At this time we change the c_{na} value in a wider range, from 10^{-7} to $10^{-10} cm^3/s$ and keep the ratio of capture coefficients between neutral and charged defect constant (R_t=R_D=0.01).

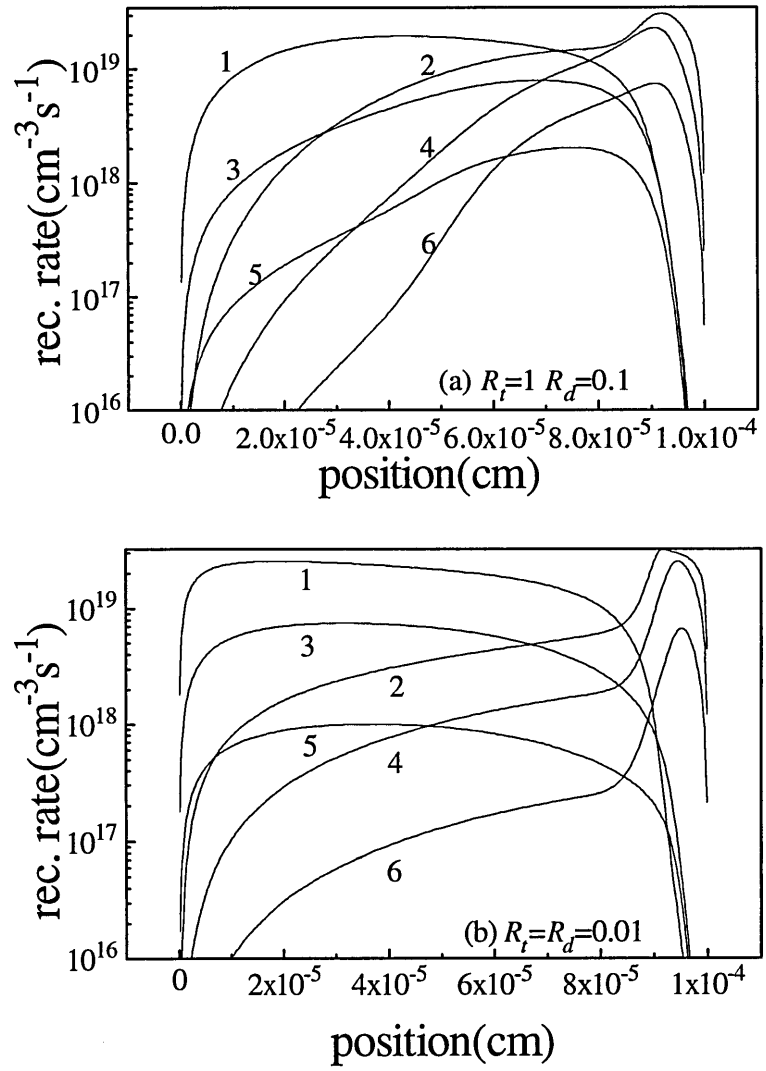

Fig 3.6 The recombination rate distribution variation with change of capture coefficient. Curves 1, 3, 5 are the recombination rate via D^+ states and curves 2, 4, 6 are the recombination rate via D^o states when capture coefficients are 10^{-7}, 10^{-8}, $10^{-9} cm^3/s$ respectively. Graph (a) for the case when R_t=1 and R_D=0.1, graph (b) for R_t=R_D=0.01

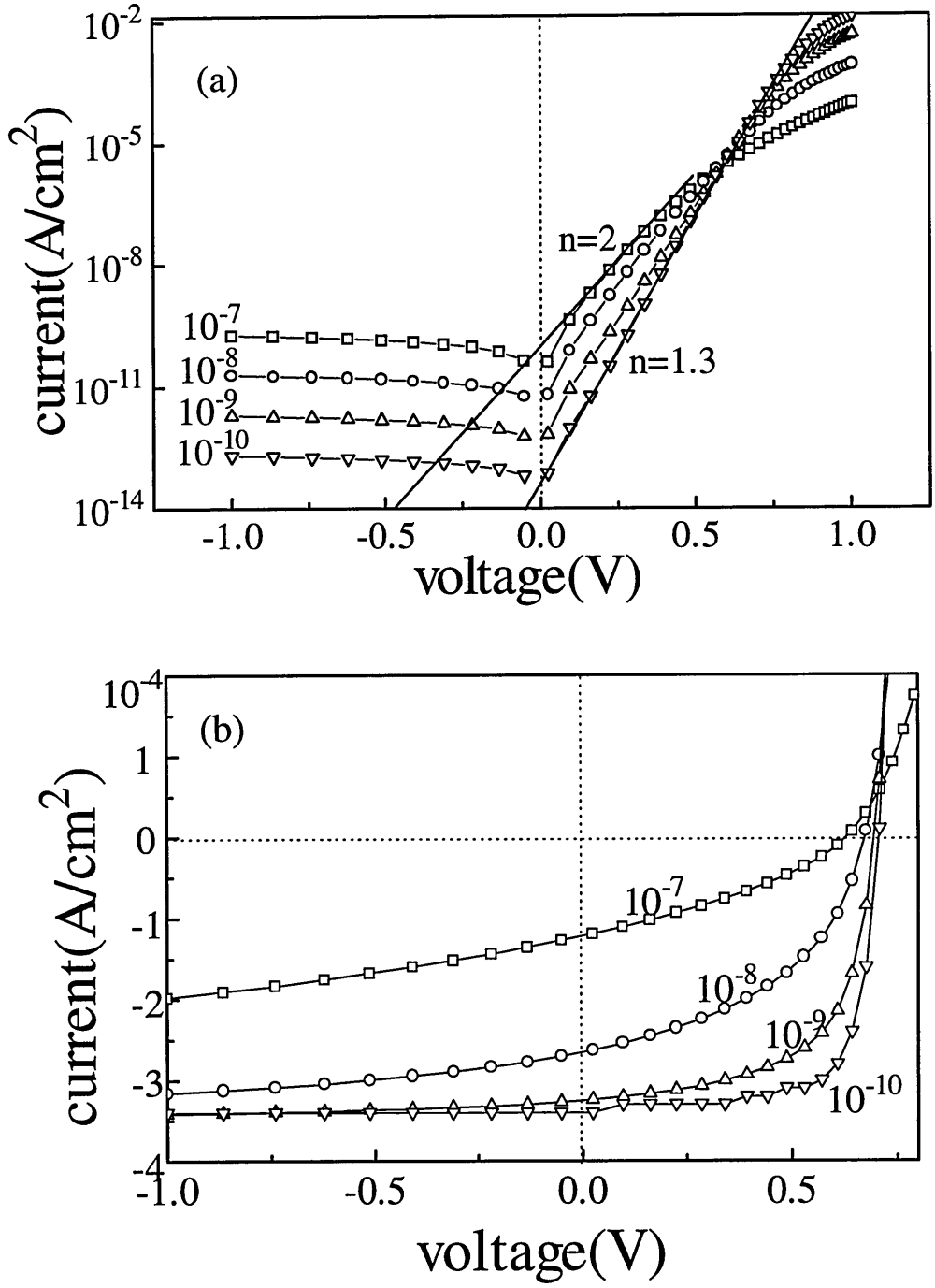

Fig 3.7 Light and dark *I-V* characteristics of a 0.5μ*m p-i-n a-Si:H* diode for different capture coefficients, 10^{-7}, 10^{-8}, 10^{-9} and 10^{-10} cm^3/s, respectively when the ratio between the capture coefficients for neutral and charged states constant, R_i=R_D=0.01. For the light conditions see text (section **3.2**)

Similar phenomena are observed in Fig 3.4. In the dark *I-V* characteristics, the reverse part of the plot shows a good linear relation between dark reverse current and c_{na}. In the dark and reverse bias situation, the current comes from the *thermal generation* via defects (either bandtail states or dangling bond states), so that the recombination rate returned is *negative*. The thermal emission rate is proportional to the capture coefficient, so when the capture coefficient is smaller, the thermal emission rate will also be smaller, then the dark depletion current due to the thermal emission will decrease accordingly.

On the forward part of the *I-V* curve, when c_{na} is small ($c_{na}=10^{-10}cm^3/s$), the quality factor n_q is about 1.3, and the transport is mainly controlled by carrier drift and diffusion. When the c_{na} is large, recombination is enhanced and the transport is mostly controlled by the bulk recombination. The quality factor increases accordingly so that $n_q=2$ when $c_{na}=10^{-7}cm^3/s$). At higher forward bias voltage, the transport changes to a space charge limited current regime, changing the capture coefficient only changes the total recombination rate, and the output current becomes inversely proportional to the c_{na}. We note that in practical solar cells, values of quality factor in the range 1.2 to 1.7 have been observed. Ideally, a value close to unity is desirable, indicating minimum recombination loss.

From plot (b), under illumination conditions, due to the carrier generation by light, thermal emission phenomena disappear, and instead the recombination mechanism controlled by the c_{na} value takes over. When c_{na} is small (10^{-9} or $10^{-10}cm^3/s$), the recombination loss is small, photogenerated carriers are mostly collected, and this represents good *I-V* characterisitcs, with the highest value for open circuit voltage, short circuit current and fill factor. When c_{na} is large, the transport is mainly controlled by the recombination. This feature is represented by the dramatically reduced short circuit current and recombination cotrolled collection profile in the reverse voltage part.

3.3.2 Thick *p-i-n* structures

Another potential application of *a-Si:H* is photodetectors. A special advantage of amorphous silicon material is that it is easily deposited on large area substrates, so the fabrication cost will be much lower than for crystalline products. Photodetectors normally are thicker than *a-Si:H* solar cells in order to absorb more photons, and mostly work under reverse bias voltages. The reason for this is mainly because the depletion layer extends rapidly under reverse bias and widths of up to $50\mu m$ are possible at high bias (Perez Mendez et al 1989). If no bias is applied, the depletion width is only about $1\mu m$ from each side, basically this is why *a-Si:H* solar cells are normally thin. From the following simulation results, it will be seen that this particular situation in thick *a-Si:H p-i-n* diodes introduces significantly different phenomena in the internal characteristics of the diodes.

The following test was made under similar experimental conditions as mentioned in the beginning of this section except the following changes are made. The thickness of the device is now $20\mu m$, and p^+ and n^+ layers are $20nm$ thick. With the increase of the thickness, in order to keep reasonable accuracy, the number of slices in the finite difference method is also increased accordingly but not proportionally. 500 slices is used in the following test. Nonuniform slice width distribution will keep 7 slices within the doped p^+ and n^+ layers. Capture coefficients used for carriers by neutral bandtail states are $c_{na}=10^{-8}cm^3/s$, the $R_t=0.01$ and $R_D=0.1$.

(i) Reverse bias (low field region)

Compared with a thin diode, most of the *i*-layer in a thick diode far from the *p-i* and *i-n* interface is left field free due to the limited width of the depletion region. From this point of view, a photon dectector will normally work in a reverse bias condition, ie a high reverse bias voltage will be applied to the diode in order to reach highest collection efficiency. Fig 3.8 shows the internal field changes with the applied bias voltage. Curve 1 is at 0 volt and dark, for comparison.

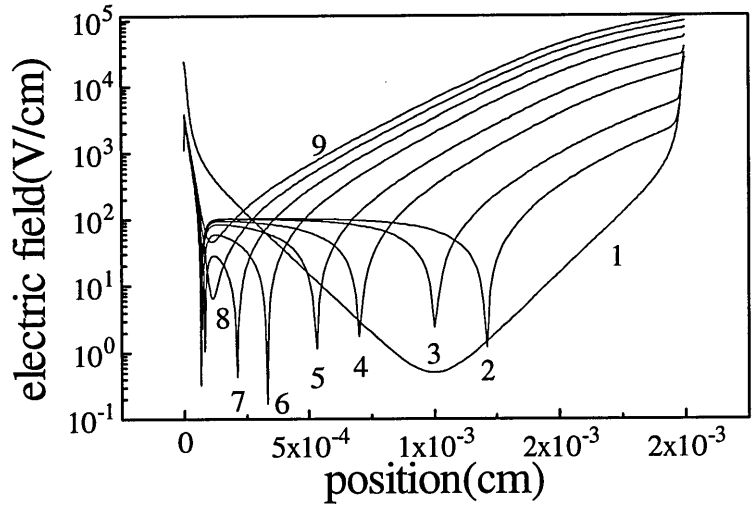

Fig 3.8 The internal field of a 20μ*m p-i-n* diode under light conditions varying with reverse bias voltage. Curve 1 is at 0 volt dark, curves 2-9 are in the light condition with bias voltage 0, 1, 5, 10, 20, 30, 40, 50 volts respectively. For the light condition see section **3.2**.

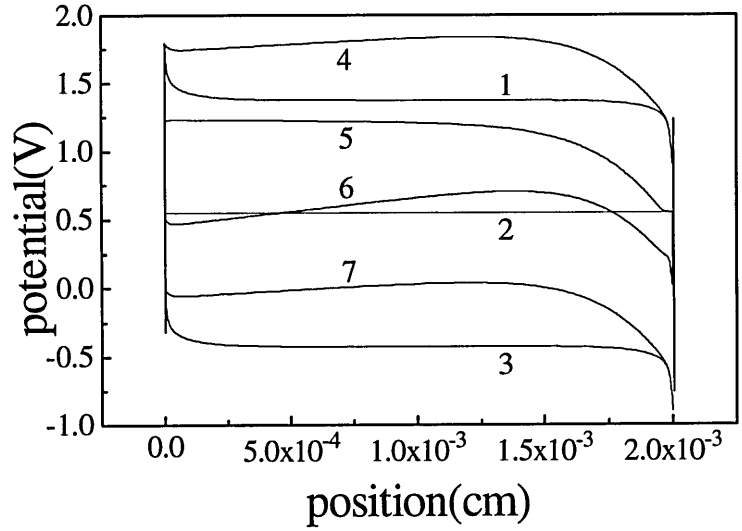

Fig 3.9 The band edge and Fermi-levels under dark and light condition with no bias voltage. See text for the light conditions. Curves 1, 2, 3 are conduction band edge, Fermi-level and valence band edge in the dark condition, curves 4-7 are conduction band edge, electron quasi-Fermi-level, hole quasi-Fermi-level and valence band edge respectively.

In fig 3.8, the spatial variation of internal field is plotted. Curve 1 shows the thermal equilibrium situation for this 20μm thick sample. It is easily seen that the highest field is located near two interfaces, while outside that range, the interal field exponentially decreases towards the middle of the device. Fig 3.9 shows that the depletion width in this case is about 1μm at each side and the middle part of the *i*-layer is field free, so the band edge is a flat line.

When the light is directed onto the diode, photogenerated carriers cannot drift away due to the low field region in most of the *i*-layer. Most of the carriers are trapped and recombined. The space charge existing inside the device not only screens the field from outside but also creates a 'reversed' field in the middle of the device. When the reverse bias voltage increases, the depletion region extends, and the trapped carrier density reduces. As the result of this, the 'reversed' field region shrinks. When the reverse bias voltage is high enough, the depletion region extends through the entire device, and the reversed field disappears. It is noticable that the field gets more uniform when the reverse bias voltage increases.

(ii) Forward bias

It has been found that forward bias is a particularly difficult case for computer simulation, especially for thick samples. From figure 3.10 to 3.12 we show the comparison of different characteristics of two *p-i-n* diodes with different thicknesses. The plots (a) are for a 20μm sample with a doped layer of 20nm for each, and plots (b) are for a 1μm sample with 10nm thick doped layers. Fermi-levels in *p* and *n*-layers are 0.55eV and 0.35eV, respectively.

Fig 3.10 shows the electric field variation with bias voltage for two different thicknesses. When the diode is thin (fig3.10 (b) 1μm) and when no bias is applied, the depletion regions in the *p-i* junction and *i-n* junction are well overlapped so as to show a relatively uniform field distribution inside the *i*-layer. Compare this with the thick diode: (fig3.10 (a) 20μm) at 0 volt bias, the depletion width is only about 1μm on each junction, the field distribution inside the *i*-layer is a good exponential decay towards the centre of the device, ie, there is virtually no field in the *i*-layer.

When a small forward bias is applied, carrier injection from both sides is introduced into the device; this process increases the space charge density inside the device. The space charge forms an electric field opposite to the built-in field so that the field intensity in the middle of the diode is reduced significantly and also the depletion regions shrink backwards toward the *p/i* and *i/n* interfaces. With the increase of the forward bias voltage, the depletion regions shrink further back and leave the central part of the device controlled by the space charge. At some point, when the forward bias voltage is large enough, the field formed by the large space charge density in the central

part of the diode cancels the original internal field and results in a reversed field in the centre of the device.

For thick devices, since the field intensity in the centre of the *i*-layer was originally very small, i.e. the depletion regions from two junctions are well separated, the field reverses imediately when a very small voltage bias is applied. For thin samples, due to the originally large field in the centre, the applied forward bias needs to be large enough in order to reverse the field. (for a 20μ*m* device, this value is smaller than 0.01volt, for 1μ*m* device, field reverses between 0.4-0.5volt.) When the forward bias voltage is very large, the junction may disappear. For example in the 5volts case for a 1μ*m* sample, the *p-i* junction has been overcome by the applied bias voltage; however the *i-n* junction is still there.

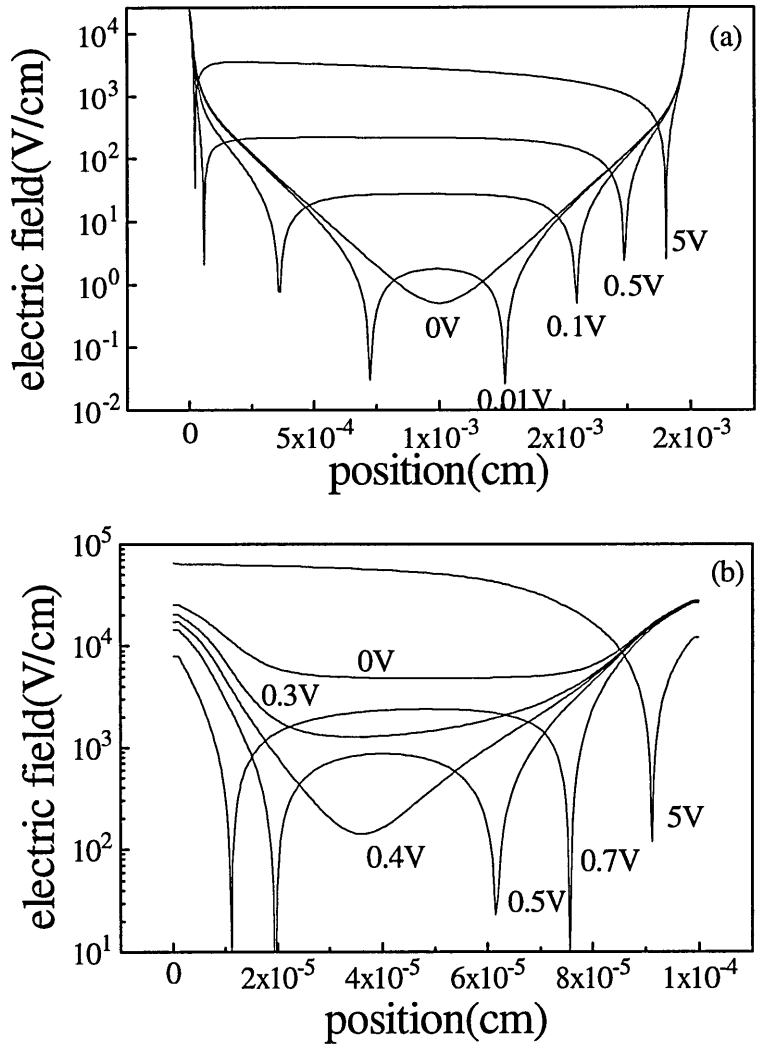

Fig 3.10 Electric field distribution under different forward bias voltage in the dark condition for two samples. (a) 20μ*m* and (b) 1μ*m*. The other conditions see section **3.2**.

It is reported (Street 1991b) that due to undoped *a-Si:H* being slightly *n*-type, the depletion region from *p-i* junction normally extends wider than from *i-n* junction, this

is true only when the ionized charge density in *p*-layer is higher than that in *n*-layer. In this example, since the activation energy in *n*-side is smaller than in *p*-side (0.35*eV* in *n*-side and 0.55*eV* in *p*-side), the free electron density in the *n*-side is several orders higher than the free hole density in *p*-layer. The depletion width from *i/n* interface will be wider than that from *p/i* interface, so that the low field region will be closer to the *p/i* interface. When reverse bias is applied, the depletion region extends from the *i/n* interface towards the *p/i* interface, and when forward bias is applied, the *i/n* depletion region shrinks first.

From fig 3.10 (b), it is clear that the field intensity drops near the *p/i* interface, and finally this depletion region disappears first. From fig3.10 (a), we could only see the tilt of the field distribution, showing that the reverse field is stronger near the *p/i* interface than *i/n* interface.

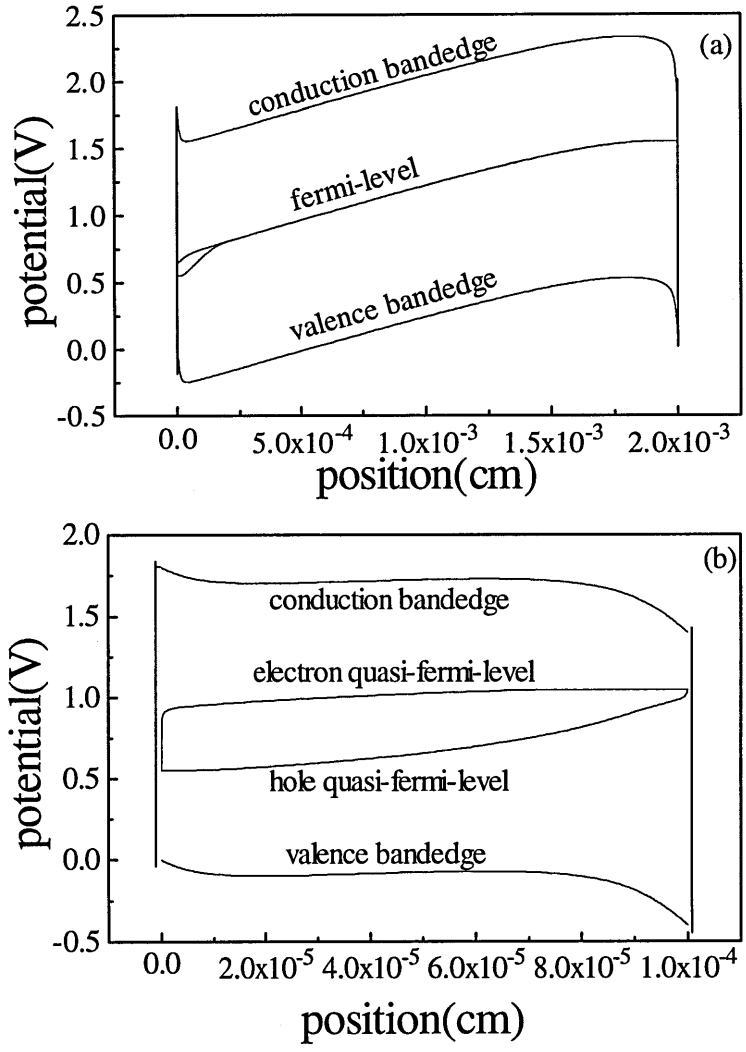

Fig 3.11 The band edge and Fermi-level plot under forward bias. (a) 1volt 20μ*m*, in which the split of the quasi-Fermi-level near the *p*-side can be seen, (b) 0.5volt 1μ*m* .

Fig 3.11 shows two band edges and Fermi-level diagram examples as modelled in the two different thickness samples. Fig 3.11(b) shows that the Fermi-level is well split due to the carrier injection in the forward bias situation. In thermal equilibrium, the free

electron density is much higher than free hole density, so the hole injection from the *p*-side changes the hole density significantly, and this is reflected in the wider split of the quasi-Fermi-level near the *p-i* interface. At the same time, the same amount of electrons are injected from the *n*-side, but, however compared with the dark electron density, this amount of injection has much less effect in splitting the quasi-Fermi-level. If we look at the thick sample case, since there is a high resistance from the thick *i*-layer, 1volt forward bias can only split the Fermi-level very little compared with the thin sample, and the change near the *n*-side is totally negligible.

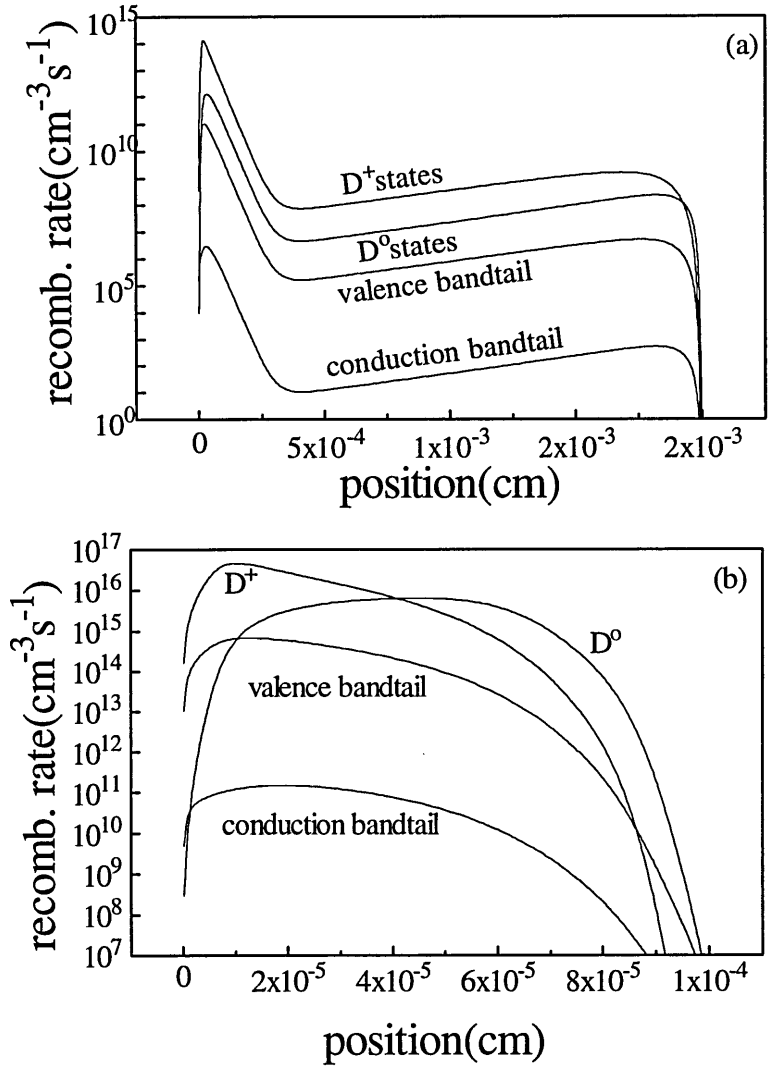

Fig 3.12 Spatial variation of the recombination rate at (a) 1volt 20μm case and (b) 0.5volt 1μm. Four curves represent four different recombination routes existing in *a-Si:H* material are shown in the plot.

Figure 3.12 shows the recombination distribution corresponding to the two examples in fig 3.11. For the thick sample, the recombination rate is very high near the *p*-side, this is because in the dark, over most of the device, the electron density is predominant, and only within the depletion region near the *p-i* interface, is the hole density higher than the electron density. So when forward bias is applied, the hole

injection from the *p*-side increases the hole density significantly, since the recombination rate is controlled by the minority carrier, and increasing the hole density increases the recombination rate greatly. On the other side, the increasing of the electron density due to the electron injection from *n*-side, does not increase the recombination rate very much since the hole density is the controlling factor, and this is five orders smaller than at the *p-i* interface.

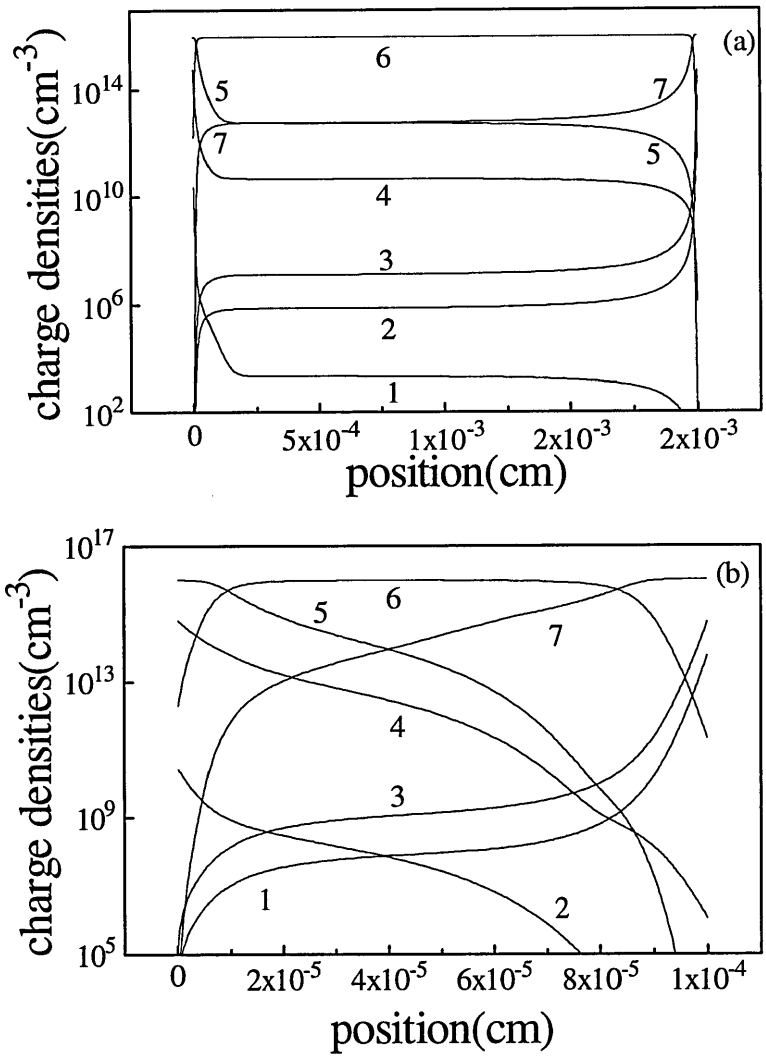

Fig 3.13 The spatial variation of space charge density occupying different states. (1) and (2) free electron and hole density; (3) and (4) charge density in conduction and valence band tail states, (5), (6) and (7) the occupation densities of D^+, D° and D^- states. (a) 20μm thick diode under 1volt forward bias voltage, (b) 1μm thin diode under 0.5volt forward bias voltage.

The peak near the *p/i* interface corresponds with the zero field position in fig 3.10(a). It is reasonable that when holes are injected from the *p*-side, in the first half micrometer distance, the holes have to diffuse towards the reverse field region, and once they enter this region, the holes will rapidly drift through the central reversed field region. When they approach the other end, they also need to diffuse to reach the other electrode. It is because of these two diffusion process, that the recombination rate in

these two regions is higher than in the middle, especially near the *p/i* interface, due to the reason mention above, giving a much higher peak. Approaching the *n/i* interface, a significant fraction of the holes has been recombined during the process of the transition, so that there is not a obvious peak on the recombination plot.

The other feature from fig 3.12 (a) is that recombination is mainly via D^+ states (electron captured by D^+ and hole captured by D° states). Actually, from fig 3.13, it is very clear that over most of the device, the D° states are dominant, so when holes are injected from the *p*-side, they will quickly be captured by these dominant D° states recombining with the electron already in those states. Since the charge density in the two bandtails is less than in the dangling bond states, recombination via these routes is also small.

In the case of the thin diode, D° states are still dominant over most of the device, however, the D^- state has a larger capture coefficient for holes than D° states (100 times larger in the simulation), so near the *n*-side, the recombination via D° states (electron capture by D° states and hole capture by D^- states) overtakes the recombination rate via D^+ states and becomes dominant in the right half of the device. In the thick device case, since the density of D° states is 1000 times larger than the densities of the other two (fig 3.13 (a)), the recombination rate via D^+ is dominant all the way across the device.

Comparing fig 3.12 (a) and (b), it is clear that higher carrier injection in thin devices causes higher recombination rates, and lower carrier injection causes lower recombination rates. In the thermal equilibrium situation, the free carrier densities for electrons and holes in the two different thickness devices are more or less at the same level, but due to the overlapping of the depletion regions, the free carrier densities in the thin device are rather less than in the thick device. However, when a forward bias voltage is applied, the increase of the hole density in the thin device is much greater than that in the thick device, nearly reaching the same level as the electron density. On the contrary, the carrier densities in the thick device do not change very much. This is another explanation for the higher recombination rate in thin devices.

3.4 Summary

In this chapter, we demonstrated several tests of the program developed in this work, on some special test cases. We demonstrated the change of many internal features in thin devices, such as field, lifetime and recombination rate, and external featutres *I-V* characteristics, when capture coefficients are changed, and we also demonstrated the changes in the dark and with illumination, with reverse and forward bias voltage for very thick devices in comparison with thin devices. Some detailed discussion was given in order to have a better understanding of *a-Si:H p-i-n* devices. These tests give a brief idea of the capability of the computer program and should be helpful for any further applications on amorphous semiconductors.

Chapter four

THE DEFECT POOL MODEL

4.1 Introduction

Following the discovery by Spear and LeComber (1975) that amorphous silicon can be viably doped *n*-type and *p*-type, so that the fabrication of a *p-n* junction devices became a practically possibility, the Staebler-Wronski effect was found in 1977 (Staebler and Wronski 1977), which became a constant background feature in the development of the amorphous silicon. It has long been believed that there are deep defects due to the existence of dangling bonds which play an important part in device performance. The following are some of the defect reaction phenomena observed in *a-Si:H*:

Firstly, the density of spin-associated defects in undoped material as deposited depends on deposition conditions The best films produced by all techniques exhibit bulk spin densities N_s between 10^{15} and 10^{16} cm^{-3}. Non-optimized conditions usually produce both higher spin densities and wider band tails. The density of defects also increases as the square root of incorporated dopant concentration as measured by sub-bandgap optical absorption (Street 1982).

Secondly, all films with good electronic transport properties, and many films with not-so-good transport properties, exhibit a degradation in transport properties upon prolonged illumination - the Staebler-Wronski effect. The number of defects generated by a short light soak rises as the films are doped more and more heavily. In *p-i-n* and *p-i-p* structures, double- or single-carrier injection (by the application of a forward bias in the *p-i-n* case) degrades devices in a way similar to light soaking - i.e. by the generation of defects. A *p-i-n* structure held under reverse-bias during illumination such that the density of free carriers is greatly suppressed, degrades much more slowly if at all (Staebler et al 1981). This effect demonstrates that light is not required for defect generation, only free carriers.

Thirdly, the Staebler-Wronski defects can be removed by annealing, i.e., holding the film at elevated temperature in the dark, e.g. 200°*C* for 30 minutes (Stutzmann et al 1985).

Fourthly, solar cell structures which are held under reverse bias during annealing show an enhancement in performance directly traceable to a reduction in the density of defects in the *i*-layer below the level achieved when the devices were previously annealed or are subsequently annealed, *without* bias (Swartz 1984).

Finally, when thin film transistors are held under strong gate bias (pulling the undoped *a-Si:H* channel into strong accumulation or inversion, i.e., strongly displacing the Fermi-level off its initial value), the number of states near the channel/insulator interface increases. These interface states induce a shift in the gate voltage required for

turn-on (the threshold voltage). The process is also reversed by annealing (Hepburn et al 1986).

It is clearly demonstrated from these phenomena that the dangling bond density is strongly dependent on the free electron and hole density, and the defect density is no longer fixed at deposition, but will change during operation and can be reversed by annealing at an elevated temperature.

In view of the special behaviour of the defect state noted above, it has been proposed that defects in *a-Si:H* can be thought of as the product of a chemical reaction, the equilibrium point of which can be pushed back and forth at will. This perspective is radically different from the previously held view of *a-Si:H* material. It was thought that the defect states were essentially fixed by deposition conditions, so dangling bonds were just those sites which managed to miss grabbing hold of a hydrogen atom during film growth, and these sites stayed permanently unhydrogenated as the 'stable' defects. However, it is believed now that the light-soaking involves a reaction occurring at special sites which 'toggle' back and forth between defect and non-defect configurations.

In 1982 Street for the first time proposed that a form of chemical-reaction equilibrium existed at the growing surface between dopants and defects. He also suggested that this implied that the Staebler-Wronski effect arose from a similar mechanism. Then in 1985, Smith and Wagner suggested that the 'stable' dangling bonds were actually produced by the same reaction that led to the Staebler-Wronski dangling bonds.

In addition to all the experimental evidence, many attempts had been made to calculate the formation energy of the dangling bonds U_{form}. but values either from the calculation or from the experiments vary over a wide range, and it is still a most uncertain value. Alongside this, after the key importance of the paramagnetic (g=2.0055) defect was established, the location in the bandgap of the associated defect levels is perhaps the longest-standing controversy in the physics of *a-Si:H*. As Fritzsche (1987) said: "perhaps we are asking the wrong question". With the improvement of experiment, it became quite clear that the defect positions determined in doped and undoped films really are in different places. Thus a unique answer to the question may not be possible.

Based on all these controversies, a new model was needed. The model for the defect-forming reaction normally involves the breaking of *Si-Si* bonds, which are generally thought to be stabilized by diffusive hydrogen motion through breaking and reforming *Si-H* bonds, although microscopic models that do not require hydrogen have been proposed (Crandall 1991). The equilibrium density of dangling-bond states depends on the Fermi energy, which leads to a higher density of dangling bonds for doped amorphous silicon than undoped amorphous silicon

When the energy of the dangling-bond state can take a range of values due to the inherent disorder of the amorphous network, a proper consideration of the chemical equilibrium model leads to an energy shift of the peak of the formed defects due to the

minimization of free energy. Furthermore, this energy shift is different for defects formed in the different charge states (+, 0, -). This is the so-called defect-pool model. For a sufficiently wide pool, the model leads to negatively charged defects in *n*-type amorphous silicon having a lower energy than positively charged defects in *p*-type amorphous silicon, even when the correlation energy is positive, a previously puzzling result found in many experiments.

The first work on the defect pool model was done by Bar-Yam and Joannopoulos (1987), who first pointed out that the formation energy of a defect depends on its charge state and that the difference in the formation energies depends on the Fermi energy and the energy of the defect itself. This paper predicted the essential result of the defect-pool model. Stutzmann (1987) introduced the weak-bond dangling-bond conversion model and Smith and Wagner(1987) identified the weak-bond energies with the valence-band-tail states, which are exponentially distributed in energy, giving a further distribution of formation energies. In a separate development (see for example Street 1991a) the importance of hydrogen in providing a mechanism for defect equilibration was proposed. This work was important in identifying possible microscopic mechanisms, but also in introducing additional entropy from the hydrogen reactions and so lowering the defect chemical potential. Strictly speaking, hydrogen is not part of the essential defect-pool model, but it was the proposal that could provide a plausible microscopic mechanism with sufficient entropy to lower the defect chemical potential, and so give the experimentally measured defect densities.

Winer (1990) brought together these different aspects in a classic paper, which defined the modern defect-pool model. He calculated the density of states in undoped and doped *a-Si:H* and produced the key result that negatively charged defects in *n*-type material were lower in energy than positively charged defects in *p*-type material. Winer assumed that the density of states was dominated by defects of only one charge state in each type of material (negative in *n*-type, positive in *p*-type, and neutral in intrinsic). While this could be a good approximation in doped material, it was not a good approximation in intrinsic material.

Schumm and Bauer (1991) extended Winer's work by first considering the simultaneous formation of defects in all three charge states, but only later realized the importance of weak-bond depletion by defects of all three charge states. Their results showed more charged defects than neutral defects in undoped material. Branz and Silver (1990) also concluded there were more charged defects than neutral defects, with a model similar to Schumm and Bauer's model, but expressed in terms of potential fluctuations. However, Branz and Silver (1990) did not include weak-bond dangling-bond conversion nor did they include any hydrogen entropy in their model. Schumm and Bauer considered different microscopic reactions, with zero, one, or two *Si-H* bonds mediating the weak-bond-breaking process, but concluded that the extra entropy only affected the absolute densities of states formed and not their energy spectrum.

To improve the model, building on this previous work, Deane and Powell (1993) proposed an improved defect pool model. Some errors and approximations were eliminated from previous models, and they showed that the energy spectrum of the density of states does depend on the number of *Si-H* bonds mediating the weak-bond-breaking reaction. A simple expression was produced for the energy separation of positively and negatively charged defects. They also investigated how the density of states depends on the principal parameters of the defect-pool model and predicted that there are approximately four times as many charged defects as neutral defects in good-quality intrinsic amorphous silicon. They calculated the bulk density of states, using the best input parameters drawn from experiments, and concluded that the best agreement with experimental results is found for a rather wide defect pool and for a microscopic model where two *Si-H* bonds break for every weak bond converted into two dangling bonds (Powell and Deane 1993).

Several attempts have been made to apply the results of Deane and Powell to real *a-Si:H* devices (Zeman 1995). However, most of this work has concerned *TFT* devices or purely on *a-Si:H* material itself (Deane and Powell 1994), and there are still many difficulties in deciding appropriate model parameters for *a-Si:H p-i-n* devices. In this chapter, we investigate the possibility of applying the defect pool model to *a-Si:H p-i-n* structures by adjusting the input parameters.

4.2 Description of the model

The general principle of the model is that dangling bonds are formed by the breaking of weak *Si-Si* bonds and that the density of these bonds is determined by a chemical equilibrium between the weak bonds and the dangling bonds. We can consider the dangling bonds to be formed by one of three different microscopic chemical reactions, depending on how many *Si:H* bonds are involved in the process,

$$\begin{aligned} WB &\Leftrightarrow (2D) && i=0 \\ Si-H+WB &\Leftrightarrow (D+Si-H)+D && i=1 \\ 2Si-H+WB &\Leftrightarrow (Si-H-H-Si)+2D && i=2 \end{aligned} \qquad (4.1)$$

where i indicates the number of *Si:H* bonds mediating the weak-bond-breaking chemical reaction. Here the parentheses indicate species which are intimately connected and cannot diffuse apart. For i=0, the weak bond is broken, but the dangling bonds cannot move apart without the involvement of hydrogen diffusion. For i=1, one *Si-H* bond is broken and the hydrogen atom diffuses to the weak-bond site, breaking the weak bond. For i=2, a second *Si-H* bond is broken, resulting in a doubly hydrogenated weak-bond site and two isolated dangling bond defects. It may be noted here that the present work

differs from some others about the probable number of hydrogen atoms involved in the reaction as will be discussed later.

By adding the entropy of hydrogen per defect at energy E, the general expression for the defect chemical potential is as follows:

$$\mu_d(E) = E + kT\ln\left(\frac{f^o(E)}{2}\right) + \frac{ikT}{2}\ln\left(\frac{iD(E)}{2HP(E)}\right) \tag{4.2}$$

where $P(E)$ is the energy distribution of sites which would form defects at energy E (the defect-pool function), $f^o(E)$ is the occupancy function for neutral dangling-bond states, H is the total concentration of hydrogen.

A further calculation leads to a final expression for the defect pool model

$$D(E) = \gamma\left[\frac{2}{f^0(E)}\right]^{\rho kT/E_{v0}} P\left[E + \frac{\rho\sigma^2}{E_{v0}}\right] \tag{4.3}$$

where $D(E)$ is the energy variation of the defect state density in the gap, and γ is composed of a group of constants which gives the total defect density for certain circumstances.

$$\gamma = \left[\frac{2N_{v0}E_{v0}^2}{2E_{v0} - kT}\right]^{\rho}\left[\frac{i}{2H}\right]^{\rho-1}\exp\left[-\frac{\rho}{E_{v0}}\left(E_p - E_v - \frac{\rho\sigma^2}{2E_{v0}}\right)\right]$$

$$P(E) = \left(2\sigma^2\pi\right)^{-1/2}\exp\left[-\frac{\left(E - E_p\right)^2}{2\sigma^2}\right] \tag{4.4}$$

$$\rho = \frac{2E_{v0}}{2E_{v0} + ikT}$$

$P(E)$ is the Gaussian distribution of the defect pool model, which will be distorted due to the involvement of the function in the second square bracket in equation 4.3, so that the final defect pool is no longer Gaussian. At the frozen-in temperature, the system is in thermal equilibrium, and the occupation functions for different charge states are as follows:

$$f^+(E) = \frac{1}{1 + 2\exp\left[\left(E_F - E\right)/kT\right] + \exp\left[\left(2E_F - 2E - U\right)/kT\right]} \tag{4.5}$$

$$f^0(E) = \frac{2\exp[(E_F - E)/kT]}{1+2\exp[(E_F - E)/kT]+\exp[(2E_F - 2E - U)/kT]} \tag{4.6}$$

$$f^-(E) = \frac{\exp[(2E_F - 2E - U)/kT]}{1+2\exp[(E_F - E)/kT]+\exp[(2E_F - 2E - U)/kT]} \tag{4.7}$$

so that the charge density of the dangling bond states can be written :

$$\begin{aligned} D^+(E) &= D(E)f^+(E) \\ D^0(E) &= D(E)f^0(E) \\ D^-(E) &= D(E)f^-(E) \end{aligned} \tag{4.8}$$

These formulae express the density of states at equilibrium, which is maintained for temperatures above the frozen-in temperature T^*. To calculate $D(E)$ at lower temperatures, the defect pool distribution has to be calculated at the frozen-in temperature first and then Eqs 4.5 to 4.8 can be used to calculate the low temperature defect charge distribution under operating conditions. This means the values at T^* must be used for the parameters in Eqs.(4.3) and (4.4), and in particular, E_{vo} should be replaced by E^*_{vo} and E_F by E^*_F and T by T*, where the asterisk indicates the value of a temperature-dependent parameter at the equillibration temperature. $D(E)$ is not a function of temperature below T^*, since the equilibrium density of states is assumed to be frozen-in.

4.3 Test of the model

Although the defect pool model possesses some clarity and includes the important physical processes occurring in the material and devices, we have in this work encountered problems in its application to solar cells or other *p-i-n* device using the original set of parameters used in *TFT* studies. In this section, we report an investigation of the possibility of applying the defect pool model to *a-Si:H p-i-n* devices. At first, the parameters used in published papers will be applied to the *a-Si:H p-i-n* structure to demonstrate the main features of the model and its consequences, and then different variations of the parameters will be tried in order to better fit the measurement data for such devices. We also try to use so called the reverse modelling (Zeman 1994) method to perform this process. The material parameters and operational conditions are listed in tables 4.1 and 4.2.

The first test is carried out in dark conditions. The 3-*D* image of the dangling bond density calculated from the defect pool model is plotted in Figure 4.1. This graph only plots the dangling bond density distribution, and does not include the bandtail states for the sake of simplicity. The calculation was carried out in the following sequence: At

the frozen-in temperature (e.g. 500°*K*), in the dark, the Fermi-level in *p*- and *n*-layers is fixed so that the required doping density can be calculated for the *p*- and *n*-layers. In this case E_F is $0.45eV$ above valence bandedge for the *p*-layer and $0.3eV$ below the conduction bandedge for the *n*-layer, equivalent to a doping density for the *p*-layer of $8.43\times10^{18}cm^{-3}$ and for the *n*-layer of $5.05\times10^{18}cm^{-3}$. Based on these boundary conditions, the initial guesses for electron and hole distribution and potential distribution can be made. Following this is the algorithm to solve the transport equations (Poisson equation and continuity equations).

Table 4.1 parameters used in the program

free electron mobility	$\mu_n = 10\ cm^2/(Vs)$
free hole mobility	$\mu_p = 1\ cm^2/(Vs)$
band edge density	$G_c = G_v = 2\times10^{21}\ cm^{-3}/eV^{-1}$
band tail slope for conduction band tail	$E_a = 0.025\ eV$
band tail slope for valence band tail	$E_d = (0.036^2 + kT^2)^{-2}$
mobility gap	$1.9\ eV$
diffusion coefficient	$D_{n,p} = \mu_{n,p}kT/q$ (Einstein's relation)
hydrogen density	$H = 5\times10^{21}\ cm^{-3}$
capture coeff. of electron by *C* band tail	$c_{na} = 1\times10^{-8}\ cm^3/s$
capture coeff. of electron by *V* band tail	$c_{nd} = 1\times10^{-8}\ cm^3/s$
capture coeff. of *e* and *h* by *D*° states	$c_n^o = c_p^o = 1\times10^{-8}\ cm^3/s$
capture coeff. of *e* by D^+ states and *h* by D^-	$c_n^+ = c_p^- = 1\times10^{-7}\ cm^3/s$

Table 4.2 The operating conditions used to test the program.

Fermi-level positions:
p-side 0.45 *eV* above valence band
n-side 0.3 *eV* below conduction band
p- and *n*-layer thicknesses 10*nm*
Overall device thickness 0.5 μ*m*
Abrupt *n-i*, *p-i* interfaces
Defect Pool $E_n = 1.27\ eV$ $U = 0.2\ eV$
Pool width σ 0.178 *eV*
Temperature 299°*K*
Bias voltage 0 volt
Number of energy slices across gap 30
Number of spatial slices 149
Freeze-in temperature 500°*K*

The difference from the usual calculation in this case is that as the iterations proceed and the spatial variation of the Fermi-level position within the gap converges toward its solution, continuous updates must be made for the dangling bond density distribution since in the defect pool model, the total defect density and its distribution are both related to the Fermi-level position. Compared to other, simpler defect models, a significant amount of computing time is taken at this freeze-in temperature iteration to form the defect distribution. However, this is not too restricting since only 30 iterations are needed to reach 10^{-9} relative accuracy in about 15 seconds on the *hp710* workstation used. When the iteration converges at the freeze-in temperature, the defect density is then fixed, ie. the shape in Fig 4.1 will not change in successive parts of the simulation. At the next stage, the temperature is set to the operating temperature, say 300°*K*, and the transport equations are solved again at this new temperature with corresponding operational conditions.

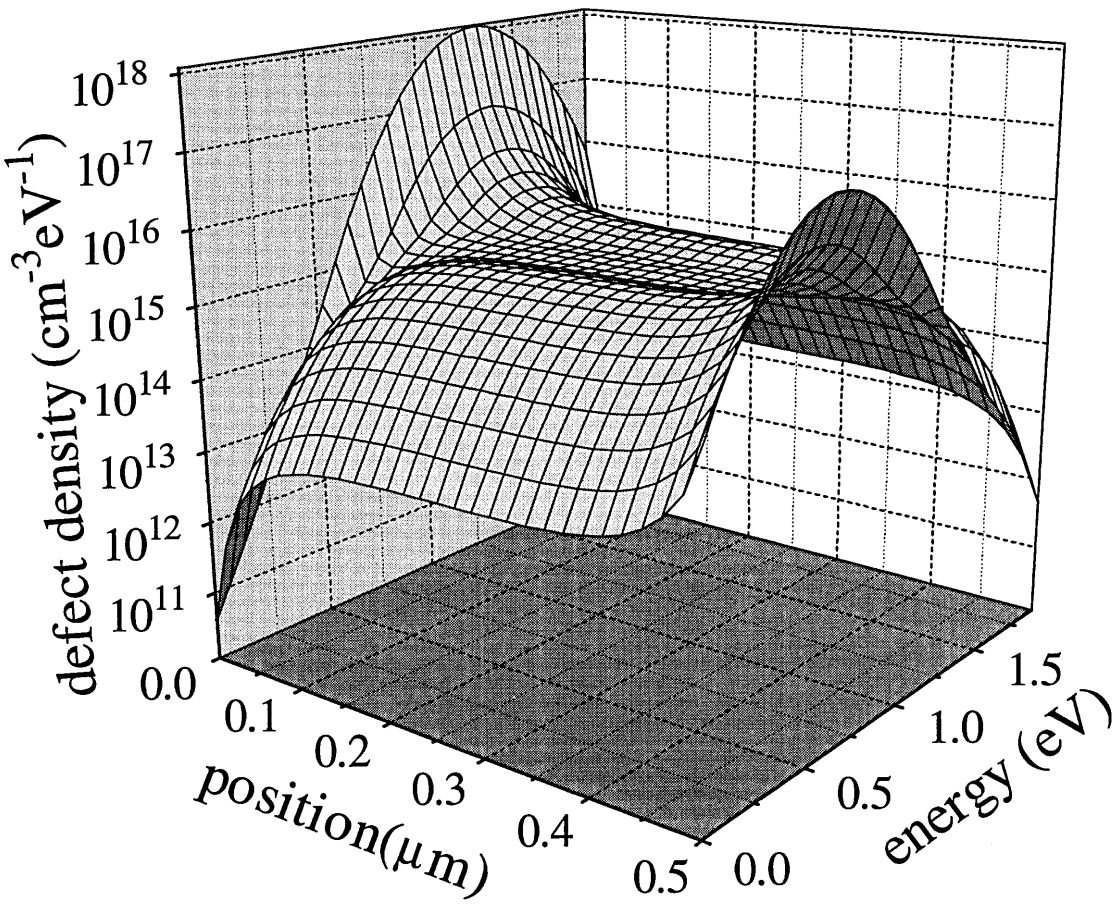

Fig 4.1 The 3-*D* spatial and energetic variation of the dangling bond density calculated by the defect pool model under the conditions listed above. This shows that at the *p*-side, most of the dangling bonds are in D^+ states, and the depletion region width is about 100*nm*, while beyond that the Fermi-level is basically in the midgap, so that the charge neutrality condition is kept, and the defect density distribution is symmetric about the D^o peak even though the D^- and D^+peaks are larger than D^o peak. Moving towards the *i-n* junction, the charge neutrality condition is no longer valid, the D^- peak becomes larger, the D^+ peak shrinks and the total dangling bond density increases dramatically - as also seen in the next figure.

Fig 4.1 is a typical defect pool distribution in positional and energetic dimensions. It shows that the defect distribution in the gap changes with the spatially changing Fermi-level in the device. Near the *p*-side, the Fermi-level is shifted downwards towards the valence band edge, so the defect peak is near the conduction band tail. At the frozen-in temperature, the defects are mainly D^+ states. Within the *i*-layer, where the Fermi-level returns to its intrinsic position, the distribution returns to a double-peak shape, where the total density of charged defect states is larger than that of neutral states. Approaching the *n*-layer, the Fermi-level is shifted upwards toward the conduction band edge, the peak of the defect distribution is near the valence band, and most of the dangling bonds are D^- states. Such a three dimension plot of defect pool distribution only gives a qualitative image of the defect density in the device. What this distribution will do to the device has to be seen by looking at the operating characteristics based on this frozen-in defect density of states.

Fig 4.2 is an integrated spatial variation of defect density distribution, where the integration is done across the mobility gap, representing the total dangling bond density of states including all charge states in unit volume. Fig 4.2 clearly shows the depletion region at the frozen-in temperature (about 100*nm* at each side). Since the defect density is sensitive to the Fermi-level position, the difference of the total defect densities between the edge and the middle is about 2.5 orders of magnitude. The plateau part of the dangling bond distribution shows the intrinsic part of the device where the Fermi-level is not shifted noticeably. However it should be kept in mind that this is the situation at the freeze-in temperature, while at the operating temperature, there will be a redistribution of all the charge states.

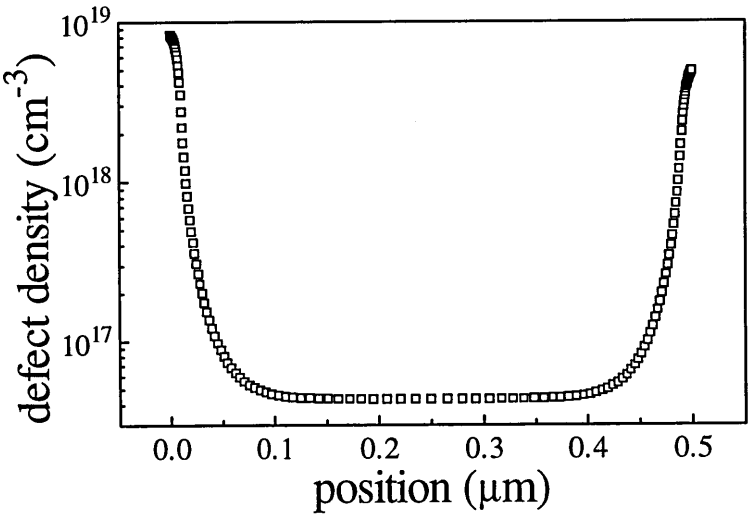

Fig 4.2 The spatial variation of the integrated dangling bond density formed at the frozen-in temperature. The total density in *p*- and *n*-layers is two and half orders larger than the defect density in the *i*-layer. Also note that the Fermi-level in the *p*-layer is 0.45*eV* from the band edge, larger than the 0.3 *eV* separation on the *n*-side, but the total dangling bond density is larger than that of *n*-side. This is because the broader valence band tail needs more charge to shift the Fermi-level.

Fig 4.3 shows the electric field distribution of the device under 0 volt and -1 volt reverse bias voltage conditions in the dark. The exponentially decreasing field at 0 volts shows a field free feature in the middle part of the device (It is more clear from figure 4.4 that the band edge is flat in the middle of the device). The two spikes close to the two edges show the increase of the field from the boundaries towards the *p-i* and *i-n* interfaces. The potential is mostly dropped in the area where the defect density is high and doping density is also high so that the recombination rate will be high. This is all due to the inhomogenous distribution of the defect density.

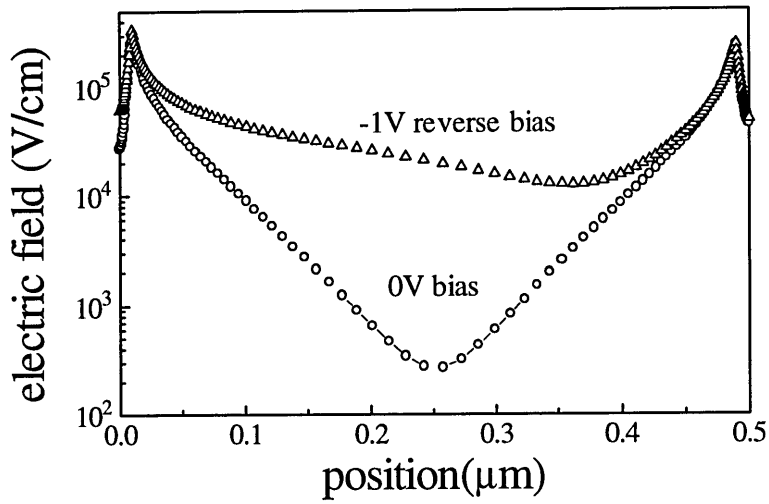

Fig 4.3 The electric field distributions for 0 volt bias and for -1 volt bias. It can be seen that in the 0 volt case, the electric field exponentially decays towards the middle of the device, being directly related to the electron and hole depletion conditions. When -1 volt bias voltage is applied, the depletion region widens, and the field increases mainly in the *i*-layer. At the *p-i* and *n-i* interface, due to the fact that the carriers are already depleted, no further field increase occurs here.

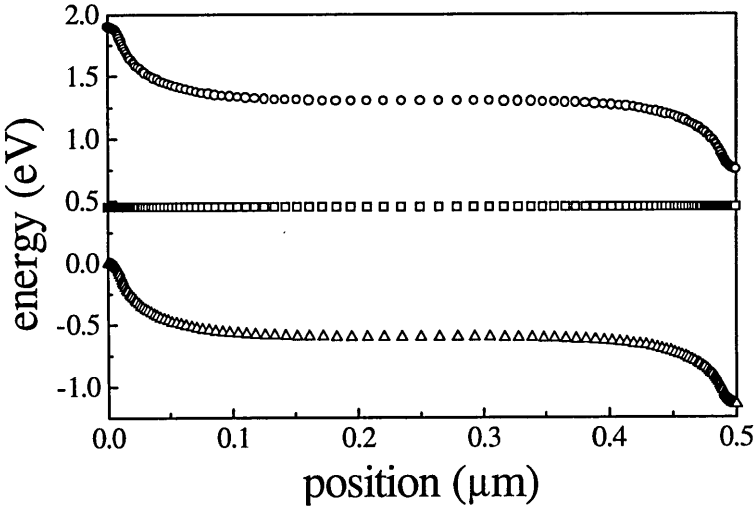

Fig 4.4 The bandgap and Fermi-level graph for thermal equilibrium. The Fermi-level in the *p*-layer is 0.45 *eV* above the valence band and in the *n*-layer is 0.3 *eV* below the conduction band. This is equivalent to a doping density for the *p*-layer of $8.43\times10^{18}\ cm^{-3}$ and for the *n*-layer $5.05\times10^{18}\ cm^{-3}$. It is noticeable that the smaller doping density in the *n*-layer results in the smaller energy and larger doping density in *p*-layer results in the larger energy. This is because of the relatively wider valence band tail in amorphous silicon. Also of note is the flatness of the bands in the middle of the device.

When a reverse bias voltage is applied to the device, it extends the depletion region towards the central part of the device, and due to the low defect density in most of the *i*-layer, the depletion region is easily extended through the whole *i*-layer. However, since the intrinsic *a-Si:H* is slightly *n*-type and the *p*-layer doping is heavier than in the *n*-layer in this case, the carrier densities change dramatically near the *p-i* interface, causing a high space charge density and a high field region here. On the *other* side, near the *i-n* interface, since the *i*-layer is slightly *n*-type, the depletion region extends wider but the space charge density is relatively low. At -1volt bias, the depletion regions from both sides are well overlapped. Due to the higher space charge density in the depletion region from *p/i* interface, the low field region is closer to the *i/n* interface even though the depletion region from *i/n* interface extends wider.

Figs 4.4 to 4.6 show the basic internal features of the *a-Si:H* diode. The band energy plot in fig 4.4 shows a flat band edge in the middle of the device at zero bias which is related to the low field region in fig 4.3. Fig 4.5 shows the band energy plot at −1 volt reverse bias, illustrating roughly how the Fermi-energy splits and how the band edges bend causing the change in internal field distribution. It also shows the depletion situation in this condition, the hole density staying low for more than half of the device, indicating a longer depletion region extending from the *n*-side. On the contrary, depletion of electrons from the *p*-side occurs over a shorter distance causing a larger change in the space charge density. Band bending near the *p-i* interface is larger than at the *i-n* interface, so the resultant field is higher.

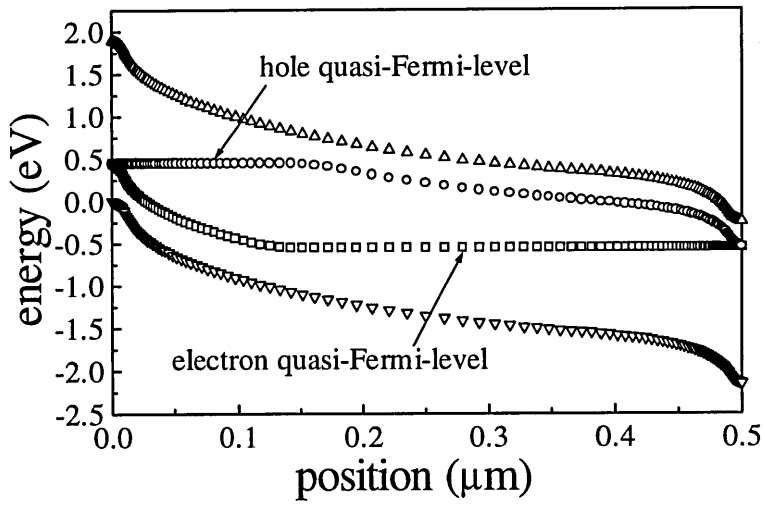

Fig 4.5 The band edge and quasi-Fermi-level distribution for -1 volt reverse bias voltage in the dark showing that the whole device is depleted. The fully depleted region for holes is wider than the depletion region for electrons. The division region is around 0.3μ*m*, only because the free hole density is smaller than electron density. It can be seen that E_c-E_{fe} and E_{fh}-E_v are nearly constant from the *p*-side to 0.15μ*m* for electrons and from 0.15 μ*m* to *n*-side for holes.

Fig 4.6 shows the electron and hole density distributions for 0 volt and -1 volt reverse bias voltage cases. The reverse bias extracts the holes more thoroughly than

electrons, because the depletion region extends further from the *n*-side. The fully depleted electron region is relatively narrower.

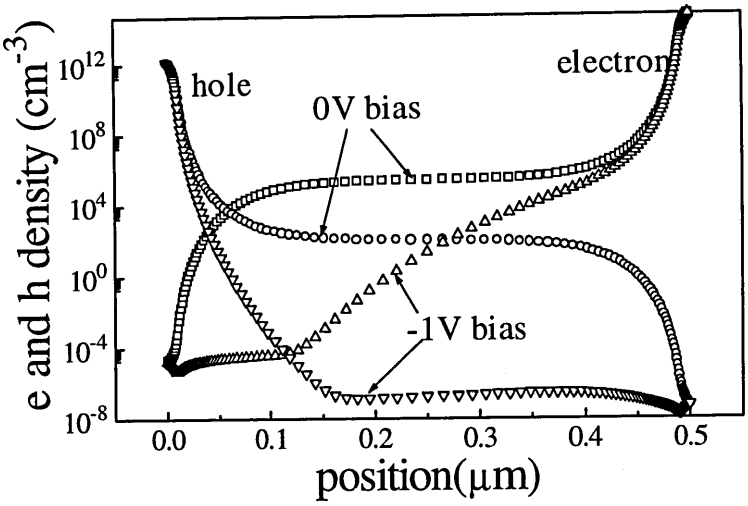

Fig 4.6 Spatial variation of the electron and hole density at 0 volt bias and -1 volt reverse bias voltage, showing that the electron density in most of the device is about 3 to 4 orders larger than the hole density. At -1volt reverse bias, the electrons and holes are depleted over much of the device to the density value they have as minority carrier in the opposite doped layers, i.e., electrons in the *p*-layer and holes in the *n*-layer.

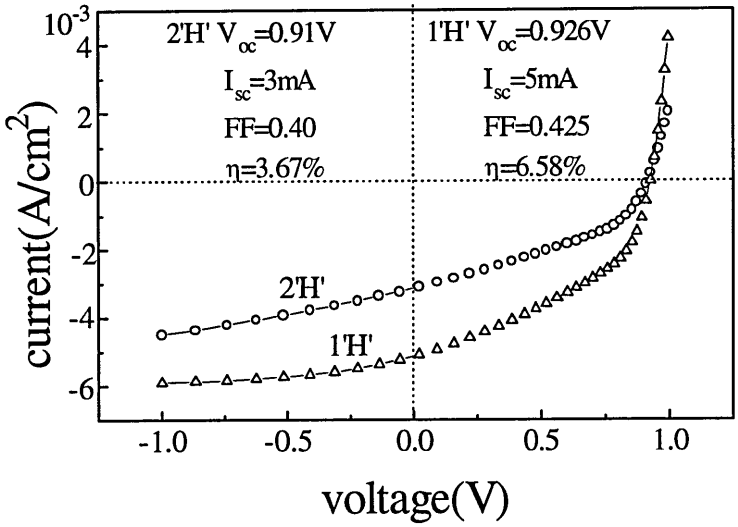

Fig 4.7 *I-V* characteristics calculated from Deane and Powell's defect pool model. The conditions is listed in table 4.1 and 4.2. The 2'H' and 1'H' represent the hydrogen atoms involved in the chemical reaction of defect creation.

In amorphous silicon solar cells, when the diffusion length of the free carriers is not long enough, the increased field will greatly help the charge collection. But when there is no applied reverse bias as in *a-Si:H* solar cell case, the carrier life time is much shorter than the transit time, so that the recombination will govern the behaviour of the device. In this case, poor *I-V* characteristics can be expected.

We have used the parameters Deane and Powell used in their model to plot an *I-V* curve as a test which is plotted in figure 4.7. The conditions are listed in table 4.1 and 4.2. We tried two cases - when the number of hydrogen atoms involved in the chemical reaction equals 1 and 2, respectively. The "two hydrogen" description corresponding to $i=2$ is the parameter Deane and Powell used in their model. The light is directed on the *p*-side with photon flux $1\times10^{17} cm^{-2}s^{-1}$ and wavelength of $650nm$ (corresponding to the absorption coefficient of $1\times10^{4} cm^{-1}$).

According to the photon flux and the absorption coefficient, 100% collection of the photon generated current should be about $6.3 mA cm^{-2}$. In the two hydrogen case, the short circuit current is only $3 mA cm^{-2}$, less than 50% of the full collection, and at -1volt the collection has only reached 71%. The fill factor is bad, only 0.4. (for a good solar cell, a fill factor of more than 0.65 can be expected). The conversion efficiency in this case is 3.67% (count the total illuminated photon flux) and 9.33% (only counting the absorbed photons).

In the one hydrogen case, it is seen that the collection efficiency in short circuit conditions is significantly improved, reaching about 80%; at -1volt, achieving 93%. The detail of the *I-V* characteristics is listed in the graph. Although the fill factor is still low, 0.425, the conversion efficiency has greatly improved compared with the two hydrogen case, 6.58% (counting the total illuminating photon flux) and 16.75% (only counting the absorbed photons). This difference due to different number of hydrogen atoms involved in the chemical reaction has a substantial effect on the Fermi-energy dependency of the defect density so as to change the device properties significantly. The detailed simulation and discussion will be mentioned later in this chapter.

4.4 Adjusting the defect pool model for the *a-Si:H p-i-n* diode.

As has been seen the defect pool model does not work properly in the *p-i-n* diode if there is no substantial change made to the original parameters published by Powell and Deane (1993). In this section, different trials for this purpose are reported. There are quite a few parameters in the model based on experimental measurements. Due to the complexity of *a-Si:H* material, different parameter values may be suggested by different experimental results and variations can occur between different batches of material. In the following we adjust some of the parameters for which definitive values are not available to try to fit experiment with simulation.

4.4.1 Pool width σ

The pool width σ in equation 4.3 is not an experimental datum. The value Powell and Deane (1993) used in their model is chosen in such a way as to make the energy separation Δ between negatively charged defects in *n*-type *a-Si:H* and positively charged

defects in *p*-type *a-Si:H* equal to $0.44eV$. However, this Δ value varies experimentally between $0.4eV$ and $0.7eV$ from different authors (see for example Winer et al 1988). So from this point of view, the pool width is far from being definitively fixed. In the following part of this section, we change the pool width from $0.14eV$ to $0.18eV$ to investigate the resulting systematic change in the device.

In the previous section, it was shown that the high defect density near the interface causes high space charge density, so that the depletion region for the no bias situation is limited, within a narrow region near *p-i* and *i-n* interfaces. Most of the potential falls across these regions. As a result of this defect distribution, the operating characteristics of the diode are seriously deteriorated. In order to improve this, the effect of changing the pool width σ was investigated. Fig 4.8 shows the change in the spatial variation of the defect distribution when the pool width is changed from 0.18 *eV* to 0.14 *eV*. It is obvious that the defect density in the *i*-layer is reduced gradually, and also the defect density near the *n*-layer. This reduction of defect density will be seen to help to improve the behaviour of the device. From fig 4.9, we can see the field in the *i*-layer has very much improved due to the decrease of the defect density in *i*-layer, and also the potential drop at the *n-i* interface is reduced. The depletion region has greatly extended towards the centre of the device. However, not much change is seen near the *p*-side. The relatively smaller change near the *p-i* interface compared with *i-n* interface, due to the change of pool width can be explained as follows:

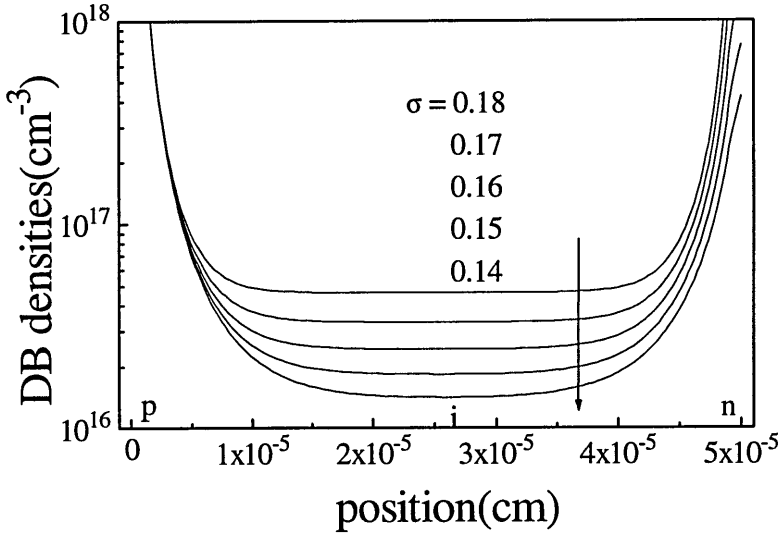

Fig 4.8 Spatial variation of the integrated defect density distribution at different pool width values. Following the arrow, the pool width changes from 0.18 *eV* to 0.14 *eV*

When the pool width is reduced, the total defect density will reduce according to equation 4.4, and the peak position of the pool moves towards the conduction band edge, (equations 4.3 and 4.4). However, the relative changes in *p*-type and *n*-type materials are different. In the *p*-layer, when the pool width is reduced, the defect density should be reduced as well, but this decrease is compensated by another movement, ie the

movement of the peak position towards the conduction band. As a result of this change, the defect density and the field etc are kept more or less unchanged near the *p*-layer. On the contrary, in the *n*-layer, this change is enhanced by the moving of the peak position of the pool. From fig 4.11, it can be seen that in the *n*-layer, while the distribution is changing with the pool width, and the height of the peak is also changing significantly, the change being much larger than in the *p*-layer.

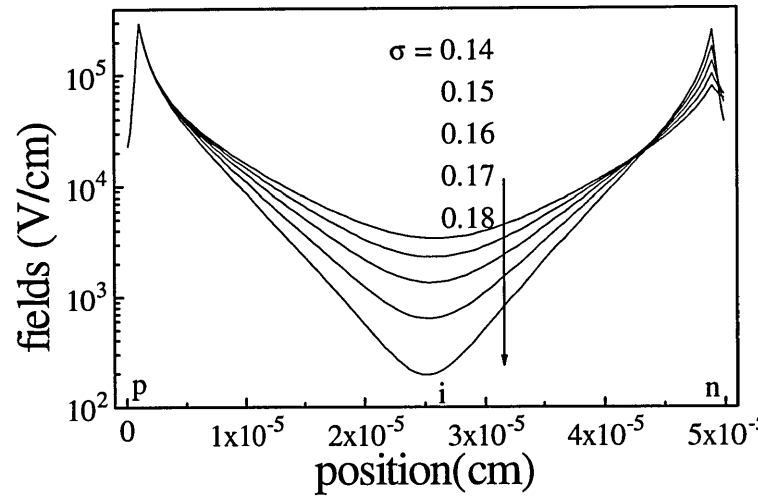

Fig 4.9 Spatial variation of the internal field distribution for different pool widths. No bias voltage is applied. Following the direction of arrow, the pool width changes from 0.14 *eV* to 0.18 *eV*.

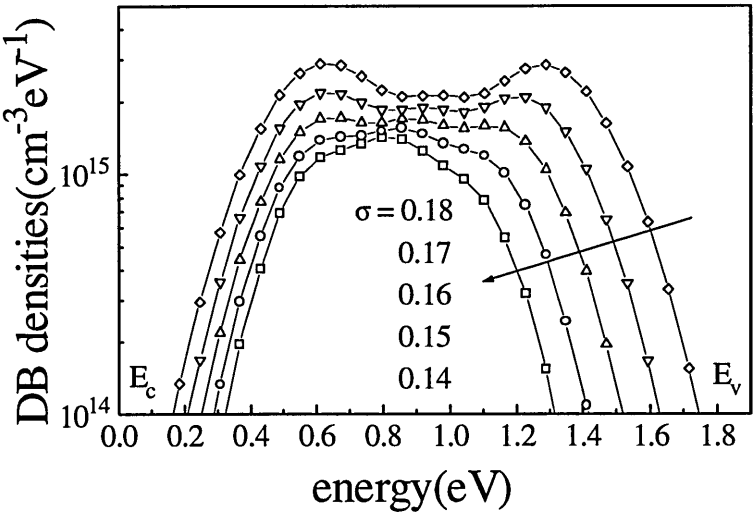

Fig 4.10 Defect pool distribution in intrinsic *a-Si:H* material for different pool widths. Following the direction of the arrow, the pool width changes from 0.18 *eV* to 0.14 *eV*.

Fig 4.10 is the defect energy distribution in the middle of the device. Basically, it is the defect distribution in the *i*-layer where the Fermi-level is not shifted from the mid-gap. When the pool width is changed, the shape of the defect distribution is changed. When $\sigma \geq 0.16$ *eV*, there are still two peaks, ie, at low temperature, the total charged

defect density will be larger than neutral defect density. When $\sigma<0.16eV$, the pool has only one peak, ie the neutral defect density in intrinsic *a-Si:H* will be as large as or larger than the charged defect density. The other feature visible is that the position of the peak has moved towards the conduction band edge.

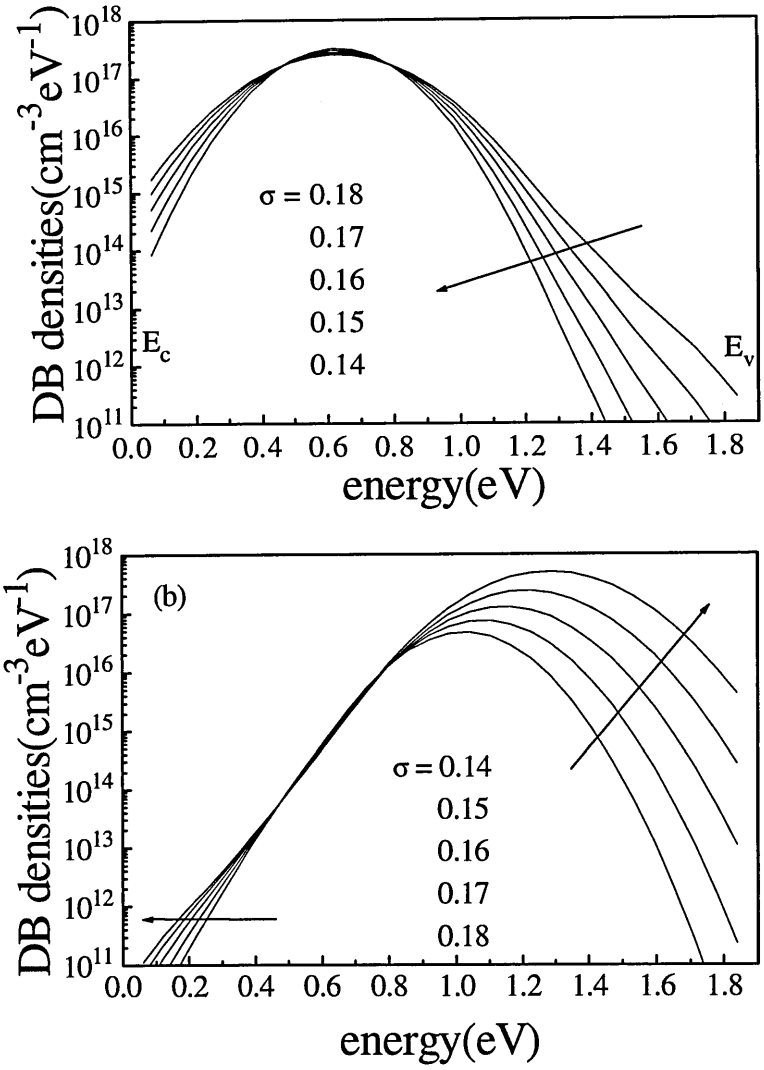

Fig 4.11 Defect pool distributions in (a) *p*-type, and (b) *n*-type *a-Si:H* material for different pool width σ. Following the direction of the arrow, the pool width changes from $0.18eV$ to $0.14eV$.

Fig 4.11 shows the defect distribution in *p*- and *n*- type material, actually taken from the *p*- and *n*-layers in the *p-i-n* diode. When the pool width is reduced, the peak position in *p*-type material does not change very much, remaining fixed at $0.6eV$ below the conduction band edge, with only the width of the distribution getting narrower. On the other side, in the *n*-layer, when the pool width is reduced, not only is the width of the defect distribution reduced, but the height and the position of the peak also changes. When the pool width changes from $0.18eV$ to $0.14eV$, the peak value of the defect is reduced more than one decade, and the peak position moves from about $1.3eV$ below the

conduction band edge to 1.0eV below the conduction band edge. Concerning the value Powell and Deane used in their paper, Δ=0.44eV, it is shown here that Δ changes from 0.45eV to 0.25eV when the pool width changes from 0.18eV to 0.14eV.

Fig 4.12 shows the influence of the pool width on the illuminated *I-V* characteristics of a *p-i-n* solar cell. (photon flux $1\times10^{17}\ cm^{-2}s^{-1}$ and absorption coefficient $5\times10^{3}cm^{-1}$ equivalent to photon energy of 1.823eV or 680nm in wavelength). When the pool width reduces, the light *I-V* curves show that the short circuit current improves accordingly. However the collection is far from complete, the collection efficiency at 0 volts being only 46-64.5% when the pool width σ is changed from 0.18eV to 0.14eV. Recombination in the *i*-layer due to the low internal field must still be playing an important part in determining the collection efficiency. When the pool width is reduced, the *I-V* slope at 0 volt bias increases slightly (the fill factor changes from 0.388 to 0.404), so there is no significant improvement. The open circuit voltage does not change very much, and the forward characteristic seems improved only slightly, ie the quality factor is reduced which shows the conversion from recombination controlled transport to drift and diffusion controlled transport.

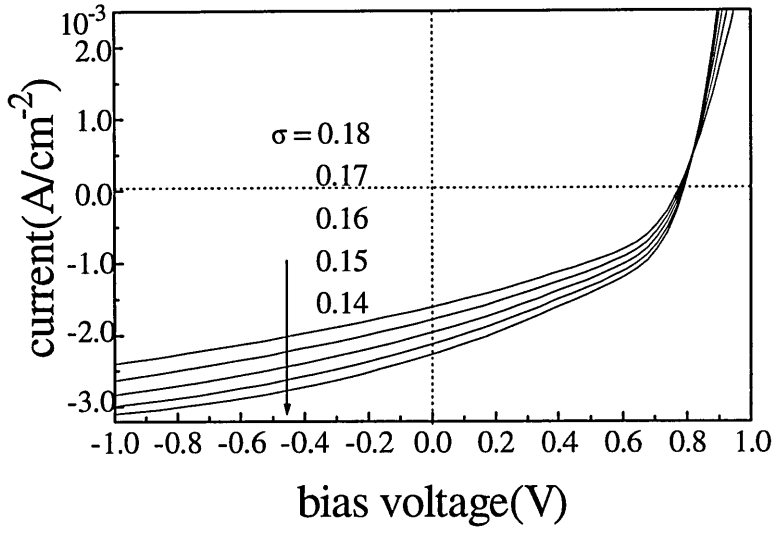

Fig 4.12 Illuminated *I-V* characteristics of an *a-Si:H p-i-n* diode at different pool widths. Following the direction of the arrow, the pool width changes from 0.18 *eV* to 0.14 *eV*.

4.4.2 Correlation energy *U*

Correlation energy U is another value with some uncertainty. Measured data give U between 0.1eV and 0.4eV from different authors (see for example Lee and Schiff 1992). Considering the difficulties of applying the defect pool model to the *p-i-n* device, we would like to know the influence of the value of U. To do this, we chose two sets of parameters. One set has the Fermi level at the *p*-side boundary set at E_{fp}=0.45eV, and the width of the pool is σ=0.178eV (the values used by Powell and Deane 1993). The other set has E_{fp}=0.6eV and σ=0.14eV to make a comparison.

Figure 4.13 shows the dangling bond distribution for different correlation energy under these two groups of conditions. Combined with figure 4.14 it is clear that when the correlation energy is getting larger, the dangling bond density in the *i* and *n* layer is reduced, so this will help to extend the depletion region in the *i*-layer and improves the modelled performance of the *p-i-n* device.

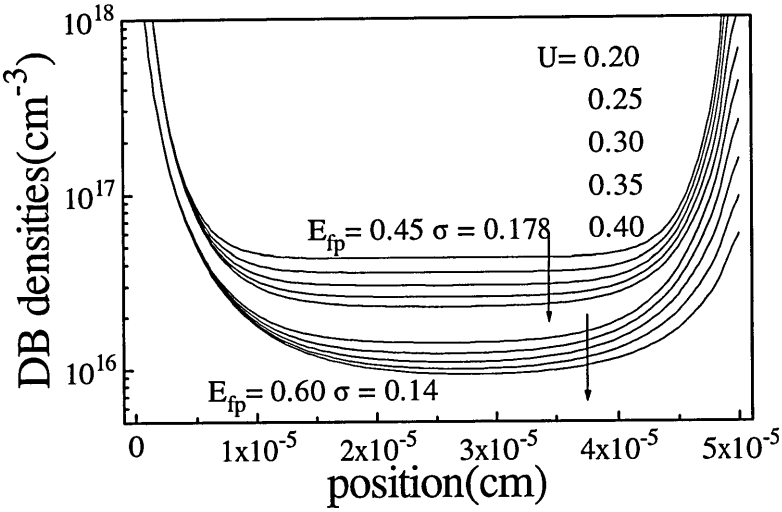

Fig 4.13 Dangling bond distributions under different conditions. The parameters for the upper group are - Fermi-level in *p*-type material 0.45*eV* above valence band edge and pool width 0.178*eV*. The parameters for the lower group are: Fermi-level in *p*-type material 0.6*eV* above valence band edge and pool width 0.14*eV*. Following the direction of the arrow, the correlation energy changes from 0.2*eV* to 0.4*eV*.

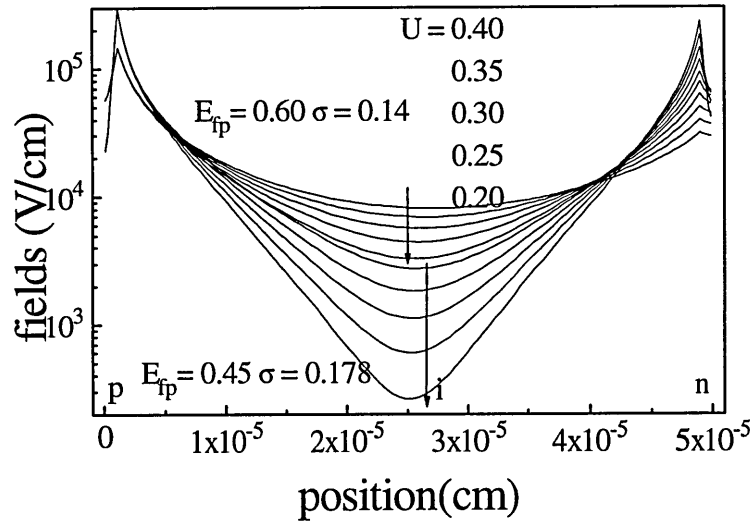

Fig 4.14 The spatial variation of the electric field for different correlation energies under two different conditions. The condition for the upper group is - Fermi-level in *p*-type material at 0.6*eV* above valence bandedge and the pool width 0.14*eV*. The condition for the lower group is Fermi-level in *p*-type material 0.45*eV* above valence bandedge and the pool width is 0.178*eV*. Following the direction of the arrow, the correlation energy changes from 0.4*eV* to 0.2*eV*.

The model adjustments made above do not seem capable of reducing the dangling bond density near the *p-i* interface to more favourable values. The density does not

change with the pool width or correlation energy. Shifting the Fermi-level in the *p*-layer towards midgap can efficiently reduce the dangling bond density so as to increase the internal field accordingly but will inevitably sacrifice the built-in potential which is bad for the solar cell. From fig 4.14 we can see a continuous change of the electric field profile, split into to two groups of conditions. The figure shows that reducing the pool width and increasing the correlation energy have similar effects on the dangling bond distribution and so on the internal field.

Up to this point, the effort of trying to apply the defect pool model to the *p-i-n* device has not proved to be practicable. The model gives far too high a defect density near the interface and this degrades the transport capability of the device, so further modification is needed.

4.4.3 The number of hydrogen atoms involved in the reaction.

In Powell and Deane's paper (1993), three microscopic chemical reactions are considered as described in equation 4.1. When i=0, the weak bond is broken, but the dangling bonds cannot move apart without the involvement of hydrogen diffusion. For i=1, one *Si-H* bond is broken and the hydrogen atom diffuses to the weak-bond site, breaking the weak bond. For i=2, a second *Si-H* bond is broken, resulting in a doubly hydrogenated weak-bond site and two isolated dangling bond defects. It has been believed that the involvement of hydrogen adds extra entropy to the defect chemical potential since the defects can gain entropy by swapping hydrogen from *Si-H* bonds, transferring the defect to a distant *Si-H* site.

Whether above treatment is mathematically or thermodynamically correct or not is not considered in this section. In this work, a simplified model is adopted, that only one hydrogen atom is involved in the chemical reaction. The argument for this is that when the first dangling bond is swapped with a remote hydrogen, the other one left is already isolated with the other dangling bonds. Since the weak bond site is randomly located and is only 10^{-4} of the number of *Si-Si* bonds, a further swap between the hydrogen and a dangling bond will not add extra entropy to the system. To require two hydrogen atoms to be involved in the chemical reaction is then not necessary. In the following calculation, only *one* hydrogen is assumed to be involved in the reaction.

Fig 4.15 shows the dangling bond density distribution obtained for different pool widths with the above assumption. Comparing with fig 4.8 and fig 4.13, the dangling bond density is significantly reduced across the device, not only the in doped layers but also in the intrinsic layer. As a result of this lower defect density, the internal field shows a high and relatively uniform distribution as shown in fig 4.16. For pool widths between $0.17eV$ to $0.18eV$, the internal field is relatively uniform and should give a good carrier collection on *I-V* characteristics plot.

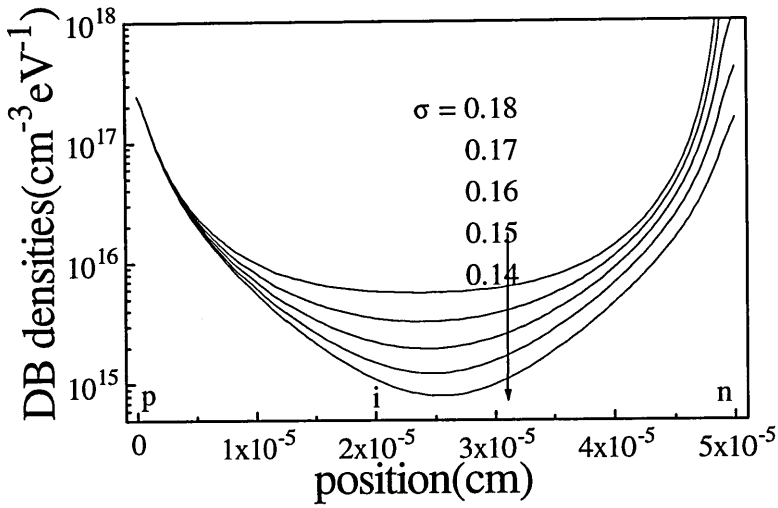

Fig 4.15 The spatial variation of the dangling bond densities for different pool widths when only one hydrogen atom is involved into the chemical reaction. Following the direction of the arrow, the pool width changes from $0.18eV$ to $0.14eV$.

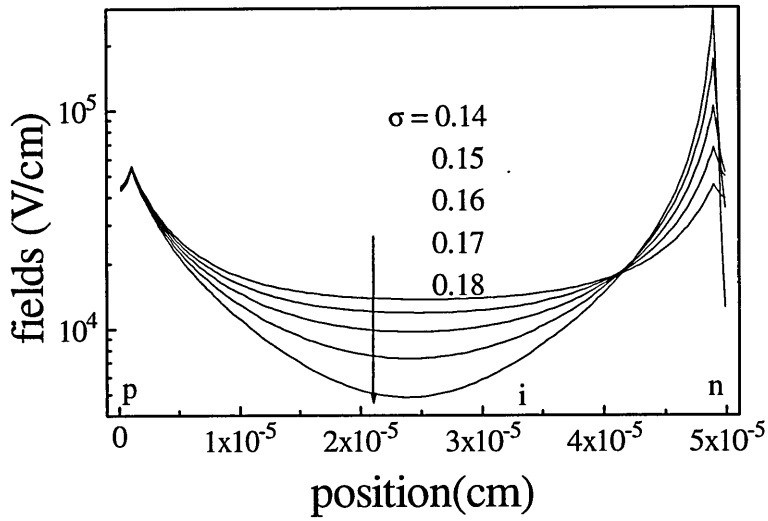

Fig 4.16 the spatial variation of the electric field for different pool widths when only one hydrogen atom is involved into the chemical reaction. Following the direction of the arrow, the pool width changes from $0.14eV$ to $0.18eV$

Fig 4.17 shows illuminated *I-V* characteristics of a *p-i-n* device for different defect pool width. Compared with fig 4.12, there is relatively smaller change accompanying the different pool widths. Nevertheless, the improvement in the collection when pool width is reduced is easy to spot. The collection efficiency at 0 volts increases from 80 to 87% when pool width changes from $0.18eV$ to $0.14eV$, and the overall *I-V* characteristic is better (fill factor increase from 0.43 to 0.49) than those in fig 4.12. This result shows that the model with one hydrogen involved in the chemical reaction gives results nearer to a real *a-Si:H* device.

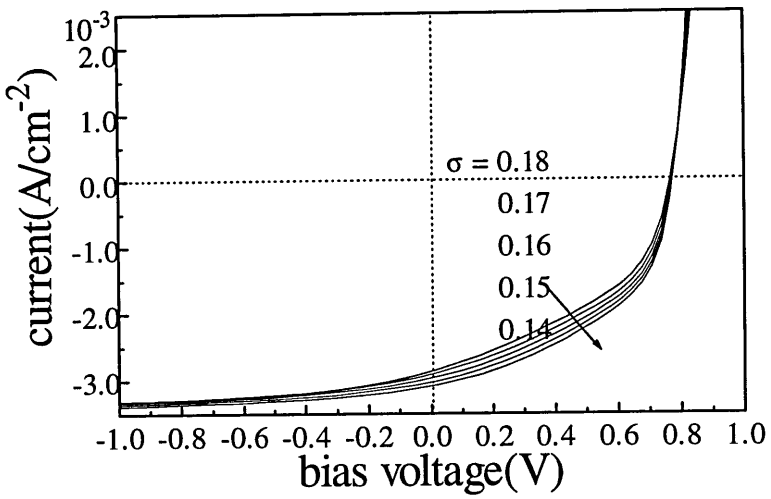

Fig 4.17 Light *I-V* characteristics for different pool widths when only one hydrogen atom is involved into the chemical reaction. Following the direction of the arrow, the pool width changes from $0.18eV$ to $0.14eV$.

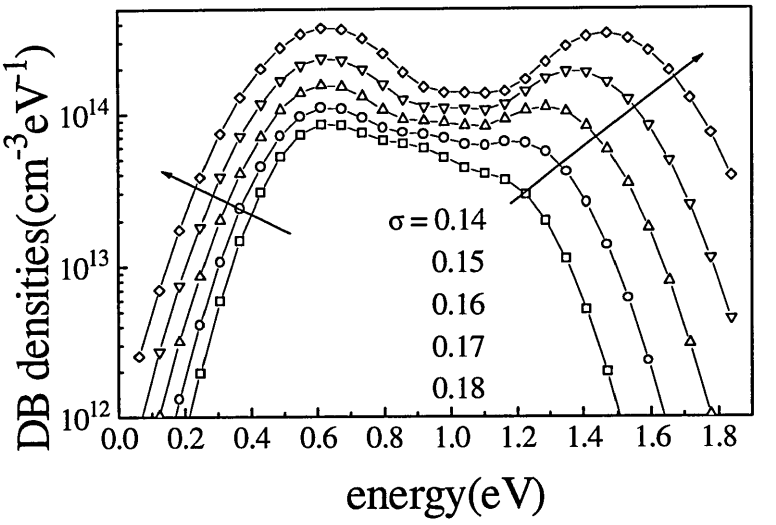

Fig 4.18 Defect density distribution in the energy gap for different pool widths when only one hydrogen atom is involved in the chemical reaction. This is in the middle of the *i*-layer but may not be very representative of intrinsic since the band bending does not have a flat part as in the previous section. Following the direction of the arrow, the pool width changes from $0.14eV$ to $0.18eV$.

From fig 4.18 and 4.19 we can find that the basic defect pool distribution does not change much except for the amplitude of the peak. To fit the energy separation between negatively charged defects in *n*-type *a-Si:H* and positively charged defects in *p*-type *a-Si:H* Δ=$0.44eV$, the pool width should best be $0.16eV$ for a correlation energy of $0.2eV$.

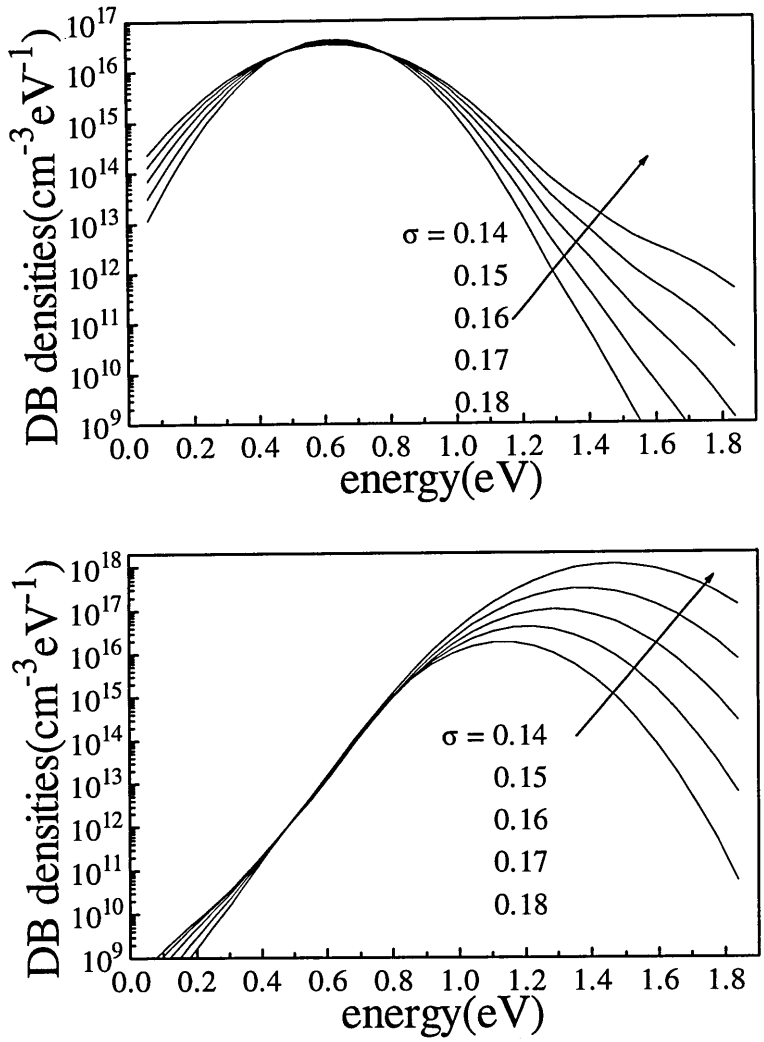

Fig 4.19 The pool distribution in *p*-layer and *n*-layer when only one hydrogen atom is involved in the chemical reaction. Following the direction of the arrow, the pool width changes from 0.14*eV* to 0.18*eV*.

4.4 Reverse modelling for the *p-i-n* diode

The "reverse modelling" method was proposed by M.Zeman et. al (1994). It is a method to extract some unmeasureable parameters from measurable data, like *I-V* characteristics of a *p-i-n* solar cell. Intuitively speaking, it is unlikely that reverse modelling can extract an accurate parameter since so many uncertainties exist in the input data. However, it might be a qualitative way to compare some of the important values which are not easily measured. What we wish to do in this section is to try to use reverse modelling method to simulate most closely the *I-V* characteristics measured in one of the *a-Si:H p-i-n* samples used in the project.

The *p-i-n* device sample we used in our measurement was fabricated by *PECVD* method with a 3.4 μ*m* thick *i*-layer, and includes a 200Å thick p^+ layer and a 200Å thick n^+ layer deposited on a 7059 substrate, with 2*mm* diameter semi-transparent top and bottom *Cr* electrodes. With two semitransparent *Cr* electrodes in this *Cr*/(p^+)*a-Si:H*/(*i*)*a-*

Si:H/(n^+)*a-Si:H/Cr/*glass device we are able to shine the light from both sides of the device and do different measurements.

I-V characteristic measurement was carried out by using a red *LED* as the light source (660*nm* wavelength, equivalent to 1.88*eV* photon energy and absorption coefficient in *a-Si:H* of $8.8\times10^3 cm^{-1}$). The light is directed from the *p*-side, and a *Farnell ET30/2* power supply was used to apply bias voltage to the *p-i-n* diode (from -2 to +2 volts), and to drive the *LED*. A *Keithley 610C* electrometer was used to measure current.

The curve with the solid diamond symbol in Fig 4.20 is the measured curve and the others show the computer simulations. After adjusting the input parameters in the computer model, the defect pool model shows a good fit to the experimental data. The parameters used are mostly the ones Powell and Deane used (see table 4.1 and following text), except that the bandgap of *a-Si:H* has been reduced to 1.75*eV* and the peak value of the defect pool has accordingly reduced to 1.17*eV*. The number of hydrogens involved in the reaction is now 1 instead of 2 and the Fermi-levels in the *p*- and *n*-layer boundaries are set to 0.56*eV* and 0.3*eV*, respectively.

The so called reverse modelling is a processes to adjust input parameters in order to fit the measurement data the best. In our modelling, the parameters adjusted are mainly the photon flux of the light source (a value difficult to measure accurately) and the width of the defect pool distribution σ. From the previous section, it has been found that the defect density decreases when the pool width decreases, so the *I-V* characteristic is improved. The collection efficiency at high reverse bias voltage is supposed to be 100%, which is equivalent to a current comes from the number of photons being absorbed per unit time. By changing the photon flux of the incident light, the full collected current can be adjusted. By adjusting the photon flux of the incident light and the pool width, the *I-V* characteristics of the *p-i-n* diode can to great extent be adjusted to fit the measured *I-V* curve. Of course this is under the condition that the model is basically reasonably good, corresponding to the sample being measured. In fig 4.19, for the best fit curve using the defect pool model, the photon flux value is $2.7\times10^{14} cm^{-2}s^{-1}$ and the pool width of the defect pool is 0.17*eV*.

It has to be noted that the diode we are using is not a typical solar cell; instead it is closer to a photon sensor or detector (with a thick *i*-layer). It is to be expected that the light *I-V* characteristics will not be very good at a low excitation rate. However, this will not affect the result of the simulation.

Considering the measurement accuracy and the instability of the *a-Si:H* material, the fit using the defect pool model is good. To make a comparison, the best fit by a single energy simple model and by a Gaussian distribution model are also plotted in the same graph.

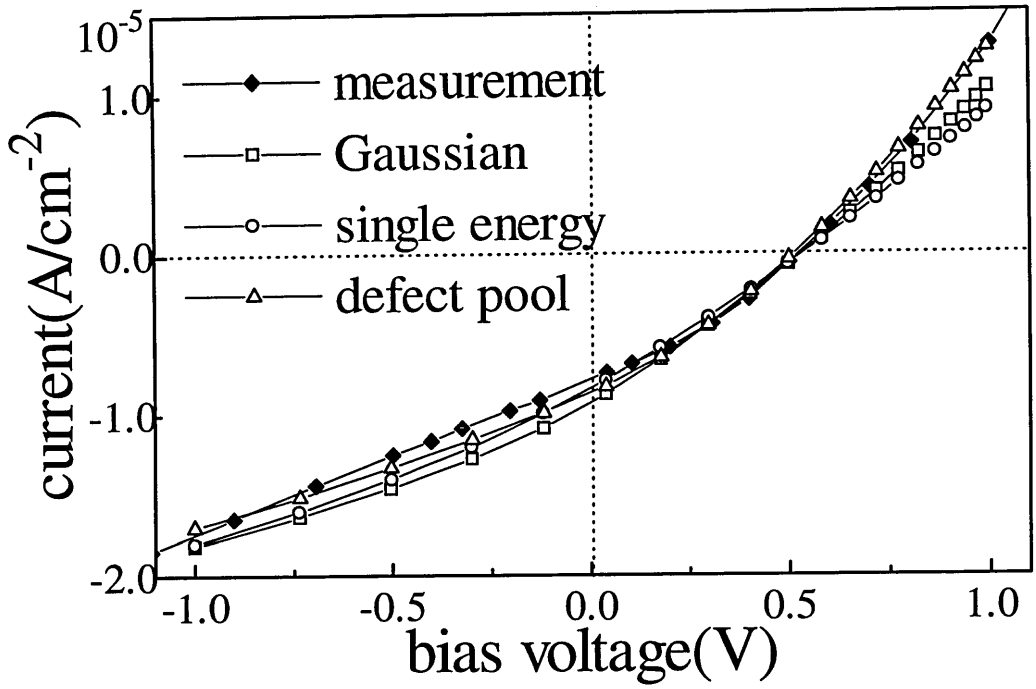

Fig 4.20 Light *I-V* measurement of a *p-i-n* diode and computer simulations by different models. The best fit is defect pool model when only one hydrogen atom is involved in the chemical reaction.

From the detailed simulation for this thick *p-i-n* diode including internal electronic transportation in the device, the uniformly distributed dangling bond density in the *i*-layer can be easily extracted. This is mainly because for this thick diode, the depletion region is limited within a relatively narrow region near the interface, so that in thermal equilibrium, the Fermi-level in most of the undoped layer is unshifted. Thus the defect density has a constant value over most of the *i*-layer. The value found for dangling bond density from the spatial variation of the integrated dangling bond density plot (similar to fig 4.2) is also used by the single defect energy model and the Gaussian distribution model as an input parameter to carry out the comparison.

The parameters used in the these two simpler models are as follows: The dangling bond density extracted from the defect pool model result is $1.18\times10^{16}cm^{-3}$. The $D^{+/o}$ transition and correlation energies are set at $0.9eV$ and $0.2eV$ respectively. For the single energy model, the value for photon flux incident on the device is $4\times10^{14}\ cm^{-2}s^{-1}$, and for the Gaussian defect distribution model, the photon flux is $3.5\times10^{14}\ cm^{-2}s^{-1}$. The rest of the parameters are the same as in the defect pool model.

The first thing to be noticed from Fig 4.20 is that in order to get a similar fit to the experimental *I-V* curve, the photon flux for the single energy, for Gaussian and for defect pool are 4×10^{14}, 3.5×10^{14} and $2.7\times10^{14}cm^{-2}s^{-1}$, respectively. This decreasing trend shows that when the defect distribution in the energy gap is getting wider, the total recombination via dangling bond states is reduced, so that less photons are needed in order to output the same amount of current. This feature can also be seen from the forward part of the *I-V* characteristics. Going from defect pool to Gaussian to single

energy distribution, the forward part of the *I-V* curve shows an increasing recombination control feature. It is not difficult to imagine that when the defect distribution is getting wider, the defect density near the Fermi level position which plays an important part in the recombination processes will be less, so that the total recombination rate will be reduced due to this change.

4.5 Summary

In this chapter, a detailed description of the defect pool model has been given. After several basic tests on the model, it is clear that the defect pool width and correlation energy all have well defined effects on the results calculated from the defect pool model. The original model has been proved not suitable in application to *p-i-n* diodes if no substantial change is made to the original published parameters of Deane and Powell. The reason for this is simply because the sensitivity of the dangling bond density to the Fermi-level position is overestimated, and this results in a far too a high defect density near the doped layers resulting in deteriorated performance of the *p-i-n* diode.

From the basic analysis of the defect pool model, it is found that the assumption of two hydrogen atoms involved in the chemical reaction is not necessary. By involving only one hydrogen atom into the reaction, much better results have been obtained. By so called reverse modelling, the best fit of a measured *I-V* curve has been found to be using the defect pool model. The single energy defect model and Gaussian defect distribution have also been tried, and could not give better result than the defect pool model.

Chapter five

THE *DICE* METHOD

5.1 introduction

The improvement of the stabilised efficiency of *a-Si:H* solar cells is of paramount importance for the future of this technology. The basic approach for solving this problem has been to search for more stable materials. More recently, several studies have focused on alternative ways of improving the efficiency of a degraded cell by changing the cell design (see for example Fischer et al 1993 and 1994). In a degraded cell, poor collection is due to the combination of two effects: a deformation (and lowering) of the internal field and an increase in defect density. If one can keep the internal field high, collection can be significantly improved. The strategy used has been to enhance the field in those specific, critical regions of the degraded cell by 'defect engineering', 'band gap engineering' or 'micro-doping' (see for example Schropp et al 1993a and 1993b). The practical success of these methods depends on the availability of a tool for the experimental determination of the internal electrical field profile.

In order to improve the conversion efficiency, analyses of solar cell photovoltaic characteristics have been developed by many researchers. A number of reports on the theoretical conversion efficiencies have been presented using various methods (see for example Hack and Shur 1985). However, in these calculations many physical parameters, such as the distribution of the gap state density, the mobility and the free-carrier lifetime product were required, and various kinds of assumptions were made. Therefore, the physcial parameters cannnot necessarily be deduced from the practical solar cell characteristics.

The Dynamic Inner Collection Efficiency (*DICE*) method was introduced firstly by Takahama et al in 1986 using the fact that the inner distribution of photovoltaic characteristics can be obtained from the collection efficiency spectrum in any solar cell by using only a few assumptions. The features of this method are that their value can be obtained in any operating condition by a non-destructive method and that the correspondence to a practical solar cell is clear.

Following Takahama's work, several authors published work on this subject. Some applications using this approach have been attempted. It has been used to determine the internal field distribution (Wyrsch et al 1994), to investigate the buffer layer degradation (Saeng-udom et al 1992) or to investigate the effect of low-level doping in the intrinsic layer (Fischer and Shah 1994). However, it has been noted that the success of this method is hindered by the deficiency of the so called Singular Value Decomposition (*SVD*) algorithm which is a necessary part of the *DICE* analysis. It has generally been criticised that the numerical manipulations and fitting procedures involved

can produce ambiguous and unphysical results. With its low level of confidence, it was argued, the *DICE* method could have no advantage over the direct interpretation of the spectral response plots (Hof et al 1994).

In this chapter, we will demonstrate the new results recently achieved by computer modelling. We use computer modelling to find out the substantial reason which limits the use of the *DICE* method. The main reason for the unreliability of the method has been found -even quite small errors introduced from the measurements seem to be a fatal problem for the *SVD* algorithm. Otherwise, this method can in principle solve the problem properly.

5.2 Algorithms

During the computer experiment on *DICE*, not only is the *DICE* method simulated in detail, but as a further testing method, another method called the *IDEAL* method is used as the supplement of the *DICE* method.

5.2.1 *DICE* method

In this section the initial idea, basic theory, and equations of the *DICE* method are described. As the absorption coefficient of *a-Si:H* film decreases with an increase of the wavelength of the light, the penetration depth for a light depends on its wavelength, so that the collection-efficiency spectrum of an *a-Si:H* solar cell should include implicitly such information as the depth profile of the solar cell characteristics. The problem involves the deconvolution of spatial information from the measured spectral information.

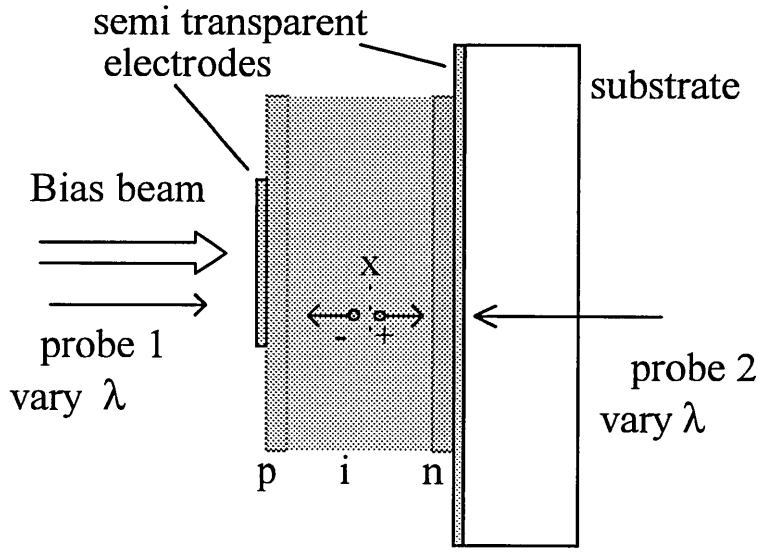

Figure 5.1 *DICE* - Measures the contribution to terminal current of carriers created at depth x by the probe beam - i.e. spatial variation $\eta_q(x)$ of collection probability.

The *DICE* method in its simplest form, involves illumination by two beams - a steady bias beam on the front *p*-side, often *AM*1, and a less intense probe beam, of variable wavelength, which is usually chopped. With the assumption that for carriers created by the probe beam the collection efficiency is unity at high reverse bias, the spectral response at lower voltages is normalised, giving relative terminal spectral collection efficiencies, $\eta_{coll}(\lambda)$. Since the absorption constant $\alpha(\lambda)$ of the probe beam varies with λ, it is then possible to relate the spectral collection efficiency to the spatially dependent internal collection efficiency, $\eta_q(x)$ which denotes the probability of collection of a carrier pair generated at depth x. The computation of the *DICE* value $\eta_q(x)$ is described and investigated in this chapter. The present work is based on a modified method in which a *monochromatic* bias beam is used instead of *AM*1 illumination, to allow the effects of varying the optical bias absorption profile to be studied, and also probe illumination on *either* side of the device - the 'bifacial' *DICE* method.

The *DICE* value is thus defined as the probability that an electron-hole pair generated at a certain depth in the generation region of a solar cell becomes part of the output current under given bias conditions. The *DICE* value can be obtained from the collection-efficiency spectra under variable bias-light and variable bias-voltage conditions. Thus, the following equation is obtained:

$$\eta_{col}(\lambda) = \int_0^d \eta_q(x)\Psi(\lambda,x)dx. \tag{5.1}$$

The procedure assumes that one photon exicites one electron-hole pair at a wavelength region where the photon energy is larger than the band-gap energy. In this equation $\Psi(\lambda,x)$ is the absorbed number of photons as a function of depth and wavelength, represented by the following equation:

$$\Psi(\lambda,x) = F_o\alpha(\lambda)\{\exp[-\alpha(\lambda)x] + rf(\lambda)\exp[-\alpha(\lambda)(2d-x)]\} \tag{5.2}$$

here d is the thickness of the device, $rf(\lambda)$ the reflectivity at the back electrode and F_o the incident photon flux at the front surface.

With equations 5.1 and 5.2 we can obtain the value of $\eta_q(x)$ since the values of $\eta_{coll}(\lambda)$ and $\alpha(\lambda)$ can be measured and $\Psi(\lambda,x)$ is independent of solar cell operational conditions such as the bias voltage etc. The assumption of optically homogenous *a-Si:H* material will give a simple exponential decay of the generation rate along the thickness direction of the device. The photon flux value F_o is independent of the depth x and its measurement is complicated because the absorption and reflection coefficients at different wavelengths of each surface and interface are not accurately known. However, according to the features of the *DICE* method, it will be seen that the value F_o will be cancelled during the calculation. What is important is the *fraction* of the photons absorbed which contribute to the output current, so that the total photon absorption by

the device may be measured. Theoretically, this is the integral of the equation 5.2. Normalizing equation 5.1 by this integral we have

$$\eta_n(\lambda) \equiv \frac{\eta_{col}(\lambda)}{\eta_{col0}(\lambda)} = \frac{\int_0^d \eta_q(x)\Psi(\lambda,x)dx}{\int_0^d \Psi(\lambda,x)dx} \tag{5.3}$$

where $\eta_n(\lambda)$ is defined as the normalized collection efficiency and η_{col0} is the collection efficiency under the condition that $\eta_q = 1$. It is an important assumption of the method that this condition (full collection) is realized at a sufficiently high reverse bias voltage. Therefore, the value of F_o can be cancelled through this normalization.

In order to calculate the *DICE* value from measurement data of the collection efficiencies by computer, the integration has to be changed to a summation. Therefore, the normalized equation can be re-expressed as

$$\eta_n(\lambda_k) = \frac{\sum_{j=1}^{m} \eta_q(x_j)\Phi_{jk}}{\sum_{j=1}^{m} \Phi_{jk}} \tag{5.4}$$

where

$$\Phi_{jk} = \exp\left[-\alpha(\lambda_k)x_{j-1}\right] - \exp\left[-\alpha(\lambda_k)x_j\right] + R(\lambda_k)\exp\left[-2\alpha(\lambda_k)d\right]$$

$$\times\left\{\exp\left[-\alpha(\lambda_k)x_j\right] - \exp\left[-\alpha(\lambda_k)x_{j-1}\right]\right\} \tag{5.5}$$

Here λ_k is the wavelength ($1 \le k \le n$) and x_j is the depth from the incident side ($1 \le k \le m$). Equation (5.4) can be expressed as a matrix equation:

$$\begin{bmatrix} \eta_n(\lambda_1) \\ \eta_n(\lambda_2) \\ \vdots \\ \eta_n(\lambda_n) \end{bmatrix} = \begin{bmatrix} \Phi_{11} & \Phi_{12} & \cdots & \Phi_{1m} \\ \Phi_{21} & \Phi_{22} & & \vdots \\ \vdots & & \ddots & \vdots \\ \Phi_{n1} & \cdots & \cdots & \Phi_{nm} \end{bmatrix} \begin{bmatrix} \eta_q(x_1) \\ \eta_q(x_2) \\ \vdots \\ \eta_q(x_m) \end{bmatrix} \tag{5.6}$$

where $\Phi_{jk} = \dfrac{\Phi_{jk}}{\sum_{j=1}^{m} \Phi_{jk}}$ is the normalized photon flux absorbed in slice *j*.

The left hand vector of equation 5.6 is the spectral response measurement data. The matrix is the normalised photon intensity data for different wavelengths at different depths in the device. The right column vector is the *DICE* profile - the spatial variation of the *DICE* value across the device which we require to find.

Eq. 5.6 is a system of n linear equations for the m unknown *DICE* values. (in our case, we set $n=m$) Due to the typical uncertainties introduced both from the model and from the spectral response data, it turns out that Eq 5.6 is extremely ill-conditioned, and the *DICE* solution based on the sole criterion of the 'smallest error' typical of standard linear equation solvers is a very rapidly spatially oscillating physically meaningless function.

Additional constraints are required to suppress the influence of errors, and to extract a physically reasonable collection profile. This is done by using Singular Value Decomposition (*SVD*) of Eq.5.6 instead of a least-square optimisation. With this method, the solution space of Eq. 5.6 can be controlled by suppressing the fast oscillating parts of the solution, and thus adjusting the resolution of the extracted collection profiles to the measurement errors. This adjustment is governed by the "rank parameter".

5.2.2 *SVD* algorithm

It is known that the equation 5.6 is very ill-conditioned, so that normal Gaussian elimination or *LU* decomposition methods fail to give satisfactory results. However, there exists a very powerful set of techniques for dealing with sets of equations or matrices that are either singular or else numerically very close to singular. This set of techniques, known as singular value decomposition, or *SVD*, will diagnose what the problem is. In some cases, *SVD* will not only diagnose the problem, it will also solve it, in the sense of giving out an useful numerical answer, although, not necessarily 'the' answer that we thought we should get.

SVD methods are based on the following theorem of linear algebra, whose proof is beyond the scope of this thesis: Any $M\times N$ matrix A whose number of rows M is greater than or equal to its number of columns N, can be written as the product of an $M\times N$ column-orthogonal matrix U, an $N\times N$ diagonal matrix W with positive or zero elements (the singular values), and the transpose of an $N\times N$ orthogonal matrix V. The various shapes of these matrices will be made clearer by the following :

$$\begin{pmatrix} \\ A \\ \\ \end{pmatrix} = \begin{pmatrix} \\ U \\ \\ \end{pmatrix} \begin{pmatrix} w_1 & & & \\ & w_1 & & \\ & & \ddots & \\ & & & w_1 \end{pmatrix} \begin{pmatrix} \\ V^T \\ \\ \end{pmatrix} \qquad (5.7)$$

The matrices U and V are each orthogonal in the sense that their columns are orthonormal,

$$\sum_{i=1}^{M} U_{ik}U_{in} = \delta_{kn} \qquad 1 \le k \le N \quad 1 \le n \le N$$
$$\sum_{j=1}^{N} U_{jk}U_{jn} = \delta_{kn} \qquad 1 \le k \le N \quad 1 \le n \le N \tag{5.8}$$

since V is square, it is also row-orthonormal.

The decomposition can always be done, no matter how singular the matrix is, and it is 'almost' unique. That is to say, it is unique up to (i) making the same permutation of the columns of U, elements of W, and columns of V (or rows of V^T), or (ii) forming linear combinations of any columns of U and V whose corresponding elements of W happen to be exactly equal. An important consequence of the permutation freedom is that for the case $M<N$, a numerical algorithm for the decomposition need not return zero w_j's for $j=M+1,...,N$; the N-M zero singular values can be scattered among all positions $j=1,2,...,N$

We solve the equation 5.6 by using *SVD* method, a routine, *svdcmp*, taken from *Numerical Recipes in Fortran* (1992) which performs *SVD* on an arbitrary matrix A, replacing it by U (they are the same shape) and returning W and V separately. This routine is based on a routine by Forsythe et al(1977), which is in turn based on the original routine of Golub and Reinsch (1971). The algorithm is very stable, and it is very unusual for it ever to misbehave.

For a matrix equation $\boldsymbol{A \cdot X = b}$, after the decomposition, the equation can be solved as

$$\boldsymbol{X = V \cdot [diag(1/w_j)] \cdot (U^T \cdot b)} \tag{5.9}$$

we can pretend that matrix $\boldsymbol{A}$ either is singular or else is not. That is of course true analytically. Numerically, however, the far more common situation is that some of the w_j's are very small but nonzero, so that the matrix is ill-conditioned. In that case, the direct solution methods of LU decomposition or Gaussian elimination may actually give a formal solution to the set of equations (that is, a zero pivot may not be encountered): But the solution vector may have wildly large components whose algebraic cancellation, when multiplying by the matrix $\boldsymbol{A}$, may give a very poor approximation to the right-hand vector $\boldsymbol{b}$. In such cases, the solution vector $\boldsymbol{X}$ obtained by zeroing the small w_j's and then using equation 5.10 is very often better (in the sense of the residual $|\boldsymbol{A \cdot X - b}|$ being smaller) than both the direct-method solution and the *SVD* solution where the small w_j's are left nonzero.

It may seem paradoxical that this can be so, since zeroing a singular value corresponds to throwing away one linear combination of the set of equations that we are trying to solve. The resolution of the paradox is that we are throwing away precisely a combination of equations that is so corrupted by roundoff error as to be at best useless; usually it is worse than useless since it 'pulls the solution vector way off towards infinity

along some direction that is almost a nullspace vector. In doing this it compounds the roundoff problem and makes the residual $|A \cdot x - b|$ large.

The *SVD* algorithm is said to be a powerful technique to deal with the ill-conditioned matrix equation like Eq 5.6. However, even with the highly advanced *SVD* algorithm, the solution of Eq. 5.6 is still not fully satisfied, and as will be demonstrated, the rank problem may be a barrier to further applications of this method. It turns out that in the normal case, only 4 or 5 singular values can be used (rank 4 or 5) to get the final *DICE* profile, so the solution is of such low resolution that it may not be used with confidence to prove anything.

5.2.3 *IDEAL* method

In order to test the reliability of the *DICE* method, an exact (but physically unrealisable) method has been used to create the theoretical *DICE* profile by computer modelling. The "*IDEAL*" method is based on one of the semiconductor simulation programs *SPIN.F* which can deal with the transport problems in *p-i-n* devices. The details of this program are described in Chapter 2. The procedure for this so called *IDEAL* calculation is as follows:

Firstly a steady state calculation has to be carried out under the required operating conditions to get a set of background data. Then on the top of the steady state generation rate profile, for each slice in turn, we add a small increment of generation rate, so that there will be a small increment of terminal output current. The ratio of the output current increment and the amount of additional generation rate in a given slice is the internal collection efficiency for that slice under the given operating conditions. This calculation is carried out for all the slices across the device so that the spatial variation of the internal collection efficiency accross the sample can be plotted to produce a complete, theoretically exact *DICE* profile. The small addition on the generation profile is set to be so small (10^{-3} of the steady generation rate at most), that we should be sure that the internal conditions such as field have not been significantly disturbed (of this, more later) The profile returned in this way will be able to be used as a reference for the actual *DICE* method.

The small generation addition can be constant all the way across the device or it can also be a set fraction of the background bias generation rate at each location. Although special care has been taken to make sure that the small addition on the generation rate profile is always small enough so that the system should not be disturbed by this addition, we still found that the relative effect of this addition did not diminish when the size of the addition was reduced even to a very low level. In some special situations, a *DICE* value more than unity was found no matter how small the fraction of photo generation rate added. This inconsistency with the basic assumption of the *IDEAL* method (and the experimental *DICE* procedure) is caused by a special effect called the

photo-gating effect (first reported in a minor form by Maruska et al 1984). This effect not only implies that the *DICE* method and many other quantum efficiency measurements are possibly invalid under some circumstances but also introduces the interesting possibility of taking advantage of this effect to do something useful. The details of this effect are discussed in Chapter 6.

Of course, the small additional local generation increment can not be infinitely small since the size of the addition will not change the final result. Also, the addition can be too small if the increment is set to be a fraction of the local generation rate, which because of optical absorption, may also be small. The final result may then mostly be influenced by the numerical error accumulated during the calculation.

5.2.4 Bifacial method

Considering the accuracy of the solution of equation 5.6 to be very much limited by the rank deficiency of the *SVD*, Hof et al (1994) introduced a *bifacial DICE* analysis method. The idea here was, instead of doing the spectral measurement from only one side of the device, if the measurement can be done from both sides of the device, the accuracy of the solution would be improved significantly. It was found that by simultaneously analysing both the spectral responses measured with probe light entering from the *p*-side and from the *n*-side, the resolution of the analysis is found to be more homogeneously distributed over the whole *i*-layer, and also quantitatively clearly improved. The improvement is brought about through a doubling of the optimal rank of the *SVD* conversion of the *DICE* equations. An empirical relation for optimal ranks was found as follows

$$R_b=2(R_m-1) \tag{5.10}$$

where R_b is the optimal rank of the bifacial method and R_m is the optimal rank of the monofacial method. This relation is applicable in the range of 4-5 of the R_m value. The increased rank leads to a fundamental improvement in the resolution of the different test profiles.

5.3 *DICE* Measurement

The *DICE* measurement was carried out using the procedures described below:

(1) *LED*s are used as the stationary bias light source with different wavelengths;
(2) A monochromator is used to supply chopped low level "probe" light with wavelength which can be changed fron 400*nm* to 700*nm*.
(3) A silicon photodiode is used to monitor the photon flux from the probe light.
(4) Two lock-in amplifiers are used to measure the photocurrent from the photodiode and from the *a-Si:H p-i-n* diode under test.

(5) Two power supplies are used to drive the *LED* and to bias the *p-i-n* diode respectively. Another *DC* power source is used to drive the amplifier circuit of the output current from the *p-i-n* diode and from silicon diode.

The measurement was carried out in the following sequence: Firstly, the photon flux from the *LED* is measured by measuring the output current from the *BPX65* silicon diode operating in photoconductive mode. This is referred to as the bias light. Secondly, the bias voltage applied on the sample is set at the required value. Thirdly, the probe light from the monochrometer is chopped at a low frequency between 5-10*Hz* and applied to both the *p-i-n* diode sample and a *BPX65* silicon diode monitor. Finally, the *DICE* measurement is carried out. The readings from two lock-in amplifiers are the photo current from the sample *p-i-n* diode and from the *BPX65* silicon diode which respectively give the collected current from the *p-i-n* diode at that wavelength and the photon flux which can be found using the standard spectral response of the the *BPX65* photodiode. Either monofacial or bifacial measurements can be done since the sample has two semitransparent electrodes which allows the light to be directed from either *p*-side, *n*-side or both. When the measurement is finished, we have spectral response data, so to get a *DICE* profile, computation is necessary.

To calculate the *DICE* profile, at first we need the absorption profile of the probe light directed into the *p-i-n* diode for each wavelength used. If only exponential decay is assumed, the only thing we need is the absorption coefficient for each wavelength. For the thick sample of the type used in this work, the reflection from the bottom electrode can be neglected.

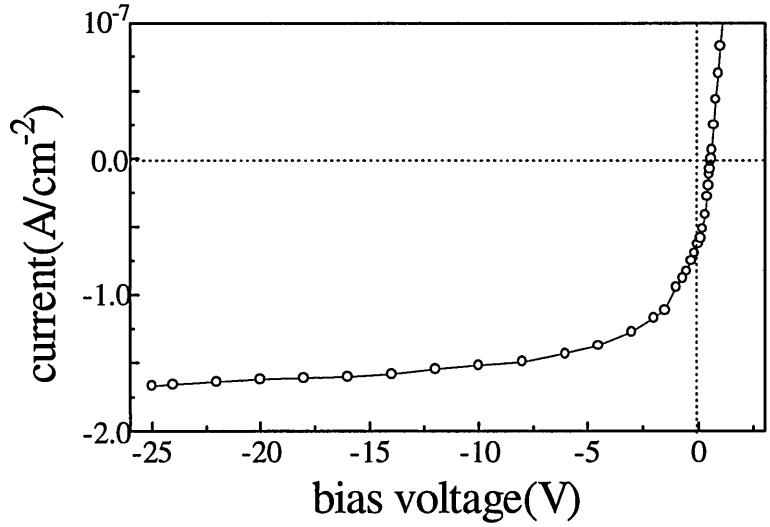

Fig 5.2 *I-V* characteristics of a 3.4μ*m a-Si:H p-i-n* diode. Light source green *LED* (550*nm*)

It has been mentioned that equation 5.3 is based on the assumption that the collection will reach 100% at high enough reverse bias voltage; spectra measured at lower voltages are normalised to this spectrum. However, when we measured several

samples, the collection efficiency at -25volts did not appear to be saturated since the *I-V* characteristic had not levelled out. This is mainly because, at high reverse bias voltage, on one hand, due to the thickness of the device, the collection has not reached 100% yet, and on the other hand, the internal thermal generation rate (which may be field dependent) via defects has become significient at high voltage. The mixture of these two factors makes the assumption of the 100% collection invalid. So as an alternative, we tried to measure the actual photon flux reaching the sample. Although this approach includes a few more measurements and calculations, it can also confirm the data to be used are correct.

In order to calculate the absorbed photon flux accurately, the absorption by electrode and glass substrate has to be measured. To do this accurately, a special arrangement was made using a black mask with an aperture smaller than the electrode diameter of the *p-i-n* diode. The modulated light from the monochrometer is directed through the small aperture onto the sample (*Cr*/glass). The photon detector *BPX65* silicon diode is directly behind the small aperture so the light transmitted through the sample will be detected. For each wavelength, two data are read, one the transmission for *Cr* + glass, the other for glass only. Scanning from 400*nm* to 1000*nm*, gives the transmission profile as shown in fig 5.3

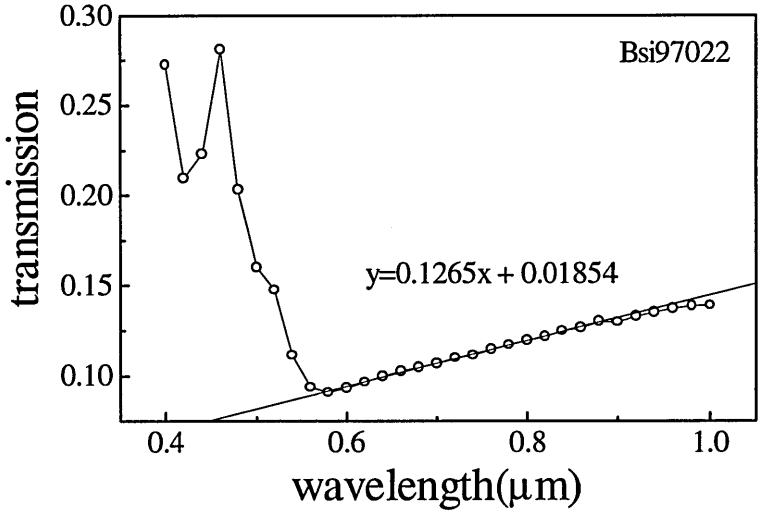

Fig 5.3 Transmission profile for 7059glass and *Cr* electrode.

From Fig 5.3 it is seen that at long wavelength, from 1μ*m* to 0.6μ*m*, the transmission rate declines slowly and linearly from 15% to 10%, and after that, starts to increase when the wavelength is reduced below 0.5μ*m*. However, the measurement within short wavelength may not be very accurate, but fortunately, the useful part of the range we normally use for the probe beam in *DICE* is between 600*nm* to 700*nm* and data are accurate in this range. A linear transmission - λ relation can be used for more detailed calculations as shown in the figure. The reason for using this wavelength range is purely due to the consideration of best generation profile distribution in the thick *p-i-n* diode

structures under investigation. From the measured photon flux data plus the deduction of the absorption of the electrode, we can get the photon flux absorbed by the *a-Si:H p-i-n* diode.

Another measurement was also carried out, now including the *a-Si:H* film in the measurement. By comparing the transmission of *a-Si:H*/glass *and a-Si:H/Cr*/glass any difference in electrode transmission due to the refractive index of *Cr* and glass will be eliminated, according to the formula

$$R = \left(\frac{n_1 - n_2}{n_1 + n_2} \right)^2$$

if the refractive indices of air, glass, *Cr* and *a-Si:H* at 620*nm* wavelength are 1, 1.5, 3.5 and 3.5, respectively, the error introduced by doing the simple measurement as in fig 5.2 will be 26%. However, for this improved measurement, the wavelength range is limited by the influence of the *a-Si:H* film, which has high absorption for wavelengths shorter than 600*nm*. At long wavelength, the interference of the light in the *a-Si:H* film made an accurate measurement difficult. Within the range we can measure (600*nm*-700*nm*), the electrode transmission measured in this way is close to double the figure shown in fig. 5.3.

5.4 Results

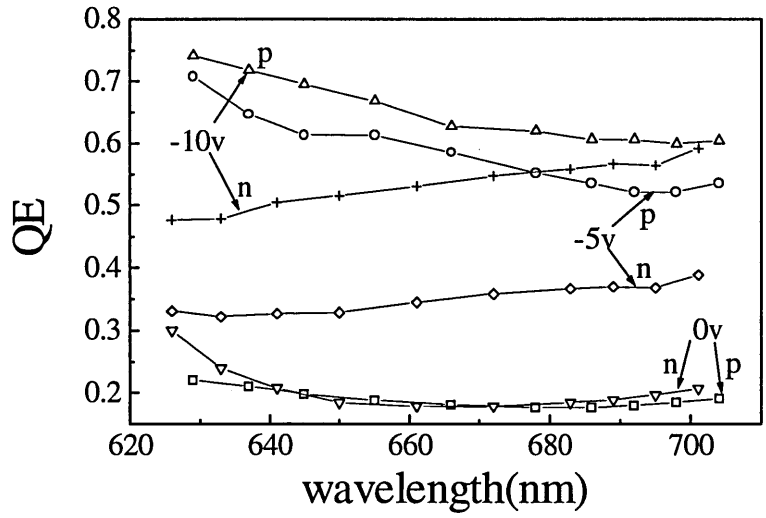

Fig 5.4 Spectral response bifacial measurement for *DICE* calculation. There are three groups of data - each corresponds to one reverse bias voltage. The bias light is always from the *p*-side (green *LED* 550*nm* wavelength, photon flux roughly $10^{15} cm^{-2}s^{-1}$). Modulated probe light (photon flux roughly $10^{11} cm^{-2}s^{-1}$ is directed from both *n*- and *p*-side as indicated on the graph.

Figure 5.4 shows the spectral response data from the above measurement. It is seen from the spread of points that the accuracy is not very good and poor accuracy of the data turns out to be a vital problem for the success of the *DICE* method which will be discussed later.

The attempts to extract the *DICE* profile from the bifacial measurement in this work have not been encouraging. The rank deficiency deteriorates the method when the accuracy of the spectral response data is low. The best rank that can be used without oscillation in the solution is too low (2-3) to give a reasonable result.

5.5 Error assessment

To convert from the spectral response measurement to the internal *DICE* profile we need to solve equation 5.6. However, even with the highly advanced *SVD* algorithm, the solution is still not fully satisfied even when smoothing treatment is applied to the data. The rank problem seems to be a barrier to further application of this method. In the normal case, only 4 or 5 singular values (w_j) can be used (rank 4 or 5) to get the final *DICE* profile without oscillation, so the solution is not good enough to give useful resolution. There have been several numerical evaluations of this method, but they are either incomplete or they use artificial mathematically accurate data which is impossible to achieve in experiment (Takahama et al 1986, Von der Linden et al 1992 and Hof et al 1994). In order to have a better understanding on *DICE* method and its limitations, it is necessary to have a detailed and realistic analysis of the characteristics and the advantages and disadvantages of this method.

5.5.1 The computer simulation of the *DICE* method

The simulation was carried out in several different ways. The first approach is to use the *IDEAL* method to calculate the *DICE* profile. We assume at this point that if the small increment on the generation profile is small enough, the internal field will not be changed by it and the collection efficiency data from this calculation will be true (in the normal situation, for example uniformly absorbed light, thin sample etc, the photogating effect mentioned earlier is not very important).

The second approach is to use *SPIN.F* (described in Chapter 2) to simulate closely the whole *DICE* measurement process. The model starts with weakly absorbed bias light (the same light as was used in the *IDEAL* method), and then the probe light is added at each wavelength either from one side or from both sides, i.e. monofacial or bifacial. For each of these illumination conditions, the total generation profile is the combination of the bias light and the probe light. For each wavelength, the spectral response data arising from the probe light can be calculated - by subtraction of the computed terminal current with bias only from terminal current with combined excitation. For a series of different wavelengths, a spectral response profile against the probe wavelength can be obtained. On the basis of these spectral response data, Eq (5.6) can be set up as for experimental data and can be solved by *SVD* algorithm. Some of the parameters used in the programme are as follows:

device thickness	0.5μ*m* (*p* and *n* layers are both 10*nm*)
reverse bias voltage	-1volt
monofacial method	light from *p*-side
neglect back reflection.	
number of slices for the analysis 20	

The *SVD* calculations were carried out in four different combinations -- monofacial and bifacial; uniform and non-uniform grid. It has to be noted that the grid distribution during the *SVD analysis* has no direct relation to the spectral response measurement, i.e. theoretically, the matrix of Eq (5.6) can be generated on a uniform grid or on a non-uniform grid without changing the final result. In each combination, the result with rank number from 3 to 7 has been calculated separately in order to compare the results with the *DICE* profile simulated for the same bias conditions by the *IDEAL* method.

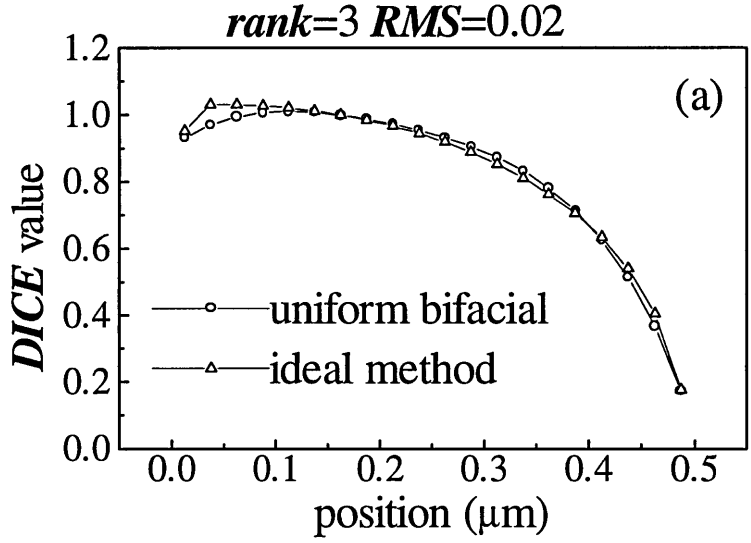

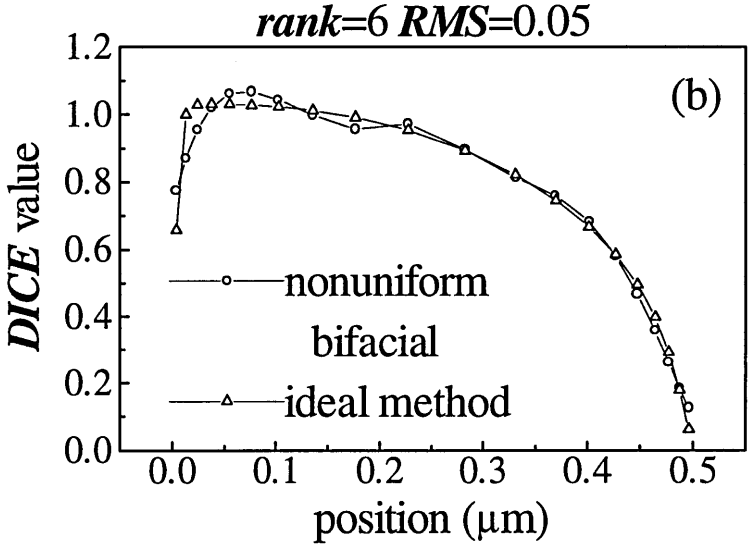

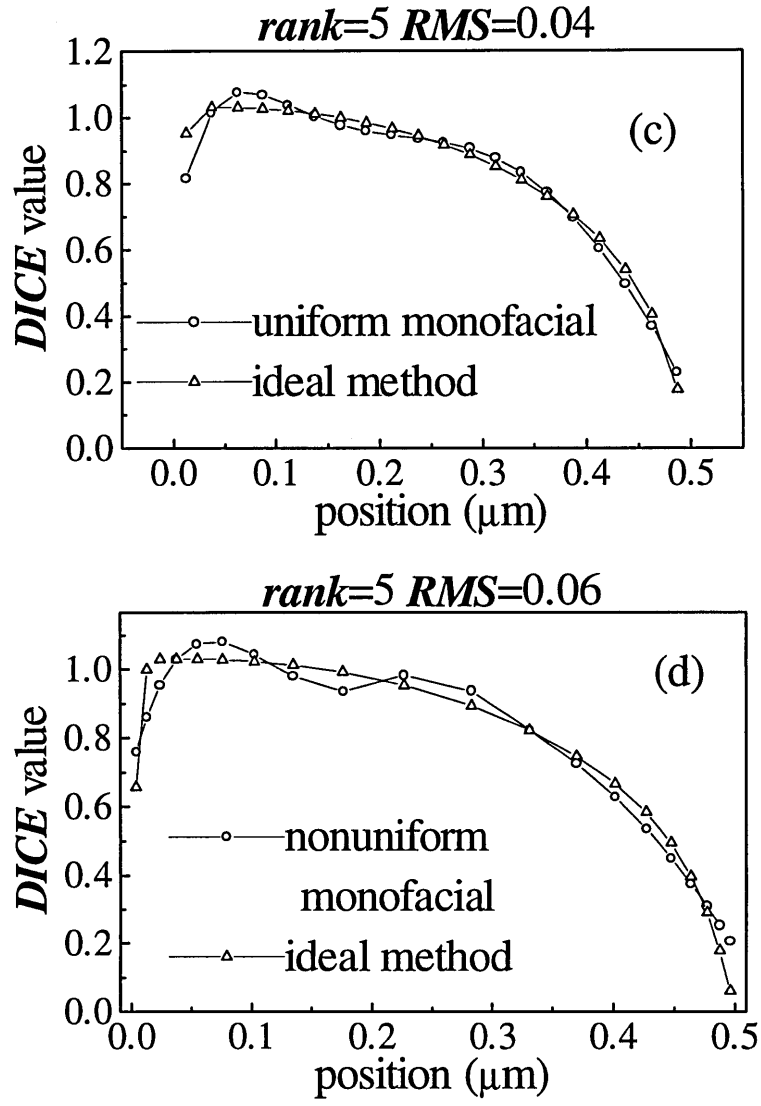

Fig 5.5 Comparison between the *DICE* profiles generated by the *IDEAL* method and by the simulation *SPIN+SVD* under different conditions. (a) uniform grid bifacial; (b) non uniform grid bifacial; (c) uniform grid monofacial and (d) non uniform grid monofacial.

All the four graphs in fig 5.5 are selected from rank 3 to rank 7 results. They are the ranks that give the minimum *RMS* deviation values. It can be seen that a uniform grid normally gives better results than the non uniform grid which gives out slightly oscillating results. Due to this oscillation, the *RMS* errors for the non uniform grid are larger than those for the uniform grid. This extra error is believed to be purely introduced during the *SPIN* simulation. The small amount of error due to the non-uniform grid in the *SPIN* calculation will cause a large difference in the extracted *DICE* profile, as will be shown later.

For the same grid distribution, the monofacial method increases the *RMS* errors, though not changing the main features of the curve very much. The bifacial method, based on the result of Hof et al (1994), can provide more information on the back side of the device, and increases the resolution on that side as well. In fig 5.5, it can be seen that the bifacial method improves the total resolution evenly throughout the device. The

improvement in resolution appears to be symmetrical. When the relative errors were plotted against the position, the largest error always happened near two sides and good fits were found in the middle of the curve (about 80%-90% of the curve).

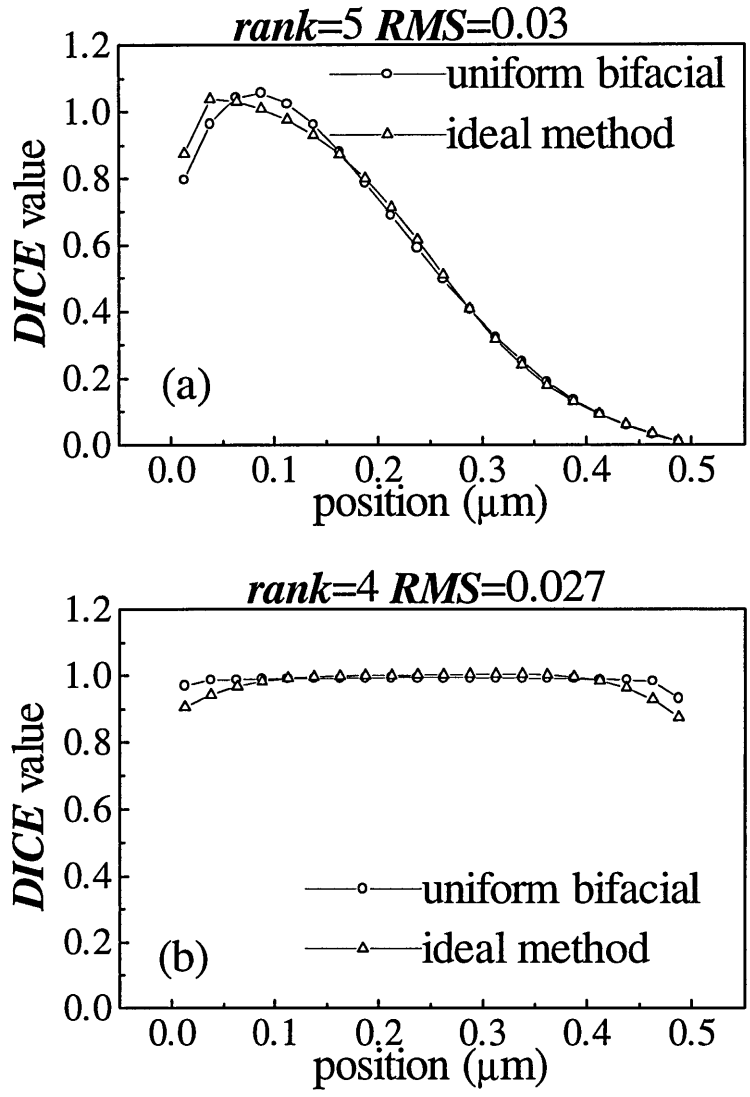

Fig 5.6 Comparison between the *DICE* profiles generated by the *IDEAL* method and by the *SPIN+SVD* method at two different bias voltages. (a) 0 volts, (b) -5volts

Fig 5.6 shows the results for 0 volts and -5 volts reverse bias situations. It can be seen that the collection efficiencies increase with increasing reverse bias. At -5 volts, the *DICE* profile is nearly unity. In the 0 volt case the *DICE* value is much higher on the *p*-side than *n*-side. This is due to the redistribution of the internal field by the bias light illumination on the sample. A detailed analysis can be found in Chapter 3.

The number of slices used is a parameter which needs to be considered, since not only does it define the number of probe light wavelengths used on the diode, but also it is the number of equations in the matrix equation 5.6 to be solved. To choose the optimum number of slices in this calculation may not only allow highest accuracy, but also can

save computation time. The *IDEAL* method and *SPIN* computer simulation are used again to make the comparison. Having chosen different numbers of slices, the *DICE* profiles are calculated from the *IDEAL* method and from the *SPIN* computer simulation. During the simulation, the *DICE* profiles for different ranks are all calculated, and comparisons made with the *IDEAL DICE* curve, so the *RMS* deviation values for different rank and for different number of slices are all calculated. Fig 5.7 shows the best *RMS* (deviation) value for each number of slices. When the number of slices increases, the *RMS* value decreases first, then after 20 it starts to increase again. The reason for this may be because when the number of slices is small, the divisions are too coarse, and cannot take details into account, and when the number of slices is large, rounding error will accumulate when the equation is solved.

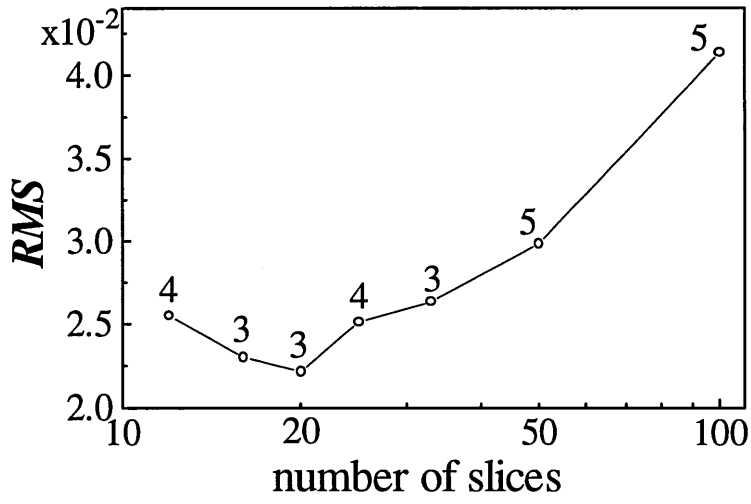

Fig.5.7 The best *DICE* results for different numbers of slices. The numbers on the curve are the ranks giving the smallest *RMS* error value for the given number of slices.

It needs to be mentioned that relatively speaking, the number of slices of the device is not very important for the final result. It will not change the optimal rank, nor will it improve or deteriorate the resolution very much. However it is quicker to have a smaller number. 20 is the number we used to give reasonable resolution to the curve.

Another phenomenon that is controversial is the rank. From Fig 5.5. there is no obvious evidence for Hof et al's relation (eq 5.10). Instead, it is found that the *DICE* profiles with rank from 3 to 6 are more or less the same shape, with only a little difference in the *RMS* error. When the rank is less than 3 and larger than 6, the *DICE* profiles are either unreasonable or oscillating.

The Fig.5.8 shows the *RMS* error plot against the rank of *SVD* showing that the errors do not have a regular relation with the rank. Indeed, for the non uniform grid, the difference between the monofacial and bifacial result is not systematic. The reason for this is probably because the non-uniform grid introducs an extra source of error that is

more important than the improvement from the bifacial tactics. However the bifacial method is generally slightly better than the monofacial method.

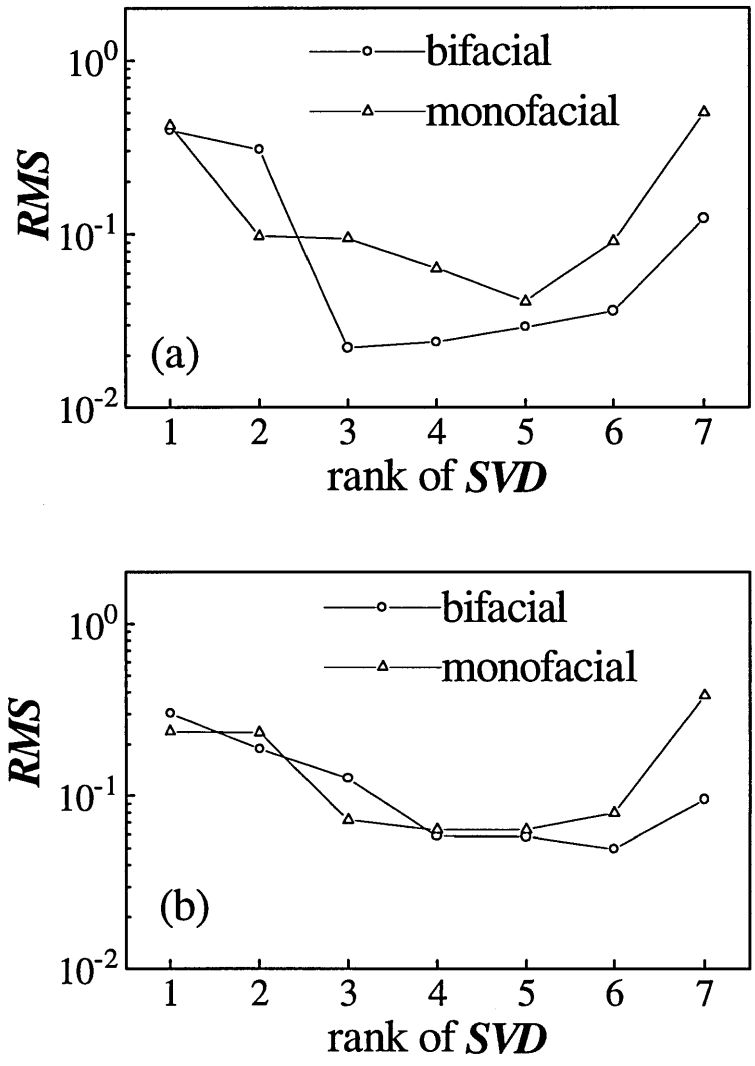

Fig 5.8 The *RMS* error against rank of *SVD*, calculated based on the comparison between the *SPIN* + *SVD* computer simulation under different conditions, and the *IDEAL* method. (a) uniform grids, (b) non uniform grid.

During the *SPIN+SVD* computer simulation and the calculation of the *IDEAL* method, double precision arithmetic (16 decimal places) was always used. For these computer calculated results, the best rank is still surprisingly low, considering that when the best rank of *SVD* is between 3 and 5, the random error should be around 10%, a figure much larger than the rounding error expected using double precision arithmetic. The significance of this part of the simulation is that it simulates the real measurement processes. The reason why errors still appear when double precision arithmetic is used will be discussed in Chapter 6, where the so called photo-gating effect appears as the culprit.

5.5.2 The test of the *SVD*

It has long been realised that the algorithm used to solve Eq (5.6) is crucially important for the success of the *DICE* method. Previous research has always done some kind of testing. However, these tests were either on error free data or not thoroughly investigated. The purpose of this test is to try to find out the influence of the error during the spectral response measurement.

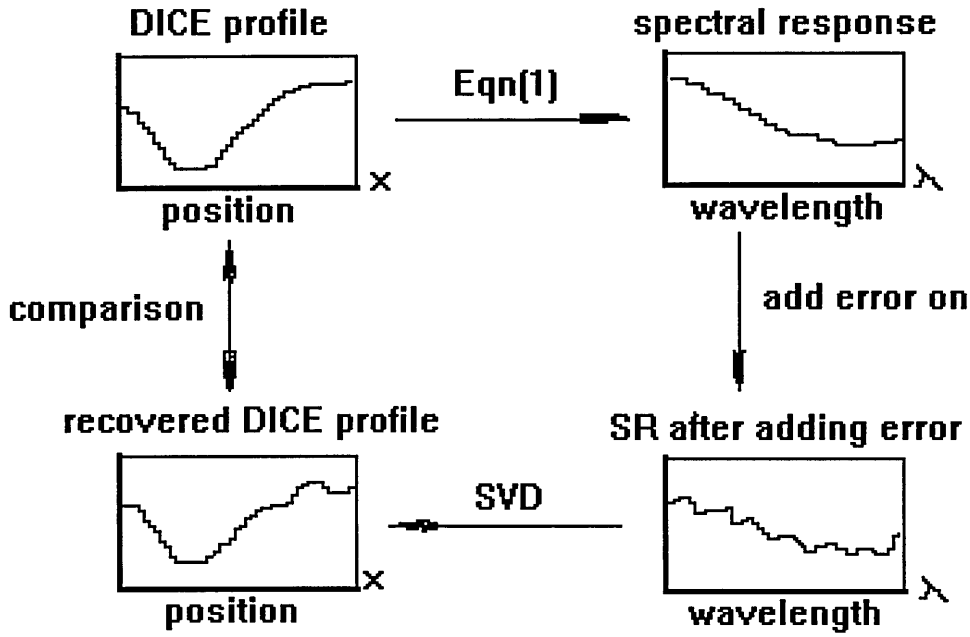

Fig 5.9 Schematic diagram of the testing process.

The testing method can be described as follows

(i) Create a *DICE* profile artificially. In present case, we choose a profile that may happen in the thick sample (>1μm) with high reverse bias. This is a difficult situation for *SVD* analysis.

(ii) Calculate the quantum efficiency data from Equation (5.1) under illumination of different wavelength light, monofacial and bifacial. The number of wavelengths is set to be 20, so the number of equations is also 20. We choose the range of the wavelengths in such a way that the spatial generation profiles created by different wavelength will be separated as much as possible in order to get the maximum resolution.

(iii) Add different (0-10%) systematic and random errors on the spectral response data to simulate the real measurement.

(iv) Normalise the spectral response and solve equation 5.6 by the *SVD* method, calculating the solution for all the different numbers of singular values (from 1 to 20)

(v) Compare the results with the original artificially created *DICE* profile, calculating the Root Mean Square (*RMS*) deviation values.

All the calculations were carried out by using double precision variables (15-16 decimal digits)

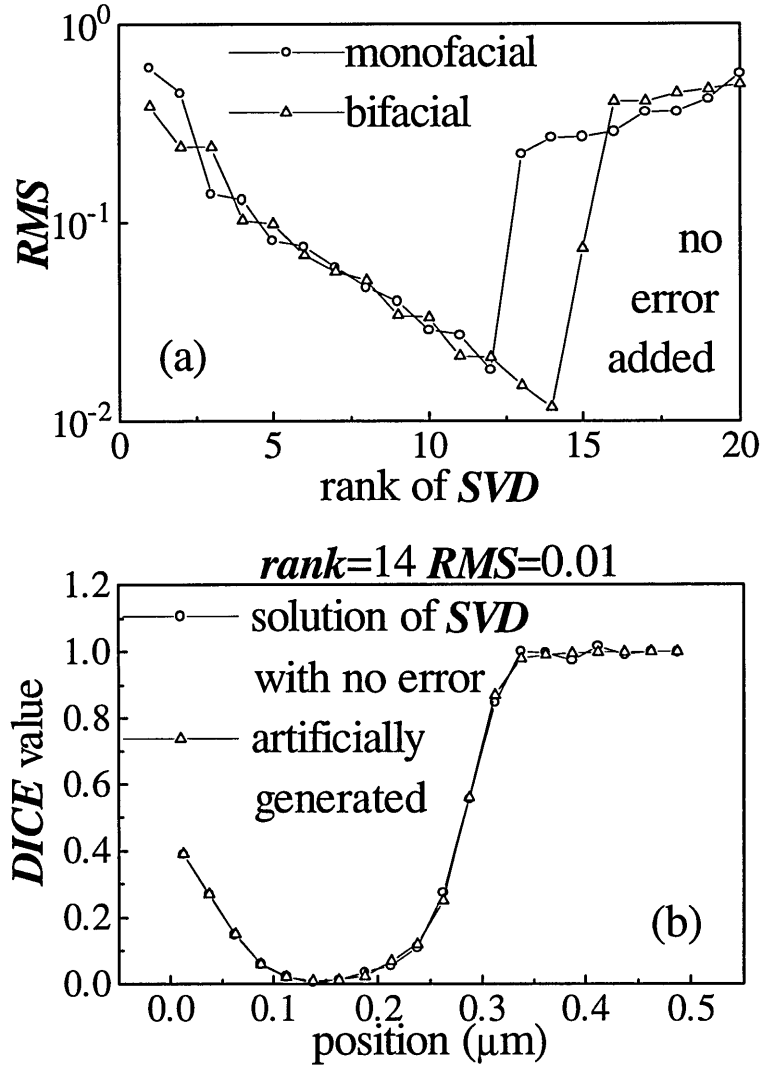

Fig 5.10 Calculation results for the 'no error' case (a). the root mean square error value vs. the rank of *SVD*, monofacial and bifacial (b). the best result recovered when rank is 14, when no additional error is added.

Figure 5.10 shows the "no error" case in which the *DICE* profile is recovered very well with its best rank of 14 (the *RMS* error is only 0.01 which is lower than we normally can get from measurement). Fig 5.10(b) plots the artificially created *DICE* profile and the calculated *DICE* profile with no error added. The two curves fit quite well. It has been found that if the artifically made *DICE* profile has no sudden discontinuity, i.e. the first derivative is continuous, the *DICE* method may be able to solve the problem properly. Fig 5.10(a) shows that the bifacial method can not make the *RMS* error value lower than the monofacial method under the same rank. The best rank

which the bifacial method can get is 14 which is probably limited by the variable precision used during the calculation. The best rank the monofacial method can reach is 12, only 2 ranks lower. This result does not follow the Hof 's result, and the relation may take the simpler form

$$R_b=R_m+2 \text{ (or 1)} \tag{5.11}$$

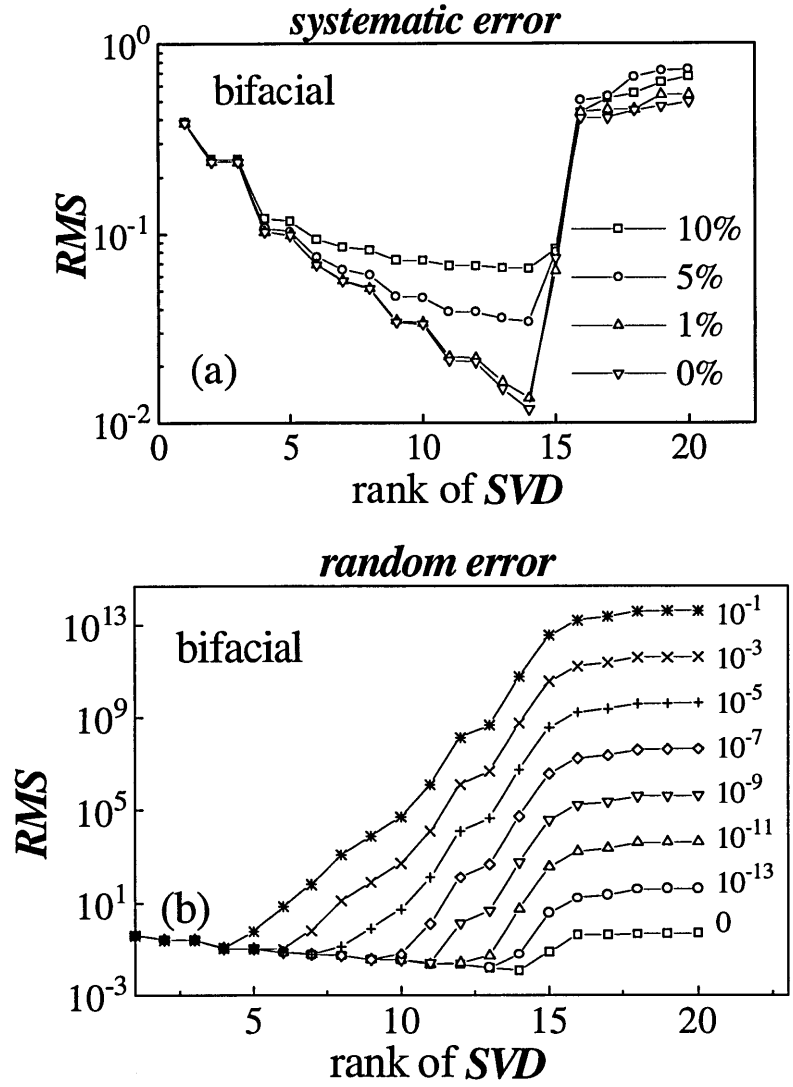

Fig 5.11 *RMS* deviation value changes with the types and the values of the error introduced, (a). systematic errors up to 10%, which changes the results relatively less. (b). the random error changes the accuracy dramatically.

Different kinds of error added to the spectral response data (derived from the artificially made *DICE* data according to the Eq (5.1)) change the final result in quite different ways. Fig 5.11(a) shows the *RMS* deviation value vs. the rank of *SVD*. Up to 10% *systematic* error only changes the *RMS* value within one decade with the best result still for rank 14. On the other hand, the *SVD* method shows very high sensitivity to *random error* in the spectral response. At 10% random error in the spectral response, the best rank is reduced to 4, and the recovered *DICE* profile has changed significantly.

When the random error decreases, the best rank increases, being approximately 1 rank higher when the error is one order lower. At 10^{-5} random error, the rank goes up to 7, at 10^{-14} random error, the rank goes up to 14. Considering a practical possible measurement accuracy of 1% at best, only rank 5 can be expected.

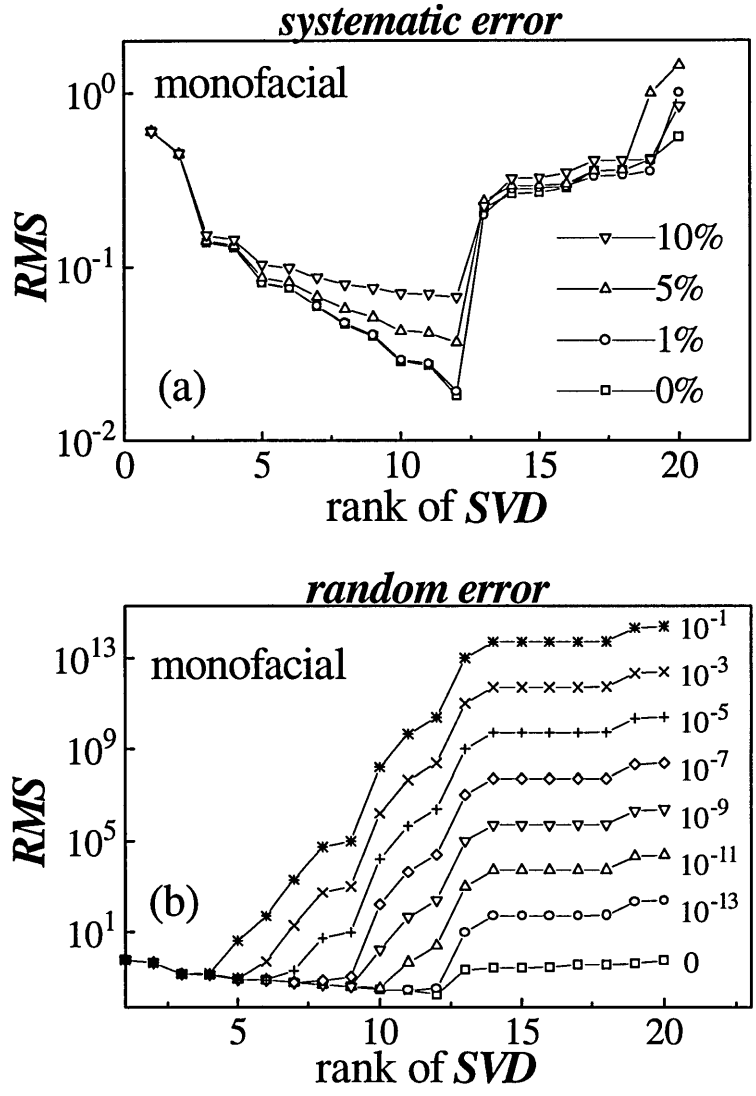

Fig 5.12 *RMS* error value changes with the types and the values of the error introduced to the spectral collection efficiency, (a). systematic errors up to 10%, which changes the results relatively less. (b). random error changes the accuracy dramatically.

Fig.5.12 shows the same situation for the monofacial method. For the no error case (also see Fig 5.10(a)), the best rank is 12, and the *RMS* deviation for that is relatively higher. Actually, the two curves are coincident before rank 12. This means as long as the same rank is obtained, you would be able to expect the same accuracy. The monofacial method offers less information so that the *DICE* solution starts to oscillate earlier. However, rank 12 is acceptable. If we compare the Fig 5.11 and Fig 5.12, there is little difference between them, except that the bifacial method is, for some errors, one or

two ranks better than the monofacial method. This also verifys the relation given in equation 5.11.

5.6 Discussion

Since the *DICE* method was introduced, several papers have been published on the topic, but it has clearly not become a standard way of characterising amorphous silicon solar cells due to its poor resolution on the recovered internal collection profile. From the present investigation, we found that the *DICE* method may still be a useful approach to investigate some inner characteristics qualitatively, not quantitatively, on the condition that some care is taken to reduce the error introduced during the spectral response measurement. It is found that a polynomial fitting to the spectral response measurement data or computer controlled measurement can reduce the error to some extent, and this may improve the resolution of the extracted *DICE* profile. More work needs to be done on this subject in order to reduce the error to an acceptable level. Also, if the computer modelling can be accompanied or associated with the measurement, more information will be obtained.

5.7 Conclusions

Computer simulation and error testing of the *SVD* algorithm for the *DICE* method have been carried out. The *DICE* method proved still to be a useful approach to investigate the inner characteristics or processes occurring inside semiconductor devices on the condition that some data treatment has been applied to reduce the error introduced during the spectral response measurement (for example, polynomial fitting to the *QE* measurement data or computer controlled measurement). However, the error introduced from the measurement of spectral response seriously affects the resolution of the final results. By minimising the error either from the measurement or from the calculation, the accuracy of the final *DICE* profile may be controlled within several percent. However, the *DICE* profile can only give the general tendency of the collection properties. Detailed features are "washed out" by the *SVD* algorithm due to the low resolution associated with rank deficiency of the solution.

chapter six

APPLICATIONS OF THE PROGRAM

6.1 Introduction

Analytical models have long been used to investigate the behaviour of the semiconductor devices, either crystalline or amorphous semiconductors. Such models have been very successful when applied to crystalline materials because of the regularity of the crystalline structure and the resulting completeness of the theory. In the case of amorphous semiconductors, with distributions of band tail states and dangling bond deep states, analytical models are normally subject to significant simplification, such as "regional approximation" (Crandall 1982 and 1983), "zero temperature approximation" (Hack and Shur 1983), "no diffusion" (Shah and Hubin 1989), "no trapping" (Hubin et al 1992) and many others (e.g. Misiakos and Lindholm 1988 or Hubin et al 1989). Based on these assumptions, the conclusions are then often contradictory. For example, there is disagreement about the controlling, or limiting carrier type, in charge collection processes. In these cases, numerical modelling can normally help to clear up the difficulties and give a detailed explanation. On the other hand, there are other kinds of problem which probably can only be solved by numerical modelling, for example a quantum efficiency greater than unity. In this chapter, the program *SPIN.F* described in chapter 2 and 3 will be used to solve the problems just mentioned and to demonstrate some other applications.

6.2 Quantum efficiency much greater than unity

The existence of quantum efficiencies larger than unity have been an interesting topic recently, not only for the phenomenon itself, but also for the possibility of applying *a-Si:H* based photovoltaic devices as optical radiation detectors with internal gain (Rubinelli 1994). The quantum efficiency referred to in this chapter is that measured for low intensity probe illumination superimposed on a higher intensity bias illumination, as in the *DICE* technique described in chapter 5.

Originally, quantum efficiency measurements under bias light conditions have assumed that small signal conditions have been satisfied, i.e. the photon flux of the probe light has to be much smaller than that of the bias light, so that the electric field will not be substantially disturbed by the addition of the probe light. However, in 1984, Maruska et.al, for the first time, found the $QE>1$ in a Schottky diode when blue bias light and a red modulated probe light were applied from the same (*p*-) side, while other studies published afterwards did similar measurements and computer simulations on *a-Si:H* Schottky diode and *p-i-n* structures (Hou and Fonash 1992, Chatterjee 1994). The

origin of this *QE*>1 phenomenon has been well discussed, one explanation being that the bias light creates, near the front contact, a low field region that acts as a series resistance (a misnomer in our view) to control the bias current to a low value. The addition of the probe light modulates the field profile, increases the field in the low field region so as to release bias light created carriers previously stopped by the low field. Under small signal conditions, this modulation to the electric field should have a linear relation with the probe light intensity even though it has not ever been demonstrated.

Since the output current measured in a *QE* measurement is not purely the photo-generated current due to the probe light, the word 'photogating' was used to describe this special effect (Hou and Fonash 1992). The low field region near the front *p*-layer arising from the high mid gap defect density has been believed to be necessary for the photogating effect. Blue bias light is not the only way to create the low field region; a combination of a relatively higher mid gap defect density and red bias light is another way. Chatterjee (1994), has shown that by using red bias light, simply increasing the defect density can also produce *QE*>1. This effect has been attracting more and more interest, being described as an optically controlled amplification processes with some potential of being used in some kind of photodetector (Rubinelli 1994). However, the *QE* values mentioned so far are only slightly larger than unity, not enough to be eligible for any real practical applications. The present investigations have been carried out under different conditions. A brief list of the experiments previously done may be helpful for the further analysis of this interesting effect.

TABLE 6.1 Experimental conditions in some published studies

authors	BL(λ) (*nm*)	DB density	PL	low field region	QE value	device type	bias voltage
Maruska et al (1984)	436*f*	*AM*1 400*h*	*f*	near rear	~1.06	*m-i-n*	0
Hou & fonash (1992)	460 *f*	2.4×10^{16}	*f*	near front	~1.7	*p-i-n*	0
Chatterjee (1994)	>600*f*	10^{18}	*f*	near front	~1.1	*m-i-n*	0
Rubinelli (1994)	400*f*	annealed	*f*	near front	~1.7	*m-i-n*	0.2*V fd*

f for front (*p*-side) *fd* for forward

It is noteworthy that all these measurements or computer simulations were carried out with probe light directed from the front, i.e. *p*-side, under no bias voltage or under small *forward* bias voltage. From the point of view of application as either a photovoltaic radiation detector or an optically controlled amplifier, this may not be the best geometry. In this work, we investigate this phenomenon under different bias light and probe light combinations, and, unlike previous researchers, under reverse bias voltage conditions, reveal a much more dramatic effect that may make the application mentioned above practicable.

6.2.1 Experimental results

In this work we measure the spectral response of a *Cr/(p^+)a-Si:H/(i)a-Si:H/(n^+)a-Si:H/Cr*/glass *p-i-n* solar cell under bias light conditions. The *Cr* electrodes are semitransparent. The structure consists of 20*nm* heavily doped p^+ and n^+ layer and a 3.4μm intrinsic *i*-layer. *QE* measurement was carried out by applying a blue bias light (450*nm* $7.65\times10^{14} cm^{-2}s^{-1}$) from the *p*-side, and monochromatic probe light from the *n*-side. The photon flux for the probe light is kept at $3.7\times10^{11} cm^{-2}s^{-1}$ during the measurement. These two photon flux values for bias and probe lights have taken the absorption of chromium electrodes into account, so the above are actual photon flux values incident on the *a-Si:H* film surface. A reverse bias voltage is applied in this experiment, varying from -5 volts to -25 volts. While an *AC* technique, chopping the probe beam and detecting with a lock-in amplifier would normally be used in this kind of measurement, it was possible and necessary to use a *DC* method due to the relatively slow response time for the thick *a-Si:H* device. The experimental procedure is described as follows:

(1) Set the reverse bias voltage.

(2) Measure the photocurrent on applying only bias light from the *p*-side, giving I_{bl}.

(3) Measure the photocurrent by applying bias light from the *p*-side and probe light from the *n*- side, giving I_{tot}. When the wavelength of the probe light is changed, the photon flux, monitored using a *BPX*65 photodiode, was kept constant at $3.7\times 10^{11} cm^{-2}s^{-1}$.

(4) Subtract the two currents to give a collected current for the probe light at that particular wavelength and bias voltage. i.e. $I_c=I_{tot}-I_{bl}$

(5) Divide the collected current by the photon flux of the probe light, ie. $I_c/flux$ to give the *QE* value for that condition.

The calculation of the probe light photon flux includes the calibration of the photodiode readings used to monitor the probe light and the absorption data of the chromium electrode for different wavelengths as described in chapter 5.

Figure 6.1 shows the *QE* measurement result for the sample mentioned above at −10 volts reverse bias voltage. It is easily seen that the *DC* measurement gives a much larger result than that of the *AC* measurement carried out at 5 *Hz*. When the probe light is chopped into an *AC* signal, it was found using an oscilloscope that the output signal from the *p-i-n* sample to the lock-in amplifier is not a square wave, instead, more like a triangular waveform. This is due to the slow response time of this thick sample. Using such a *DC* method to read the current data straight from multimeter is relatively inaccurate, and a standard waiting time strategy was adopted, waiting for 2-3 minutes to take each reading when it stabilizes. Note that figure 6.1 also shows the *QE* value can go up to as high as 50 or more under -10volts reverse bias voltage.

Figure 6.2 shows the *QE* value measured in the peak wavelength range (from 1.9*eV* to 2.2*eV*) under different reverse bias voltage conditions. It can be seen that the *QE* value increases when the reverse bias voltage increases, then when approaching -25 volts, it starts to saturate gradually. Another phenomenon is the broad peak with relatively flat plateau between 577*nm* and 636*nm* which does not change in shape when the reverse bias voltage is changed.

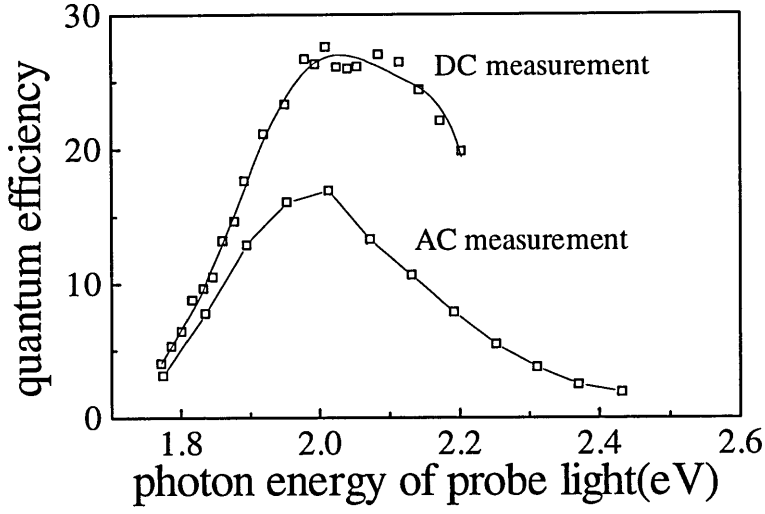

Fig 6.1 Measured *QE* characteristics of a *p-i-n* solar cell at -10volts reverse bias voltage. Illumination conditions can be found in the text.

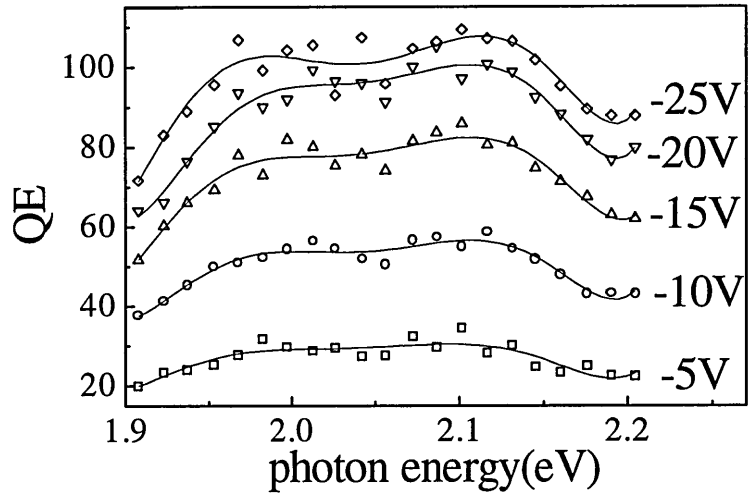

Fig 6.2 Measured *QE* characteristics of a pin solar cell as reverse bias voltage is varied. Illumination conditions are the same as in figure 3.14. The polynomial fitting used for the experimental data may not show the proper trends at the edge of the curves.

6.2.2 Computer simulation

A computer program based on the *SPIN.F* source code was developed to analyse the actual measurement processes (*DC* measurement) by calculating the *QE* value under different conditions following as exactly as possible the experiment procedures. The

computation is carried out at room temperature, 300°*K*. Table 6.2 is a list of the input parameters used in the model. It was been found that a single energy dangling bond δ–function distribution could not simulate this effect correctly, and it was necessary as a minimum to introduce a Gaussian energy distribution for the dangling bonds.

TABLE 6.2 Principal input parameters for the *a-Si:H p-i-n* solar cell

Device thickness 3.4μ*m*;
Boundary conditions are E_F 0.35*eV* above valence band on the *p*-side and 0.25*eV* below conduction band in *n*-side;
Bandtail slopes for conduction and valence band tails are 0.025 and 0.045*eV* respectively;
Thickness of the doped *p*- and *n*-layers 20*nm*;
Optical gap 1.8*eV*;
Band edge density in both conduction and valence band is $2\times10^{21} cm^{-3}$;
Dangling bond energy and correlation energy are E_0=0.8*eV*, *U*=0.35*eV*;
Gaussian distribution for dangling distribution, width σ=0.25*eV*;
Mobilities for free electrons and holes are 10 and $1 cm^2/(Vs)$;
Capture coefficient of electron by *D*° is $1\times10^{-8} cm^3 s^{-1}$;
The reflectance index is 0.8.

The following subsections are the computer simulations based on table 6.2. Some parameters are subject to change and the rest are kept constant.

6.2.3 Photogating effect

The physics of this phenomenon has been discussed to some extent in previous work, while in this study, some similar evidence has also been found through computer simulation as well as some novel conclusions. Figure 6.3 shows the electric field change during such a measurement. This is the case with 10 volts reverse bias, and simulated light conditions as in the experiment. The *QE* value for the particular probe light wavelength (616*nm*) is around 50, close to the experimentally measured value.

In figure 6.3, when only the bias light is applied, due to the short absorption depth ($\alpha^{-1}=3\times10^{-6} cm$ for 450*nm* blue light in *a-Si:H* from Dawson 1992), a low field region is apparent close to the *p-i* interface. The field in this region is so low that it actually has reversed under these conditions even though not necessarily in other bias conditions. This low field (or reversed field) region acts as a kind of large scale potential trap for electrons, in other words, it will stop most of the carriers drifting through the device. This is similar to the so called space charge limited current (*SCLS*) mode. In this case, photogenerated electrons and holes will move towards their respective electrodes. Since strongly absorbed light is applied from *p*-side, then except for those holes recombining, holes will be collected by the *p*-side electrode and electrons will be trying to move towards the *n*-side electrode. In this low field region near the *p/i* interface,

although the recombination rate is high, the electron and hole carrier densities are so high that the small relative difference in density represents a substantial electron reservoir. The high reverse bias voltage applied helps to increase the collection efficiency of carriers created in the high field regions of the device, where recombination is reduced, but the total current is mainly controlled by this low field region.

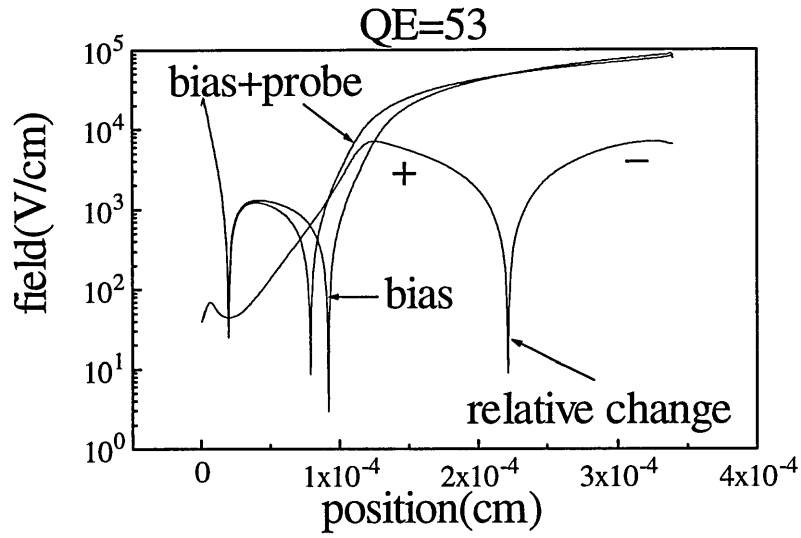

Fig 6.3 The electric field profile in the device before and after the probe light is applied. The signs on the "relative change" curve show the sense of the relative change; + means increase and - means decrease. The probe light photon energy is 2.0*eV*, and the other conditions are the same as in the experiment and table 6.2.

It turns out that in a certain bias voltage range, the field in the low field region is strongly dependent on dangling bond density. The higher the *DB* density, the higher the space charge density, and the lower the field. When the *DB* density is high enough, a reversed field will appear. When the probe light is applied from the other side, the holes will drift through the device towards the left, recombining with the electrons trapped in the mid gap defects in the high field region in the *i*-layer. (The absorption depth of the 616*nm* probe light is $4.17\times10^{-5}cm$, only 12% of the sample thickness), Due to the reduction of the space charge in the *i*-layer, the field will be modified. Figure 6.3 shows this results in an electric field *increase* in the left half, and a *reduction* in the right half of the device. This modified field releases many more electrons from the low field region, or in other words, it is the bias light-created electron reservoir which releases electrons and causes the output current to be much larger than the current increment purely from the probe light itself.

It is generally believed that the low field region due to the high defect density and bias light is responsible for the larger than unity *QE* value. However, figure 6.7 shows that the *QE* value is still larger than unity even when the defect density is so small that the low field region has disappeared (when the *DB* density is smaller than $5\times10^{14}cm^{-3}$). This is not due to a different mechanism, but is just the photogating effect discussed above, reduced to a low level but still operating. It can be described simply as follows.

When the dangling bond density is small, the resulting local space charge density is also small, so that the space charge limited current mode no longer exists, and the field distribution is quite uniform. In this case, high reverse bias will wipe out nearly all the photogenerated carriers, ie the recombination process for bias light is not important. This also means that the carriers photogenerated by the probe light also have little chance to recombine, ie. the collection efficiency for probe light is close to unity only by itself. So that a much smaller photogating effect in this situation can still push the collection efficiency greater than unity.

Under this condition, the small component of space charge density (the amount is still comparable to the probe light photon flux) trapped in the relatively low field region will still play an important role when a low intensity probe light is applied. Under the same mechanism, the carriers from probe light will recombine with those trapped electrons and modulate the field so as to release considerable amount of electrons to contribute to the output current. Thanks to the high reverse bias, the recombination rate has been significantly reduced so that this small photogating effect can still be observed.

This result shows that the presence of a high reverse bias voltage and blue bias light are more important than just a high defect density in switching the device into photogating. In previous work, no reverse bias voltage was applied or only a forward bias voltage, in which case recombination plays an important role in reducing the collection efficiency for probe light, or even in diminishing this effect, especially when the effect is small. This may be the reason why a *QE* value larger than unity has been difficult to find. Also this is the reason, obtained in the present study, for the reduction in *QE* when the defect density is larger than an optimum value, - because of increased recombination. To conclude, the modification of the field is the only reason for this photogating effect, even though it can be caused by different sources.

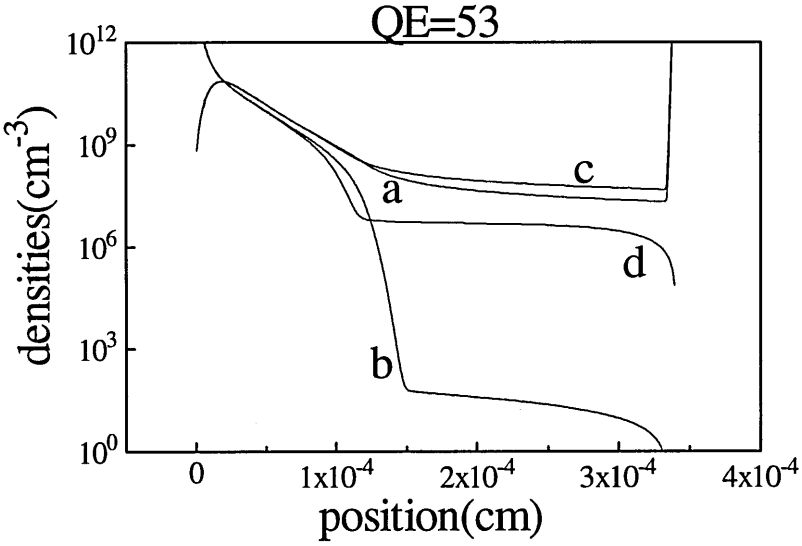

Fig 6.4 computer simulated electron and hole density distribution changes before and after the probe light is added. (a) electron density by bias light only, (b) hole density by bias light only; (c) electron density by bias and probe light; (d) hole density by bias and probe light.

Figures 6.4 and 6.5 show the spatial variation and relative change of electron and hole densities before and after the probe light is added. It can be seen that the electron density change is larger than the hole density change when the probe light is directed on the *n*-side. Figure 6.4 gives most clear pictorial evidence for the photogating effect, although the detail may vary in other operating situations. For example, when the defect density is low, the system can not enter the *SCLC* mode, and the relative change for holes can be a major part of the current increment. However, the photogating effect can still stand as we just discussed before.

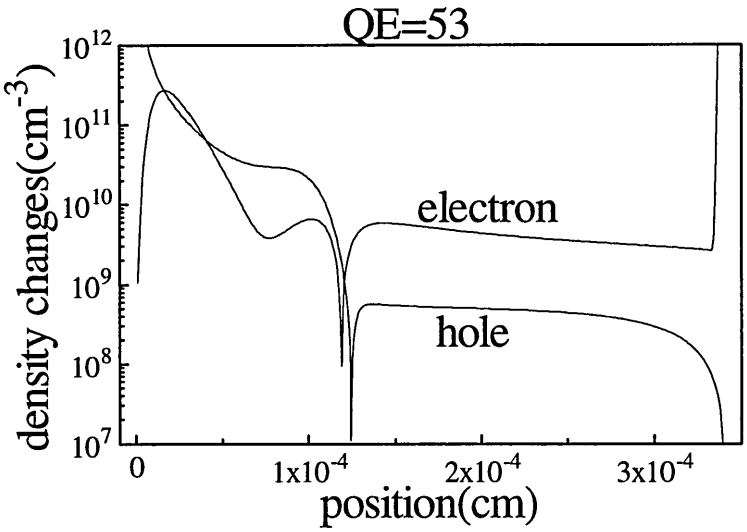

Fig 6.5 The relative change of electron and hole density distribution before and after probe light is applied. The left halves of the curves are negative i.e. reduced, and right halves are positive, i.e. increased

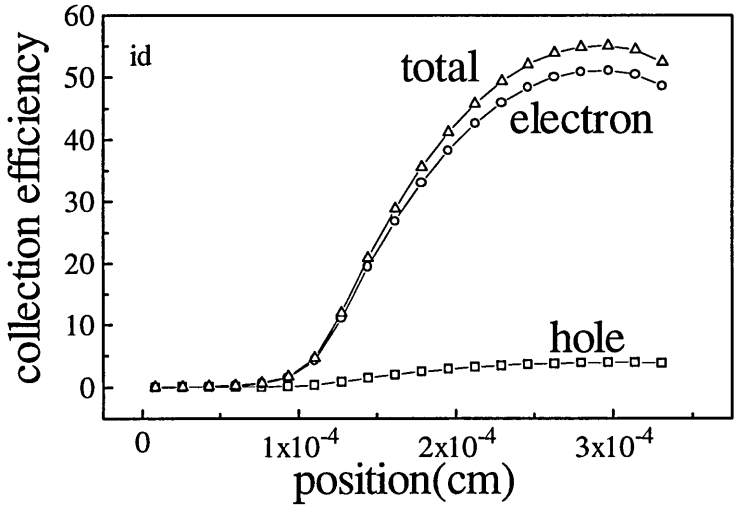

Fig 6.6 The internal collection efficiency distribution in the diode. The operating conditions are the same as in fig 6.5. The method called *IDEAL* has been described in chapter 5

Fig 6.6 shows the computed internal collection efficiency for the same conditions as in the experiment. We used the *IDEAL* method which will be described in Chapter 5 in detail. The fig 6.6 shows that the high *QE* value (external collection efficiency) in fig 6.2

is mainly contributed by electrons, which we have discussed before, and the most sensitive position (in terms of location of absorbed probe light) in the device is in the rear part, ie. the same change (i.e. generation rate) introduced by probe light in the rear part of the device will contribute more than a change in the front part of the device. The reason for this can be briefly described as follows:

When the probe light is added from the *n*-side, the high field existing in the device will sweep the photogenerated carriers to the two electrodes. At a position near to the *n*-side electrode, back diffusing electrons will recombine with the photogenerated holes, so that the contribution of electrons here to the photogating effect will be reduced by recombination loss. At the position near the middle of the device, since the internal field is significantly reduced by the existing reservoir of electrons, the photogenerated holes here will have more chance to recombine with photogenerated electrons from the probe light so that these holes will not contribute to the photogating effect. Finally, only the photogenerated holes not too close to the electrode and still in the high field region will successfully drift to the electron reservoir and contribute to the photogating effect.

6.2.4 Simulation results

The sample we used was not subjected to degradation treatment before the measurement, so it is assumed to have relatively low dangling bond density. Following previous work on this topic, it was believed that the midgap defect density plays an important role in this particular phenomenon, and that the effect would be more obvious when the midgap density increases. However, the computer simulation in this study gives a somewhat different answer.

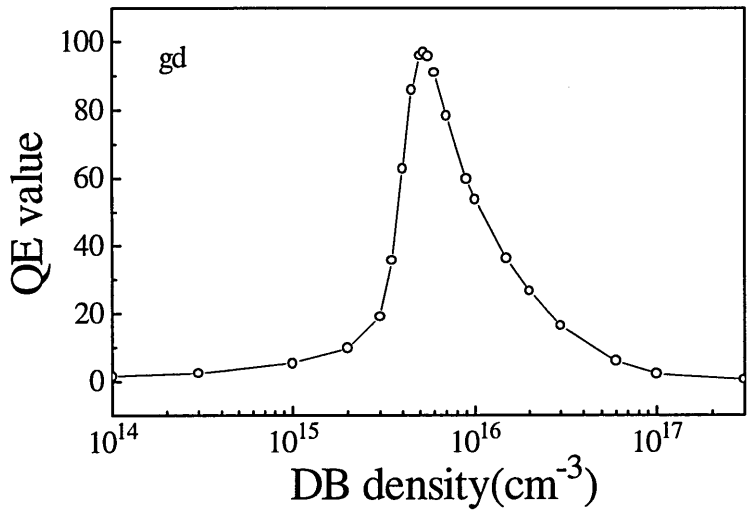

Fig 6.7 Computer simulation of Quantum Efficiency against dangling bond density under 10 volts reverse bias voltage with the same photon flux conditions as in the experiment except that the probe light photon energy is exactly 2.0*eV*.

Figure 6.7 shows the computer simulated *QE* value vs. dangling bond density plotted under the same experimental conditions as used in the measurements with 10 volts reverse bias voltage. A sharp peak can be seen at around $5\times10^{15}cm^{-3}$ dangling bond density, showing that the *QE* value has a high sensitivity to the dangling bond density. The peak *QE* value is close to 100, dropping down steeply when the dangling bond density changes, but it is still larger than unity even when the dangling bond density is very small ($1\times10^{14}cm^{-3}$) and also very large ($3\times10^{17}cm^{-3}$). Fig 6.7 also tells us there are two dangling bond densities which can give a *QE* value in agreement with the experimental value. The reason for this has been discussed in a previous subsection. However, in view of the expected dangling bond density value in this situation, we used $1\times10^{16}cm^{-3}$ as the value for dangling bond density in the rest of the simulation.

The computer simulation for blue bias light from *n*-side does not show such a strong photogating effect. Rubinelli (1994) did a similar plot for a Schottky barrier structure when the blue light is shining from the front contact. That plot showed a peak value of *QE* at $3\times10^{15}cm^{-3}$, but the peak value was only 2.6, and only between $10^{15}cm^{-3}$ and $10^{16}cm^{-3}$ was the *QE* value larger than unity. Beyond this, the *QE* value became smaller than unity. This result tells us that the mid-gap density can change the *QE* value significantly, but the bias light itself (wavelength, intensity) and the relative direction of illumination on the device are more important on determining the quantum efficiency in this kind of measurement. From figure 6.7 we now know that the *QE* value does not always increase when the mid-gap defect density increases. Instead, there is an optimum density value, which is the result of competition between the photogating effect and the recombination rate.

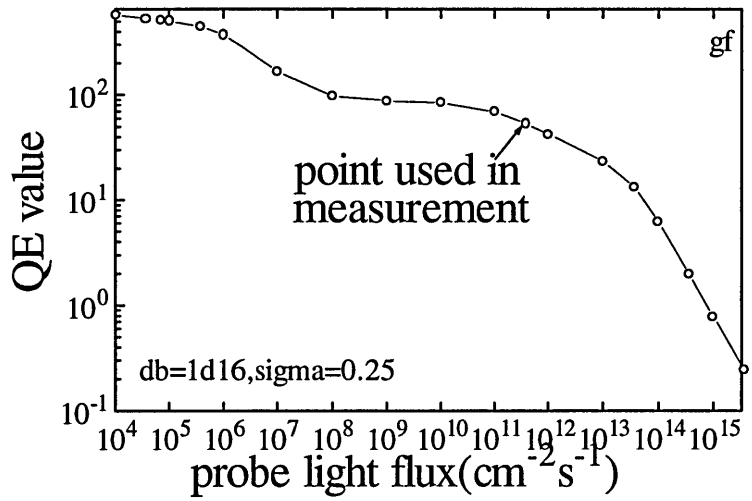

Fig 6.8 The computer simulation of *QE* value against the probe light photon flux The photon energy of probe light is 2.0*eV*. Other conditions are the same as in table 6.2.

Figure 6.8 is a plot of the *QE* value against the probe light photon flux. When the probe light photon flux is large, close to the bias light photon flux, the quantum efficiency value is small, showing that the small signal condition is not satisfied. When

the probe photon flux is reduced, the *QE* value increases, and when the value is small enough, the *QE* value approaches a plateau region indicating the satisfaction of the small signal condition. However, when the photon flux is reduced to even smaller values, the computed *QE* value increases again. The reason for this is not yet clear, but one possible reason is simply the numerical error arising when extremely small relative changes are made to the excitation. In fact, the probe excitation involved would be much too small to be measured in practice. It can be concluded that when the small signal condition is satisfied, the collection efficiency is independent of the photon flux of probe light showing a constant value down to a very low photon flux. This actually means the modulation of the electric field by probe light is proportional to the probe light photon flux in the small signal regime. When the photon flux of the probe light is larger than a certain value, the small signal condition is no longer satisfied, and the disturbance of the probe light is too large to keep the system steady, so the *QE* value drops. With further increase in probe beam intensity, the *QE* value becomes smaller than unity.

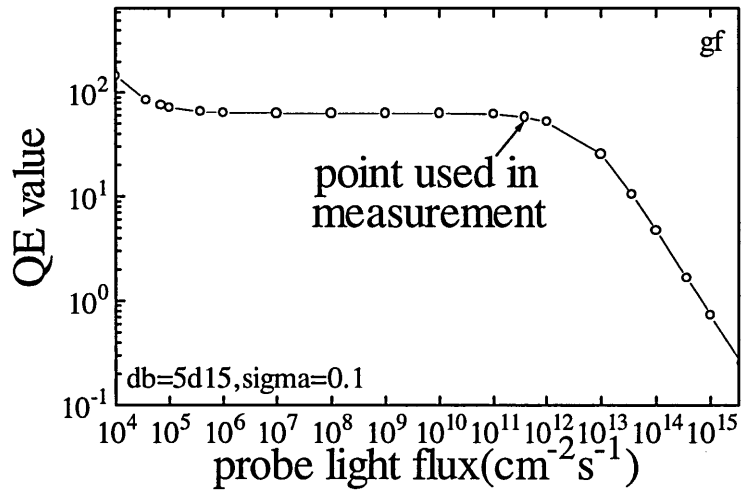

Fig 6.9 The same calculation as in fig 6.8 for different dangling bond distributions. This plot shows much clearer picture for the small signal condition criterion.

Fig 6.9 is the same calculation but for different dangling bond distribution. In fig 6.9, the plateau region is wider and flatter and the large signal regime shows a reduction following a power law straight line. The values used in this simulation (DB=$5\times10^{15}cm^{-3}$ and σ=0.1) are rather closer to the values often used in the past.

Figure 6.10 shows the relation of the collection efficiency against the photon energy of the bias light. It shows a peak at $2.1eV$ i.e. $590nm$ a yellow light. Through the analysis (details mentioned later), it is believed that the shorter the bias wavelength, the deeper the electron reservoir will be, so the photogating effect will be more obvious, i.e. higher *QE* value for probe light. However, when bias wavelength decreases, the absorption depth also decreases, so that the recombination loss in the heavily doped layer will increase. This may be due to the back diffusion of the holes which can not be collected by the front electrode due to the low field close to the front electrode. The

recombination loss reduces the amount of electrons in the reservoirs so as to reduce the photogating effect for probe light. Due to the compromise between the absorption depth and the recombination loss in the doped layer, there appears a peak in figure 6.10. Of course, this peak wavelength (590*nm*) only applies in this special case. For different samples, it may be a different value. When bias wavelength is longer than 636*nm* (1.95*eV*), the photogating effect disappears, and the *QE* value is smaller than unity.

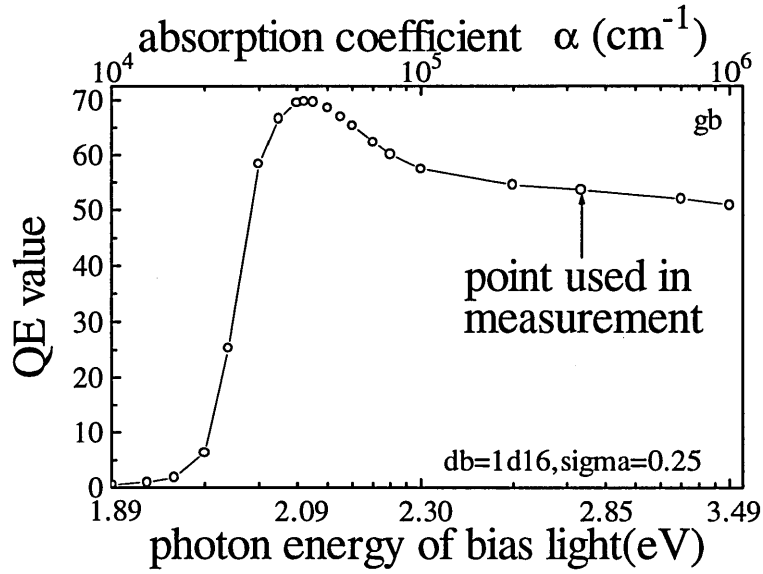

Fig 6.10 *QE* variation with the absorption coefficient of the bias light. The photon energy of the probe light is 2.0*eV*; other conditions are the same as in table 6.2.

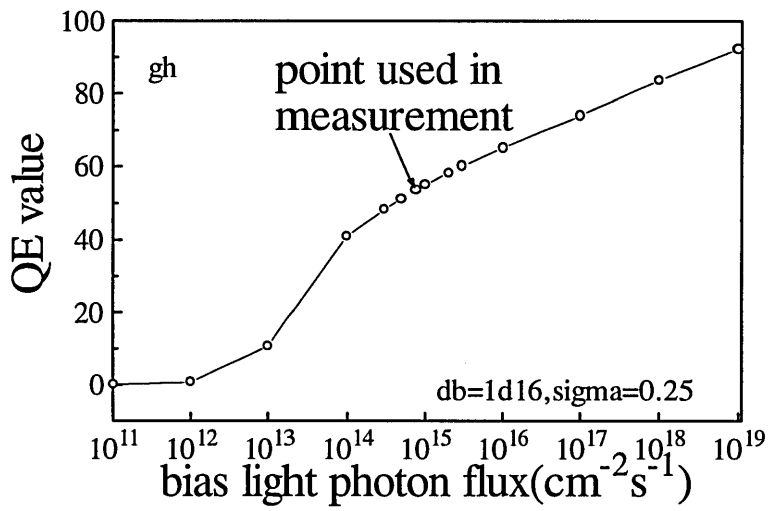

Fig 6.11 Computer simulation of the *QE* value against the photon flux of bias light. The photon energy of the probe light and bias light are 2.0 and 2.75*eV*, respectively, the remainder of the conditions are the same as in the experiment.

Figure 6.11 shows the relation between the *QE* value and the bias light photon flux. The whole curve can be divided into three parts. In the first part, when the photon flux is smaller than $1\times10^{12}cm^{-2}s^{-1}$, the *QE* value is smaller than unity, which implies that

the space charge limited current mode can not be established due to the small bias light photon flux and high reverse bias voltage. The second part, between 1×10^{13} to 1×10^{14} $cm^{-2}s^{-1}$, is a steeply increasing part, showing a quickly built up space charge so that the photogating effect has passed a threshold value. In the third part, above $1\times10^{14}cm^{-2}s^{-1}$, the *QE* value is linearly increasing with bias light photon flux, in the regime where the small signal condition (for the probe) is satisfied. Increasing the bias light photon flux increases the amount of electrons accumulated inside the reservoir, so that the photogating effect for the same probe light will proportionally increase with the bias light intensity.

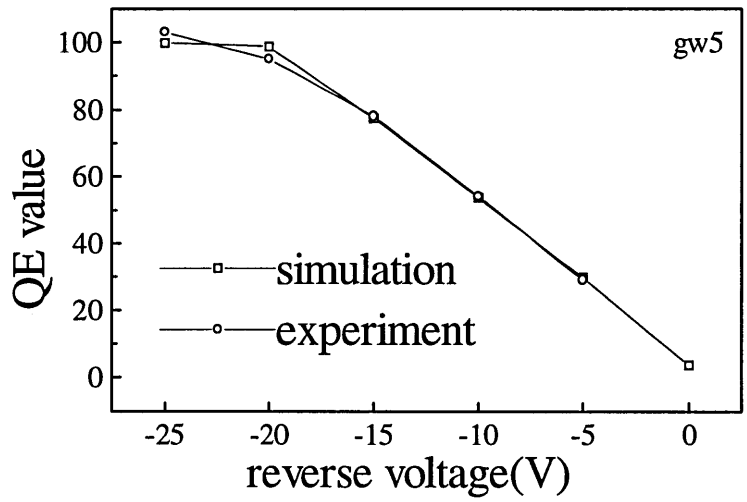

Fig 6.12 the computer simulation of *QE* value against the reverse bias voltage. This is the simulation of the actual measurement at a probe light photon energy of $2.0eV$. Dangling bond density is approx. $1\times10^{16}cm^{-3}$ and all the other conditions are the same as in the experiment and table 6.2.

Figure 6.12 shows the relation between *QE* value and the reverse bias voltage. This is also a test of the computer program we are using. It is seen that under the conditions listed in table 6.2, the simulation gives a good fit to the experimental data, especially at the lower bias voltages.

6.2.5 Conclusion

A detailed study of the photogating effect has been carried out, and a quantum efficiency very much larger than unity has been found both theoretically and experimentally, under reverse bias voltage conditions for the first time. Experimental results show the relation between the reverse bias voltage and the *QE* value, which can reach over 100 at high reverse bias voltage. From computer simulation, the reason for the photogating effects has been clearly demonstrated, including a linear relation between the photogating effect and the probe light photon flux. It was shown that the modification of the field is the only reason for this photogating effect, even though it can

be caused by different sources. The low field region plays an important part in determining the collection efficiency for the probe light, but it is not the most important factor, instead, in this study, high reverse bias and blue bias light make the *QE* value always larger than unity within the experiment conditions. The reverse bias voltage applied to the device helps to reduce the carrier recombination loss from bias light so as to achieve higher collection efficiency. Through computer simulation, a good match with experimental measurement is achieved by applying in the model, blue bias light from the *p*-side and green probe light from the *n*-side, and also, by changing the experimental conditions, the possibility of making the *QE* value even higher. This dual beam combination makes an optically controlled amplifier closer to practicable applications, and the high *QE* shows realistic possibilities for an optically controlled amplifier which may be useful in photodetection.

6.3 The controlling carrier problem

The controlling carrier problem has been a controversial issue for some time - *viz* - which carrier controls the charge collection in a solar cell ? The $\mu\tau$ as evaluated from the measurement of the collection efficiency of *p-i-n* under uniform illumination has been attributed by some researchers to the holes (believed to have the shorter drift length (for example, Chu et al 1989) and by others to the electrons (believed to have the longer drift length) (for example, Crandall et al 1989). Hubin et al (1992) derived their own closed form expression for the recombination function in steady-state illuminated hydrogenated amorphous silicon under some approximations and found that the limiting carrier in an *a-Si:H p-i-n* solar cell under reverse voltage should be either the one with the *longer* drift length when using the Shockley-Read-Hall (*SRH*) recombination formula or the one with the *shorter* drift length by using their own recombination expression. With the help of the numerical computer model, it is possible to have a clear conclusion on this question.

When describing the regional approximation approach, Crandall (1983) wrote in his paper: "It is common to make a constant recombination regime approximation in modelling the transport in *a-Si:H* and use $R=p/\tau_p$ over the entire *i* layer. A justification used for this approximation is the common assumption that, since the material is usually *n*-type and because the hole has a low mobility as well as a short lifetime, that the hole will have a short drift length and thus will determine the solar cell transport. This is a common misconception. Since the solar cell is a primary photoconductor it is actually the carrier with the longer drift length that determines the solar cell behaviour. This is because the charge induced in the external circuit is proportional to the distance a charge carrier moves before being trapped and eventually recombining. If the hole as assumed has the shorter drift length, then it does not contribute as much to the current as the electron. Since the electrons and holes recombine in pairs charge neutrality is preserved. There are just more trapped holes than trapped electrons".

In opposition to Crandall's conclusion, Hubin et al (1989) derived a closed-form approximate analytical expression for the recombination function in steady-state illuminated hydrogenated amorphous silicon, concluding that the limiting carrier in an *a-Si:H p-i-n* solar cell under reverse voltage is shown to be the one with the *longer* drift length when using the Shockley-Read-Hall recombination formula, or the one with the *shorter* drift length using the formula for dangling bond recombination used in their derivation.

Within this disagreement on the controlling carrier problem in charge collection, the concept needs to be clarified. In Crandall's statement, the carrier which contributes most to the output current is treated as the carrier which determines the solar cell behaviour. However, the issue in Hubin's paper is which carrier changes the behaviour more rapidly, and the analytical expressions in Hubin's paper give a clear definition of this problem. By using the *SRH* recombination equation, the collection function can be written as

$$\eta = 1 - \frac{L}{2} \times \frac{(l_n + l_p)(l_n - l_p) + 2 l_n l_p \ln(l_p / l_n)}{(l_n - l_p)^3},$$

when their own recombination equation is used the collection function is as follows,

$$\eta = 1 - \frac{L}{2} \times \frac{(l_n + l_p)}{l_n l_p},$$

where the terms are defined below.

However, when Hubin did the comparison between his simplified model and the more precisely derived *SRH* recombination formula, his result became less convincing since the *SRH* formula was derived subject to less simplifying assumptions and included all the trapping and recombination transitions (albeit assuming one-electron occupation statistics), while Hubin's derivation assumed no trapping and assumes most of the dangling bonds are in the neutral state. In any case, Hubin highlighted a possible discrepancy.

Based on these controversial results, we used the numerical method to investigate this problem, which is directly related to the carrier drift lengths (under reverse bias, diffusion is normally ignored) l_p and l_n. Analytically, the drift length is defined as

$$l_p = \mu_p \tau_p E$$
$$l_n = \mu_n \tau_n E$$

and $\tau = (\nu \delta N_n)^{-1}$ (see equation 3.1) is the general form for different lifetimes. The thermal velocity of the carriers is ν, δ is the capture cross section for different capture processes and N_n the recombination centre density.

In the present work, there is a computer program specially developed to deal with the charge collection problem which is described in detail in chapter 5. Basically, the

program will simulate the real quantum efficiency measurement processes, and will give out the external collection efficiency data.

6.3.1 Results

In the numerical modelling carried out, only the mobilities were changed to vary the drift lengths for electrons and holes. The other conditions are as follows:

Illumination from the *n*-side, photon flux $1\times10^{14}cm^{-2}s^{-1}$, and absorption coefficient set at $1\times10^{3}cm^{-1}$ to give $10\mu m$ absorption depth and so uniform excitation for the $0.5\mu m$ thin device under investigation. The *p*- and *n*-layers are $10nm$ each and the Fermi energy - band edge spacings set for the two doped layers are $0.35eV$ and $0.25eV$ for *p*- and *n*-side respectively, when the bandgap is 1.8eV. No bias voltage is applied. The dangling bond density used is $1.0\times10^{16}cm^{-3}$, uniformly distributed in the device, and the simple single energy defect model is used with the $D^{+/o}$ transition energy E_o and correlation energies U set to $0.8eV$ and $0.35eV$, respectively. The bandtail slopes are $0.025eV$ and $0.045eV$ for conduction and valence band tail states, respectively. The capture coefficients for electrons and holes by conduction band tail states is $1\times10^{-9}cm^3/s$ and $1\times10^{-7}cm^3/s$, respectively. For dangling bond states, the capture coefficients for neutral and charged states are also 1×10^{-9} and $1\times10^{-7}cm^3/s$, respectively. This set of parameters may not be the most suitable one, however, it is simple in order to clarify the question raised above.

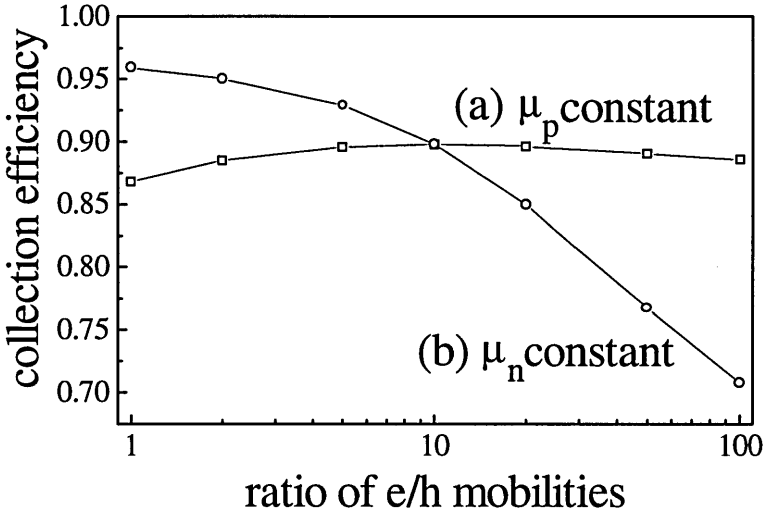

Fig 6.13 The relation between the collection efficiency of an *a-Si:H p-i-n* solar cell and the value of electron and hole mobilities under the uniform illumination. (a), when hole mobility is kept constant, (b) when electron mobility is kept constant. The electron mobility is always larger than or equal to the hole mobility.

Fig 6.13 shows the relation between the charge collection and the ratio of electron and hole mobilities. For curve (a), the electron mobility is varied between 1-100 $cm^2V^{-1}s^{-1}$ while the hole mobility is kept at $1cm^2V^{-1}s^{-1}$, and for curve (b), the hole mobility is varied between 0.1-$10cm^2V^{-1}s^{-1}$ while electron mobility is kept at $10cm^2V^{-1}s^{-1}$. It is

easily seen that when μ_n changes, even though the total collection length (defined as $(\mu_p\tau_p+\mu_n\tau_n)E$ the summation of the drift lengths of electron and hole) changes significantly due to the much larger value of μ_n than μ_p, the total collection efficiency does not change much, while when μ_p changes, even though the total collection length does not change very much, the total collection efficiency is subject to a large change. It is noticeable that when μ_p is getting very small (towards the larger value of the ratio μ_n/μ_p), the collection efficiency drops significantly.

From this result, we conclude that it is the carrier with the *shorter* drift length which determines the behaviour of *p-i-n* solar cells in collection efficiency measurements.

6.3.2 Discussion

Fig 6.14 shows recombination detail for a few cases from fig 6.13 when the mobility ratio is 1 (curves 1 and 4), 10 (curve 2), 100 (curves 3 and 5). The general trend is that the recombination rate is higher near the two interfaces. This is because the higher electron density near *i-n* interface and higher hole density near *p-i* interface make the D^- and D^+ dominant in these two region, respectively. Since the charged states have much higher capture coefficients than neutral states (in this model), the recombination rate even for this spatially homogeneous model becomes higher in these two interface regions than in the *i*-layer where D° is dominating.

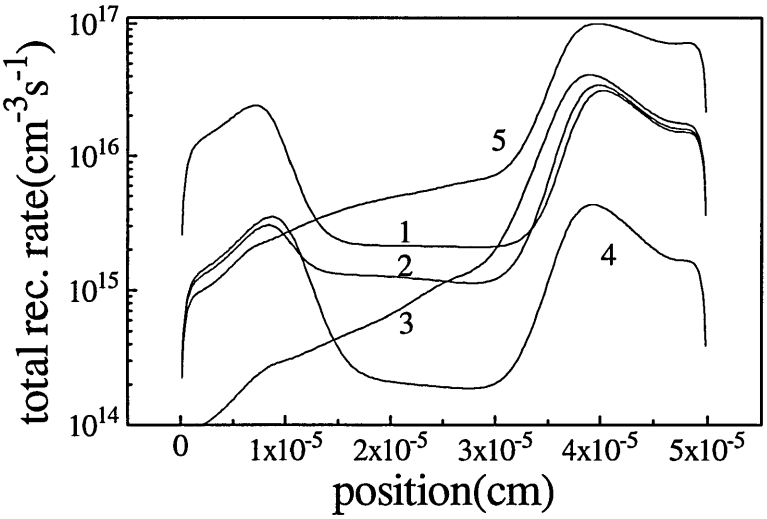

Fig 6.14 The total recombination rate for five different circumstances, (1) μ_n=1and μ_p=1; (2) μ_n=10 and μ_p=1; (3) μ_n=100 and μ_p=1; (4) μ_n=10 and μ_p=10; (5) μ_n=10 and μ_p=0.1. The unit of mobility is $cm^2V^{-1}s^{-1}$ On the figure, left - *p*-side, right - *n*-side.

When we look at curves 1 and 4, the mobility *ratios* are both 1, only the collection length for curve 4 is 10 times larger than for curve 1, and the recombination rate is relatively symmetrical, only the magnitudes are different. For curve 2, due to the difference of the mobilities between two carriers, the recombination rate near the *i-n*

interface is much higher than near the *p-i* interface. Since holes have the lower mobility, the hole density near *i-n* interface will be higher, and as a minority carrier, it increases the recombination rate due to its higher density. On the contrary, near the *p-i* interface, even though the hole mobility is low, it does not change the steady state captured hole density. Since the recombination rate is virtually determined by the minority carrier, and the electron density does not change much, so the recombination rate does not change much. Generally, when the electron mobility is kept constant, the recombination rate near the *p/i* interface is relatively stable when hole mobility is varied over a large range. On the other side, the recombination rate near *i/n* interface does not change much when the hole mobility is kept constant and the electron mobility is varied over a large range.

Actually, if we look at Fig 6.14 carefully, it can be easily spotted that when, for example, the electron mobility increases, the recombination rate drops on the left half (*p*-side), but, perhaps unexpectedly increases slightly on the right half, while the same thing happens when the hole mobility is changed. What is the reason for this?

The answer comes from the electric field distributions under these situations as shown in Figure 6.15. This plot shows that the electric fields in different situations are quite uniform, the difference between the field in the middle and near the edge being only a factor of 2 which is quite small. This proves that the "uniform field" assumption in many published analytical models is correct in this case. Reverse bias voltage is not yet applied. If it is, the field will be more uniform.

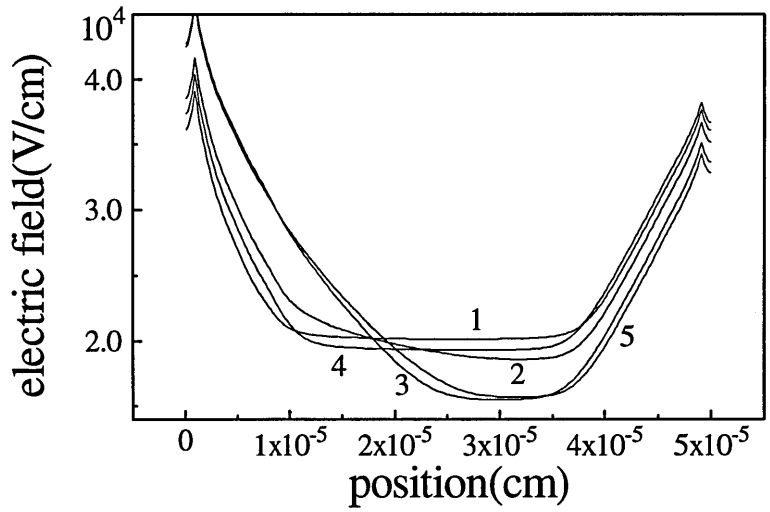

Fig 6.15 The field profile in different circumstances as in fig 3.26. (1) μ_n=1and μ_p=1; (2) μ_n=10 and μ_p=1; (3) μ_n=100 and μ_p=1; (4) μ_n=10 and μ_p=10; (5) μ_n=10 and μ_p=0.1. The unit of the mobility $cm^2V^{-1}s^{-1}$

However, the change of mobility does change the field to some extent. Basically, when the mobility ratio is increased from 1 to 100, the field in the *i*-layer decreases a little, in the area near the *i/n* interface, and increases on the left half in the area near *p/i* interface. The reason for this is that on the left half, since the hole mobility is relatively

small, the hole density will be relatively larger in this area, as the majority carrier, its increased density increases the total space charge which in turn increases the electric field in this area and screens the field on the rest of the device. On the other side, the change of the hole density has been mostly recombined since it is minority carrier on this side which does not change the system very much except the recombination rate. Following this argument, we can look at two different cases. The first one, in which electron mobility increases and hole mobility does not, the decreased electron density near the *p/i* interface reduces the recombination rate, which in turn increases the trapped hole density and increases the field there. Due to the reduction of the field near the *i/n* interface, the drift length for both carriers are reduced, and this causes the increase of the recombination rate on this side of the device. In the second case, for similar reasons, when the hole mobility reduces and electron mobility does not, the space charge density in the *p/i* interface area increases so that the field increases. This effect increases the drift speed of minority carrier electrons and reduces the recombination rate there.

6.3.3 Conclusion

By using our specially developed program, the charge collection measurement in *a-Si:H p-i-n* devices has been simulated. It has been clearly demonstrated that it is the carrier with the *shorter drift length* which controls the behaviour of the device, ie. the charge collection process is more sensitive to the change of the carrier with shorter drift length, *contrary* to Crandall's assertion.

6.4 Application to two or three dimensions

The present model (*SPIN.F*) used to simulate *a-Si:H p-i-n* solar cells is a one dimensional model which is good enough for large area thin film devices such as *a-Si:H* solar cells. The assumption is thus already made which is that the quantities involved in the modelling do not change laterally with respect to the dimension being considered, or on the other words, the lateral changes can be neglected. Under the same consideration, this one dimension model can also been used in some other cases which are not obviously one dimensional. For example, a coplanar structure is the central part of thin film transistor (*TFT*) and is very commonly used in photoconductivity measurements. In these devices, since the gap between source and drain is not infinitely wide compared with the thickness of the film, it cannot normally be treated as a one dimension device. However, in some cases, the change of quantities along the gap or channel, parallel to the surface are very small. The interesting feature of the device for its operation reduces to one of the cross section of the gap. In these cases, a one dimensional (normal to the surface of the film) approach can still be used which will simplify the problem

significantly and considerable computing time can be saved. The following is an example we used on the case of *n*-type *a-Si:H* photoconductivity (Main et al 1995).

The basis of the work reported here is an explanation of the dependence of photoconductivity σ_p on generation rate G in *n*-type doped *a-Si:H*. This dependency should possess the form of $\sigma_p \sim G^{\gamma}$, where γ is between 0.5 and 1 according to *'Rose'*s model (Rose 1963). From experimental measurements, a sublinear characteristic with exponent γ as low as 0.4 has been observed by many groups (see for example Main et al 1991). Additionally, the observation carried out in our laboratory shows that in a moderately doped material, this sublinear relation can hold for very low excitation - so low that the photoconductivity is several orders of magnitude below the dark conductivity.

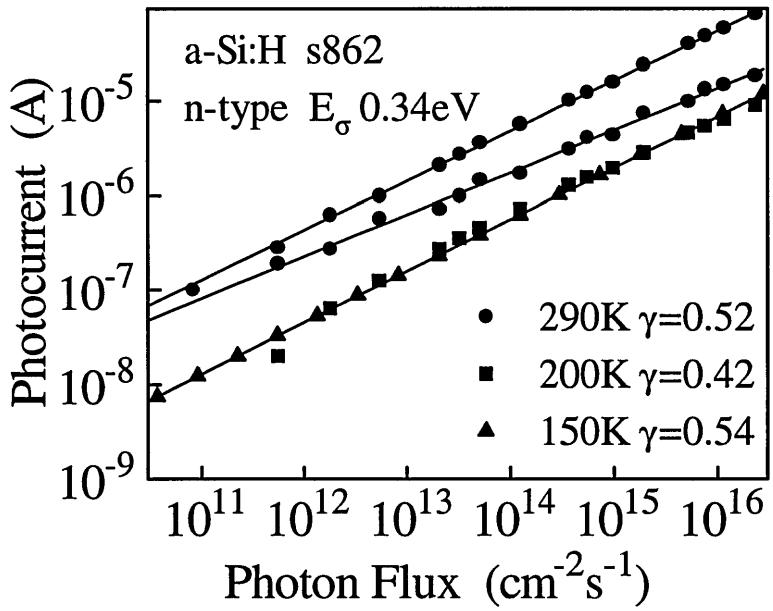

Fig. 6.16. Photocurrent vs Photon Flux plotted on a log-log basis for an *n*-type *a-Si:H* gap-cell, measured at three temperatures, 150°*K*, 200°*K* and 290°*K*. Film thickness 2μ*m*, E_s=0.34*eV*, applied field $10^3 Vcm^{-1}$

Figure 6.16 shows the measured steady state photocurrent vs photon flux for a moderately doped 2μ*m* thick *n*-type sample (E_c-$E_F \approx 0.34eV$) at three temperatures. It can be seen that the photocurrent-flux relation is sublinear, with γ close to 0.5 at 150°*K* and 290°*K*, and even less than 0.5 at an intermediate temperature of 200°*K*. Also the figure shows that at 290°*K*, the sublinear relation holds for photocurrents some orders of magnitude below the dark current.

Numerous explanations of sublinear photoconductive behaviour in *a-Si:H* have been published (for example Balberg and Lubianiker 1993), and include variations on the classic *'Rose'* model, bimolecular recombination, and the influence of surface defects and surface band bending. They cannot explain the result found in our laboratory, and a new model needs to be found. The *'Rose'* model uses a simple relation between the tail-

trapped electron density and the free electron density and leads to the a well known result

$$\gamma=T_c/(T+T_c),$$

where T_c is bandtail slope. In this model, the transition between linear (γ=1) and sublinear (γ=0.5) dependence happens at $\delta n \approx n$.

Since the simple '*Rose*' model does not explain the experimental result, several authors (for example Solomon and Brodsky 1980) have invoked the effects of band-bending at surfaces to explain sublinear photoconductivity in *n*-type *a-Si:H* and in *TFT* structures. An upward shift of the Fermi-level at the surface caused by surface charge or a surface layer with high defect density will produce a field which separates photo-generated charges, increasing effective lifetimes. Reduction in the height of this band bending by increasing excitation will lead to sublinearity. Fornarini et al. (1991) also find that in thin films ($\leq 0.5\mu m$ thick) the exponent γ remains low for reduced excitation such that $\delta\sigma < n_o$.

In the following part of this section, we attempt to use the modified program to simulate this special case, to explain the observed sublinear photoconductivity phenomenon in this *n*-type *a-Si:H*. In order to do this, several assumptions need to be clarified first.

6.4.1 The description of the model

In order to apply the modified one dimension model to a *TFT* structure, the structure of the model device and the boundary conditions all need to be adjusted.(for the details see chapter 5)

(1). Zero current criterion

When the direction normal to the device free surface is under investigation, the total current along that direction must be constantly zero, ie I_{total}=0. This is true in the *TFT* device and is a strict condition for the one dimension model.

(2). Boundary condition

We can write

$$\varepsilon_{sem}\left.\frac{\partial\psi}{\partial m}\right|_{sem} - \varepsilon_{ins}\left.\frac{\partial\psi}{\partial m}\right|_{ins} = Q_{int} \qquad (6.1)$$

where ε_{sem} and ε_{ins} are the relative permittivities of the semiconductor and the insulator, and Q_{int} is the interface charge density. $\partial\psi/\partial m$ is the gradient of the potential ψ along the direction normal to the interface.

To deal with the interface, the law of Gauss (see Selberherr 1984) in differential form must be obeyed. This in a general form involves semiconductor and insulator, but if

only the semiconductor is involved, the second term on the left hand side of the equation can be omitted, ie.

$$\varepsilon_{sem} \left. \frac{\partial \psi}{\partial m} \right|_{sem} = Q_{int} \tag{6.2}$$

If the ideal case of free surface with no surface charge is under investigation, the right hand side of the equation can also be omitted, ie.

$$\varepsilon_{sem} \left. \frac{\partial \psi}{\partial m} \right|_{sem} = 0 \tag{6.3}$$

(see Selberherr 1984 for details). In our simplified model, there is no insulator layer between surface and semiconductor layer, and also since there is no total current across the device, equation 6.2 will be satisfied automatically.

We attempt to simulate the surface charge effect according to the band bending model proposed by Solomon (Solomon and Brodsky 1980) and Fornarini (1991) which includes the involvement of a charged surface layer which bends the bands upwards, or downwards, so that the photogenerated carriers can be separated spatially by the built-in field so reducing the recombination rate.

6.4.2 Simulation and result

The simulation uses the *p-i-n* model already developed, replacing the layers with a homogeneous *n*-type film. The end-electrodes with thermal equilibrium boundary conditions as before, are retained in the model but two interior planes are used to represent the actual film surfaces. Thin charged or defective layers are inserted at these two interfaces to set up field and current conditions at these *internal* boundaries to represent the film surface conditions described above. The region within the internal boundaries is the cross section of the device; the regions outside are "dummy" regions, ignored in the results.

In order to make sure there is no total current in our one dimension model, at first the thickness of the *n*-type doped semiconductor has to be roughly doubled so that the end electrode boundary conditions will not influence the situation near the internal interfaces. Then heavily doped *p*-type thin layers are inserted into the position of the internal interfaces at 1/4 and 3/4 of the sample thickness so that a n^+-p^+-n^+-p^+-n^+ structure is formed. The Fermi-levels for these layers are set at $0.3eV$ and $1.48eV$ for n^+ and p^+ below the conduction band edge, respectively, in order to get roughly $0.3eV$ band bending at the (internal) surfaces. The thickness of these inserted layers is $10nm$ The results based on this structure are shown on the (a) series plots in the following figures. The other set of simulations which modelled more general asymmetrical circumstances

are shown in the (b) series of plots in the following figures representing the structure of n^+-n-n^+-p^+-n^+. The difference between series (b) and series (a) is that instead of inserting two identical thin layers, one of the inserted thin layer is not p-type, instead, is weakly doped n-type *a-Si:H* material. The Fermi-level for this layer is set at $0.5eV$, which will cause smaller (and hence asymmetrical) bandbending. These comparisons in the following figures will demonstrate the general suitability of the present one dimension model.

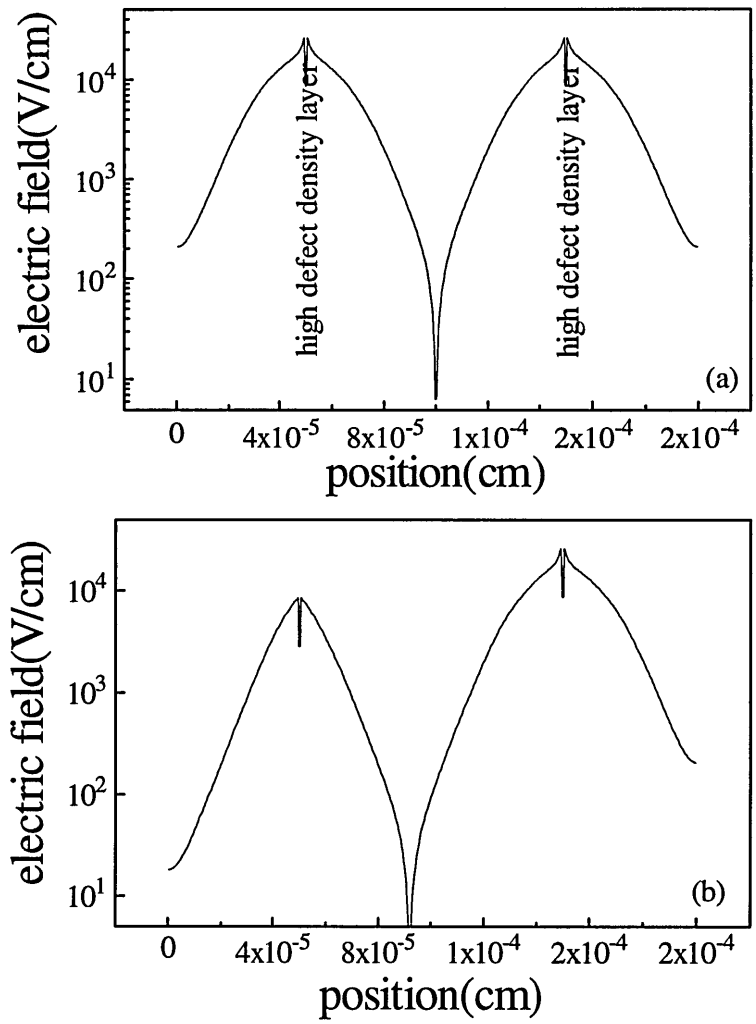

Fig 6.17 Spatial variation of electric field in the n^+-p^+-n^+-p^+-n^+ (a) and n^+-n-n^+-p^+-n^+ (b) one dimensional structures. Fields directed from centre and outsides towards inserted p-layers separate the photogenerated carriers to enhance the photoconductivity. In either (a) and (b), there is a low field point where the internal fields change directions.

Other conditions of the simulation are as follows: photon flux, $10^{14}cm^{-2}s^{-1}$; absorption coefficient $\alpha=10^2$ which equivalent to photon energy of $1.59eV$, or $780nm$ wavelength. The generation rate based on this condition is $10^{16}cm^{-3}s^{-1}$ uniformly distributed accross the device. The band gap is $1.8eV$ and densities of states at the two bandedges are $2\times10^{21}cm^{-3}eV^{-1}$. The bandtail slope of conduction and valence bandtails are 0.025 and $0.045eV$, respectively. A spatially homogeneous dangling bond density of $10^{17}cm^{-3}$ is used for the n-doped material. The $D^{+/o}$ transition energy E_o and correlation

energy U are 0.8 and $0.35eV$ respectively. The capture coefficient for electrons by conduction band tail states is $10^{-9}cm^3s^{-1}$ and the ratio of capture coefficients between charged and neutral state is 1 for bandtail states and 10 for dangling bond states; the operation temperature is $300°K$.

The above geometrical arrangement will satisfy the required boundary and operation conditions. Fig 6.17 is the electric field distribution in this model. Detailed investigation near the highly doped thin layers shows that the field possesses good symmetry about the central line of the doped thin layer so if the thin layer is treated as a surface layer, equation 6.2 can be easily satisfied. In this case, the surface charge density given by eq. 6.2 is $2.0\times10^{11}cm^{-2}$, the electric field will be $3\times10^4V/cm$. In the model, the doping density used in the thin layer is $2.36\times10^{17}cm^{-3}$. This doping density times $10nm$ the thickness of the layer, gives effectively $2.36\times10^{11}cm^{-2}$ surface charge density which is very close to the value obtained from equation 6.2. If the central line of the doped layer is used as a free surface, equation 6.3 can also be applied.

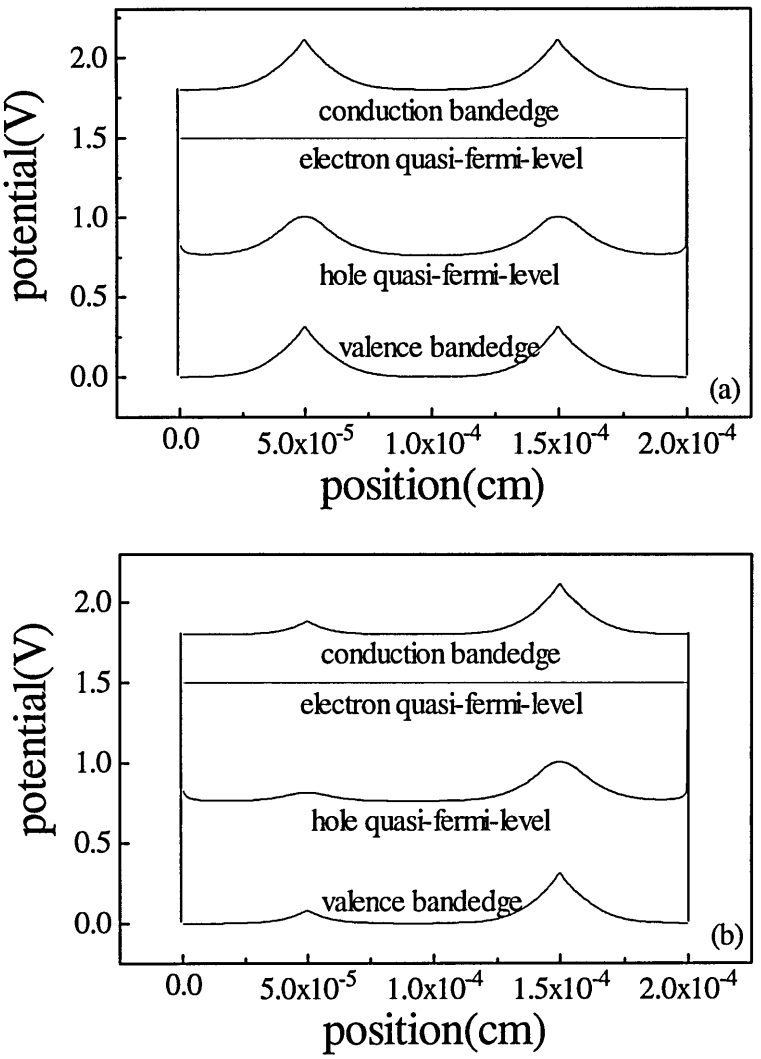

Fig 6.18 Spatial variation of energy profile in n^+-p^+-n^+-p^+-n^+ (a) and n^+-n-n^+-p^+-n^+ (b) one dimensional structures. Due to the heavily doped p-layers at the 1/4 and 3/4 position in (a) case, the upward band bending is about $0.25eV$. In case (b), at 1/4 position, the band bending is smaller correspondence with the weakly doped n-layer.

Due to the band bending, the field is directed towards the two p-layers and so separates the photogenerated carriers so as to reduce the recombination rate. In fig 6.17(b), the weakly doped n-layer also forms a depletion region with the adjacent n^+-layer, and there is still a field symmetrically about the layer, although the field strength is less compared with the p^+ layer as expected. It is easily seen that in this more general case, the boundary conditions mentioned above are still valid. The total trans-section current computed for the (a) case is $1.9\times10^{-11}A$, while in (b), it is $2.37\times10^{-11}A$, so small that it can be neglected (i.e. the zero-current boundary condition is held).

Figure 6.18 shows the band bending plot for this one dimensional model. The two figures just demonstrate the band bending situation corresponding to the insertion of the thin layers of different doping densities. It can be seen that when the outer boundaries used in the simulation are far away from the inner boundaries and the area of interest, and the potential at the two outer boundaries is set to be the same, then the $I_{total}=0$ condition will be automatically satisfied. When the n-type material used in the three zones is identical, the band bending about the inserted layer is symmetrical. We interpret this to mean that the outer electrodes and dummy layers do not affect conditions in the area of interest, so the model will be valid to simulate the real film in this simplified form.

Fig 6.19(a) shows the spatial conductivities under light and dark condition. This figure only plots the part of the device of interest, between the interior boundaries. In the dark, the conductivity is dominated by electrons in the middle of the sample. Near the p-layer boundaries, the depletion region depletes the free electrons so that the conductivity drops to a very low value. Under uniform illumination, if the generation rate is not very high, the relative change of electron density in the middle of the sample is not very large, so the photoconductivity due to the photogeneration is still smaller than dark conductivity. Also due to the low field in the middle of the sample, the recombination rate here is still high showing a trough in the middle of the plot. This is a low generation case and is located in the linear part of the photoconductivity versus generation rate profile.

Figure 6.19(b) shows the other case where there is only a lightly doped n-layer inserted on the left, which obviously will not form a strong electric field to perform the separation of the photogenerated carriers, so that the recombination rate is high on the left, causing a reduction of the photoconductivity. However, in the dark, due to the incomplete depletion on the left, the dark conductivity on the left is larger than on the right where the depletion due to the insertion of a heavily doped p-layer is quite complete.

Fig 6.20 shows the charge occupation distribution in different states for the two cases. It shows that D^+ density in the n-type material layer is very low except close to the p-type surface layers. The hole density also low even near the p-type surface due to the depletion, and so is the valence bandtail state trapped charge. Curve 5 shows the effect of depletion on the D° states. Near the p-layer, due to the depletion of the free carriers,

the D° density of states increases significantly to a high value, surpassing D^{-} states at the surface.

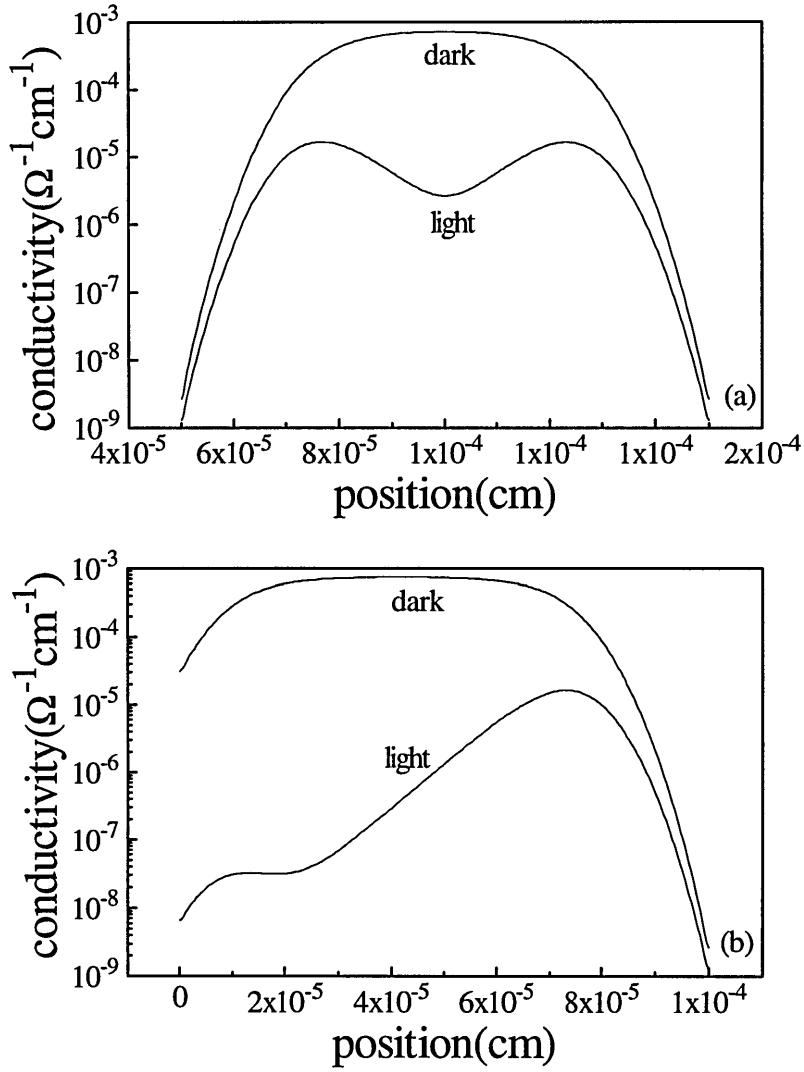

Fig 6.19 The spatial distribution of the photoconductivity of the sample with heavily doped *p*-layers on the surface. (a), symmetrical case and (b), unsymmetrical case. Compared with the figs 6.17 and 6.18, this is only the plot for the inner part between 1/4 and 3/4 of the whole structure.

Conduction bandtail state charge and free electron density are all high in the middle of the sample, but the doubly occupied D^{-} state density is much higher than any other states. Curve 4 shows the total net charge density distribution accross the sample, revealing a very high charge density in the inserted thin layers, decreasing a lot towards the middle of the sample meaning that the depletion region is not fully extended.

Fig 6.21 shows the simulated photoconductivity against generation rate plot. It is seen that the turn over point is around 10^{16} to 10^{17} $cm^{-3}s^{-1}$ generation rate at which the photoconductivity is somewhat lower than the dark conductivity but is much higher than observed experimentally.

It is perhaps not surprising that the result can not explain the experimental result because this model is a quite simple realization of the band bending model used by other authors. It does show that this model can get similar results to the ones other authors have obtained, and it works the same way as the other models do. It means the one dimensional model to some extent can be used on two or even three dimensional devices under certain circumstances using acceptable assumptions.

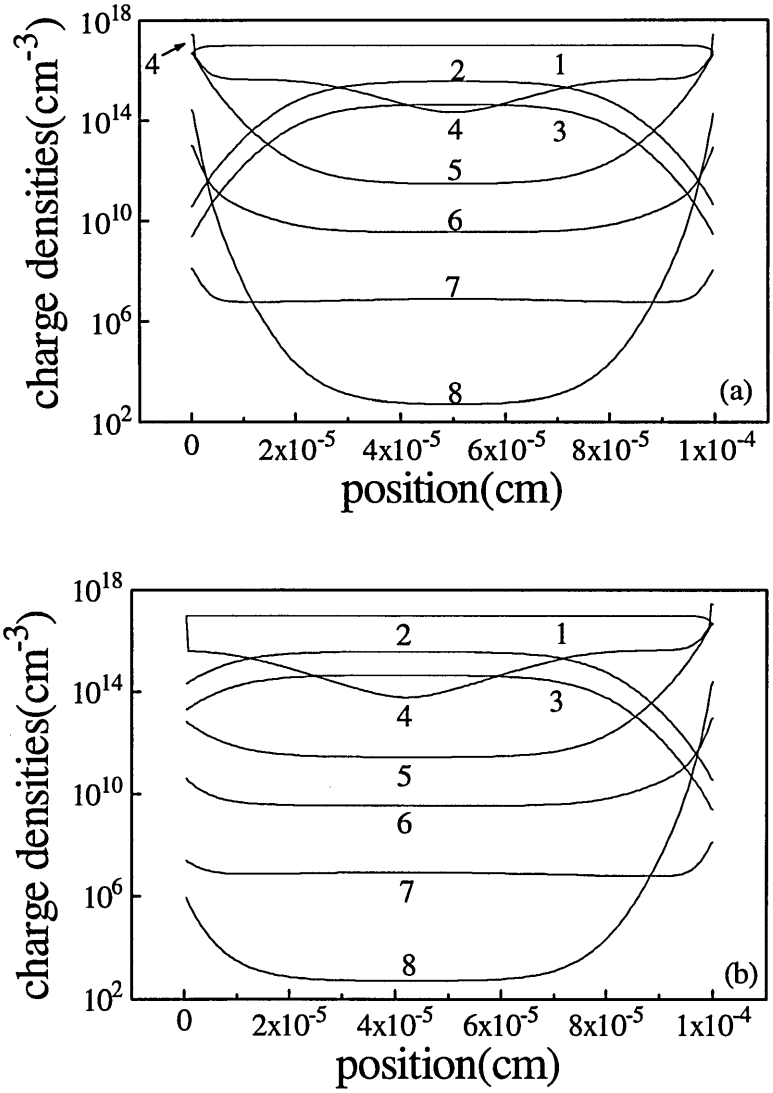

Fig 6.20 The space charge distributions (1) D^- states, (2) Conduction band tail, (3) Electron density, (4) Total space change, (5) D° states; (6) Valence bandtail; (7) Hole density; (8) D^+ states. Note the x-axis, this is only for the 'real' device itself between 1/4 and 3/4 of the whole structure. fig 6.20 (a) is for n^+-p^+-n^+-p^+-n^+ and (b) for n^+-n-n^+-p^+-n^+ one dimensional structures, it is noticable that in (b) the peak positions of all the charged states are moved towards the left hand side, showing the effect of unbalanced inserting of the doped layers.

The simulation results shown above use a surface charge approach to get band bending, another approach increases the defect density in those thin layers, and this is also easy to realize in the program.

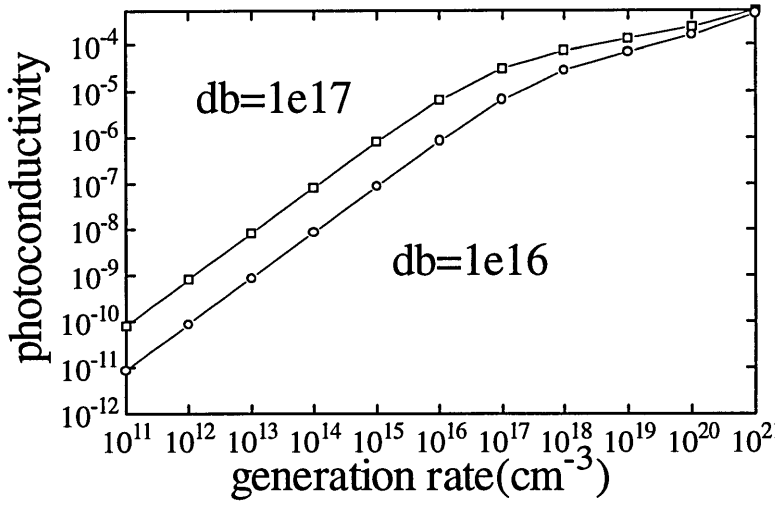

Fig 6.21 The photoconductivity verses generation rate at two different dangling bond densities. It is seen that the linear to sublinear transition happens at $10^{17}cm^{-3}s^{-1}$ generation rate when the photoconductivity is about $10^{-5}\Omega^{-1}cm^{-1}$.

6.4.3 Conclusion

A modified one dimensional computer model was produced by using a special device structure and boundary. It was shown that the model can sucessfully simulate a two dimensional case of surface band bending effects and give usable results. However, since it does not fit the experimental results observed in our laboratory, the details of model still require attention.

6.5 Summary

In this chapter, the program *SPIN.F* is used for several different situations. It is found that the program is a useful tool for investigating transport in *a-Si:H* solar cells or other devices.

A detailed study of the *photogating* effect has been carried out, and a quantum efficiency much larger than unity has been found both theoretically and experimentally. Experimental results show that the *QE* value can reach over 100 at high reverse bias voltage. From computer simulation, we verified that the modification of the field is the main reason for the photogating effect, even though it can be caused by different sources. The low field region in the device plays an important part in determining the collection efficiency for the probe light, but its existence is not the most important factor, instead, in this study, high reverse bias and blue bias light make the *QE* value always larger than unity within the experimental conditions. Reverse bias voltage applied to the

device helps to reduce recombination loss of the bias light produced carriers and also those from the probe light so as to achieve higher collection efficiency. Through computer simulation, a good fit has been achieved to the experimental results over the whole bias voltage range. The combination of blue bias light from *p*-side and green probe light from *n*-side under high reverse bias makes an optically controlled amplifier closer to practical application, and the high *QE* shows possibilities for optically controlled amplifiers which may be useful in photodetection.

By using numerical modelling, the "controlling carrier type" problem has been solved. During the charge collection measurement, under reverse bias voltage, or short circuit conditions, it is the carrier which has the *shorter* drift length which controls the behaviour of the device, (contrary to Crandall's assertion) and it is the hole in this case. A detailed analysis of this issue was carried out showing a clear picture of the transport and recombination processes occurring during the measurement.

Finally, an attempt to use a one dimensional computer model on two or three dimensional semiconductor devices has been made, the application being the sublinearity of photoconductivity in *n*-type *a-Si:H*. Even though the result still can not explain the experimental result, it demonstrated the consistency of this model with similar models proposed by other authors. The validity of this approach has been demonstrated and it may by used to solve the real problem after some modification.

Summary and conclusions

Computer source codes have been developed during the course of the study. The major program *SPIN.F* deals with the steady state electronic processes for amorphous semiconductor material and devices under different circumstances. It uses Shockley-Read-Hall statistics to deal with trapping and recombination processes via exponential bandtail states, and uses modified statistics to deal with the amphoteric dangling bond defect states in the midgap. Three defect distribution models have been incorporated in the program; single energy defect model, Gaussian distribution of defect density and the defect pool model. The computer model also allows several spatial variations for the defect states. Special care has been taken in the current calculation to obtain the highest accuracy. The device can be divided uniformly or nonuniformly, and it is also possible to define the number of slices in the doped layer manully.

The model outputs many internal and external characteristics of interest. *Spatial distributions* are computed, including band and Fermi-energy, electric field, free electron and hole densities, space charge densities, carrier life times, drift and diffusion lengths, recombination and generation rate and others. *Energy distributions* are also computed, including band tail distributions, and dangling bond distributions including 3-component defect pool model. External output includes the simulation of *I-V* characteristics (also including short circuit, maximum power and open circuit options), collection efficiency measurement and quantum efficiency measurement. These allow a range of functions for users for different purposes.

Accuracy tests on the *SPIN.F* program have been carried out. We have demonstrated the variation of many internal properties (field, lifetime and recombination rate etc) and external (*I-V* characteristics) properties when parameters such as the capture coefficients are changed. Also demonstrated are the variations under dark and light conditions, reverse and forward bias voltage for thin and thick devices. This testing gives us an overview of the capability of the computer program and demonstrate that it is a robust program fit to carry out simulations and calculations under different operating conditions. It should be helpful for further applications in amorphous semiconductors.

A detailed description of the defect pool model and its simulation has been done. After several basics test on this model, the effects of parameters such as the defect pool width and correlation energy have been shown. The original model parameters have been proved not suitable in application to the *p-i-n* diode. The reason for this is simply that the sensitivity of the dangling bond density on the Fermi-level position is overestimated, resulting in far too high a defect density near the doped layers giving a very inferior performance for the simulated *p-i-n* diode. A modification to the defect pool expression, changing the effective number of hydrogen atoms involved in defect formation kinetics is shown to give a substantial improvement. When comparing various defect models' fit to

p-i-n diode *I-V* characteristics the best fit is now found for the modified defect pool model.

The computer simulation and error testing of the *SVD* algorithm used in the *DICE* method have been carried out. The *DICE* method is proved still to be a useful approach to investigate the inner characteristics or processes inside semiconductor devices on the condition that some data treatment has been done to reduce the error introduced during the spectral response measurement (for example, polynomial fitting to the *QE* measurement data or computer controlled measurement). Computer modelling reveals that the error incurred in spectral response measurement seriously affects the resolution of the final results. By minimising the error either from the measurement or from the calculation, the accuracy of the final *DICE* profile may be controlled within several percent. However, the *DICE* profile can only give the general tendency of collection properties at low resolution. Many of the more detailed features may be artefacts because of the errors produced during the *SVD* solution.

A detailed study of a photogating effect has been carried out, and a quantum efficiency much larger than unity has been found theoretically and experimentally, for the first time under reverse bias voltage conditions. Experimental results shows the relation of *QE* value with the reverse bias voltage, which can reach over 100 at high reverse bias voltage. From computer simulations, the origin of the photogating effect has been clearly demonstrated. We showed that the modification of the field is the reason for this photogating effect, even though it can be caused by different sources. The low field region produced by strongly absorbed bias light plays an important part in determining the collection efficiency for the probe light, but it is not the most important factor. Instead, in this study, high reverse voltage bias and blue bias light make the *QE* value always larger than unity within the experiment conditions. The reverse bias voltage applied to the device helps to reduce the carrier recombination loss from bias light and also from probe light so as to achieve higher collection efficiency. Through computer simulation, a good fit has been achieved with the experimental results, and larger than 100 *QE* values can be achieved under 25volts reverse bias voltage. The combination of strongly absorbed blue bias light from the *p*-side and green probe light from the *n*-side under high reverse bias gives optimum *QE* gain, and raises the possibility of an optically controlled amplifier which may be useful in photodetection. It is also shown by modelling that the *QE* is a sharply peaked function of defect density.

By using numerical modelling, a recently debated question regarding the carrier type controlling collection in a solar cell has been solved. During charge collection measurement, under reverse bias voltage, or short circuit condition, it is the carrier which has the shorter drift length which controls the behaviour of the device. A detailed analysis on this issue was carried out, showing a clear picture of the transport processes occurring during the measurement.

It has been demonstrated that the one dimensional computer model developed in this work can be applied to two or three dimensional situations under certain symmetry conditions. The method is applied to investigate the effects of surface states in coplanar photoconductivity in *n*-type *a-Si:H*. Although the model does not fully explain the experimental results, it demonstrates the consistency of this model with similar models proposed by other authors, and proves the validity of the approach.

Appendix 1 Command file and source code of SPIN.F

0.6,0.3	Fermi-levels at two boundaries
1d-6,1d-6	thicknesses of two doped layers
0	bias light photon flux
5d3	absorption coefficient for bias light
1	side bias light directed to. 1 for left 2 for right
0	probe light photon flux
2.4d4	absorption coefficient for probe light
2	side probe light directed to. 1 for left 2 for right
5d-5	thickness of the device(include doped layers)
0,0	relative thickness of the transition layers
1.9	bandgap
2d21	bandedge density of states
299	operational temperature
0.025	slope of conduction bandtail states
0.036	slope of valence bandtail states at zero temperature
3	choice for DB distribution. 1 single energy, 2 Gaussian, 3 defect pool
500	frozen-in temperature in defect pool model
1.27	peak position of the defect pool in defect pool model
5d21	hydrogen density in a-Si:H material
1	number of hydrogen atom involved in the reaction(1/2)
1d16	dangling bond density
0.8	energy for Do states(used in single and Gaussian)
0.2	correlation energy(used both in all defect models)
0.16	pool width(used in defect pool model)
3	spatial distribution of DB(not in defect pool model)
10,3,1,3,10	five levels for five level distribution of DB
1d-6,5d-6,1d-5,5d-6,1d-6	thicknesses of five divisions of the device
10,0.1	two parameters in function option of DB distribution
10,1	mobilities of electron and hole
1d-8	capture coefficient of electron by CBT states
0	reflection ccoeffiicent of the back electrode
1	ratio of electron and hole at a CBT state
2	slice distribution choice, 1 uniform, 2 nonuniform
5	the number of slices in doped layer
2	operational choices, 1, chort circuit, 2,any bias,
3,	open circuit condition, 4 maximum power point and 5 I-V curve
0	bias value(volt)
-1,1	voltage range in I-V curve(volts)
40	number of point in I-V curve(no more than 50)
piw16	output file name(5 characters)

```
STEADY STATE PHOTOCONDUCTIVITY OF A PIN SOLAR CELL

jnl is number of spatial slices, inl is the number of energy slices Isl is the number of
energy slices for Gaussian distribution of dangling bond states
REMIND YOU THE jnl+1 HAS TO BE DIVISIBLE BY 30 IN ORDER TO
GET THE BEST OUTPUT RESULTS FOR THREE DIMENSION DEFECT
POOL PLOT

      PARAMETER(jnl=149,inl=30,Isl=20)
      IMPLICIT DOUBLE PRECISION (a-h,k-y)
      CHARACTER*24 title,yaxis,xaxis,pref*5,name*3,yopt*3

C Characters are all used for output data

      DIMENSION Vol(50),Zc(50),Zv(50),gc(inl),gv(inl),n1(inl),Ran1(inl),
     +     p1(inl),Rd1(inl),Rdn1(inl),Revb(jnl-1),B(jnl-1),Cur(50),
     +     Diag(jnl-1),Recb(jnl-1),Ra1(inl),Redp(jnl-1),Sub(jnl-1),
     +     Sup(jnl-1),dx(jnl),G(jnl-1),Re(jnl-1),ide(2),Efn(0:jnl),
     +     Ef(jnl),RJ(jnl),RJn(jnl),RJp(jnl),RJpdr(jnl),RJpdi(jnl),
     +     RJndr(jnl),RJndi(jnl),Dope(0:jnl),Redn(jnl-1),TL(0:jnl),
     +     Efp(0:jnl),Psi(0:jnl),n(0:jnl),p(0:jnl),ZnE(jnl),ido(9),
     +     Zg(6*(jnl-1)),Zxg(8*(jnl-1)),idon(5),idoe(8),Znj(7*jnl),
     +     Zxe(7*jnl),Zf(0:4*(jnl+1)-1),Cdp(jnl-1),Gd(0:jnl),iv(2),
     +     Zdb(0:jnl),Cdn(jnl-1),Zl(4*(jnl-1)),Zt(2*(jnl-1)),ib(2),
     +     DBm(Isl),DBn(Isl),Zed(6*Isl),Zdx(6*Isl),DBp(Isl),igc(3),
     +     Cct(jnl-1),Cvt(jnl-1),idg(7),Zxp(30*inl),iidb(7),idl(5),
     +     Zx(0:4*(jnl+1)-1),Zcc(8*(jnl-1)),D(inl,jnl-1),npcp(inl),
     +     nncn(inl),pmcm(inl),Zp(30*inl),idt(3),ip(31),Ctt(jnl-1),
     +     DDp(inl),DDn(inl),Zd(0:jnl),Cdm(jnl-1),pncn(inl),
     +     Zgc(2*inl),Zgx(2*inl)

C Use FIND to locate a variable

      WRITE(*,*)'input the fermi-level in the boundaries (p,n)'
      READ(*,*)fmp,fmn
      WRITE(*,*)'Input the thicknesses of the doping layers (tp,tn)'
      READ(*,*)tp,tn
      WRITE(*,*)'Input the bias light photon flux'
      READ(*,*)Fo
      WRITE(*,*)'Input the absorption coeffient for bias light'
      READ(*,*)alfa
      WRITE(*,*)'From which side? (1)left, (2)right'
      READ(*,*)Isb
      WRITE(*,*)'Input the probe light photon flux'
      READ(*,*)fp
      WRITE(*,*)'Input the absorption coeffient for probe light'
      READ(*,*)alfp
      WRITE(*,*)'From which side? (1)left, (2)right'
      READ(*,*)Isp
      WRITE(*,*)'Input the thickness of the device'
      READ(*,*)L
      WRITE(*,*)'How thick are the transition layers tpg,tng?'
      WRITE(*,*)'Input the ratios tpg/tp and tng/tn'
      READ(*,*)tpt,tnt
      tpg=tpt*tp
      tng=tnt*tn
      IF(tpg.EQ.0)THEN
            tpg=1d-30
      END IF
      IF(tng.EQ.0)THEN
            tng=1d-30
      END IF
      WRITE(*,*)'Input the band gap'
      READ(*,*)Eg
      WRITE(*,*)'Input the bandedge density of state'
      READ(*,*)GEc
      WRITE(*,*)'Input the temperature'
      READ(*,*)Tr
      WRITE(*,*)'Input the slope of the conduction bandtail'
      READ(*,*)kTc
      WRITE(*,*)'Input zero temp slope of the valence bandtail'
      READ(*,*)Evo
      WRITE(*,*)'Energy distribution of DB: (1)single enregy
     +     (2) Gaussian distribution and (3) defect pool'
      READ(*,*)Ied
      WRITE(*,*)'Input frozen-in temperature itmp'
      READ(*,*)itmp
      WRITE(*,*)'Input peak position of the pool'
      READ(*,*)Ep
      WRITE(*,*)'Input hydrogen density'
      READ(*,*)H
      WRITE(*,*)'Input the number of hydrogen atom involved'
      READ(*,*)ih
      WRITE(*,*)'Input the dangling bond density'
      READ(*,*)Gdb
      WRITE(*,*)'Input Eo'
      READ(*,*)Eo
      WRITE(*,*)'Input U'
      READ(*,*)U
      WRITE(*,*)'Input pool width segma'
      READ(*,*)segma
      WRITE(*,*)'spatial distribution of DB: (1)5 steps; (2)function; (3) uniform'
      READ(*,*)Idb
      WRITE(*,*)'Input five levels(relative to Gdb) and widthes'
      READ(*,*)lvl1,lvl2,lvl3,lvl4,lvl5
      READ(*,*)w1,w2,w3,w4,w5
      WRITE(*,*)'Input the edge density(relative to Gdb) and the decreasing speed'
      READ(*,*)edge,sped
      WRITE(*,*)'Input mobilities'
      READ(*,*)Miun,Miup
      WRITE(*,*)'Input capture coeffient of electron by cbt state'
      READ(*,*)Cna
      WRITE(*,*)'Input reflection coefficient'
      READ(*,*)rf
      WRITE(*,*)'Input capture ratio for e & h at a cbt state Ra=Cn/Cp'
      READ(*,*)Ra
      WRITE(*,*)'uniform slice width(1) or nonuniform(2)'
      READ(*,*)Isw
      WRITE(*,*)'how many slices do you need in doped layers?'
      READ(*,*)Inb
      Rd=1.0/Ra
      k=8.617D-5
      pi=3.1415926535897932

C used for limit the energy range for Gaussian distribution of dangling
C bond distribution

      Dle=segma*DSQRT(log(1D5))
      dEE=2*Dle/(Isl-1)
      Es=Eg-Eo-Dle
      Cnd=Cna*Rd
      Cnnot=Cna
      Cpnot=Cnnot
      Cnplus=10*Cnnot
      Cpminus=Cnplus
      ee=1.6d-19
      eb=6.6D6
      v=1/eb
      dE=Eg/(inl+1)

C following block is to calculate the spatial distribution of slice
C width and node positions

      const1=1d-3
      const2=1d3
2     const3=(const1+const2)/2
      TLL=0
      DO 10 i=1,jnl
            IF(Isw.EQ.1)THEN
              dx(i)=1
            ELSE
              dx(i)=exp(-ABS(jnl/2-i)/const3)
            END IF
            TLL=TLL+dx(i)
10    CONTINUE
      TL(0)=0
      DO 20 i=1,jnl
            dx(i)=dx(i)*L/TLL
            TL(i)=TL(i-1)+dx(i)
20    CONTINUE
      IF(tp/Inb.GE.L/jnl)THEN
            WRITE(*,*)'number of slices in doped layers is less than
     +      average, increase Inb and start again (Ctrl-C)'
            Pause
      END IF
      IF(TL(Inb)-tp.GT.0)THEN
            IF(DABS((TL(Inb)-tp)/tp).GT.0.01)THEN
              const2=const3
              GOTO 2
            END IF
      ELSE IF(TL(Inb)-tp.LT.0)THEN
            IF(DABS((TL(Inb)-tp)/tp).GT.0.01)THEN
              const1=const3
              GOTO 2
            END IF
      END IF

C following block calculate basic variable arrays

      IF(Ied.EQ.3)THEN
            T=itmp+1
      ELSE
            T=Tr
      END IF
1     kT=k*T
      Ncc=GEc*kT
      nopo=Ncc*Ncc*DEXP(-Eg/kT)
      w=v/kT
      kTv=DSQRT(Evo*Evo+kT*kT)
      DO 30 i=1,inl
```

```
            E=i*dE
            gc(i)=dE*GEc*exp(-E/kTc)
            gv(i)=dE*GEc*exp(-(Eg-E)/kTv)
            n1(i)=Ncc*exp(-E/kT)
            p1(i)=Ncc*exp(-(Eg-E)/kT)
            Ra1(i)=Ra*n1(i)+p1(i)
            Rd1(i)=Rd*n1(i)+p1(i)
            Ran1(i)=Ra*n1(i)
            Rdn1(i)=Rd*n1(i)

C for defect pool option

            IF(Ied.EQ.3)THEN
              n1plus=0.5*Ncc*exp(-E/kT)
              n1not=2.0*Ncc*exp((U-E)/kT)
              p1not=2.0*Ncc*exp((E-Eg)/kT)
              p1minus=0.5*Ncc*exp(-(Eg-E+U)/kT)
              npcp(i)=n1plus*Cnplus
              nncn(i)=n1not*Cnnot
              pncn(i)=p1not*Cpnot
              pmcm(i)=p1minus*Cpminus
            END IF
 30 CONTINUE

C for single energy model

    IF(Ied.EQ.1)THEN
            n1plus=0.5*Ncc*DEXP((Eo-Eg)/kT)
            n1not=2.0*Ncc*DEXP((Eo+U-Eg)/kT)
            p1not=2.0*Ncc*DEXP(-Eo/kT)
            p1minus=0.5*Ncc*DEXP(-(Eo+U)/kT)
            n1pCnp=n1plus*Cnplus
            n1nCnn=n1not*Cnnot
            p1nCpn=p1not*Cpnot
            p1mCpm=p1minus*Cpminus
    END IF
    nn=Ncc*DEXP(-fmn/kT)
    np=nopo/nn
    pp=Ncc*DEXP(-fmp/kT)
    pn=nopo/pp
    DO 40 i=0,jnl
            n(i)=pn*(nn/pn)**(TL(i)/L)
            p(i)=nopo/n(i)
 40 CONTINUE

C defect pool model at frozen-in temperature

    IF(T.GT.itmp)THEN
            segs=segma*segma
            se2=segs*2
            spi=segma*DSQRT(2*pi)
            rt=1/(kTv+ih*kT/2)
            ro=kTv*rt
            rop=kT*rt
            rse=ro*segs/kTv
            pre=2*GEc*kTv*kTv/(2*kTv-kT)
            prer=(pre**ro)*((H*2/ih)**(1-ro))
            gama=prer*exp(rt*(rse/2-Ep))
    END IF

C calculate spatial distribution of dangling bond states if it is not
C defect pool model

    IF(Ied.NE.3)THEN
            DO 50 i=0,jnl
              IF(Idb.EQ.1)THEN
                IF (TL(i).LE.w1)THEN
                        Gd(i)=lvl1*Gdb
                ELSE IF(TL(i).LT.w1+w2)THEN
                        Gd(i)=lvl2*Gdb
                ELSE IF(TL(i).LT.w1+w2+w3)THEN
                        Gd(i)=lvl3*Gdb
                ELSE IF(TL(i).LT.L-w5)THEN
                        Gd(i)=lvl4*Gdb
                ELSE
                        Gd(i)=lvl5*Gdb
                END IF
              ELSE IF(Idb.EQ.2)THEN
                hw=0.5*jnl
                Gd(i)=Gdb*(1+(edge-1)*DEXP(-sped*(hw-DABS(i-hw))))
              ELSE
                Gd(i)=Gdb
              END IF
 50   CONTINUE
    END IF

C Boundary condition calculation. Given fermi-level position to decide
C electron and hole density and doping density. First one for the left
C boundary and second one for the right. Also output energy distribu-
C tion for defect pool model at two boundaries.

 6  CALL CHARGESUM(pp,pn,Ra,Rd,dop,p1,Ra1,Rd1,Rdn1,gc,gv,Gd(0),inl,
   +  p1minus,n1plus,p1not,n1not,Cnplus,Cpnot,Cnnot,Cpminus,dEE,Es,
   +  Eg,Eo,segma,U,DBp,DBn,DBm,Ncc,Isl,Ied,kT,T,rop,rse,se2,spi,
   +  gama,dE,fmp,DDp,Ddtp,itmp,Ep)
    WRITE(*,*)'dopep=',dop
    IF(Ied.EQ.3)WRITE(*,*)'Ddt(0)=',Ddtp
    IF (Ied.EQ.2)THEN
            DO 60 i=1,Isl
              Zed(i)=REAL(DBp(i))
              Zed(i+Isl)=REAL(DBn(i))
              Zed(i+2*Isl)=REAL(DBm(i))
              Zdx(i)=REAL(Eg-Es-(i-1)*dEE)
              Zdx(i+Isl)=Zdx(i)
              Zdx(i+2*Isl)=Zdx(i)+REAL(U)
 60   CONTINUE
    END IF
    fnn=Eg-fmn
    CALL CHARGESUM(np,nn,Ra,Rd,don,p1,Ra1,Rd1,Rdn1,gc,gv,Gd(jnl),inl,
   +  p1minus,n1plus,p1not,n1not,Cnplus,Cpnot,Cnnot,Cpminus,dEE,Es,
   +  Eg,Eo,segma,U,DBp,DBn,DBm,Ncc,Isl,Ied,kT,T,rop,rse,se2,spi,
   +  gama,dE,fnn,DDn,Ddtn,itmp,Ep)
    WRITE(*,*)'dopen=',don
    IF(Ied.EQ.3)WRITE(*,*)'Ddt(jnl)=',Ddtn
    IF (Ied.EQ.2)THEN
            DO 70 i=1,Isl
              Zed(i+3*Isl)=REAL(DBp(i))
              Zed(i+4*Isl)=REAL(DBn(i))
              Zed(i+5*Isl)=REAL(DBm(i))
              Zdx(i+3*Isl)=Zdx(i)
              Zdx(i+4*Isl)=Zdx(i)
              Zdx(i+5*Isl)=Zdx(i)+REAL(U)
 70   CONTINUE
            DO 80 I=1,6
 80     iidb(i)=Isl
            iidb(7)=0
    END IF
    DO 90 i=1,inl
            Zgc(i)=REAL(gc(i))
            Zgc(i+inl)=REAL(gv(i))
            Zgx(i)=REAL(i*dE)
            Zgx(i+inl)=Zgx(i)
 90 CONTINUE
    igc(1)=inl
    igc(2)=inl
    igc(3)=0

C calculate doping distribution across the device

    DO 100 i=0,jnl
            IF (TL(i).LE.tp)THEN
              Dope(i)=dop
            ELSE IF(TL(i).LT.tp+tpg)THEN
              Dope(i)=dop*(tpg+tp-TL(i))/tpg
            ELSE IF(TL(i).LT.L-tng-tn)THEN
              Dope(i)=0
            ELSE IF(TL(i).LT.L-tn)THEN
              Dope(i)=(TL(i)-L+tng+tn)*don/tng
            ELSE
              Dope(i)=don
            END IF
100 CONTINUE

C Start to solve transport equations for defect pool model

    bias=0
    Psio=Eg-fmp-fmn
    Psip=0
    IF(Ied.EQ.3.AND.T.GT.itmp)THEN
       Gen=0
       CALL CALCULATION(Psio,n,p,Psi,Dope,dx,ee,w,v,inl,jnl,nopo,Gen,
   +    alfa,kT,T,Miup,Miun,n1pCnp,Cpnot,Cnplus,p1nCpn,n1nCnn,
   +    Cpminus,Cnnot,p1mCpm,Gd,D,Cna,Cnd,Ra,Rd,Ra1,Rd1,Ran1,Rdn1,
   +    n1,p1,gc,gv,Sub,Sup,Diag,B,Ef,RJpdr,RJpdi,RJndr,RJndi,RJp,
   +    RJn,RJ,RI,G,Re,Recb,Revb,Redp,Redn,Cct,Cvt,Cdp,Cdn,Cdm,
   +    Ctt,rf,Gen,alfp,dE,itmp,dEE,Es,Eg,Eo,segma,U,Isl,rop,
   +    rse,se2,spi,gama,npcp,pncn,nncn,pmcm,Ied,Ncc,Tl,L,Isb,Isp,
   +    Psip,bias,Ep)
            T=Tr
            Go to 1
    END IF

C Choose an operational condition

    WRITE(*,*)'Would you like to calculate'
    WRITE(*,*)'  (1) short circuit condition'
    WRITE(*,*)'  (2) any bias'
    WRITE(*,*)'  (3) open circuit condition'
    WRITE(*,*)'  (4) maximum power point'
    WRITE(*,*)'or (5) an I-V curve'
```

```
      READ(*,*) Ich
      WRITE(*,*)'Input the bias'
      READ(*,*)bias
      WRITE(*,*)'Input the voltage range'
      READ(*,*)volt1,volt2
      WRITE(*,*)'Input the number of the points'
      READ(*,*)In
      IF(Ich.LE.2)THEN
              IF(Ich.EQ.2)THEN
                Psio=Psio-bias
              END IF

C option 1 and 2

       CALL CALCULATION(Psio,n,p,Psi,Dope,dx,ee,w,v,inl,jnl,nopo,Fo,
     +     alfa,kT,T,Miup,Miun,n1pCnp,Cpnot,Cnplus,p1nCpn,n1nCnn,
     +     Cpminus,Cnnot,p1mCpm,Gd,D,Cna,Cnd,Ra,Rd,Ra1,Rd1,Ran1,Rdn1,
     +     n1,p1,gc,gv,Sub,Sup,Diag,B,Ef,RJpdr,RJpdi,RJndr,RJndi,RJp,
     +     RJn,RJ,RI,G,Re,Recb,Revb,Redp,Redn,Cct,Cvt,Cdp,Cdn,Cdm,
     +     Ctt,rf,fp,alfp,dE,itmp,dEE,Es,Eg,Eo,segma,U,Isl,rop,
     +     rse,se2,spi,gama,npcp,pncn,nncn,pmcm,Ied,Ncc,Tl,L,Isb,Isp,
     +     Psip,bias,Ep)
      ELSE IF(Ich.EQ.3)THEN

C option 3

       CALL OC(n,p,Psi,dx,inl,jnl,Eg,ee,kT,T,Miup,Miun,Dope,w,v,nopo,
     +     n1pCnp,Cpnot,Cnplus,p1nCpn,n1nCnn,Cpminus,Cnnot,p1mCpm,Gd,
     +     D,Cna,Cnd,Ra,Rd,Ra1,Rd1,Ran1,Rdn1,n1,p1,gc,gv,RJpdr,RJpdi,
     +     RJndr,RJndi,RJp,RJn,RJ,Ef,Sub,Sup,Diag,B,Fo,L,alfa,G,Re,
     +     Recb,Revb,Redp,Redn,Psio,Cct,Cvt,Cdp,Cdn,Cdm,Ctt,rf,fp,
     +     alfp,dE,itmp,rop,rse,se2,spi,gama,npcp,pncn,nncn,pmcm,
     +     dEE,Es,Eo,segma,U,Isl,Ied,Ncc,Tl,Isb,Isp,Psip,Ep)
      ELSE IF(Ich.EQ.4)THEN

C option 4

       CALL MP(n,p,Psi,dx,inl,jnl,ee,kT,T,Miup,Miun,Dope,w,v,nopo,
     +     Psio,n1pCnp,Cpnot,Cnplus,p1nCpn,n1nCnn,Cpminus,Cnnot,
     +     p1mCpm,Gd,D,Cna,Cnd,Ra,Rd,Ra1,Rd1,Ran1,Rdn1,n1,p1,gc,gv,
     +     RJpdr,RJpdi,RJndr,RJndi,RJp,RJn,RJ,Ef,Sub,Sup,Diag,B,Fo,L,
     +     alfa,G,Re,Recb,Revb,Redp,Redn,Cct,Cvt,Cdp,Cdn,Cdm,Ctt,rf,
     +     fp,alfp,dEE,Es,Eg,Eo,segma,U,Isl,Ied,Ncc,Tl,dE,itmp,
     +     rop,rse,se2,spi,gama,npcp,pncn,nncn,pmcm,Isb,Isp,Psip,Ep)
      ELSE

C option 5

       CALL JV(n,p,Psi,dx,inl,jnl,ee,kT,T,Miup,Miun,Dope,w,v,nopo,
     +     Psio,n1pCnp,Cpnot,Cnplus,p1nCpn,n1nCnn,Cpminus,Cnnot,
     +     p1mCpm,Gd,D,Cna,Cnd,Ra,Rd,Ra1,Rd1,Ran1,Rdn1,n1,p1,gc,gv,
     +     RJpdr,RJpdi,RJndr,RJndi,RJp,RJn,RJ,Ef,Sub,Sup,Diag,B,Vol,
     +     Cur,Zv,Zc,iv,Fo,L,alfa,G,Re,Recb,Revb,Redp,Redn,Cct,Cvt,
     +     Cdp,Cdn,Cdm,Ctt,rf,fp,alfp,dE,itmp,dEE,Es,Eg,Eo,segma,
     +     U,Isl,Ied,Ncc,Tl,rop,rse,se2,spi,gama,Isb,Isp,volt1,
     +     volt2,In,Psip,npcp,pncn,nncn,pmcm,Ep)
      END IF

C Start to output data. Check the call savedat part to identify the
C details of the output files(compare the title and the variable array)

      IF(Ied.EQ.3)THEN
              DO 110 j=0,29
                DO 120 i=1,inl
                  Zxp(i+j*inl)=REAL(i*dE)
120           CONTINUE
                ip(j+1)=inl
110           CONTINUE
              ip(31)=0
              DO 130 i=1,inl
                Zp(i)=REAL(DDp(i))
                Zp(i+30*inl)=REAL(DDn(i))
130           CONTINUE
              DO 140 j=1,29
                DO 150 i=1,inl
                  Zp(i+j*inl)=REAL(D(i,j*((jnl+1)/30)))
150           CONTINUE
140           CONTINUE
              Zd(0)=REAL(Ddtp)
              Zd(jnl)=REAL(Ddtn)
              DO 160 i=1,jnl-1
                Zd(i)=0
                DO 170 j=1,inl
                  Zd(i)=Zd(i)+REAL(D(j,i))
170           CONTINUE
160           CONTINUE
        END IF
        DO 180 i=0,jnl
              Efn(i)=Eg+kT*log(n(i)/Ncc)-Psi(i)
              Efp(i)=-kT*log(p(i)/Ncc)-Psi(i)
              Zf(i)=REAL(Efn(i))
              Zf(i+jnl+1)=REAL(Efp(i))
              Zf(i+2*(jnl+1))=REAL(Eg-Psi(i))
              Zf(i+3*(jnl+1))=REAL(-Psi(i))
              IF(Ied.NE.3)Zdb(i)=REAL(Gd(i))
              Zx(i)=REAL(TL(i))
              Zx(i+jnl+1)=Zx(i)
              Zx(i+2*(jnl+1))=Zx(i)
              Zx(i+3*(jnl+1))=Zx(i)
180     CONTINUE
        DO 190 i=1,jnl
              ZnE(i)=REAL(Ef(i))
              Znj(i)=REAL(RJn(i))
              Znj(i+jnl)=REAL(RJp(i))
              Znj(i+2*jnl)=REAL(RJ(i))
              Znj(i+3*jnl)=REAL(RJndr(i))
              Znj(i+4*jnl)=REAL(RJndi(i))
              Znj(i+5*jnl)=REAL(RJpdr(i))
              Znj(i+6*jnl)=REAL(RJpdi(i))
              Zxe(i)=Zx(i)-dx(i)/2
              Zxe(i+jnl)=Zxe(i)
              Zxe(i+2*jnl)=Zxe(i)
              Zxe(i+3*jnl)=Zxe(i)
              Zxe(i+4*jnl)=Zxe(i)
              Zxe(i+5*jnl)=Zxe(i)
              Zxe(i+6*jnl)=Zxe(i)
190     CONTINUE
        DO 200 i=1,jnl-1
              Zcc(i)=REAL(n(i))
              Zcc(i+jnl-1)=REAL(p(i))
              Zcc(i+2*(jnl-1))=REAL(Cct(i))
              Zcc(i+3*(jnl-1))=REAL(Cvt(i))
              Zcc(i+4*(jnl-1))=REAL(Cdp(i))
              Zcc(i+5*(jnl-1))=REAL(Cdn(i))
              Zcc(i+6*(jnl-1))=REAL(Cdm(i))
              Zcc(i+7*(jnl-1))=REAL(Ctt(i)-Dope(i))-Zcc(i)+Zcc(i+jnl-1)
              Zg(i)=REAL(Recb(i))
              Zg(i+jnl-1)=REAL(Revb(i))
              Zg(i+2*(jnl-1))=REAL(Redp(i))
              Zg(i+3*(jnl-1))=REAL(Redn(i))
              Zg(i+4*(jnl-1))=REAL(Re(i))
              Zg(i+5*(jnl-1))=REAL(G(i))
              ton=n(i)/Re(i)
              top=p(i)/Re(i)
              Efm=(Ef(i)+Ef(i+1))/2
              nmn=ton*Miun
              pmp=top*Miup
              ldn=nmn*Efm
              ldp=pmp*Efm
              Zt(i)=REAL(ton)
              Zt(i+jnl-1)=REAL(top)
              Zl(i)=REAL(ldn)
              Zl(i+jnl-1)=REAL(ldp)
              Zl(i+2*(jnl-1))=REAL(DSQRT(nmn*kT))
              Zl(i+3*(jnl-1))=REAL(DSQRT(pmp*kT))
              Zxg(i)=Zx(i)
              Zxg(i+jnl-1)=Zx(i)
              Zxg(i+2*(jnl-1))=Zx(i)
              Zxg(i+3*(jnl-1))=Zx(i)
              Zxg(i+4*(jnl-1))=Zx(i)
              Zxg(i+5*(jnl-1))=Zx(i)
              Zxg(i+6*(jnl-1))=Zx(i)
              Zxg(i+7*(jnl-1))=Zx(i)
200     CONTINUE
        DO 210 i=1,6
210     idg(i)=jnl-1
        DO 220 i=1,4
220     idon(i)=jnl+1
        DO 230 i=1,7
230     idoe(i)=jnl
        DO 240 i=1,8
240     ido(i)=jnl-1
        DO 250 i=1,4
250     idl(i)=jnl-1
              idl(5)=0
              ido(9)=0
              idoe(8)=0
              idon(5)=0
              ide(1)=jnl
              ide(2)=0
              idt(1)=jnl-1
              idt(2)=jnl-1
              idt(3)=0
              ib(1)=jnl+1
              ib(2)=0
        WRITE(*,*)'input the prefix of the file name'
        READ(*,*)pref
        IF (Ied.EQ.2)THEN
              name='gdb'
              title='db Gaussian distribution'
```

```
            xaxis='energy(eV)'
            yaxis='density(/cm3/eV)'
            yopt='LOG'
            CALL savedat(Zdx,Zed,iidb,pref,name,title,xaxis,yaxis,yopt)
      END IF
      name='lth'
      title='dri & diff length'
      xaxis='position(cm)'
      yaxis='length(cm)'
      yopt='LOG'
      CALL savedat(Zxg,Zl,idl,pref,name,title,xaxis,yaxis,yopt)
      name='tim'
      title='e & h life time'
      xaxis='position(cm)'
      yaxis='life time (sec)'
      yopt='LOG'
      CALL savedat(Zxg,Zt,idt,pref,name,title,xaxis,yaxis,yopt)
      name='crt'
      title='current densities'
      xaxis='position(cm)'
      yaxis='current(A/cm2)'
      yopt='LOG'
      CALL savedat(Zxe,Znj,idoe,pref,name,title,xaxis,yaxis,yopt)
      name='fld'
      title='electric field'
      xaxis='position(cm)'
      yaxis='field(V/cm)'
      yopt='LOG'
      CALL savedat(Zxe,ZnE,ide,pref,name,title,xaxis,yaxis,yopt)
      name='nrg'
      title='fermi-levels and band edges'
      xaxis='position(cm)'
      yaxis='energy(eV)'
      yopt='LIN'
      CALL savedat(Zx,Zf,idon,pref,name,title,xaxis,yaxis,yopt)
      name='rcb'
      title='recombination'
      xaxis='position(cm)'
      yaxis='rec(cm-3.s-1)'
      yopt='LOG'
      CALL savedat(Zxg,Zg,idg,pref,name,title,xaxis,yaxis,yopt)
      name='ocp'
      title='occupation'
      xaxis='position(cm)'
      yaxis='densities(cm-3)'
      yopt='LOG'
      CALL savedat(Zxg,Zcc,ido,pref,name,title,xaxis,yaxis,yopt)
      IF(Ied.NE.3)THEN
            name='dbd'
            title='DB distribution'
            xaxis='position(cm)'
            yaxis='densities(cm-3)'
            yopt='LOG'
            CALL savedat(Zx,Zdb,ib,pref,name,title,xaxis,yaxis,yopt)
      END IF
      name='btl'
      title='band tail states'
      xaxis='energy(eV)'
      yaxis='densities(/cm3/eV)'
      yopt='LOG'
      CALL savedat(Zgx,Zgc,igc,pref,name,title,xaxis,yaxis,yopt)
      IF(Ied.EQ.3)THEN
            name='def'
            title='defect distribution'
            xaxis='position(cm)'
            yaxis='densities(cm-3)'
            yopt='LOG'
            CALL savedat(Zx,Zd,ib,pref,name,title,xaxis,yaxis,yopt)
            name='3dd'
            title='defect pool'
            xaxis='energy(eV)'
            yaxis='densities(1/cm3eV)'
            yopt='LOG'
            CALL savedat(Zxp,Zp,ip,pref,name,title,xaxis,yaxis,yopt)
      END IF
      STOP
      END

C open circuit option--two guesses and then bisection method

      SUBROUTINE OC(n,p,Psi,dx,inl,jnl,Eg,ee,kT,T,Miup,Miun,Dope,w,v,
     +      nopo,n1pCnp,Cpnot,Cnplus,p1nCpn,n1nCnn,Cpminus,Cnnot,
     +      p1mCpm,Gd,D,Cna,Cnd,Ra,Rd,Ra1,Rd1,Ran1,Rdn1,n1,p1,gc,
     +      gv,RJpdr,RJpdi,RJndr,RJndi,RJp,RJn,RJ,Ef,Sub,Sup,Diag,
     +      B,Fo,L,alfa,G,Re,Recb,Revb,Redp,Redn,Psio,Cct,Cvt,Cdp,
     +      Cdn,Cdm,Ctt,rf,fp,alfp,dE,itmp,rop,rse,se2,spi,gama,
     +      npcp,pncn,nncn,pmcm,dEE,Es,Eo,segma,U,Isl,Ied,Ncc,Tl,
     +      Isb,Isp,Psip,Ep)
      IMPLICIT DOUBLE PRECISION (a-h,k-y)
      bias=1.0
      Voc=1
      Psi1=Eg
      CALL CALCULATION(Psi1,n,p,Psi,Dope,dx,ee,w,v,inl,jnl,nopo,Fo,alfa,
     +   kT,T,Miup,Miun,n1pCnp,Cpnot,Cnplus,p1nCpn,n1nCnn,Cpminus,
     +   Cnnot,p1mCpm,Gd,D,Cna,Cnd,Ra,Rd,Ra1,Rd1,Ran1,Rdn1,n1,p1,gc,
     +   gv,Sub,Sup,Diag,B,Ef,RJpdr,RJpdi,RJndr,RJndi,RJp,RJn,RJ,RI,G,
     +   Re,Recb,Revb,Redp,Redn,Cct,Cvt,Cdp,Cdn,Cdm,Ctt,rf,fp,alfp,
     +   dE,itmp,dEE,Es,Eg,Eo,segma,U,Isl,rop,rse,se2,spi,gama,npcp,
     +   pncn,nncn,pmcm,Ied,Ncc,Tl,L,Isb,Isp,Psip,bias,Ep)
      RJ1=RI
      WRITE(*,*)'RJ1=',RI
      Psi2=0
      CALL CALCULATION(Psi2,n,p,Psi,Dope,dx,ee,w,v,inl,jnl,nopo,Fo,alfa,
     +   kT,T,Miup,Miun,n1pCnp,Cpnot,Cnplus,p1nCpn,n1nCnn,Cpminus,
     +   Cnnot,p1mCpm,Gd,D,Cna,Cnd,Ra,Rd,Ra1,Rd1,Ran1,Rdn1,n1,p1,gc,
     +   gv,Sub,Sup,Diag,B,Ef,RJpdr,RJpdi,RJndr,RJndi,RJp,RJn,RJ,RI,G,
     +   Re,Recb,Revb,Redp,Redn,Cct,Cvt,Cdp,Cdn,Cdm,Ctt,rf,fp,alfp,
     +   dE,itmp,dEE,Es,Eg,Eo,segma,U,Isl,rop,rse,se2,spi,gama,npcp,
     +   pncn,nncn,pmcm,Ied,Ncc,Tl,L,Isb,Isp,Psip,bias,Ep)
      RJ2=RI
      WRITE(*,*)'RJ2=',RI
      IF(RI.GT.0)THEN
            FF=Psi2
            RR=RJ2
            Psi2=Psi1
            RJ2=RJ1
            RJ1=RR
            Psi1=FF
      END IF
260   Psi3=(Psi1+Psi2)/2
      IF(DABS((Psio-Psi3-Voc)/Voc).LT.1D-5)THEN
            RETURN
      END IF
      Voc=Psio-Psi3
      WRITE(*,*)'Voc=',Voc
      CALL CALCULATION(Psi3,n,p,Psi,Dope,dx,ee,w,v,inl,jnl,nopo,Fo,alfa,
     +   kT,T,Miup,Miun,n1pCnp,Cpnot,Cnplus,p1nCpn,n1nCnn,Cpminus,
     +   Cnnot,p1mCpm,Gd,D,Cna,Cnd,Ra,Rd,Ra1,Rd1,Ran1,Rdn1,n1,p1,gc,
     +   gv,Sub,Sup,Diag,B,Ef,RJpdr,RJpdi,RJndr,RJndi,RJp,RJn,RJ,RI,G,
     +   Re,Recb,Revb,Redp,Redn,Cct,Cvt,Cdp,Cdn,Cdm,Ctt,rf,fp,alfp,
     +   dE,itmp,dEE,Es,Eg,Eo,segma,U,Isl,rop,rse,se2,spi,gama,npcp,
     +   pncn,nncn,pmcm,Ied,Ncc,Tl,L,Isb,Isp,Psip,bias,Ep)
      RJ3=RI
      Psip=Psi3
      WRITE(*,*)'RJ3=',RI
      IF(RJ3.GT.0)THEN
            Psi1=Psi3
      ELSE
            Psi2=Psi3
      END IF
      GO TO 260
      END

C maximum power point--start from one point to find the zero point of
C dVI/dV the slope of VI vs V plot

      SUBROUTINE MP(n,p,Psi,dx,inl,jnl,ee,kT,T,Miup,Miun,Dope,w,v,nopo,
     +      Psio,n1pCnp,Cpnot,Cnplus,p1nCpn,n1nCnn,Cpminus,Cnnot,
     +      p1mCpm,Gd,D,Cna,Cnd,Ra,Rd,Ra1,Rd1,Ran1,Rdn1,n1,p1,gc,
     +      gv,RJpdr,RJpdi,RJndr,RJndi,RJp,RJn,RJ,Ef,Sub,Sup,Diag,
     +      B,Fo,L,alfa,G,Re,Recb,Revb,Redp,Redn,Cct,Cvt,Cdp,Cdn,
     +      Cdm,Ctt,rf,fp,alfp,dEE,Es,Eg,Eo,segma,U,Isl,Ied,Ncc,Tl,
     +      dE,itmp,rop,rse,se2,spi,gama,npcp,pncn,nncn,pmcm,
     +      Isb,Isp,Psip,Ep)
      IMPLICIT DOUBLE PRECISION (a-h,k-y)
      bias=1
      step=0.1
      vol1=step
      Psi1=Psio-vol1
      CALL CALCULATION(Psi1,n,p,Psi,Dope,dx,ee,w,v,inl,jnl,nopo,Fo,alfa,
     +   kT,T,Miup,Miun,n1pCnp,Cpnot,Cnplus,p1nCpn,n1nCnn,Cpminus,
     +   Cnnot,p1mCpm,Gd,D,Cna,Cnd,Ra,Rd,Ra1,Rd1,Ran1,Rdn1,n1,p1,gc,
     +   gv,Sub,Sup,Diag,B,Ef,RJpdr,RJpdi,RJndr,RJndi,RJp,RJn,RJ,RI,G,
     +   Re,Recb,Revb,Redp,Redn,Cct,Cvt,Cdp,Cdn,Cdm,Ctt,rf,fp,alfp,
     +   dE,itmp,dEE,Es,Eg,Eo,segma,U,Isl,rop,rse,se2,spi,gama,npcp,
     +   pncn,nncn,pmcm,Ied,Ncc,Tl,L,Isb,Isp,Psip,bias,Ep)
      Piv1=vol1*RI
      vol2=vol1+step
270   Psi2=Psio-vol2
      CALL CALCULATION(Psi2,n,p,Psi,Dope,dx,ee,w,v,inl,jnl,nopo,Fo,alfa,
     +   kT,T,Miup,Miun,n1pCnp,Cpnot,Cnplus,p1nCpn,n1nCnn,Cpminus,
     +   Cnnot,p1mCpm,Gd,D,Cna,Cnd,Ra,Rd,Ra1,Rd1,Ran1,Rdn1,n1,p1,gc,
     +   gv,Sub,Sup,Diag,B,Ef,RJpdr,RJpdi,RJndr,RJndi,RJp,RJn,RJ,RI,G,
     +   Re,Recb,Revb,Redp,Redn,Cct,Cvt,Cdp,Cdn,Cdm,Ctt,rf,fp,alfp,
     +   dE,itmp,dEE,Es,Eg,Eo,segma,U,Isl,rop,rse,se2,spi,gama,npcp,
     +   pncn,nncn,pmcm,Ied,Ncc,Tl,L,Isb,Isp,Psip,bias,Ep)
      Piv2=vol2*RI
      Psip=Psi2
      WRITE(*,*)'V=',vol2,'   IV=',Piv2
      IF(vol2.GT.vol1)THEN
```

```
            slop=(Piv2-Piv1)/(vol2-vol1)
      ELSE
            slop=(Piv2-Piv1)/(vol1-vol2)
      END IF
      WRITE(*,*)'slop=',slop
      IF(DABS(slop).GT.1d-7)THEN
            IF(slop.GT.0)THEN
              vol1=vol2
              Piv1=Piv2
            ELSE
              vol1=vol2
              Piv1=Piv2
              step=-step/2
            END IF
            vol2=vol2+step
            GOTO 270
      END IF
      RETURN
      END

C I-V curve--set the voltages and go for it.

      SUBROUTINE JV(n,p,Psi,dx,inl,jnl,ee,kT,T,Miup,Miun,Dope,w,v,nopo,
     +      Psio,n1pCnp,Cpnot,Cnplus,p1nCpn,n1nCnn,Cpminus,Cnnot,
     +      p1mCpm,Gd,D,Cna,Cnd,Ra,Rd,Ra1,Rd1,Ran1,Rdn1,n1,p1,gc,
     +      gv,RJpdr,RJpdi,RJndr,RJndi,RJp,RJn,RJ,Ef,Sub,Sup,Diag,
     +      B,Vol,Cur,Zv,Zc,iv,Fo,L,alfa,G,Re,Recb,Revb,Redp,Redn,
     +      Cct,Cvt,Cdp,Cdn,Cdm,Ctt,rf,fp,alfp,dE,itmp,dEE,Es,
     +      Eg,Eo,segma,U,Isl,Ied,Ncc,Tl,rop,rse,se2,spi,gama,
     +      Isb,Isp,volt1,volt2,In,Psip,npcp,pncn,nncn,pmcm,Ep)

      IMPLICIT DOUBLE PRECISION (a-h,k-y)
      DIMENSION Vol(*),Cur(*),Zv(*),Zc(*),iv(*)
      CHARACTER*30 title,yaxis,xaxis,pref*5,name*3,yopt*3
      DO 280 i=1,In
          ai=i-1
          Vol(i)=volt1+(volt2-volt1)*(1.0975-0.545*DEXP(0.7-ai*2.45/(In-1)))
          Psi1=Psio-Vol(i)
       CALL CALCULATION(Psi1,n,p,Psi,Dope,dx,ee,w,v,inl,jnl,nopo,Fo,
     +      alfa,kT,T,Miup,Miun,n1pCnp,Cpnot,Cnplus,p1nCpn,n1nCnn,
     +      Cpminus,Cnnot,p1mCpm,Gd,D,Cna,Cnd,Ra,Rd,Ra1,Rd1,Ran1,Rdn1,
     +      n1,p1,gc,gv,Sub,Sup,Diag,B,Ef,RJpdr,RJpdi,RJndr,RJndi,RJp,
     +      RJn,RJ,RI,G,Re,Recb,Revb,Redp,Redn,Cct,Cvt,Cdp,Cdn,Cdm,
     +      Ctt,rf,fp,alfp,dE,itmp,dEE,Es,Eg,Eo,segma,U,Isl,rop,
     +      rse,se2,spi,gama,npcp,pncn,nncn,pmcm,Ied,Ncc,Tl,L,Isb,Isp,
     +      Psip,Vol(i),Ep)
              Cur(i)=-RI
              Psip=Psi1
              WRITE(*,*)i,' vol=',vol(i),' i=',Cur(i)
              Zv(i)=REAL(Vol(i))
              Zc(i)=REAL(Cur(i))
280   CONTINUE
      iv(1)=In
      iv(2)=0
      WRITE(*,*)'input the prefix of the file name'
      READ(*,*)pref
      name='I-V'
      title='I-V curve'
      xaxis='voltage(V)'
      yaxis='current(A/cm2)'
      yopt='LIN'
      CALL savedat(Zv,Zc,iv,pref,name,title,xaxis,yaxis,yopt)
      STOP
      END

C central part of the program--solving the transport equations

      SUBROUTINE CALCULATION(AA,n,p,Psi,Dope,dx,ee,w,v,inl,jnl,nopo,Fo,
     +      alfa,kT,T,Miup,Miun,n1pCnp,Cpnot,Cnplus,p1nCpn,n1nCnn,
     +      Cpminus,Cnnot,p1mCpm,Gd,D,Cna,Cnd,Ra,Rd,Ra1,Rd1,Ran1,
     +      Rdn1,n1,p1,gc,gv,Sub,Sup,Diag,B,Ef,RJpdr,RJpdi,RJndr,
     +      RJndi,RJp,RJn,RJ,RI,G,Re,Recb,Revb,Redp,Redn,Cct,Cvt,
     +      Cdp,Cdn,Cdm,Ctt,rf,fp,alfp,dE,itmp,dEE,Es,Eg,Eo,
     +      segma,U,Isl,rop,rse,se2,spi,gama,npcp,pncn,nncn,pmcm,
     +      Ied,Ncc,Tl,L,Isb,Isp,Psip,bias,Ep)
      IMPLICIT DOUBLE PRECISION (a-h,k-y)
      DIMENSION dx(*),Ef(*),n(0:*),p(0:*),Psi(0:*),RJpdr(*),RJpdi(*),
     +      RJndr(*),RJndi(*),RJp(*),RJn(*),RJ(*)
      inumb=0
      iii=0
      fff=Fo+fp

C assign the first guess for potential Psi and in some simple case n
C or p

      IF(T.GT.itmp)THEN
            DO 290 i=0,jnl
              Psi(i)=-kT*DLOG(p(i)/p(0))
              n(i)=nopo/p(i)
290   CONTINUE
      ELSE
            IF(DABS(Psip).LT.1d-30)THEN
            write(*,*)'psip=',psip,bias
              DO 300 i=0,jnl
                Psi(i)=AA*i/jnl
300   CONTINUE
            ELSE
              DO 305 i=0,jnl
                Psi(i)=Psi(i)*AA/Psip
305   CONTINUE
            END IF
      END IF

C solve Poisson equation

310   CALL POISSON(n,p,Psi,Dope,dx,w,v,inl,jnl,nopo,n1pCnp,Cpnot,Cnplus,
     +      p1nCpn,n1nCnn,Cpminus,Cnnot,p1mCpm,Gd,D,Cna,Cnd,Ra,Rd,Ra1,
     +      Rd1,Ran1,Rdn1,n1,p1,gc,gv,Sub,Sup,Diag,B,dE,itmp,dEE,Es,
     +      Eg,Eo,segma,U,Isl,Ied,Ncc,rop,rse,se2,spi,gama,T,kT,npcp,
     +      pncn,nncn,pmcm,Bmaxp,fff,bias,Ep)

C solve continuity equations

      CALL CONTINUITY(n,p,Psi,kT,T,dx,inl,jnl,nopo,n1pCnp,Cpnot,Cnplus,
     +      p1nCpn,n1nCnn,Cpminus,Cnnot,p1mCpm,Gd,D,Cna,Cnd,Ra,Rd,Ra1,
     +      Rd1,Ran1,Rdn1,n1,p1,Fo,L,alfa,Miup,Miun,gc,gv,Sub,Sup,Diag,B,
     +      Bmaxc,G,Re,Recb,Revb,Redp,Redn,Cct,Cvt,Cdp,Cdn,Cdm,Ctt,rf,fp,
     +      alfp,dE,itmp,dEE,Es,Eg,Eo,segma,U,Isl,Ied,Ncc,Tl,rop,rse,
     +      se2,spi,gama,npcp,pncn,nncn,pmcm,Isb,Isp,fff,bias,Ep)

C calculate the maximum change in this iteration and print it on the
C screen(the frequency can be chosen as wish by change if condition for
C iii in this part)

      Bmax=DMAX1(Bmaxp,Bmaxc)
      inumb=inumb+1
      iii=iii+1
      IF(T.GT.itmp)THEN
            IF(iii.EQ.1)THEN
              WRITE(*,*)inumb,' thermleq=',Bmax
              iii=0
            END IF
            IF(Bmax.GT.1D-6)GOTO 310
      ELSE
            IF(iii.EQ.50)THEN
              WRITE(*,*)inumb,'change=',Bmax
              iii=0
            END IF
            IF(Bmax.GT.1D-8)GOTO 310
      END IF

C calculate electric field, current components etc in secondary nodes

      DO 320 i=1,jnl
            FF=Psi(i)-Psi(i-1)
            Ef(i)=-FF/dx(i)
            MEp=Miup*ee*Ef(i)
            MEn=Miun*ee*Ef(i)
            pam=FF/kT
            gam=pam/2
            egm=DEXP(gam)
            mgm=DEXP(-gam)
            epam=1-DEXP(pam)
            mpam=1-DEXP(-pam)
            egam=1-egm
            mgam=1-mgm
            dre=egam/epam
            drm=mgam/mpam
            die=egm/epam
            dim=mgm/mpam
            RJpdr(i)=MEp*(p(i-1)*dre+p(i)*drm)
            RJndr(i)=MEn*(n(i-1)*drm+n(i)*dre)
            RJpdi(i)=MEp*(p(i-1)*die+p(i)*dim)
            RJndi(i)=MEn*(n(i-1)*dim+n(i)*die)
            RJp(i)=RJpdr(i)+RJpdi(i)
            RJn(i)=RJndr(i)+RJndi(i)
            RJ(i)=RJp(i)+RJn(i)
320   CONTINUE
      RI=-RJ(1)
      RETURN
      END

C Subroutine used to calculate charge neutrality boundary conditions

      SUBROUTINE CHARGESUM(p,n,Ra,Rd,dope,p1,Ra1,Rd1,Rdn1,gc,gv,Gdb,
     +      inl,p1minus,n1plus,p1not,n1not,Cnplus,Cpnot,Cnnot,Cpminus,
     +      dEE,Es,Eg,Eo,segma,U,DBp,DBn,DBm,Ncc,Isl,Ied,kT,T,rop,
     +      rse,se2,spi,gama,dE,Eff,Dbd,Ddt,itmp,Ep)
      IMPLICIT DOUBLE PRECISION (a-h,k-y)
      DIMENSION Dbd(*),p1(*),gc(*),gv(*),Ra1(*),Rd1(*),Rdn1(*)
```

```
C parameters

      sc=0
      sv=0
      Ddt=0
      Dplus=0
      Dminus=0
      Ran=Ra*n
      Ranp=Ran+p
      Rdn=Rd*n
      Rdnp=Rdn+p

C arrays used in defect pool model

      IF(T.GT.itmp)THEN
              DO 330 i=1,inl
                E=i*dE
                bas=exp((Eff-Eg+E)/kT)
                bbs=exp((2*(Eff-Eg+E)-U)/kT)
                dems=1+2*bas+bbs
                Fnots=2*bas/dems
                bd=Eg-E-Ep+rse
                PP=(DEXP(-bd*bd/se2))/spi
                Dbd(i)=dE*PP*gama*(2/Fnots)**rop
 330    CONTINUE
      END IF

C for Gaussian distribution of dangling bond go to another subroutine
C return charge density in dangling bond states Dplus and Dminus

      IF(Ied.EQ.2)THEN
          Call Dbond(n,p,dEE,Es,Isl,Eg,kT,Gdb,Eo,U,segma,Cnnot,Cpnot,
     +     Cnplus,Cpminus,Fminus,Fplus,DBp,DBn,DBm,Ncc,Dplus,Dminus)

C for single energy model it is simple Dplus and Dminus

      ELSE IF(Ied.EQ.1)THEN
              Pnot=n1plus*Cnplus+p*Cpnot
              Nplus=n*Cnplus+p1not*Cpnot
              Pminus=n1not*Cnnot+p*Cpminus
              Nnot=n*Cnnot+p1minus*Cpminus
              fdbdenom=Nplus*Pminus+Pnot*Pminus+Nnot*Nplus
              Fplus=Pnot*Pminus/fdbdenom
              Fminus=Nnot*Nplus/fdbdenom
              Dminus=Gdb*Fminus
              Dplus=Gdb*Fplus
      END IF

C calculate charge density in bandtail states

      DO 340 i=1,inl
              E=i*dE
              fe=(Ran+p1(i))/(Ra1(i)+Ranp)
              fv=(Rdn1(i)+p)/(Rdnp+Rd1(i))
              sc=sc+gc(i)*fe
              sv=sv+gv(i)*fv

C charge density in dangling bond states in defect pool model output
C Dplus and Dminus

              IF(Ied.EQ.3)THEN
                ba=exp((Eff-Eg+E)/kT)
                bb=exp((2*(Eff-Eg+E)-U)/kT)
                dem=1+2*ba+bb
                fplus=1/dem
                fnot=2*ba/dem
                fminus=bb/dem
                Ddt=Ddt+Dbd(i)
                Dp=Dbd(i)*fplus
                Dm=Dbd(i)*fminus
                Dplus=Dplus+Dp
                Dminus=Dminus+Dm
              END IF
 340  CONTINUE

C Total space charge and free carrier difference equals to the doping density

      dope=sv-sc-n+p-Dminus+Dplus
      RETURN
      END

C Subroutine dealing with the Gaussian distribution of the dangling bond states

      SUBROUTINE DBOND(n,p,dEE,Es,Isl,Eg,kT,Gdb,Eo,U,segma,Cnnot,Cpnot,
     +     Cnplus,Cpminus,Fminus,Fplus,DBp,DBn,DBm,Ncc,Dplus,Dminus)
      IMPLICIT DOUBLE PRECISION(a-h,k-y)
      DIMENSION DBp(*),DBn(*),DBm(*)
      A=0
      Fmi=0
      Fpl=0
      Do 350 i=1,Isl

C calculate the occupation function not beyond the optical gap.

              fd=DEXP(-((i*dEE+Es-Eg+Eo)/segma)**2)
              n11plus=0.5*Ncc*DEXP(-(i*dEE+Es)/kT)
              p11not=2*Ncc*DEXP((i*dEE+Es-Eg)/kT)
              IF(U.GT.0)THEN
                IF((U-i*dEE-Es).GT.0)THEN
                  n11not=0
                  p11minus=0
                ELSE
                  n11not=2*Ncc*DEXP((U-i*dEE-Es)/kT)
                  p11minus=0.5*Ncc*DEXP((i*dEE+Es-Eg-U)/kT)
                END IF
              ELSE
                IF((-U+i*dEE+Es).GT.Eg)THEN
                  n11not=0
                  p11minus=0
                ELSE
                  n11not=2*Ncc*DEXP((U-i*dEE-Es)/kT)
                  p11minus=0.5*Ncc*DEXP((i*dEE+Es-Eg-U)/kT)
                END IF
              END IF
              P2not=n11plus*Cnplus+p*Cpnot
              N2plus=n*Cnplus+p11not*Cpnot
              P2minus=n11not*Cnnot+p*Cpminus
              N2not=n*Cnnot+p11minus*Cpminus
              F2dbdenom=N2plus*P2minus+P2not*P2minus+N2not*N2plus
              F2plus=P2not*P2minus/F2dbdenom
              F2minus=N2not*N2plus/F2dbdenom
              DBp(i)=fd*F2plus
              DBn(i)=fd*(1-F2plus-F2minus)
              DBm(i)=fd*F2minus
              A=A+fd
              Fmi=Fmi+fd*F2minus
              Fpl=Fpl+fd*F2plus
 350  CONTINUE
      DO 360 i=1,Isl
              DBp(i)=Gdb*DBp(i)/A
              DBn(i)=Gdb*DBn(i)/A
              DBm(i)=Gdb*DBm(i)/A
 360  CONTINUE
      Fminus=Fmi/A
      Fplus=Fpl/A
      Dminus=Gdb*Fminus
      Dplus=Gdb*Fplus
      Return
      End

C Subroutine to solve Poisson equaiton--Scharfetter & Gummel algorithm

      SUBROUTINE POISSON(n,p,Psi,Dope,dx,w,v,inl,jnl,nopo,n1pCnp,Cpnot,
     +     Cnplus,p1nCpn,n1nCnn,Cpminus,Cnnot,p1mCpm,Gd,D,Cna,Cnd,
     +     Ra,Rd,Ra1,Rd1,Ran1,Rdn1,n1,p1,gc,gv,Sub,Sup,Diag,B,
     +     dE,itmp,dEE,Es,Eg,Eo,segma,U,Isl,Ied,Ncc,rop,rse,se2,
     +     spi,gama,T,kT,npcp,pncn,nncn,pmcm,Bmaxp,fff,bias,Ep)
      IMPLICIT DOUBLE PRECISION (a-h,k-y)
      DIMENSION Psi(0:*),n(0:*),p(0:*),dx(*),Sub(*),Diag(*),Sup(*),B(*),
     +     Dope(0:*),Gd(0:*)
 371  DO 370 i=1,jnl-1

C calculate the elements in tridiagnal matrix equation

              Sdx=dx(i+1)+dx(i)
              Sub(i)=2/(dx(i)*Sdx)
              Sup(i)=2/(dx(i+1)*Sdx)

C call subroutine to calculate all the parameters needed

              CALL PARAMETERS(n(i),p(i),i,inl,T,kT,Ncc,U,rop,rse,se2,spi,
     +     gama,nopo,n1pCnp,Cpnot,Cnplus,p1nCpn,n1nCnn,Cpminus,Cnnot,
     +     p1mCpm,Gd(i),D,Cna,Cnd,Ra,Rd,Ra1,Rd1,Ran1,Rdn1,n1,p1,gc,
     +     gv,Pt,Nt,ptp,ptn,ntp,ntn,Dpt,Dnt,Dmt,Dppt,Dpnt,Dmpt,Dmnt,
     +     Rcbt,Rvbt,Rplus,Rnot,RP,RN,dE,itmp,dEE,Es,Eg,Eo,segma,
     +     Isl,Ied,npcp,pncn,nncn,pmcm,fff,bias,Ep)
                  Diag(i)=-2/(dx(i+1)*dx(i))-w*(p(i)*(1+ptp-ntp+Dppt-Dmpt)
     +       +n(i)*(1-ptn+ntn-Dpnt+Dmnt))
                  B(i)=-2*((Psi(i+1)-Psi(i))/dx(i+1)-(Psi(i)-Psi(i-1))/dx(i))/
     +     Sdx-v*(p(i)-n(i)+Pt-Nt-Dope(i)+Dpt-Dmt)
 370  CONTINUE

C solve the tridiagnal equation

      CALL TRID(Sub,Diag,Sup,B,jnl)

C calculate the relative change in this calculation and update psi

      Bmaxp=0
      DO 380 i=1,jnl-1
```

```
            Bmaxp=DMAX1(Bmaxp,DABS(B(i)/Psi(i)))
            Psi(i)=Psi(i)+B(i)
380  CONTINUE

C  in defect pool model and at frozen-in temperature update n and p

     IF(T.GT.itmp)THEN
            DO 390 i=1,jnl-1
              p(i)=p(0)*DEXP(-Psi(i)/kT)
              n(i)=nopo/p(i)
390    CONTINUE
c      IF(Bmaxp.GT.1d-8)GOTO 371
     END IF
c    WRITE(*,*)'poissonbmax=',Bmaxp
     RETURN
     END

C  Subroutine to solve continuity equations for n and p

     SUBROUTINE CONTINUITY(n,p,Psi,kT,T,dx,inl,jnl,nopo,n1pCnp,Cpnot,
    +       Cnplus,p1nCpn,n1nCnn,Cpminus,Cnnot,p1mCpm,Gd,D,Cna,Cnd,
    +       Ra,Rd,Ra1,Rd1,Ran1,Rdn1,n1,p1,Fo,L,alfa,Miup,Miun,gc,
    +       gv,Sub,Sup,Diag,B,Bmax,G,Re,Recb,Revb,Redp,Redn,Cct,
    +       Cvt,Cdp,Cdn,Cdm,Ctt,rf,fp,alfp,dE,itmp,dEE,Es,Eg,Eo,
    +       segma,U,Isl,Ied,Ncc,Tl,rop,rse,se2,spi,gama,npcp,pncn,
    +       nncn,pmcm,Isb,Isp,fff,bias,Ep)

     IMPLICIT DOUBLE PRECISION (a-h,k-y)
     DIMENSION Psi(0:*),n(0:*),p(0:*),dx(*),Sub(*),Sup(*),Diag(*),B(*),
    +       G(*),Re(*),Recb(*),Revb(*),Redp(*),Redn(*),Cct(*),
    +       Cvt(*),Cdp(*),Cdn(*),Cdm(*),Ctt(*),Gd(0:*),Tl(0:*)
     Bmaxp=0
     Bmaxn=0
     ij=0
400  DO 410 i=1,jnl-1
            Df=Psi(i)-Psi(i-1)
            Df1=Psi(i+1)-Psi(i)
            pam=Df/kT
            pam1=Df1/kT
            dx2=dx(i+1)+dx(i)
            Miupx=2*Miup/dx2
            Miunx=2*Miun/dx2
            Dfx=(Psi(i)-Psi(i-1))/dx(i)
            Dfx1=(Psi(i+1)-Psi(i))/dx(i+1)
            dxi=dx(i)/2
            dxii=dx(i+1)/2
            y=Tl(i)

C  most accurate expression for generation rate profile including
C  the averaging within one slice and the reflection from the back

            IF(Isb.EQ.1)THEN
          Gb=Fo*(DEXP(-alfa*y)*(DEXP(alfa*dxi)-DEXP(-alfa*dxii))+
    +     rf*DEXP(alfa*(y-2*L))*(DEXP(alfa*dxii)-DEXP(-alfa*dxi)))/(dxi+dxii)
            ELSE
          Gb=Fo*(DEXP(alfa*(y-L))*(DEXP(alfa*dxii)-DEXP(-alfa*dxi))+
    +     rf*DEXP(-alfa*(y+L))*(DEXP(alfa*dxi)-DEXP(-alfa*dxii)))/(dxi+dxii)
            END IF
            IF(Isp.EQ.1)THEN
          Gp=fp*(DEXP(-alfp*y)*(DEXP(alfp*dxi)-DEXP(-alfp*dxii))+
    +     rf*DEXP(alfp*(y-2*L))*(DEXP(alfp*dxii)-DEXP(-alfp*dxi)))/(dxi+dxii)
            ELSE
           Gp=fp*(DEXP(alfp*(y-L))*(DEXP(alfp*dxii)-DEXP(-alfp*dxi))+
    +     rf*DEXP(-alfp*(y+L))*(DEXP(alfp*dxi)-DEXP(-alfp*dxii)))/(dxi+dxii)
            END IF
            G(i)=Gb+Gp
            CALL PARAMETERS(n(i),p(i),i,inl,T,kT,Ncc,U,rop,rse,se2,spi,
    +      gama,nopo,n1pCnp,Cpnot,Cnplus,p1nCpn,n1nCnn,Cpminus,Cnnot,
    +      p1mCpm,Gd(i),D,Cna,Cnd,Ra,Rd,Ra1,Rd1,Ran1,Rdn1,n1,p1,gc,
    +      gv,Pt,Nt,ptp,ptn,ntp,ntn,Dpt,Dnt,Dmt,Dppt,Dpnt,Dmpt,Dmnt,
    +      Rcbt,Rvbt,Rplus,Rnot,RP,RN,dE,itmp,dEE,Es,Eg,Eo,segma,
    +      Isl,Ied,npcp,pncn,nncn,pmcm,fff,bias,Ep)

C  from parameter subroutine recombination rate components can be
C  calculated within one slice

            Cct(i)=Nt
            Cvt(i)=Pt
            Cdp(i)=Dpt
            Cdn(i)=Dnt
            Cdm(i)=Dmt
            Ctt(i)=Cvt(i)+Cdp(i)-Cct(i)-Cdm(i)
            Recb(i)=Rcbt
            Revb(i)=Rvbt
            Redp(i)=Rplus
            Redn(i)=Rnot
            Re(i)=Rcbt+Rvbt+Rplus+Rnot
            GR=G(i)-Re(i)

C  calculate the elements in tridiagnal matrix equation for p and n

            IF(ij.EQ.0)THEN
              Sub(i)=Miupx*Dfx/(1-DEXP(pam))
              Diag(i)=Miupx*(Dfx/(1-DEXP(-pam))-Dfx1/(1-DEXP(pam1)))+
    +         RP+RN*n(i)/p(i)
              Sup(i)=Miupx*Dfx1/(DEXP(-pam1)-1)
              B(i)=GR+RP*p(i)+RN*n(i)
            ELSE
              Sub(i)=Miunx*Dfx/((DEXP(-pam)-1))
              Diag(i)=Miunx*(Dfx1/(1-DEXP(-pam1))-Dfx/(1-DEXP(pam)))+
    +         RN+RP*p(i)/n(i)
              Sup(i)=Miunx*Dfx1/(1-DEXP(pam1))
              B(i)=GR+RN*n(i)+RP*p(i)
            END IF
410  CONTINUE
     IF(ij.EQ.0)THEN
            B(1)=B(1)-Sub(1)*p(0)
            B(jnl-1)=B(jnl-1)-Sup(jnl-1)*p(jnl)
     ELSE
            B(1)=B(1)-Sub(1)*n(0)
            B(jnl-1)=B(jnl-1)-Sup(jnl-1)*n(jnl)
     END IF

C  solve the tridiagnal matrix equation

     CALL TRID(Sub,Diag,Sup,B,jnl)
     IF(ij.EQ.0)THEN

C  calculate the maximum relative change and update p and n

            DO 420 i=1,jnl-1
              Bmaxp=DMAX1(Bmaxp,DABS((B(i)-p(i))/p(i)))
              p(i)=B(i)
420    CONTINUE
c      WRITE(*,*)'conpBmax=',Bmaxp
            IF(T.GT.itmp)THEN
              DO 430 i=1,jnl-1
                Psi(i)=-kT*DLOG(p(i)/p(0))
                n(i)=nopo/p(i)
430       CONTINUE
            END IF
            ij=1
            GOTO 400
     ELSE
            DO 440 i=1,jnl-1
              Bmaxn=DMAX1(Bmaxn,DABS((B(i)-n(i))/n(i)))
              n(i)=B(i)
440    CONTINUE
c      WRITE(*,*)'connBmax=',Bmaxn
            IF(T.GT.itmp)THEN
              DO 450 i=1,jnl-1
                Psi(i)=kT*DLOG(n(i)/n(0))
                p(i)=nopo/n(i)
450       CONTINUE
            END IF
     END IF
     Bmax=DMAX1(Bmaxp,Bmaxn)
     RETURN
     END

C  subroutine to solve tridiagnal matrix equation

     SUBROUTINE TRID(Sub,Diag,Sup,B,jnl)
     IMPLICIT DOUBLE PRECISION (a-h,k-y)
     DIMENSION Sub(*),Diag(*),Sup(*),B(*)

     DO 460 i=2,jnl-1
            Sub(i)=Sub(i)/Diag(i-1)
            Diag(i)=Diag(i)-Sub(i)*Sup(i-1)
            B(i)=B(i)-Sub(i)*B(i-1)
460  CONTINUE
     B(jnl-1)=B(jnl-1)/Diag(jnl-1)
     DO 470 i=jnl-2,1,-1
            B(i)=(B(i)-Sup(i)*B(i+1))/Diag(i)
470  CONTINUE
     RETURN
     END

C  Subroutine to calculate the parameters used in the Poisson and
C  continuity equations

     SUBROUTINE PARAMETERS(n,p,j,inl,T,kT,Ncc,U,rop,rse,se2,spi,gama,
    +       nopo,n1pCnp,Cpnot,Cnplus,p1nCpn,n1nCnn,Cpminus,Cnnot,
    +       p1mCpm,Gdb,D,Cna,Cnd,Ra,Rd,Ra1,Rd1,Ran1,Rdn1,n1,p1,gc,
    +       gv,Pt,Nt,ptp,ptn,ntp,ntn,Dpt,Dnt,Dmt,Dppt,Dpnt,Dmpt,
    +       Dmnt,Rcbt,Rvbt,Rplus,Rnot,RP,RN,dE,itmp,dEE,Es,Eg,
    +       Eo,segma,Isl,Ied,npcp,pncn,nncn,pmcm,fff,bias,Ep)
     IMPLICIT DOUBLE PRECISION (a-h,k-y)
     DIMENSION Ra1(*),Rd1(*),Ran1(*),Rdn1(*),n1(*),p1(*),gc(*),gv(*),
    +       D(inl,*),npcp(*),pncn(*),nncn(*),pmcm(*)
```

```
      npd=n*p-nopo
      NCnp=n*Cnplus
      nCnn=n*Cnnot

C this part calculate the trapping and recombination via dangling bond
C states when single energy model is used

      IF(Ied.EQ.1)THEN
            Pnot=n1pCnp+p*Cpnot
            Nplus=NCnp+p1nCpn
            Pminus=n1nCnn+p*Cpminus
            Nnot=nCnn+p1mCpm
            Pnm=Pnot*Pminus
            Nnp=Nnot*Nplus
            NpPm=Nplus*Pminus
            denom=NpPm+Pnm+Nnp
            Fminus=Nnp/Denom
            Fplus=Pnm/Denom
            Fnot=NpPm/Denom
            CnpPm=Cnplus*Pminus
            CnpNn=Cnplus*Nnot
            CnnNp=Cnnot*Nplus
            CpnPm=Cpnot*Pminus
            CpmPn=Cpminus*Pnot
            CpmNp=Cpminus*Nplus
            CnpFp=Cnplus*Fplus
            CnnFn=Cnnot*Fnot
            NCN1C=nCnn-n1pCnp
            fdbdenom=denom*denom
            Fplusn=-Pnm*(CnpPm+CnpNn+CnnNp)/fdbdenom
            Fplusp=Nplus*(CpnPm*(Pminus+Nnot)+CpmPn*Nnot)/fdbdenom
            Fminusn=Pminus*(CnnNp*(Nplus+Pnot)+CnpNn*Pnot)/fdbdenom
            Fminusp=-Nnp*(CpmNp+CpmPn+CpnPm)/fdbdenom
            Fnotn=Pminus*(CnpPm*Pnot-CnnNp*Nplus)/fdbdenom
            Fnotp=Nplus*(CpmNp*Nnot-CpnPm*Pminus)/fdbdenom

C this if block set recombination rate to zero when in thermal
C equilibrium condition

            IF(DABS(fff).GT.1d-10.OR.DABS(bias).GT.1d-5)THEN
              prem=Gdb*npd/denom
              Rplus=prem*Pminus*Cnplus*Cpnot
              Rnot=prem*Nplus*Cpnot*Cpminus
                Rdbn=Gdb*(CnpFp+CnnFn+NCnp*Fplusn+NCN1C*Fnotn-
     +          n1nCnn*Fminusn)
              Rdbp=Gdb*(NCnp*Fplusp+NCN1C*Fnotp-n1nCnn*Fminusp)
            ELSE
              Rplus=0
              Rnot=0
              Rdbn=0
              Rdbp=0
            END IF
            Dpt=Gdb*Fplus
            Dnt=Gdb*Fnot
            Dmt=Gdb*Fminus
            Dppt=Gdb*Fplusp
            Dpnt=Gdb*Fplusn
            Dmpt=Gdb*Fminusp
            Dmnt=Gdb*Fminusn

C This part calculate the trapping and recombinaton via Gaussian
C distribution of the dangling bond

      ELSE IF (Ied.EQ.2)THEN
            A=0
            Fmi=0
            Fpl=0
            Fno=0
            Fpln=0
            Fplp=0
            Fmin=0
            Fmip=0
            Fnon=0
            Fnop=0
            Rpl=0
            Rno=0
            Rdp=0
            Rdno=0
            DO 480 i=1,Isl
              fd=DEXP(-((i*dEE+Es-Eg+Eo)/segma)**2)
              n11plus=0.5*Ncc*DEXP(-(i*dEE+Es)/kT)
              p11not=2*Ncc*DEXP((i*dEE+Es-Eg)/kT)
              IF(U.GT.0)THEN
                IF((U-i*dEE-Es).GT.0)THEN
                        n11not=0
                        p11minus=0
                ELSE
                        n11not=2*Ncc*DEXP((U-i*dEE-Es)/kT)
                        p11minus=0.5*Ncc*DEXP((i*dEE+Es-Eg-U)/kT)
                END IF
              ELSE
                IF((-U+i*dEE+Es).GT.Eg)THEN
                        n11not=0
                        p11minus=0
                ELSE
                        n11not=2*Ncc*DEXP((U-i*dEE-Es)/kT)
                        p11minus=0.5*Ncc*DEXP((i*dEE+Es-Eg-U)/kT)
                END IF
              END IF
              n1pcnp=n11plus*Cnplus
              n1ncnn=n11not*Cnnot
              NCN1C=nCnn-n1pCnp
              Pnot=n1pcnp+p*Cpnot
              Nplus=NCnp+p11not*Cpnot
              Pminus=n1ncnn+p*Cpminus
              Nnot=nCnn+p11minus*Cpminus
              Pnm=Pnot*Pminus
              Nnp=Nnot*Nplus
              NpPm=Nplus*Pminus
              denom=NpPm+Pnm+Nnp
              Fminus=Nnp/Denom
              Fplus=Pnm/Denom
              Fnot=NpPm/Denom
              CnpPm=Cnplus*Pminus
              CnpNn=Cnplus*Nnot
              CnnNp=Cnnot*Nplus
              CpnPm=Cpnot*Pminus
              CpmPn=Cpminus*Pnot
              CpmNp=Cpminus*Nplus
              CnpFp=Cnplus*Fplus
              CnnFn=Cnnot*Fnot
              fdbdenom=denom*denom
              Fplusn=-Pnm*(CnpPm+CnpNn+CnnNp)/fdbdenom
              Fplusp=Nplus*(CpnPm*(Pminus+Nnot)+CpmPn*Nnot)/fdbdenom
              Fminusn=Pminus*(CnnNp*(Nplus+Pnot)+CnpNn*Pnot)/fdbdenom
              Fminusp=-Nnp*(CpmNp+CpmPn+CpnPm)/fdbdenom
              Fnotn=Pminus*(CnpPm*Pnot-CnnNp*Nplus)/fdbdenom
              Fnotp=Nplus*(CpmNp*Nnot-CpnPm*Pminus)/fdbdenom
              A=A+fd
              Fmi=Fmi+fd*Fminus
              Fpl=Fpl+fd*Fplus
              Fno=Fno+fd*Fnot
              Fpln=Fpln+fd*Fplusn
              Fplp=Fplp+fd*Fplusp
              Fmin=Fmin+fd*Fminusn
              Fmip=Fmip+fd*Fminusp
              Fnon=Fnon+fd*Fnotn
              Fnop=Fnop+fd*Fnotp

C set recombination rate to zero in thermal equilibrium condition

              IF(DABS(fff).GT.1d-10.OR.DABS(bias).GT.1d-5)THEN
                prem=fd*npd/denom
                Rpl=Rpl+prem*Pminus*Cnplus*Cpnot
                Rno=Rno+prem*Nplus*Cpnot*Cpminus
                Rdno=Rdno+fd*(CnpFp+CnnFn+NCnp*Fplusn+
     +                NCN1C*Fnotn-n1ncnn*Fminusn)
                Rdp=Rdp+fd*(NCnp*Fplusp+NCN1C*Fnotp-n1ncnn*Fminusp)
              END IF
480   CONTINUE
            Fplus=Fpl/A
            Fminus=Fmi/A
            Fnot=Fno/A
            Fplusp=Fplp/A
            Fplusn=Fpln/A
            Fminusp=Fmip/A
            Fminusn=Fmin/A
            Fnotp=Fnop/A
            Fnotn=Fnon/A
            Rplus=Rpl*Gdb/A
            Rnot=Rno*Gdb/A
            Rdbn=Rdno*Gdb/A
            Rdbp=Rdp*Gdb/A
            Dpt=Gdb*Fplus
            Dnt=Gdb*Fnot
            Dmt=Gdb*Fminus
            Dppt=Gdb*Fplusp
            Dpnt=Gdb*Fplusn
            Dmpt=Gdb*Fminusp
            Dmnt=Gdb*Fminusn

C This part calculate trapping and recombination via dangling bond
C states from defect pool model

      ELSE
            Rdbn=0
            Rdbp=0
            Rplus=0
            Rnot=0
            Dpt=0
```

```
      Dppt=0
      Dpnt=0
      Dnt=0
      Dmt=0
      Dmpt=0
      Dmnt=0
      Ef=Eg+kT*DLOG(n/Ncc)
      DO 490 i=1,inl

C At frozen-in temperature calculate defect distribution

      IF(T.GT.itmp)THEN
        E=i*dE
        ba=exp((Ef-Eg+E)/kT)
        bb=exp((2*(Ef-Eg+E)-U)/kT)
        dem=1+2*ba+bb
        Fplus=1/dem
        Fnot=2*ba/dem
        Fminus=bb/dem
        F2F=Fnot+2*Fminus
        Fplusp=Fplus*F2F/p
        Fplusn=-Fplusp*p/n
        Fnotp=Fnot*(F2F-1)/p
        Fnotn=-Fnotp*p/n
        Fminusp=Fminus*(F2F-2)/p
        Fminusn=-Fminusp*p/n
        bd=Eg-E-Ep+rse
        PP=(exp(-bd*bd/se2))/spi
        D(i,j)=dE*PP*gama*(2/Fnot)**rop
        PDPP=rop*D(i,j)*(Fplus-Fminus)/p
        PDPN=-PDPP*p/n
        Dppt=Dppt+D(i,j)*Fplusp+PDPP*Fplus
        Dpnt=Dpnt+D(i,j)*Fplusn+PDPN*Fplus
        Dmpt=Dmpt+D(i,j)*Fminusp+PDPP*Fminus
        Dmnt=Dmnt+D(i,j)*Fminusn+PDPN*Fminus

C at operation condition, calculate trapping and recombination

      ELSE
        Pnot=npcp(i)+p*Cpnot
        Nplus=NCnp+pncn(i)
        Pminus=nncn(i)+p*Cpminus
        Nnot=nCnn+pmcm(i)
        Pnm=Pnot*Pminus
        Nnp=Nnot*Nplus
        NpPm=Nplus*Pminus
        denom=NpPm+Pnm+Nnp
        Fminus=Nnp/Denom
        Fplus=Pnm/Denom
        Fnot=NpPm/Denom
        CnpPm=Cnplus*Pminus
        CnpNn=Cnplus*Nnot
        CnnNp=Cnnot*Nplus
        CpnPm=Cpnot*Pminus
        CpmPn=Cpminus*Pnot
        CpmNp=Cpminus*Nplus
        CnpFp=Cnplus*Fplus
        CnnFn=Cnnot*Fnot
        NCN1C=nCnn-npcp(i)
        fdbdenom=denom*denom
        Fplusn=-Pnm*(CnpPm+CnpNn+CnnNp)/fdbdenom
      Fplusp=Nplus*(CpnPm*(Pminus+Nnot)+CpmPn*Nnot)/fdbdenom
      Fminusn=Pminus*(CnnNp*(Nplus+Pnot)+CnpNn*Pnot)/fdbdenom
        Fminusp=-Nnp*(CpmNp+CpmPn+CpnPm)/fdbdenom
        Fnotn=Pminus*(CnpPm*Pnot-CnnNp*Nplus)/fdbdenom
        Fnotp=Nplus*(CpmNp*Nnot-CpnPm*Pminus)/fdbdenom
        Dppt=Dppt+D(i,j)*Fplusp
        Dpnt=Dpnt+D(i,j)*Fplusn
        Dmpt=Dmpt+D(i,j)*Fminusp
        Dmnt=Dmnt+D(i,j)*Fminusn
      END IF
      Dp=D(i,j)*Fplus
      Dpt=Dpt+Dp
      Dn=D(i,j)*Fnot
      Dnt=Dnt+Dn
      Dm=D(i,j)*Fminus
      Dmt=Dmt+Dm

C set recombination to zero in thermal equilibrium condition

      IF(DABS(fff).GT.1d-10.OR.DABS(bias).GT.1d-5)THEN
        Rplus=Rplus+D(i,j)*(n*CnpFp-npcp(i)*Fnot)
        Rnot=Rnot+D(i,j)*(n*CnnFn-nncn(i)*Fminus)
      Rdbn=Rdbn+D(i,j)*(CnpFp+CnnFn+NCnp*Fplusn+NCN1C*Fnotn-
     +    nncn(i)*Fminusn)
      Rdbp=Rdbp+D(i,j)*(NCnp*Fplusp+NCN1C*Fnotp-nncn(i)*Fminusp)
        END IF
490   CONTINUE
    END IF

C trapping and recombination via bandtail states

    Pt=0
    Nt=0
    Ptn=0
    Ptp=0
    Ntn=0
    Ntp=0
    Rcbt=0
    Rvbt=0
    Rbtn=0
    Rbtp=0
    Ran=Ra*n
    Ranp=Ran+p
    Rdn=Rd*n
    Rdnp=Rdn+p
    DO 500 i=1,inl
        fda=Ra1(i)+Ranp
        fdd=Rd1(i)+Rdnp
        Ranp1=Ran+p1(i)
        Ran1p=Ran1(i)+p
        Rdn1p=Rdn1(i)+p
        Rdnp1=Rdn+p1(i)
        fe=Ranp1/fda
        fv=Rdn1p/fdd
        Pt=Pt+gv(i)*fv
        Nt=Nt+gc(i)*fe
        fda2=fda*fda
        fdd2=fdd*fdd
        fen=Ra*Ran1p/fda2
        fep=-Ranp1/fda2
        fvn=-Rd*Rdn1p/fdd2
        fvp=Rdnp1/fdd2
        Ptn=Ptn+gv(i)*fvn
        Ptp=Ptp+gv(i)*fvp
        Ntn=Ntn+gc(i)*fen
        Ntp=Ntp+gc(i)*fep

C set recombination rate to zero at thermal equilibrium condition

        IF(DABS(fff).GT.1d-10.OR.DABS(bias).GT.1d-5)THEN
          Cnar=Cna*gc(i)/fda
          Cndr=Cnd*gv(i)/fdd
          Cnars=Cnar/fda
          Cndrs=Cndr/fdd
          Rcbt=Rcbt+npd*Cnar
          Rvbt=Rvbt+npd*Cndr
          Rbtn=Rbtn+(Cnars*Ran1p+Cndrs*Rdn1p)*(p+p1(i))
          Rbtp=Rbtp+(Cnars*Ranp1+Cndrs*Rdnp1)*(n+n1(i))
        END IF
500 CONTINUE
    RP=Rdbp+Rbtp
    RN=Rdbn+Rbtn
    RETURN
    END

C The subroutine to output data file

    SUBROUTINE savedat(X,Y,ind,pref,name,title,xaxis,yaxis,yopt)
    dimension x(*),y(*),ind(*)
    character*24 title,xaxis,yaxis,xopt*3,yopt*3,pref*5,name*3
510 format(a)
    xopt='LIN'
    OPEN(1,FILE=pref//name//'.dat',STATUS='unknown')
    WRITE(1,510)TITLE
    WRITE(1,510)XAXIS
    WRITE(1,510)YAXIS
    WRITE(1,510)XOPT
    WRITE(1,510)YOPT
    INUM=0
    JSTA=1
    JEND=0
    i=1
520 inum=inum+1
    i=i+1
    if (ind(i).ne.0) goto 520
    write(1,*)inum
    DO 530 I=1,INUM
        WRITE(1,*)I
        WRITE(1,*)ind(I)
        JEND=JEND+ind(I)
        DO 540 J=JSTA,JEND
          WRITE(1,*)X(J),Y(J)
540   CONTINUE
        JSTA=JEND+1
530 CONTINUE
    CLOSE(1)
    RETURN
    END
```

Appendix 2 Glossary for SPIN.F source code

alfa	absorption coefficient for the bias light
B(jnl-1)	right hand array in tridiagonal matrix equation
bias	bias voltage
Cct(jnl-1)	charge density of conduction bandtail states
Cdm(jnl-1)	charge density of D- states
Cdn(jnl-1)	charge density of Do states
Cdp(jnl-1)	charge density of D+ states
Cvt(jnl-1)	charge density of valence bandtail states
Cna	capture coeffient of electron by cbt state
Cnd	capture coeffient of hole by cbt state
Cnplus	capture coeffient of electron by D+ state
Cnnot	capture coeffient of electron by D0 state
Cpminus	capture coeffient of hole by D- state
Cpnot	capture coeffient of hole by D0 state
Ctt(jnl-1)	total charge density array
Cur(50)	current density array in I-V curve
D(inl,jnl-1)	two-dimension array for defect density from defect pool model, add DDn and DDp form a complete 3-D image
DBm(Isl)	Gaussian distribution of D- states
DBn(Isl)	Gaussian distribution of Do states
DBp(Isl)	Gaussian distribution of D+ states
DDn(inl)	defect distribution on n-type boundary from defect pool
DDp(inl)	defect distribution on p-type boundary from defect pool
dE	energy division in bandgap
dEE	energy division specially for Gaussian distribution
Diag(jnl-1)	diagonal elements in tridiagonal matrix equation
Dle	energy range for Gaussian distribution of dangling bond
don	n-type doping density calculated from boundary condition
dop	p-type doping density calculated from boundary condition
Dope(0:jnl)	spatial variation of doping density of the device
dx(jnl)	slice width array of the device
eb	permittivity of a-Si:H =6.6e6(e/Vcm)
edge	edge density(relative to Gdb)in function option for dangling bond distribution(spatial)
ee	electron charge =1.6e-19C
Ef(jnl)	electric field distribution
Efn(0:jnl)	electron quasi-fermi-level distribution
Efp(0:jnl)	hole quasi-fermi-level distribution
Eg	band gap
Eo	energy of D+ states
Ep	the peak position of the pool in defect pool model
Evo	zero temperature slope of the valence bandtail states
fmn	fermi-level position in n-type doped layer
fmp	fermi-level position in p-type doped layer
Fo	bias light photon flux(cm-2s-1)
fp	probe light photon flux(cm-2s-1)
G(jnl-1)	generation rate profile
gc(inl)	conduction bandtail density of states (cm-3)
Gd(0:jnl)	spatial variation of dangling bond density
Gdb	dangling bond density in single energy and Gaussian distribution of dangling bond model
GEc	bandedge density of states at conduction bandedge(cm-3eV-1)
gv(inl)	valence bandtail density of states (cm-3)
H	hydrogen density in the material used in defect pool model
ib(2)	array indicate the number of curves in output file of Zdb
Ich	option to choice operational condition (from 1 to 5)
Idb	option for spatial distribution of dangling bond

ide(2)	array indicate the number of curves in output file of ZnE
idg(7)	array indicate the number of curves in output file of Zg
idl(5)	array indicate the number of curves in output file of Zl
ido(9)	array indicate the number of curves in output file of Zcc
idoe(8)	array indicate the number of curves in output file of Znj
idon(5)	array indicate the number of curves in output file of Zf
idt(3)	array indicate the number of curves in output file of Zt
Ied	option for different dangling bond models
igc(3)	array indicate the number of curves in output file of Zgc
ih	the number of hydrogen atom involved in the chemical reaction in defect pool model
iidb(7)	array indicate the number of curves in output file of Zed
In	number of point in I-V curve
inb	number of slice in doped layer in nonuniform slice width
ip(31)	array indicate the number of curves in output file of Zp
Isb	the direction option for bias light
Isl	the number of energy slices for Gaussian distribution of dangling bond states
Isp	the direction option for probe light
Isw	option for uniform or nonuniform slice width
itmp	frozen-in temperature in defect pool model
iv(2)	array indicate the number of curves in output file of Zc
k	Boltzmann's constant =8.617e-5eV/K
kTc	slope of the conduction bandtail states
kTv	slope of the valence bandtail states
L	total thickness of the device
ldn	electron drift length
ldp	hole drift length
lvl1-5	relative densities in five levels option for spatial variation of dangling bond density
Miun	electron mobility
Miup	hole mobility
n(0:jnl)	free electron spatial array of the device
n1(inl)	effective electron emission density for bandtail state
n1not	effective electron emission density for D-/o transition
n1plus	effective electron emission density for Do/+ transition
Ncc	effective density of states at the bandedge
nncn(inl)	=n1not*Cnnot
nopo	electron hole product at thermal equilibrium states
npcp(inl)	=n1plus*Cnplus
p(0:jnl)	free hole spatial array of the device
p1(inl)	effective hole emission density
p1minus	effective hole emission density for Do/- transition
p1not	effective hole emission density for D+/o transition
pi	3.14159265358979323846264338327950288419716939937510582 0
pmcm(inl)	=p1minus*Cpminus
pncn(inl)	=p1not*Cpnot
psio	build-in potential of the device
Ra	capture coefficient ratio for e & h at a cbt state
Ra1(inl)	Ra*n1(inl)+p1(inl)
Ran1(inl)	Ra*n1(inl)
Rd	1/Ra
Rd1(inl)	=Rd*n1(inl)+p1(inl)
Rdn1(inl)	=Rd*n1(inl)
Re(jnl-1)	spatial variation of total recombination rate
Recb(jnl-1)	recombination rate via conduction bandtail states
Redn(jnl-1)	recombination rate via Do states
Redp(jnl-1)	recombination rate via D+ states
Revb(jnl-1)	recombination rate via valence bandtail states
rf	reflective coefficient from back electrode

RJ(jnl)	total current array(constant in steady states)
RJn(jnl)	electron current array
RJndi(jnl)	electron diffusion current array
RJndr(jnl)	electron drift current array
RJp(jnl)	hole current array
RJpdi(jnl)	hole diffusion current array
RJpdr(jnl)	hole drift current array
segma	pool width in defect pool model and in Gaussian distribution model
sped	decreasing speed in the function option for dangling bond distribution(spatial)
Sub(jnl-1)	subdiagonal elements in tridiagonal matrix
Sup(jnl-1)	supdiagonal elements in tridiagonal matrix
T	general temperature variable
TL(0:jnl)	node position array of the device
tn	thickness of the n-type doped layer
tng	thickness of the n-type transition layer
tnt	relative thickness of n-type transition layer
ton	life time of electron
top	life time of hole
tp	thickness of the p-type doped layer
tpg	thickness of the p-type transition layer
tpt	relative thickness of p-type transition layer
Tr	room temperature
U	correlation energy between D+/o and Do/- states
Vol(50)	voltage array for I-V curve
volt1,2	voltage range in I-V curve plot
w1-5	widths correspondent to the five level spatial variation of dangling bond distribution
Psi(0:jnl)	potential distribution
Zc(50)	single precision array of current density in I-V curve
Zcc(8*(jnl-1))	single precision array of charge densities for output
Zd(0:jnl)	integrated spatial variation of dangling bond density across the device from defect pool
Zdb(0:jnl)	single precision array of dangling bond density
Zdx(6*Isl)	energy coodinate for output file of Zed
Zed(6*Isl)	single precision array of DBm, DBn and DBm together
Zf(0:4*(jnl+1)-1)	single precision array of bandedges and fermi levels
Zg(6*(jnl-1))	single precision array of recombination rates
Zgc(2*inl)	single precision array of bandtail states
Zgx(2*inl)	energy coodinate for output file of Zgc
Zl(4*(jnl-1))	single precision array of drift and diffusion lengths
ZnE(jnl)	single precision array of Ef for output
Znj(7*jnl)	single precision array of currents for output
Zp(30*inl)	output array of 3-D defect density from defect pool
Zt(2*(jnl-1))	single precision array of carrier lifetime for output
Zv(50)	single precision array of voltage array in I-V curve
Zx(0:4*(jnl+1)-1)	x coordinate for output file of Zf
Zxe(7*jnl)	x coordination for output file of Znj
Zxg(8*(jnl-1))	x coordination for output file of Zl, Zt, Zcc and Zg
Zxp(30*inl)	energy coodinate for output file of Zp

Appendix 3

The relation between the absorption coefficients, reflectance index and the photon energy (Dawson et al 1992)

$h\nu(eV)$	$\alpha(cm^{-1})$	$h\nu(eV)$	$\alpha(cm^{-1})$	n	$h\nu(eV)$	$\alpha(cm^{-1})$	n
0.80	6.03×10^{-2}	1.50	1.51×10^{1}	3.840	2.50	1.85×10^{5}	4.851
0.82	6.13×10^{-2}	1.52	2.24×10^{1}	3.841	2.55	2.07×10^{5}	4.901
0.84	6.33×10^{-2}	1.54	3.39×10^{1}	3.843	2.60	2.32×10^{5}	4.927
0.86	6.64×10^{-2}	1.56	5.16×10^{1}	3.845	2.65	2.69×10^{5}	4.949
0.88	7.06×10^{-2}	1.58	7.89×10^{1}	3.850	2.70	3.04×10^{5}	4.983
0.90	7.61×10^{-2}	1.60	1.21×10^{2}	3.857	2.75	3.31×10^{5}	5.011
0.92	8.23×10^{-2}	1.62	1.85×10^{2}	3.867	2.80	3.62×10^{5}	5.042
0.94	9.12×10^{-2}	1.64	2.80×10^{2}	3.879	2.85	3.96×10^{5}	5.060
0.96	1.01×10^{-1}	1.66	4.21×10^{2}	3.893	2.90	4.33×10^{5}	5.075
0.98	1.13×10^{-1}	1.68	6.24×10^{2}	3.908	2.95	4.73×10^{5}	5.088
1.00	1.26×10^{-1}	1.70	7.45×10^{2}	3.926	3.00	5.16×10^{5}	5.094
1.02	1.41×10^{-1}	1.72	1.08×10^{3}	3.946	3.05	5.58×10^{5}	5.085
1.04	1.59×10^{-1}	1.74	1.53×10^{3}	3.966	3.10	6.04×10^{5}	5.082
1.06	1.78×10^{-1}	1.76	2.10×10^{3}	3.989	3.15	6.55×10^{5}	5.060
1.08	2.00×10^{-1}	1.78	2.81×10^{3}	4.013	3.20	6.98×10^{5}	5.050
1.10	2.24×10^{-1}	1.80	3.67×10^{3}	4.037	3.25	7.50×10^{5}	5.011
1.12	2.51×10^{-1}	1.82	4.68×10^{3}	4.063	3.30	8.03×10^{5}	4.969
1.14	2.81×10^{-1}	1.84	5.87×10^{3}	4.090	3.35	8.55×10^{5}	4.926
1.16	3.15×10^{-1}	1.86	7.25×10^{3}	4.117	3.40	9.08×10^{5}	4.878
1.18	3.53×10^{-1}	1.88	8.81×10^{3}	4.146	3.45	9.62×10^{5}	4.820
1.20	3.99×10^{-1}	1.90	1.06×10^{4}	4.174	3.50	1.01×10^{6}	4.751
1.22	4.52×10^{-1}	1.92	1.26×10^{4}	4.203	3.55	1.06×10^{6}	4.673
1.24	5.17×10^{-1}	1.94	1.48×10^{4}	4.232	3.60	1.12×10^{6}	4.593
1.26	5.99×10^{-1}	1.96	1.72×10^{4}	4.261	3.65	1.16×10^{6}	4.517
1.28	7.01×10^{-1}	1.98	1.99×10^{4}	4.290	3.70	1.21×10^{6}	4.426
1.30	8.35×10^{-1}	2.00	2.28×10^{4}	4.319	3.75	1.26×10^{6}	4.326
1.32	1.01×10^{0}	2.02	2.60×10^{4}	4.347	3.80	1.30×10^{6}	4.213
1.34	1.25×10^{0}	2.04	2.94×10^{4}	4.375	3.85	1.34×10^{6}	4.122
1.36	1.58×10^{0}	2.06	3.31×10^{4}	4.403	3.90	1.39×10^{6}	4.012
1.38	2.04×10^{0}	2.08	3.71×10^{4}	4.429	3.95	1.42×10^{6}	3.906
1.40	2.69×10^{0}	2.10	4.13×10^{4}	4.455	4.00	1.45×10^{6}	3.790
1.42	3.64×10^{0}	2.12	4.59×10^{4}	4.480	4.05	1.49×10^{6}	3.682
1.44	5.03×10^{0}	2.14	5.07×10^{4}	4.503	4.10	1.51×10^{6}	3.584

1.46	7.11×10^{0}	2.16	5.58×10^{4}	4.525	4.15	1.55×10^{6}	3.478
1.48	1.03×10^{1}	2.18	6.12×10^{4}	4.546	4.20	1.57×10^{6}	3.372
		2.20	6.68×10^{4}	4.569	4.25	1.60×10^{6}	3.278
		2.22	7.28×10^{4}	4.591	4.30	1.61×10^{6}	3.178
		2.24	7.91×10^{4}	4.613	4.35	1.64×10^{6}	3.076
		2.26	8.56×10^{4}	4.634	4.40	1.65×10^{6}	2.985
		2.28	9.25×10^{4}	4.654	4.45	1.67×10^{6}	2.982
		2.30	9.96×10^{4}	4.675	4.50	1.68×10^{6}	2.803
		2.32	1.07×10^{5}	4.696	4.55	1.70×10^{6}	2.719
		2.34	1.15×10^{5}	4.717	4.60	1.71×10^{6}	2.637
		2.36	1.23×10^{5}	4.736	4.65	1.72×10^{6}	2.561
		2.38	1.31×10^{5}	4.754	4.70	1.73×10^{6}	2.478
		2.40	1.39×10^{5}	4.771	4.75	1.73×10^{6}	2.396
		2.45	1.66×10^{5}	4.811	4.80	1.75×10^{6}	2.337

References

Allan, D., and Joannapoulos, J.D. (1984), Theory of electronic structures, in "*The Physics of Hydrogenated Amorphous Silicon II*", Topics in Applied Physics 56, chap. 2., J.D. Joannapoulos and G. Lucovske, eds., Springer-Verlag, Berlin.

Balberg, I. and Lubianiker, Y. (1993) *Phys. Rev. B* **48.** 8709.

Bar-Yam, Y. and Joannopoulos, J.D., (1987) *J. Non-Cryst. Sol.* **97&98.** 467

Branz, H.M. and Silver, M. (1990), *Phys. Rev. B* **42.** 7420

Carlson, D.E. and Wronski, C.R.(1976) *Appl. Phys. Lett.* **28.** 671

Carlson, D.E. (1989) *IEEE Trans. Electron Devices*, **36.** 2775

Chatterjee, P.(1994) *J. Appl. Phys.* **75.** 1093

Chen, I. and Lee, S. (1982) *J. Appl. Phys.* **53.** 1045

Chittick, R.C., Alexander, J.H. Sterling, H.F.(1969) *J.Electrochemical Soc.***116.** 77

Chu, V., Liu, J.A., Conde, J.P., and Wagner, S.(1989) *MRS Symp. Proc.* Vol**149**, 509

Cody, G.D., (1984), the optical absorption edge of a-Si:H, in "*Hydrogenated Amorphous Silicon*", Semiconductors and Semimetals 21B, chap. 2, Pankove J.I, ed., Academic Press, Inc., Orlando.

Cohen, J.D., Leen, T.M., and Rasmussen, R. J.,(1992) *Phys.Rev. Lett.* **69.** 3358

Cohen, J.D., Leen, T.M., (1994) *Phys.Rev. Lett.* **73.** 366

Crandall, R.S. (1982) *J. Appl. Phys.* **53.** 3350

Crandall, R.S. (1983) *J. Appl. Phys.* **54.** 7176

Crandall, R.S., Sadlon, K., Kalina, J. and Delahoy, A.E.(1989) *MRS Symp. Proc.* Vol **149**, 423

Crandall, R.S. (1991) *Phys. Rev. B* **43.** 4057

Dawson, R.M., Li, Y., Gunes, M., Nag, S. Collins, R.W., Wronski, C.R. Bennett, M. and Li, Y.M.(1992) *Proc. 11th E.C. Photovoltaic Solar Energy Conference.* 1992 Montreux, Switzerland p680

Deane, S.C. and Powell, M.J. (1993) *Phys.Rev.Lett* **70.** 1654

Deane, S.C. and Powell, M.J. (1994) *Amorphous Silicon Technology* **336.** 757

Farmer, J.W. and Su, Z., (1993) *Phys.Rev. Lett.* **71.** 2979

Fischer, D., Wyrsch, N., Fortmann, C.M. and Shah, A.V.(1993) *Proc. of the 23rd IEEE Photovoltaic Specialists Conference.* 1993 p878

Fischer, D., Pellaton, N., Wyrsch, N. and Shah, A.V.(1994) *Proc. of the 12th European Photovoltaic Solar Energy Conf.* Amsterdam, The Netherlands. 1994 p1241

Fischer, D. and Shah, A.V. (1994) *Appl. Phys. Lett.* **65.** 986

Fornarini, L.,Mittiga, A. Sebastiani, M. and Fiorini, P. (1991) *J. Non-Cryst Solids* **137&138.** 491.

Forsythe, G.E., Malcolm, M.A., and Moler, C.B. (1977), *Computer Methods for Mathematical Computations* (Englewood Cliffs, NJ: Prentice-Hall), Chapter 9

Fritzsche, H. (1987) *J. Non-Cryst. Sol.* **97&98.** 95

Golub, G.H. and Reinsch, C. (1971) *Linear Algebra*, Vol. II of Handbook for Automatic Computation Wilkinson, J.H. and Reinsch, C. ed. (New York: Springer-Verlag), Chapter I.10

Gray, J.L. (1989) *IEEE Trans. Electron Devices*, **36.** 906

Gummel, H.K.(1964) *IEEE Trans. Electron Devices*, **11.** 455

Hack, M. and Shur, M. (1983) *J. Appl. Phys.* **54.** 5858

Hack, M. and Shur, M. (1985) *J. Appl. Phys.* **58.** 997

Hall, R.N. (1952) *Physical Review.* **87.** 387

Hepburn, A.P., Marshall, J.M., Main, C., Powell, M.J. and van Berkel, C.(1986) *Phys. Rev. Lett.* **56.** 2215

Hof, C., Fischer, D. and Shah, A.V.(1994)*Proc. of the 12th European Photovoltaic Solar Energy Conf.* Amsterdam, The Netherlands. 1994 p132

Hou, J. H. and Fonash, S. J. (1992) *Appl. Phys. Lett.* **61.** 186

Hubin, J., Sauvain, E. and Shah, A.V. (1989) *IEEE Trans. Electron Devices*, **36.** 2789

Hubin, J. Shah, A.V. and Sauvain, E. (1992) *Philo. Mag. Lett.* **66.** 115

Ikegaki, T., Itoh, H., Muramatsu, S., Matsubara, S., Nakamura, N., Shimada, T., Umeda, J. and Migitaka, M. (1985) *J. Appl. Phys.* **58.** 2352

Jackson, W.B., Kelso, S.M. Tsai, C.C. Allen, J.W. and Oh. S.J. (1985) *Phys. Rev. B* **31.** 5187

Jacobsen, R.L., F.R. Jeffrey, R,K. Westenberg, and R,C,Williams, (1987), *Proc. of the 19th IEEE Photovoltaic Specialists Conference.* 1987 p588

Kemp, M., Meunier, M. and Tannous, C.G. (1989) *Solid-State Electronics* **32.** 149

Kurata, M., (1982)"Numerical Analysis for Semiconductor Devices", D.C. Heath and Comp. Lexington, (1982) Massachusetts.

LeComber, P.G., and Spear, W.E. (1970) *Phys.Rev.Lett.* **25.** 509

LeComber, P.G., and Spear, W.E. (1986), *Phil. Mag. B* **53.** 1, L1

Lee, J-K. and Schiff, E.A. (1992), *Phys. Rev. Lett.* **68.** 2972

Main, C.(1985). Teaching note.

Main, C., Berkin, J. and Merazga, A.(1990), Photoconductivity in Amorphous Semiconductors Experiment and Computer Modelling in "New Physical Problems in Electronic Materials" *Proc. of the 6th International School on Condensed Matter Physics.*(ISCMP Varna '90) Varna, Bulgaria, 1990 p55 Borissov et al ed. World Scientific

Main, C., Dick, D., Reynolds, S., Gao, W. and Gibson, R.A.G.(1995) *presented at 16th International Conference on Amorphous Semiconductors-Science and Technology, (ICAS16) Kobe Japan, Sept 1995 To be published, J. Non-Crystalline Solids*

Marshall. J.M., Berkin, J. and Main, C. (1987a) *Phil.Mag.B* **56.** 641

Marshall, J.M., Street, R.A., Thompson, M.J and Jackson, W.B.(1987b) *J. of Non-Cryst. Sol.* **97&98.** 563

Maruska, H.P., Hicks, M.C., Moustakas, T.D. and Friedman, R. (1984) *IEEE trans. on Elec. Devices.* **31.** 1343

McElheny, P.J., Arch, J.K. Lin, H.S. and Fonash, S.J. (1988) *J. Appl. Phys.* **64.** 1254

Misiakos, K. and Lindholm, F.A.(1988) *J. Appl. Phys.* **64**(1988)383

Mittiga, A, Fiorini, P., Falconieri, M. and Evangelisti, F.(1989) *J. Appl. Phys.* **66.** 2667

Miyachi, K., Ishiguro, N., Miyashita, T., Yanagawa, N., Tanaka, H., Koyama, M., Ashida, Y. and Fukuda, N. (1992) *Proc. 11th European Photovoltaic Solar Energy Conference and Exhibition.* 1992 Montreux, Switzerland p88.

Mott. N.F. (1967) *Adv. Phys.* **16.** 49

Mott, N.F. and Davis, E.A. (1979) "*Electronic Processes in Non-Crystalline Materials*" Second edition. Clarendon Press. Oxford 1979

Nakano, S., Tarui, H., Haku, H., Takahama, T., Matsuyama, T., Isomura, M., Nishikuni, M., Nakamura, N., Tsuda, S. Ohnishi, M., and Kuwano, Y. (1987). *Proc. of the 19th IEEE Photovoltaic Specialist Conference.* 1987 p678

Numerical Recipes in Fortran--The Art of Scientific Computing Second Edition Press, W.H., Teukolsky, S.A., Vetterling, W.T. and Flannery, B.P. ed. (1992) Cambridge University Press. p51

Okamoto, H., Kida, H. and Hamakawa, Y. (1984) *Phil. Mag. B.* **49.** 231

Ovshinsky, S.R., (1985), *Proc.of the 18th IEEE Photovoltaic Specialist Conference.* 1985 p1365

Ovshinsky, S.R., and J. Yang, (1987), *Proc. of the 7th E.C. Photovoltaic Solar Energy Conference, Sevilla 1986*, D. Reidel Publ. Comp., p604

Pawlikiewicz, A.H. and Guha, S. (1988) *Proc. of the 20th IEEE Photovoltaic Specialists Conference.* 1988 p251

Perez Mendez, V., Cho, G., Fujieda, I., Kaplan, S.N., Qureshi, S., and Street, R.A. (1989) *MRS Symp. Proc.* **149.** 621

Powell, M.J. and Deane, S.C. (1993) *Phys.Rev.B* **48.** 10815

Rose, A. (1963) in "*Concepts in Photoconductivity and Allied Problems*". (Interscience, New York,1963).

Rubinelli, F.A., Fonash, S.J. and Arch, J.K. (1992) *Proc. of 6th International Photovoltaic Science and Engineering Conference(PVSEC-6)* New Delhi, India,1992 p811

Rubinelli, F.A. (1994) *J. Appl. Phys.* **75.** 998

Saeng-udom, R., Kusian, W. and Bullemer, B. (1992)*Proc. of the 11th European Photovoltaic Solar Energy Conf.* Montreux, Switzerland. 1992 p609

Sah, C.D. (1967) *Proceedings of the IEEE.* **55.** 672

Scharfetter, D.L. and Gummel, H.K.,(1969), *IEEE trans. on elec. devices* **16.** 64

Schropp, R.E.I., Ouwens, J.D., Vonderlinden, M.B., Vanderwerf, C.H.M., Vanderweg, W.F. and Alkemade, P.F.A.(1993a) *Amorphous Silicon Technology* **297.** 797

Schropp, R.E.I., Sluiter, A., Vonderlinden, Ouwens, J.D., (1993b), *J. of Non-Cryst. Sol.* **166.** 709

Schumm, G. and Bauer, G.H. (1991), *Philos. Mag. B* **64.** 515

Schwartz, R.J., Gray, J.L., Turner, G.B., Kanani, D. and Ullal, H. (1984) *Proc. 17th IEEE photovoltaic Specialists Conference.* New York 1984 p369

Selberherr, S. (1984) in "*Analysis and simulation of semiconductor devices*" Springer-Verlag 1984

Shapiro, F.R., Bar-Yan, Y. and Silver, M. (1989) *IEEE Trans. on Elec. Devices.* **36.** 2785

Shah, A. and Hubin, J.(1989) *Proceedings of the fourth Photovoltaic Science and Engineering Conference* Sydney, **1**, p271

Shockley, W. (1952) *Proc. IRE* **40.** 1365

Shockley, W. and Read, W.T. (1952) *Phys. Rev.* **87.** 835

Simmons, J.G. and Taylor, G.W.(1971) *Phys.Rev. B* **4.** 502

Smith, Z.E. and Wagner, S. (1985), *Phys.Rev.B* **32.** 5510

Smith, Z.E. and Wagner, S. (1987), *Phys.Rev.Lett.* **59.** 688

Smith, Z.E. and Wagner, S. (1989) Implications of the 'Defect Pool' concept for 'Metastable' and 'Stable' defects in amorphous silicon, in "Amorphous silicon and related materials" H. Fritzsche ed. Vol A, p409.World Scientific.

Snowden, C.M. (1985) *Rep. Prog. Phys.* **48.** 223

Solomon, I., Dietle, T. and Kaplan, D. (1978), *J. Phys.* **39.** 142

Solomon, I and Brodsky, M.H. (1980) *J. Appl. Phys* **51.** 4548.

Spear, W.E. and LeComber, P.G. (1972) *J. of Non-Cryst. Sol.* **8&10.** 727

Spear, W.E.and LeComber, P.G. (1975) *Solid State Commun.* **17.** 1193

Staebler, D.L. and Wronski, C.R. (1977) *Appl. Phys. Lett.* **42.** 507

Staebler, D.L., Crandall, R.S. and Williams, R. (1981) *Appl. Phys. Lett.* **39.** 733

Street, R.A. (1982) *Phys. Rev. Lett.* **49.** 1187

Street, R.A., (1984), *Philos. Mag.* **B49.** L15

Street, R.A. (1991a) *Phys. Rev. B* **43.** 2454

Street, R.A. (1991b) "Hydrogenated Amorphous Silicon" Street, R.A ed. Cambridge University Press.1991 p311

Stuke, J., (1987), *J. of Non-Cryst. Sol.* **97&98.** 1

Stutzmann, M., Jackson, W.B. and Tsai, C.C. (1985), *Phys. Rev.B.* **32.** 23

Stutzmann, M. (1987), *Philos. Mag. B* **56.** 63

Stutzmann, M., and W.B. Jackson, (1987), *Sol. State Comm.* **62.** 153

Stutzmann, M., Biegelsen, D.K. and Street, R.A. (1987), *Phys. Rev. B* **35.** 5666

Swartz, G.A. (1982) *J.Appl. Phys.* **53.** 712

Swartz, G.A. (1984) *Appl. Phys. Lett.* **44.** 697

Takahama, T., Isomura, M., Tsuda, S., Tarui, H., Hishikawa, Y., Nakamura, N., Nakashima, Y., Matsuoka, T., Nishiwaki, H., Ohnishi, M., Nakano, S. and Kuwano, Y.(1986) *Japanese J. of Applied Phys.* **25.** 1538

Tasaki, H., Kim, W.Y., Hallerdt, M., Konagai, M. and Yamamoto, Y. (1988) *J. Appl. Phys.* **63.** 550

Vanacek, M., Nelson, B.P., Mahan, A.H. and Crandall, R.S.(1991) *J.Non-Cryst. Solids* **137&138.** 191

Von der Linden, M.B., Schropp, R.E.I., Stammeijer, J.G.F. and Van der Weg, W.F. (1992) *MRS Symposium Records*, **258.** 935

Wallace, W., E. Sabinsky, B. Stafford, and W. Luft, (1987), *Proc. of the 19th IEEE Photovoltaic Specialist Conference*. 1987 p593

Winer, K., Hirabayashi, I. and Ley, L. (1988) *Phys. Rev.B* **38.** 7680

Winer, K. (1989) *Phys. Rev.Lett* **63.** 1487

Winer, K. (1990) *Phys. Rev.B* **41.** 12150

Wronski, C.R., Lee, S., Hicks, M. and Satyendra Kumar, (1989) *Phys. Rev. Lett.* **63.** 1420

Wyrsch, N., Fischer, D. and Shah, A.(1994)*Proc. of the 12th European Photovoltaic Solar Energy Conf.* Amsterdam, The Netherlands. 1994 p73

Zeman, M., Willemen, J.A., Solntsev, S. and Metselaar, J.W. (1994) *Solar Energy Materials and Solar Cells* **34.** 557

Zeman, M., Tao, G., Trussenaar, M., Willemen, J., Metselaar, W. and Schropp, R. (1995) *MRS Symposium Proceedings* Spring Meeting 1995 (MRS, Pittsburgh, 1995), in print.

Publications and conference presentations arising from this work

(1) W. Gao C. Main, S. Reynolds, R. Brueggemann and R Gibson,. Evaluation of the *DICE* analysis method for *a-Si:H PIN* devices by computer modelling. *1994 IOP Conference, Warwick University, Dec.1994.*

(2) W. Gao, C. Main, S. Reynolds, R. Brueggemann and R Gibson, Investigation of the *DICE* Method for *a-Si:H* solar cell devices, *presented at UK Annual conference on Amorphous and Organic Semiconductors, Univ, London, 1995*

(3) W. Gao, C. Main, S. Reynolds, R. Brueggemann and R Gibson, Evaluation of the *DICE* analysis method for *a-Si:H PIN* devices. *presented at 16th International Conference on Amorphous Semiconductors-Science and Technology, (ICAS16) Kobe Japan, Sept 1995 To be published, J. Non-Crystalline Solids*

(4) C.Main, F. Dick, S.Reynolds, W.Gao and R.A.G. Gibson, sub-linear Photoconductivity in n-type a-Si:H - Analysis and Computer Modelling. *presented at 16th International Conference on Amorphous Semiconductors-Science and Technology, (ICAS16) Kobe Japan, Sept 1995 To be published, J. Non-Crystalline Solids*

(5) W. Gao, R. Brüggemann, G.H.Bauer, C. Main, *Instructions for Collection efficiencies Greater than one.* Submitted to MRS conference San Francisco,1996.

(6) J. H Zollondz, W. Gao, R. Brüggemann, C. Main and G.H.Bauer, *The study of space charge effects by spectral response, steady state charge collection and transient photocurrents in thick a-Si:H pin diodes* Submitted to MRS conference San Francisco,1996.

(7) W. Gao, C.Main, S. Reynolds, and R. Brueggemann *The investigation of quantum efficiency much larger than unity in a-Si:H diodes.* (*in preparation*).